Modeling micromorphic damage in long carbon fiber reinforced plastics at different scales

Von der Fakultät für Bauingenieurwesen
der Rheinisch-Westfälischen Technischen Hochschule Aachen
zur Erlangung des akademischen Grades eines Doktors der Ingenieurwissenschaften
genehmigte Dissertation

vorgelegt von

Lukas Martin Poggenpohl, M. Sc.

Berichter*innen:	Universitätsprofessorin	Stefanie Reese
	Universitätsprofessor	Jaan-Willem Simon
	Universitätsprofessor	Stephan Wulfinghoff

Tag der mündlichen Prüfung: 30.03.2023

Acknowledgements

This cumulative dissertation represents the academic summary of my work as research associate at the Institute of Applied Mechanics (IFAM) at the RWTH Aachen University. In what follows, I would like to express my gratitude to all the people who helped me along this academic path. The English-speaking reader may forgive me my decision to write the following personal acknowledgements in German.

Diese Dissertation wäre ohne die großartige Atmosphäre mit den tollen Arbeitskollegen am Institut nicht zustande gekommen. Den Zusammenhalt, die Hilfsbereitschaft und die angeregten Diskussionen fachlicher aber auch nicht fachlicher Natur erlebt zu haben möchte ich nicht missen. Zudem haben sich aus meiner Zeit am IFAM sehr gute Freundschaften ergeben die das Potential haben, ein Leben lang zu halten. Deswegen möchte ich Frau Prof. Dr.-Ing. habil Stefanie Reese danken, dass sie dieses Institut in dieser Konstellation zusammengeführt hat und mir die Möglichkeit bot, unter ihrer Leitung zu promovieren. Ebenfalls möchte ich mich bei ihr dafür bedanken, dass ich neben meiner Promotion auch die Chance bekam, in Industrieprojeken Erfahrungen außerhalb der akademischen Arbeit zu sammeln.

Des weiteren möchte ich meinem ersten Betreuer, Prof. Dr.-Ing. Stephan Wulfinghoff, meinen herzlichsten Dank aussprechen. Durch seine intensive und persönliche Betreuung habe ich sehr viel über das Thema der gradientenerweiterten Schädigung erfahren dürfen. Vor allem die reichlichen Diskussionen auf dem Weg zum Mittagessen waren hier sehr hilfreich. Ihm ist es zu verdanken, dass ich so gut in das Thema und auch in die Forschungsarbeit eingestiegen bin.

Mein tiefer Dank gilt auch Dr.-Ing. Tim Brepols. Bereits als Mitdoktorand konnte ich mit ihm jederzeit offene Fragen diskutieren und bekam fast immer eine Lösung präsentiert. War dem einmal nicht so, bekam ich auf jeden Fall einen vielversprechenden Lösungsansatz. Unter seiner Betreuung, dann mit ihm in der Rolle des Oberingenieurs, entstand meine erste Veröffentlichung. Seiner intensiven Korrekturen mit mehrfachen Iterationsschleifen innerhalb des Instituts ist zu verdanken, dass der Reviewprozess beim Journal so reibungslos vonstatten ging.

An dritter Stelle möchte ich mich bei Herrn Prof. Dr.-Ing. habil Jaan Simon für seine exzellente Betreuung in den letzten zwei Jahren meiner Promotion bedanken. Die fachlichen Diskussionen, aber vor allem sein Führungsstil in der CoMaS-Gruppe haben diese Dissertation erst ermöglicht. Zwei Paper über ein neues Thema zu schreiben und das mit einer zeitlichen Restriktion von zwei Jahren war nicht einfach, doch durch seine Hilfe ist dies ursprünglich sogar vor Ablauf der zeitlichen Frist gelungen. Seine Art die CoMaS-Gruppe zu leiten sehe

ich als sehr erstrebenswert an.

Wie bereits weiter oben erwähnt, herrscht am IFAM eine ganz besondere Atmosphäre des Zusammenhalts und der Hilfsbereitschaft. Deswegen möchte ich mich hier bei allen aktiven und ehemaligen Kollegen bedanken. Es ist schön, dass ich immer ein offenes Ohr für fachliches wie privates fand und Probleme oftmals im Team statt alleine gelöst wurden. Gesondert erwähnt seien hier Katharina Martin, mit der sich auch eine enge private Freundschaft entwickelt hat, Hagen Holthusen, meinem Bürokollegen, für sein schier bodenloses Fachwissen, Lukas Lamm dafür, dass er immer ein offenes Ohr hat und für diverse Späße zu haben ist, sowie Bernd Kohl für seine Expertise bei den Experimenten und Hilfe bei privaten Projekten.

Neben den Menschen am Institut möchte ich mich auch bei meinen oftmals langjährigen Freunden jenseits der RWTH und vor allem bei meiner Familie bedanken. Ihr habt mich in vielerlei Hinsicht begleitet und beeinflusst. Bei Paul Bleyer möchte ich mich dafür bedanken, dass er mich seit einigen Jahren an der Seite meiner Mutter auf meinem Lebensweg begleitet. Ebenso gilt mein Dank Julia Poggenpohl, die seit vielen Jahren unser Familienleben bereichert und uns ein neues Familienmitglied geschenkt hat. Zudem möchte ich ganz besonders meinem Bruder und meiner Mutter danken, die Zeit meines Lebens für mich da waren und immer an mich geglaubt haben. Zu guter Letzt denke ich an meinen leider verstorbenen Vater, der mir so vieles auf meinem Lebensweg mitgegeben hat. Ich wünschte, du könntest meine Dissertation mit mir feiern. Ihr alle habt mich zu dem Menschen gemacht, der ich jetzt bin und mich dorthin gebracht, wo ich jetzt stehe.

Aachen, 2022 Lukas Martin Poggenpohl

Summary

Composites have been used for a long time in the history of mankind. Already in the times of the pharaohs, clay and straw were combined to build houses out of this material. In general, composites are used to combine the positive properties of the various components and produce materials with extreme properties or properties tailored to the application needs.

Nowadays, composites made from a combination of epoxy resin with glass fibers (so-called glass fiber reinforced plastics or GFRPs) or carbon fibers (so-called carbon fiber reinforced plastics or CFRPs) are used primarily in lightweight construction. The latter offer particularly high stiffness and strength combined with low density, making them an ideal material for lightweight construction applications. CFRPs are manufactured either from layers of parallel fibers laid on top of each other in different directions or from woven fabrics with different weave structures, which are usually filled with an epoxy resin. Due to the complex microstructure, even simple load cases lead to complex stress states within the material. In addition, CFRP exhibits brittle material failure with significant scatter in material parameters, leading to high factors of safety in applications. A more accurate prediction of the material behavior, especially in the area of material damage, would lead to a reduction of the safety factors and thus to a better design of CFRP structures.

This cumulative dissertation aims to contribute to a better understanding of the damage behavior of carbon fiber reinforced plastics. It consists mainly of three previously published scientific papers from the author and several co-authors. The aim of the publications was the simulation of the damage behavior of CFRPs both at the scale of the components and at the microscopic scale of the laminates and fabrics. Here, the material model used for brittle damage, without considering plasticity, is similar for all three publications. In the material model, gradient-extended (or micromorph) damage is used to produce mesh size-independent results.

The dissertation begins with an introduction to illuminate the research-relevant questions and to present the current state of research. This is followed by the first of a total of three scientific publications. Here, an isotropic material model for large deformations was extended by an anisotropic component in order to simulate the material behavior of CFRP on a macroscopic level. Both the isotropic and anisotropic portions were given their own scalar damage variable to distinguish between damage to the epoxy matrix (isotropic part) and damage to the carbon fiber (anisotropic extension). A tension-compression asymmetry was also introduced for both parts to account for the effect of crack closure. In addition, an anisotropy was introduced in the gradient term of the isotropic material part to account for the direction de-

pendence of the crack propagation. Finally, the material parameters of the numerical model were fitted to experimental results of unidirectional CFRP and the performance of the material model was evaluated.

In the second publication, the material behavior of CFRP was investigated on the microscale. Since a geometric distinction between fiber and matrix is possible on the microscale, only the isotropic part of the previously implemented material model was used. The aim of the publication was to develop a new homogenization approach with and without consideration of the interface between epoxy matrix and carbon fiber. The homogenization approach was based on the so-called failure zone averaging and aimed at deriving a material behavior for the next larger scale from simulations of the microscale. The approach took into account the energetic components from both the mechanical part of the model and the micromorphic extension. An examination of the power components showed that the micromorphic power is non-zero in the case of failure zone averaging, and even shows power peaks that exceed those of the mechanical power. However, in terms of the total energy dissipated in the system, it was shown that the energy dissipated by the micromorphic components is negligible. The publication concluded with simulations that included the interface between fiber and matrix. Here, a generally reduced strength with simultaneously increased dissipated energy was observed.

In the last publication, the previously presented homogenization method was applied to the load cases of simple shear, pure shear and mixed mode loading. It was shown that different load-deformation curves formed depending on the type of load, the geometry and whether the tension-compression asymmetry is activated. In particular, the orientation of the failure zone had a significant influence here. The publication again concluded with simulations that took into account the interface between fiber and matrix. Here, as before, an increased dissipation with simultaneously reduced strength was shown.

The dissertation concludes with an outlook on research-relevant questions arising from the results of the three published papers for future work in this area of research.

Zusammenfassung

Komposite finden in der Geschichte der Menschheit seit langem Anwendung. Bereits zu Zeiten der Pharaonen wurden Lehm und Stroh kombiniert, um hieraus Häuser zu bauen. Im Allgemeinen werden Komposite genutzt, um die positiven Eigenschaften der verschiedenen Komponenten zu kombinieren und Materialien mit extremen oder auf die Anwendungsbedürfnisse maßgeschneiderten Eigenschaften herzustellen.

Vorallem im Bereich des Leichtbaus werden heutzutage Komposite aus einer Kombination von Epoxidharz mit Glasfasern (so genannte glasfaserverstärkte Kunststoffe oder GFKs) oder Carbonfasern (so genannte carbonfaserverstärkte Kunststoffe oder CFKs) eingesetzt. Letztere bieten eine besonders hohe Steifigkeit und Festigkeit bei gleichzeitig geringer Dichte, was sie zu einem idealen Werkstoff für Anwendungen des Leichtbaus macht. Hergestellt werden CFKs wahlweise aus in unterschiedlichen Richtungen übereinander gelegten Schichten aus parallelen Fasern oder aus Gewebe mit unterschiedlicher Webstruktur, die üblicherweise mit einem Epoxidharz ausgegossen werden. Durch die komplexe Mikrostruktur führen selbst einfache Lastfälle zu komplexen Spannungszuständen innerhalb des Materials. Zudem zeigt CFK ein sprödes Materialversagen mit signifikanter Streuung der Materialparameter, was in der Anwendung zu hohen Sicherheitsfaktoren führt. Eine genauere Vorhersage des Materialverhaltens vorallem im Bereich der Materialschädigung würde zu einer Reduktion der Sicherheitsfaktoren und damit einer besseren Auslegung von CFK Strukturen führen.

Die vorliegende kumulative Dissertation möchte einen Beitrag dazu leisten, das Schädigungsverhalten carbonfaserverstärkter Kunststoffe besser zu verstehen. Sie besteht in der Hauptsache aus drei bereits veröffentlichten wissenschaftlichen Publikationen des Autors und mehrerer Koautoren. Ziel der Veröffentlichungen war die Simulation des Schädigungsverhaltens von CFKs sowohl auf der Skala der Bauteile als auch auf der mikroskopischen Skala der Laminate und Gewebe. Das verwendete Materialmodell für spröde Schädigung, ohne die Berücksichtigung von Plastizität, ist hierbei für alle drei Veröffentlichungen ähnlich. In dem Materialmodell wird die gradientenerweiterte (oder mikromorphe) Schädigung verwendet, um netzgrößenunabhängige Ergebnisse zu erzeugen.

Die Dissertation beginnt mit einer Einleitung um die forschungsrelevanten Fragen zu beleuchten und den aktuellen Stand der Forschung darzulegen. Es folgt die erste von insgesamt drei wissenschaftlichen Veröffentlichungen. Hier wurde ein isotropes Materialmodell für große Deformationen um einen anisotropen Anteil erweitert, um das Materialverhalten von CFK auf makroskopischer Ebene zu simulieren. Sowohl der isotrope als auch der anisotrope Anteil erhielten dabei eine eigene skalare Schädigungsvariable, um zwischen der Schädi-

gung der Epoxidmatrix (isotroper Teil) und der Schädigung der Carbonfaser (anisotrope Erweiterung) zu unterscheiden. Für beide Anteile wurde außerdem eine Zug-Druck-Asymmetrie eingeführt, um den Effekt der Rissschließung zu berücksichtigen. Zusätzlich wurde eine Anisotropie im Gradiententerm des isotropen Materialanteils eingeführt, um die Richtungsabhängigkeit der Rissausbreitung zu berücksichtigen. Schlussendlich wurden die Materialparameter des numerischen Modells an experimentelle Ergebnisse von unidirektionalem CFK gefittet und die Leistungsfähigkeit des Materialmodells beurteilt.

In der zweiten Veröffentlichung wurde das Materialverhalten von CFK auf der Mikroskala untersucht. Da hierbei auf der Mikroskala eine geometrische Unterscheidung zwischen Faser und Matrix möglich ist, wurde nur der isotrope Anteil des zuvor verwendeten Materialmodells genutzt. Ziel der Veröffentlichung war die Entwicklung eines neuen Homogenisierungsansatzes mit und ohne Betrachtung der Grenzschicht zwischen Epoxidmatrix und Carbonfaser. Der Homogenisierungsansatz basierte dabei auf der so genannten Versagenzonenmittelung und hatte das Ziel, aus Simulationen der Mikroskala ein Materialverhalten für die nächstgrößere Skala abzuleiten. Der Ansatz berücksichtigte hierbei die energetischen Anteile sowohl aus dem mechanischen Anteil des Modells, als auch aus der mikromorphen Erweiterung. Eine Untersuchung der Leistungskomponenten zeigte, dass die mikromorphe Leistung im Falle der Versagenzonenmittelung nicht null ist und sogar Leistungsspitzen zeigt, die über jenen der mechanischen Leistung liegen. Bezogen auf die insgesamt im System dissipierte Energie konnte jedoch gezeigt werden, dass die durch die mikromorphen Anteile dissipierte Energie vernachlässigbar klein ist. Die Veröffentlichung schloss mit Simulationen, die die Grenzschicht zwischen Faser und Matrix mit berücksichtigten. Hierbei zeigte sich eine allgemein verringerte Festigkeit bei gleichzeitig gesteigerter dissipierter Energie.

In der letzen Veröffentlichung wurde die zuvor dargestellte Homogenisierungsmethode auf die Lastfälle der simplen Scherung, der reinen Scherung und der gemischten Belastung aus Zug und Scherung angewandt. Es zeigte sich, dass sich verschiedene Last-Verformungs-Kurven ausbilden abhängig von der Art der Belastung, der Geometrie und ob die Zug-Druck-Asymmetrie aktiviert ist. Insbesondere die Orientierung der Versagenszone hatte hier einen bedeutenden Einfluss. Die Veröffentlichung schloss wiederum mit Simulationen, die die Grenz-schicht zwischen Faser und Matrix mit berücksichtigten. Hierbei zeigte sich, wie zuvor, eine erhöhte Dissipation bei gleichzeitig verringerter Festigkeit.

Die Dissertation schließt mit einem Ausblick auf forschungsrelevante Fragen, die sich aus den Ergebnissen der drei veröffentlichten Fachartikel für zukünftige Arbeiten auf diesem Forschungsgebiet ergeben.

Contents

1 Introduction

1.1 Motivation

Composite materials, e.g. glass or carbon fiber reinforced plastics (GFRP or CFRP), are increasingly being used in modern lightweight construction applications. The application scenarios for CFRP here range from carbon reinforced concrete to wind turbine blades and automotive construction to use in the aerospace industry. For the latter, the use of different composites has increased in each new generation of aircraft. CFRPs are made from layers of parallel carbon fibers or woven carbon fiber fabrics combined in various configurations to suit the loading scenario. The layers are then embedded in an epoxy matrix to form the structural component. CFRPs are used because they have a high stiffness to density and strength to density ratio. However, they fail brittly and generally exhibit a wide variation in material properties such as ultimate strength. Therefore, high safety factors are required to prevent catastrophic failure of the components. A better understanding of the failure mechanisms would lead to improved utilization of the material.

The use of damage and fracture mechanics offers the possibility of gaining more insight into the onset and progression of stiffness degradation. However, the accurate modeling of damage and fracture – especially in composites – is still a topic of extensive research and discussion. Unlike plasticity, for which standard models such as von Mises plasticity exist, there is no standard model for modeling damage. Consequently, damage models such as the one used in this thesis are not found in industrial applications. Stress or strain-based failure criteria such as the Pucks failure criterion (see, e.g. [Puck, 1992]) in the case of fiber laminates are more commonly used here. While these criteria indicate the onset of damage, they cannot predict the evolution of damage or ultimate failure. In other models used in industrial applications, material degradation is part of a plasticity model and therefore only applicable to materials that exhibit a significant degree of plastic deformation.

The components of CFRP have very different material properties. The carbon fibers are characterized by high stiffness and strength, but usually have a small diameter of only a few $\mu\mathrm{m}$. Therefore, they can conduct the load only in the fiber direction. In contrast, the epoxy

matrix is characterized by much lower stiffness and strength, but forms a homogeneous structure after curing. The flexural and shear stiffness of CFRP results from the combination of the two components, with shear forces being transmitted through the epoxy matrix. Due to the lower strength of the matrix, the overall load-bearing capacity of CFRP is mainly determined by the strength of the epoxy resin and the interfacial strength between fiber and matrix. Due to the often complex internal structure of CFRP, even simple loading conditions such as uniaxial tension result in complex loading conditions in the material. A better understanding of damage initiation and propagation under these complex loading conditions would lead to a better understanding and performance of CFRP. Therefore, further research is needed to gain a better understanding of the initiation and propagation of damage in CFRP at the macro level, but more importantly of the complex geometry at the micro level. For the latter, new homogenization approaches are needed to obtain reliable results.

1.2 State-of-the-art in damage modeling of CFRPs at different scales

In the following, the origin as well as the state-of-the-art in damage modeling – especially of composites – will be summarized. Following the fundamental aspects of damage modeling, a brief summary of the most used damage models for CFRPs will be given. Thereafter, the origin as well as state-of-the-art of damage modeling at the micro scale is summarized.

1.2.1 Fundamentals of damage mechaincs

The first consideration of damage within the continuum mechanical framework is usually associated with [Kachanov, 1958]. Here, creep damage was studied, and the scalar variable ψ (where $0 \leq \psi \leq 1$) denoted a normalized time to fracture, with $\psi = 1$ representing an undamaged (i.e., virgin) material and $\psi = 0$ representing a fully damaged (i.e., fractured) material. In the later work of [Rabotnov, 1963, 1969] the damage variable $D = 1 - \psi$ was introduced, which is now used in most publications. Here, damage was interpreted as a reduction in cross-sectional area, a phenomenological approach that is commonly used. The concept of 'effective' stresses, considered as the magnified stresses of the reduced cross-sectional area, is based on this interpretation. In most models, the damaged state (with reduced cross section) is linked to a fictitious undamaged state (with full cross section). Most commonly, either the so-called principle of strain equivalence or the so-called energy equivalence principle is used. The first principle was introduced by [Lemaitre, 1971] and assumes that both states

undergo the same deformation. The latter principle was introduced by [Cordebois and Sidoroff, 1982] and assumes that strain energy is preserved between both states. Based on those pioneering works, damage is now applied in many material formulations (see, e.g. [Skrzypek and Ganczarski, 1999] for a comprehensive overview).

As discussed above, the irreversible reduction of material parameters such as stiffness or strength generally is associated with growth of cracks and voids that reduce the effective cross-sectional area of the material as first discussed in [Rabotnov, 1963]. Perfect spherical voids are assumed to cause the same reduction in cross-sectional area in any spatial direction, while ideal cracks cause a reduction in cross-sectional area only perpendicular to the crack plane. The former can be modeled with one scalar damage variable as was used in the early works of [Rabotnov, 1963, 1969; Lemaitre, 1971]. For the latter, a set of scalar damage variables can be used as shown in the early work of [Bažant and Gambarova, 1984]. Here, the scalar damage variables were associated to micro planes of the material. Another possibility is the use of tensorial damage variables of different order. The most common damage tensor is a tensor of second order as introduced by [Vakulenko and Kachanov, 1971; Murakami and Ohno, 1981] or applied in the more recent publications [Fassin et al., 2019*a*,*b*]. In the latter publications, a symmetric damage tensor is used and thus, six independent entries are found. By using a fourth order damage tensor, the number of independent entries can reach up to 81, while the number can be decreased to 36 or 21 depending on the symmetry conditions applied. In analogy to the stiffness tensor of fourth order, the number of independend entries can be decreased further. Amongst others, a fourth order damage tensor was used in [Chaboche, 1978, 1984; Sidoroff, 1981] where it was shown that a fourth order tensor can represent more complex damage states. However, the handling of up to 81 independent entries is a challenging task. As presented in [Chaboche, 1978], the application of an eight order tensor is possible as well, but this task is even more challenging from a mechanical as well as from a numerical point of view.

1.2.2 Damage modeling in composites

As in [Fassin et al., 2019*a*,*b*], many material models using an anisotropic damage formulation feature an initially isotropic material such as metals. The anisotropy is induced during the deformation process due to damage. However, CFRPs are initially anisotropic and consist of carbon fibers and an epoxy matrix, two materials with distinctive material properties. Thus, the most common damage mechanisms within one unidirectional ply are

- matrix cracking in tension,

- matrix shear bands in compression,
- failure of the fiber matrix interface,
- fiber cracking,
- fiber pull out and
- fiber buckling.

As introduced by [Ladevèze, 1992] and further investigated, e.g., by [Maimí et al., 2007; van der Meer and Sluys, 2009; Mukhopadhyay and Hallett, 2019; Dean et al., 2021], a set of scalar damage variables was used to account for these failure mechanisms separately. It was shown exemplary in [Cuntze, 2006; Läufer et al., 2017] that models using two damage variables gave satisfactory results while keeping a minimum number of internal variables. Here, the material response was split into an isotropic part and an anisotropic part. Usually, the isotropic part was associated with the response of the matrix material while the anisotropic part was associated with the response of the fibers. However, as shown in [Chen and Aliabadi, 2019; He et al., 2020], more freedom of choice was achieved when six scalars were introduced. Using this approach, the afore mentioned failure mechanisms were taken into account individually. But this advantage came at the cost of an increased number of internal variables. In other works like [Voyiadjis and Deliktas, 2000],[Chow and Wei, 1999] or [Ryvkin and Aboudi, 2020], the use of fourth order tensors to cover these effects was investigated. An alternative approach for the simulation of damage in woven composites was investigated, e.g. in [Bednarcyk et al., 2015] or [Simon et al., 2017]. In this approach, a general framework based on the so called damage interaction matrix was given. This interaction matrix allowed to control the evolution and interaction of the different damage mechanisms mentioned above. However, for all approaches on the modeling of damage within composites, damage initiation and evolution has to be justified either experimentally or numerically. For a numerical justification, the simulation of repeating unit cells (RUCs) has been proven useful.

1.2.3 Multiscale modeling of damage in RUCs

The terms repeating unit cell (RUC) and representative volume element (RVE) are often used interchangeably. However, not all RUCs are also RVEs. RUCs are generally used at the so-called microscale, where the various constituents such as epoxy matrix and individual carbon fibers can be resolved. Generally, RUCs and RVEs have to fulfill the condition of the separation of scales, where the size of the RUC has to be much smaller within the next higher scale

(i.e. indistinguishable from a material point). In the case of paperboard, this separation of scales can not be fulfilled. Therefore, the entire thickness of the paper is modeled. In RUCs, the geometry is generally periodic in any spatial direction. Therefore, RUCs are often used to simulate CFRP with a regular distribution of fibers. However, as will be seen in section 3.5, RUCs can also be generated with a random fiber distribution. For a RUC to become an RVE, it must be able to produce statistically meaningful results (see, e.g. [Geers et al., 2010; Geers, Kouznetsova, Matouš and Yvonnet, 2017] or [Yu, 2016]). In addition to the maximum size defined above, the RUC must still be large enough to cover the spatial distribution of its components. To prove the representativeness of a RUC, either a size convergence study or a statistical study must be performed.

Simulations of RVEs usually provide stress and strain fields as a result. With the help of the so-called homogenization approaches, representative stresses and strains are derived from these strain fields. The most common homogenization scheme is the so-called Hill's approach as introduced in [Hill, 1967, 1972]. This approach is based on the equivalence between the virtual work density of the RVE and the material point of the next higher scale. As summarized in the comprehensive work of [Geers, Kouznetsova, Matouš and Yvonnet, 2017], this equivalence together with the application of appropriate boundary conditions leads to Hill's homogenization approach. Here, the homogenized stress is the volume average of the stress field of the entire RVE. This homogenization approach is widely used in the recent literature (see, e.g. [Tsalis et al., 2013; Kammoun et al., 2015; Chatzigeorgiou et al., 2016; Elnekhaily and Talreja, 2018; He et al., 2020; Trofimov et al., 2021; Mikeš et al., 2021; Meade et al., 2021] just to name a few). However, when damage is considered, so-called localization zones are formed. These localization zones develop due to locally softened material, where strains accumulate until almost all deformation of the RVE is covered in this area. As shown by [Gitman et al., 2004, 2007] or [Geers et al., 2010], a size convergence study does not lead to a converged solution when Hill's approach is applied. For example, it was found in [Gitman et al., 2004] that the appearance of localization bands lead to a mismatch of the dimensions of the dissipative volume (i.e., the localization zone) and the stored elastic energy (i.e., volume of the RVE). Therefore, standard Hill homogenization cannot be applied when these localization phenomena are present.

In [Nguyen et al., 2010], a new homogenization approach was developed based on the work of [Verhoosel et al., 2010]. In this approach, the volume of interest is restricted to the actively damaging volume (i.e., the volume in which the damage variable D evolves) and the volume average of this region is used. In [Nguyen et al., 2010] and subsequent publications [Nguyen et al., 2011, 2012], it was shown that a representative RVE size can be found using

this approach. In other recent work by [Turteltaub et al., 2018; Turteltaub and de Jong, 2019; Turteltaub and Suárez-Millán, 2020] as well as [Ke and Van Der Meer, 2021], a similar approach is applied to simulations of cracks within RVEs. In these simulations, cohesive zone elements are used to model cracking at the microscale.

1.2.4 Localization phenomena and gradient extended damage

The stress-strain response of material models with damage usually shows three characteristic regions. In the elastic region, no damage occurs and the material shows the same stress-strain response during loading and unloading. Further loading leads to the development of damage and thus to a reduction in material stiffness (i.e., a softer material response). During unloading, the material response follows a secant between the origin and the last point of the stress-strain curve. However, the slope of the stress-strain curve at further loading is positive. Therefore, this behavior is called strain hardening. With further loading, the maximum stress is reached, and thereafter the slope of the stress-strain curve is negative. Since the stress decreases with further loading, this region is called strain softening.

If a material exhibits strain softening behavior, this can lead to bifurcation of the solution, as reported, for example, by [Jirásek, 2018]. Furthermore, the boundary value problem may exhibit an undesirable pathological mesh size dependence of the finite element simulation, as reported e.g. by [Bažant and Gambarova, 1984] or [de Borst et al., 1993]. Several methods can be used to overcome this dependence on mesh size. One of the early approaches was to fit the hardening law to the element size, as presented in [Pietruszczak and Mróz, 1981]. Later approaches considered higher order continua such as strain gradient or gradient damage models such as the micromorphic approach introduced by [Forest, 2009, 2016]. Here, the so-called micromorphic damage variable D^χ is introduced as an additional degree of freedom associated with the local damage variable D. Since D^χ is a degree of freedom, contact forces between neighboring material points of the continuum can be introduced, leading to a higher spatial order formulation. The micromorphic extension is introduced in the material model used in this dissertation. As shown in 2.4.2, 3.6.1, and 4.6.1, the micromorphic extension effectively cures the pathological mesh size dependence.

1.3 Outline of the dissertation

This dissertation is concerned with the modeling of damage of unidirectional long carbon fiber reinforced plastics (UD CFRPs) at the macro scale and the micro scale. In UD CFRPs, all car-

bon fibers have the same orientation and thus show high values of stiffness and strength in this direction as will be shown in the first publication in Chapter 2. Here, a brittle damage model was derived to simulate macroscopic failure of CFRPs using an anisotropic extension of the St. Venant-Kirchhoff material model. Two scalar damage variables were used for the isotropic part and anisotropic extension, respectively. To overcome mesh dependend results, the micromorphic extension was applied to both damage variables. Main aspect of the publication was the fitting and comparison to experimental results from uniaxial tension tests. It was shown that the standard formulation of the micromorphic extension does not lead to satisfactory failure modes. Thus, an anisotropy was introduced into the gradient term of the micromorphic extension of the isotropic material part.

In the second publication, which is presented in Chapter 3, a failure zone homogenization strategy was developed. Aim was to simulate the damage initiation and progression until final failure on the micro scale, where carbon fibers and epoxy matrix can be resolved geometrically. Both constituents were simulated using the isotropic part of the material model presented in Chapter 2. Within the failure zone homogenization approach, the volume of interest is restricted to all material points with an increasing damage variable. The new homogenization approach took into account all energetic contributions and was tested by means of a statistical analysis. In addition, different strategies for geometry generation were presented and and compared. Finally, simulations were shown who take into account the debonding of the interface between fiber and matrix. Here, a lower strength but a higher dissipated energy was found. It was concluded that this effect was due to the much higher deformation until final failure compared to simulations with perfect interfaces.

In Chapter 4, the third publication is shown. Here, micro scale simulations at shear and mixed mode loading were analyzed using the failure zone homogenization introduced in Chapter 3. Again, the isotropic part of the material model presented in Chapter 2 was used. In the case of shear loading, the load cases simple shear, as well as pure shear were investigated. It was found that different stress-stretch responses were obtained for these two shear loadings even though, the same dissipated work was found for both loadings. Further, it was shown that different stress deformation curves are found depending on the orientaion of the localization zone. At the end of the publication, simulations including debonding effects between fiber and matrix were shown. As in the second publication, a higher dissipation potential and a lower strength as well as higher deformation until final failure were observed.

2 Article 1: Towards brittle damage in carbon fiber reinforced plastics: A gradient extended approach

This article was published as:

Poggenpohl, L., Brepols, T., Holthusen, H., Wulfinghoff, S. and Reese, S. [2021], 'Towards brittle damage in carbon fiber reinforced plastics: A gradient extended approach', *Composite Structures* **255**, 112911.

Disclosure of the individual authors' contributions to the article:

S. Wulfinghoff developed the theory of the presented gradient extended framework. Furthermore, he developed the basis of the finite element code and parts of the material model used. L. Poggenpohl extended the material model and finite element code towards the use of two scalar damage variables. The introduction of the structural tensor into the micromorphic gradient term was developed and implemented by L. Poggenpohl as well. In Addition, he set up and analyzed all numerical simulations. Furthermore, L. Poggenpohl conducted the experiments, analyzed the experimental results and fitted the material parameters. H. Holthusen gave valuable advice about the content of the paper, especially section 2.3. T. Brepols and S. Reese supervised the writing of the article and gave valuable feedback about the overall structure as well as the presentation of the theory. All authors approved the publication of the final version of the manuscript.

Abstract. This work is concerned with material modeling of carbon fiber reinforced plastics (CFRPs) with the prospect of application to shear cutting. It is assumed that the use of CFRPs for body parts is of great benefit in the field of lightweight construction. The presented material model distinguishes between damage in the isotropic and anisotropic part. It represents a special case of a more general thermodynamical framework. Furthermore, the micromorphic approach is used to overcome undesired mesh dependencies. A mesh convergence study is performed and the resultant force displacement curves are analyzed quantitatively. Tension tests are performed and the material model is fitted as well as tested on this data. The experimental data is used to justify the choice of the material model. Novelty of this work lies in an comparison of the crack paths of experiments and simulations. A direction dependence is included in the gradient term of the micromorphic extension to obtain the same crack paths in simulation and experiments.

2.1 Introduction

For car manufacturing, the use of light weight design became important within the last decades. As shown in [Yamane and Furuhama, 1998; Witik et al., 2011], lighter and at the same time stiffer constructions offer better characteristics in driving dynamics and – due to the lower weight – improvements in fuel consumption. Especially for battery-operated electric vehicles, the weight of the car influences the range the vehicle can cover with one battery charge.

A smaller weight of the manufactured car can either be achieved by improving the structural design or via utilizing materials which show a better stiffness to density (specific stiffness) or strength to density (specific strength) ratio. Carbon fiber reinforced plastics (CFRPs) show good material properties for both of these categories. Depending on the type of carbon fiber, the specific strength and the specific modulus of CFRPs can be several times higher than that of metals (see, e.g. [Rösler et al., 2013]).

As shown by [Witik et al., 2011], the costs of producing and especially processing CFRPs are higher than those for aluminum or steel, the latter of which represents the majority of the used material for car body parts. [Azmi et al., 2013] state that most of the costs for processing are due to the milling and drilling of the semi-finished CFRP product. To reduce these machining costs, it is being considered to replace milling and drilling with a punching process as suggested by [Abdullah et al., 2019].

The available literature on punching of sheet metals is vast. However, there are only few publications on punching of CFRPs such as [Shirobokov et al., 2015], in which experimental investigations of unidirectional CFRP under blanking were performed. In the mentioned work, the influence of the geometry of the cutting edge as well as the clearance on the quality of the shear surface were investigated. Furthermore, results for the cutting force over punch stroke for unidirectional CFRPs are given in this publication. The curves show a characteristic, in which a recovery of material stiffness can be observed after an initial drop in the punch force. In the quite new paper of [Abdullah et al., 2019], an experimental study of the effects of the punch geometry on the maximum punch load as well as the

quality of the punched hole was conducted. To fully understand the material response of CFRPs under the complex shear and compression loading during shear cutting, further numerical and experimental investigations are needed.

The modeling of the failure beharior of CFRPs is discussed, e.g by [Tsai and Wu, 1971], [Puck and Schürmann, 2002], [Cuntze, 2006], [Catalanotti et al., 2013] or [Läufer et al., 2017], to name just a few. In [Tsai and Wu, 1971], a first approach towards a scalar failure function based on stress state analysis is introduced. [Puck and Schürmann, 2002] propose an improved stress based criterion for the failure of CFRPs. This criterion is validated by experimental test data. Furthermore, the term 'interfiber fracture' is introduced in the latter publication, indicating that matrix and fiber can damage separately. Additionally, it is stated in this paper that nonlinearities in the material response can be caused by microdamage, matrix cracking and changes in the fiber angle with increasing strains. A good literature review and a suggestion for a further improved stress based criterion can be found in [Catalanotti et al., 2013]. [Cuntze, 2006] suggests to distinguish between failure of the matrix material and failure of the fibers, respectively, an approach which is also used by [Läufer et al., 2017] and which will be applied in this study as well. In [Läufer et al., 2017] a gradient approach for each of the three introduced damage variables is used to overcome undesired mesh dependencies.

In [Poggenpohl et al., 2018] a connection is established between the suggestion of [Cuntze, 2006] and [Läufer et al., 2017] (distinction of failure in fiber and matrix part) and the findings of [Shirobokov et al., 2015] (recovery of material stiffness during punching). Basic assumptions are a matrix material which is weaker than the fibers and the consideration of finite rotations in the cutting plane. The force displacement curves are interpreted in an idealized way as follows:

1. The much weaker matrix material begins to fail first.

2. After sufficient deformation in the cutting plane, fiber reorientation takes place and an increase of the material stiffness in the cutting plane can be investigated.

3. When the deformation is large enough, fiber rupture takes place, resulting in a complete loss of material stiffness within the cutting plane.

In Fig. 2.1, a picture of a specimen after an incomplete cutting process is shown. In this picture it can be seen that the matrix material in the cutting plane is completely broken while still some intact fibers in the cutting plane can be identified. The regain of stiffness during shear cutting is in agreement with findings of [Höwer et al., 2017], who investigated fiber bridging in peeling tests of sandwich panels.

Since in this work stiffness degradation until complete failure will be simulated, continuum damage models (CDM) can lead to bifurcation of the uniform state as reported, e.g. by [Jirásek, 2018] or undesired mesh dependency of finite element simulations as it was reported by, e.g. [Bazant et al., 1984] and [de Borst et al., 1993]. One possibility to overcome these mesh dependencies is to apply the so-called micromorphic approach as it was discussed by [Forest, 2009, 2016]. Among others, [Brepols et al., 2017, 2020] used this method for the regularization of an elastoplastic damaging material model

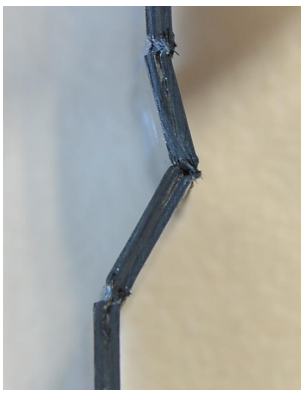

Figure 2.1: Closeup of an incomplete shear specimen from [Poggenpohl et al., 2018].

for small and finite strains, respectively. Also, [Fassin et al., 2019*a*,*b*] used the micromorphic approach for the regularization of an anisotropic damage model based on a second order damage tensor. As can be seen in [Bayerschen et al., 2015; Wulfinghoff et al., 2013], the micromorphic approach can also be applied for (gradient enhanced) plasticity models.

2.2 Derivation of the material model

In the following section, the material model will be derived. The material model is based on a specific choice of the Helmholtz free energy. From the material model presented in [Reese, 2003] simplifications as well as an extension regarding damage in a nonlocal form will be shown.

2.2.1 Choice of the Helmholtz free energy

In [Reese, 2003] a material model for the elasto-plastic, anisotropic behavior of pneumatic membranes is derived. It will be shown later on, that the material investigated shows a brittle damage behavior with negligible plasticity. Therefore, the elastic Helmholtz free energy takes the following form:

$$\psi_e = \psi_e \left(\boldsymbol{C}(\boldsymbol{F}), \boldsymbol{H} \right). \tag{2.1}$$

Here, the deformation gradient $\boldsymbol{F} = \partial \boldsymbol{x} / \partial \boldsymbol{X}$, with $\boldsymbol{x}$ and $\boldsymbol{X}$ denoting the position vectors in current ($\boldsymbol{x}$) and reference ($\boldsymbol{X}$) configurations is used. Tensor $\boldsymbol{H}$ represents the so called structural tensor. The right Cauchy Green tensor, denoted as $\boldsymbol{C}$, can be calculated from $\boldsymbol{C} = \boldsymbol{F}^T \boldsymbol{F}$. It shall be mentioned that in [Reese, 2003] two structural tensors are used, whereas for transversal isotropy, one structual tensor is sufficient.

As described in [Holthusen et al., 2020], [Cuntze, 2006] and [Läufer et al., 2017], a distinction into damage of the isotropic and damage of the anisotropic part shows satisfactory results. In other works (e.g. [Holthusen et al., 2020]), the isotropic part is referred to as matrix part, where the anisotropic

extention is referred to as fiber part, respectively. However, the first-mentioned terminology (with the terms isotropic and anisotropic part) is used in this work. Reason for this can be found in the micro geometry of CFRP. If the fibers vanished, the remaining matrix material, due to the micro geometry consisting of long holes, would still show anisotropic behavior. A clear distinction into an (isotropic) matrix and an (anisotropic) fiber part is not possible.

Following the aforementioned works, two scalar damage variables D_1 and D_2 are introduced, which are the only considered internal variables. In other works (e.g. [Brepols et al., 2017; Fassin et al., 2019*a*; Wulfinghoff et al., 2017]), a (single) damage hardening variable ξ_d in analogy to the accumulative plastic strain is introduced. However, since no damage healing is considered in this work, the evolution of damage is only positive ($\dot{D}_1 \geq 0$, $\dot{D}_2 \geq 0$) meaning that $\xi_{d,1} \equiv D_1$ and $\xi_{d,2} \equiv D_2$. The variables and internal variables of the present material model are summarized below:

$$\boldsymbol{H} = \boldsymbol{n}_r \otimes \boldsymbol{n}_r; \quad \boldsymbol{C}; \quad D_1; \quad D_2 \tag{2.2}$$

In the above, $\boldsymbol{n}_r$ describes the normalized vector fiber direction in plane w.r.t. the reference configuration. Consequently, $\boldsymbol{H}$ is a structural tensor of the reference configuration. The normalized in plane fiber direction w.r.t. the current configuration $\boldsymbol{n}_c$ can be computed via a push forward operation $\boldsymbol{n}_c = \boldsymbol{F}\boldsymbol{n}_r$. Experimental investigations in Section 2.4.1 show that the maximum endurable strain is about 2%. Thus, a St. Venant-Kirchhoff type material model is used in the following. The relation of the right Cauchy-Green tensor and the Green-Lagrange strain tensor is given via $\boldsymbol{E} = \frac{1}{2}[\boldsymbol{C} - \boldsymbol{I}]$. Having this in mind, the specialization of the general Helmholtz free energy in the present study reads

$$\psi = \quad \psi\left(\boldsymbol{E}, \boldsymbol{H}, D_1, D_2\right). \tag{2.3}$$

Since damage can lead to undesired mesh dependencies in finite element simulations, a micromorphic extension as introduced in [Forest, 2009] is used, leading to

$$\psi = \quad \psi\left(\boldsymbol{E}, \boldsymbol{H}, D_1, D_2, D_1^{\chi}, D_2^{\chi}, \nabla_0 D_1^{\chi}, \nabla_0 D_2^{\chi}\right). \tag{2.4}$$

The term D_m^{χ} in the above equation describes the micromorphic counterpart of the damage variable D_m and ∇_0 indicates the gradient w.r.t. the reference configuration. The free energy function ψ is split into two elastic terms ψ_1 and ψ_2, a hardening term ψ_h, a gradient term ψ_g and a micromorphic term ψ_{χ}:

$$\begin{aligned}\psi = [1 - D_1]^{n_1}\psi_1(\boldsymbol{E}) + [1 - D_2]^{n_2}\psi_2(\boldsymbol{E}, \boldsymbol{H}) + \psi_h(D_m) + \psi_g(\boldsymbol{H}, \nabla_0 D_1^{\chi}, \nabla_0 D_1^{\chi}) \\ + \psi_{\chi}(D_1, D_2, D_1^{\chi}, D_2^{\chi})\end{aligned} \tag{2.5}$$

It should be pointed out, that in the gradient term, structural tensor $\boldsymbol{H}$ is used. Following e.g. [Reese et al., 2020], the elastic parts of the Helmholtz free energy can be written in terms of the invariants. As

shown in [Itskov, 2009] for a material model depending on only two tensors ($\boldsymbol{E}$ and $\boldsymbol{H}$), ten invariants (J_1 to J_{10}) have to be considered. The invariants read:

$$\begin{aligned} &J_1 = \text{tr}[\boldsymbol{E}],\ J_2 = \text{tr}[\boldsymbol{E}^2],\ J_3 = \text{tr}[\boldsymbol{E}^3],\ J_4 = \text{tr}[\boldsymbol{H}],\ J_5 = \text{tr}[\boldsymbol{H}^2],\ J_6 = \text{tr}[\boldsymbol{H}^3], \\ &J_7 = \text{tr}[\boldsymbol{E}\,\boldsymbol{H}],\ J_8 = \text{tr}[\boldsymbol{E}^2\,\boldsymbol{H}],\ J_9 = \text{tr}[\boldsymbol{E}\,\boldsymbol{H}^2],\ J_{10} = \text{tr}[\boldsymbol{E}^2\,\boldsymbol{H}^2] \end{aligned} \tag{2.6}$$

Since the eigenvectors of $\boldsymbol{H}$ are formed by the unity vector $\boldsymbol{n}_r$ (see Equation (2.2)) it can be shown that this tensor is constant and the following identity holds:

$$\boldsymbol{H}^2 = \boldsymbol{H} \tag{2.7}$$

Consequently, the invariants J_4 to J_6 are equal and constant. For the same reason, the invariants J_7 and J_9 as well as the invariants J_8 and J_{10} are equal. If it is assumed that the energy density function for disappearing strains is zero, it follows that the contribution of invariants J_4 to J_6 must vanish. For the present material model, invariants J_3 and J_8 are neglected as well. Thus, only invariants J_1, J_2 and J_7 are considered in analogy to [Qiu and Pence, 1997]. Following these assumptions, the specific choice for the elastic Helmholz free energy is of linear type and reads:

$$\psi_1 = \frac{\lambda_1}{2} J_1^2 + \mu_1\, J_2 \tag{2.8}$$

$$\psi_2 = \frac{E_2}{2}\, J_7^2 \tag{2.9}$$

As can be seen in Equation (2.8), the isotropic part of the material is described using a St.Venant-Kirchhoff material model with the well known Lamé Parameters λ_1 and μ_1. As in [Qiu and Pence, 1997], the anisotropic extension (2.9) only takes into account invariant J_7. Material parameter E_2 accounts for the additional material stiffness in fiber direction and is considered a macroscopic parameter of the composite itself. A consideration of the volume fraction of the fibers, as used by [Holthusen et al., 2020] for example, is not applied in this work, but already accounted for in the macroscopic material constants. The present extension is a simplification of the general model of e.g. [Reese, 2003] where also the invariants J_5 and J_1 are accounted for in the anisotropic extension.

In Equation (2.10), the damage hardening and damage threshold terms are shown:

$$\psi_h = \sum_{i=1}^{2} \frac{K_i}{2} D_i^2 + \frac{H_i}{2} \langle D_i - D_{i,0} \rangle^2 \tag{2.10}$$

It can be seen from equation (2.10), that ψ_h takes the same form for D_1 and D_2. This holds true for ψ_g and ψ_χ and resultant quantities as well. To faciliate future terms, index i with $i = [1, 2]$ refers to values, terms or material constants corresponding to D_1 or D_2, respectively. The first terms of Equation (2.10) with material constants K_i describe the linear damage hardening. Higher values of K_i lead to a 'slow

down' of damage evolution. In the second term, $\langle * \rangle$ denotes the Macauley bracket defined as

$$\langle * \rangle = \begin{cases} 0 & \text{for } * \leq 0 \\ * & \text{for } * > 0 \end{cases} \tag{2.11}$$

Terms $H_i \langle D_i - D_{i,0} \rangle / 2$ with high values for H_i ensure that the damage threshold variables (e.g. $D_{i,0} = 0.999$) are not exceeded too much and $D_i < 1$ holds. The gradient term and the micromorphic term take the form:

$$\psi_\chi = \sum_{i=1}^{2} \frac{H_i^\chi}{2} \left(D_i^\chi - D_i \right)^2 \tag{2.12}$$

$$\psi_g = \sum_{i=1}^{2} \frac{E_i l_i^2}{2} \left(\nabla_0 D_i^\chi \cdot \boldsymbol{T}_i \left[\nabla_0 D_i^\chi \right] \right) \tag{2.13}$$

Here, term $(* \cdot *)$ corresponds to the scalar product of two vectors or tensors and term $(\boldsymbol{T}[*])$ stands for the application of tensor $\boldsymbol{T}$ on $(*)$. From the micromorphic term shown in Equation (2.12), the couplings of the local damage variables (D_i) and the (nonlocal) micromorphic damage variables (D_i^χ) become apparent. If the penalty factor H^χ is chosen high enough, the difference between D and D^χ tends to be negligibly small. In the extreme case of $H^\chi \to \infty$, the micromorphic term D^χ takes the same value as the local term D. In the gradient part (Equation (2.13)), the tensors $\boldsymbol{T}_i$ and material constants l_i are introduced. Constants E_i represent Young's Modulus and the additional stiffness in fiber direction, respectively. Parameters l_i can be linked to an internal length scale introduced by the gradient term. This formulation is also used by [Fassin et al., 2019*a*] and yields the advantage that the internal length is controlled via a length-like variable. The relation between the introduced lengths l_i and the parameters A_i as used, e.g. by [Forest, 2009; Brepols et al., 2017] can be found via the relation $l_i^2 = A_i / E_i$. With tensors $\boldsymbol{T}_i$ a direction dependency of $\nabla_0 D^\chi$ can be included. Alternatively, it can be considered that $\boldsymbol{T}_i$ influence the internal lengths in a way, that they vary in different directions. For the investigated material, the $\boldsymbol{T}_i$ are chosen as follows:

$$\boldsymbol{T}_1 = (1 - \gamma) \boldsymbol{I} + \gamma \boldsymbol{H} \tag{2.14}$$

$$\boldsymbol{T}_2 = \boldsymbol{H} \tag{2.15}$$

Equation (2.15) makes clear that the gradient of the anisotropic part has only an influence in fiber direction. It is assumed that fibers do not interact with each another and therefore this assumption is reasonable. In Equation (2.14) the rule of mixture for the isotropic part becomes visible, where γ represents the grade of asymmetry and $0 \leq \gamma \leq 1$ holds. For $\gamma = 0$, $\nabla_0 D_1^\chi$ will evolve in the general isotropic manner while for $\gamma = 1$, $\nabla_0 D_1^\chi$ will evolve in the same way as $\nabla_0 D_2^\chi$. Experiments have shown that damage of the matrix evolves mainly in fiber direction. As will be shown later in section

2.4.2.5, the introduction of $\boldsymbol{T}_i$ is needed to see the same crack paths in experiments and simulation.

2.2.2 Clausius-Duhem inequality

Introduction of ψ_χ and ψ_g with its nonlocal terms D_i^χ and their gradients $\nabla_0 D_i^\chi$ lead to the following extension of the Clausius-Duhem inequality [Forest, 2019; Diamantopoulou et al., 2018; Läufer et al., 2017]:

$$-\dot{\psi} + \boldsymbol{S} \cdot \dot{\boldsymbol{E}} + \underbrace{\sum_{i=1}^{2} a_i \dot{D}_i^\chi + \boldsymbol{b}_i \cdot \nabla_0 \dot{D}_i^\chi}_{\text{micromorphic extensions}} \geq 0 \tag{2.16}$$

Here, a_i and $\boldsymbol{b}_i$ denote the work conjugate stress like quantities of the micromorphic damage variables D_i^χ. Applying the chain rule on $\dot{\psi}$, inequality (2.16) can be rewritten as follows:

$$\left(\boldsymbol{S} - \frac{\partial \psi}{\partial \boldsymbol{E}}\right) \cdot \dot{\boldsymbol{E}} + \sum_{i=1}^{2} \left(a_i - \frac{\partial \psi}{\partial D_i^\chi}\right) \dot{D}_i^\chi + \left(\boldsymbol{b}_i - \frac{\partial \psi}{\partial \nabla_0 D_i^\chi}\right) \cdot \nabla_0 \dot{D}_i^\chi - \frac{\partial \psi}{\partial D_i} \dot{D}_i \geq 0 \tag{2.17}$$

This expression must hold for arbitrary thermomechanical processes. A common choice is now to set the terms in the brackets to zero, which results in the following relations:

$$\boldsymbol{S} = \frac{\partial \psi}{\partial \boldsymbol{E}}, \quad a_i = \frac{\partial \psi}{\partial D_i^\chi}, \quad \boldsymbol{b}_i = \frac{\partial \psi}{\partial \nabla_0 D_i^\chi} \tag{2.18}$$

The particular expressions are given in Appendix 2.6.1. As shown by [Forest, 2016], the work conjugate quantities a_i and $\boldsymbol{b}_i$ are involved in the so-called micromorphic balance equations (2.20) which have to be fulfilled additionally to the balance of linear momentum (2.19):

$$\text{Div}\,(\boldsymbol{F}\boldsymbol{S}) + \boldsymbol{f}_0 = \boldsymbol{0} \tag{2.19}$$

$$\text{Div}\,(\boldsymbol{b}_i) + a_i = 0 \tag{2.20}$$

The above equations, in which $\boldsymbol{f}_0$ denotes the conventional body force, constitute the 'strong form' of the problem, i.e. the differential equations which have to be fulfilled in every material point of the body Ω. Inserting Equations (2.18) and the definitions of (2.12) and (2.13) into the micromorphic balance equations (2.20), the latter can be rewritten as shown below:

$$0 = H_i(D_i^\chi - D_i) - E_i l_i^2 \nabla_0 \left(\boldsymbol{T}_i \left[\nabla_0 D_i^\chi\right]\right) \quad \text{in} \quad \Omega \tag{2.21}$$

As shown e.g. by [Brepols et al., 2017], boundary conditions (BC) on the surface $\partial\Omega$ of the body need to be specified in order for the problem to be fully described. These boundary conditions are summarized below, where the surface of the body ($\partial\Omega = \partial\Omega_n \cup \partial\Omega_d$) is split into Neumann ($\partial\Omega_n$) and

Dirichlet ($\partial\Omega_d$) boundaries:

$$\begin{aligned} &\underline{\text{BC for balance of linear momentum:}} && \underline{\text{BC for micromorphic balance:}} \\ &(\boldsymbol{F}\boldsymbol{S})\boldsymbol{n}_0 = \boldsymbol{t}_0 \quad \text{on} \quad \partial\Omega_{0,n} && \nabla_0 D_i^{\chi}\, \boldsymbol{n}_0 = 0 \quad \text{on} \quad \partial\Omega_0 \\ &\boldsymbol{u} = \hat{\boldsymbol{u}} \quad \text{on} \quad \partial\Omega_{0,d} \end{aligned} \tag{2.22}$$

In Equation (2.22) vectors $\boldsymbol{n}_0$ and $\boldsymbol{t}_0$ describe the (normalized) outer normal and traction vectors on the prescribed boundary, respectively. Vectors $\boldsymbol{u}$ and $\hat{\boldsymbol{u}}$ denote the displacement vector of the solution and the defined displacement prescribed on the boundary. It becomes apparent, that for the balance of the micromorphic extension, only Neumann boundary conditions are prescribed. Consequently, these conditions have to hold for the full boundary $\partial\Omega$.

Having relations (2.18) in mind, Clausius-Duhem inequality (2.17) can be simplified towards a reduced dissipation inequality:

$$\sum_{i=1}^{2} \underbrace{-\frac{\partial \psi}{\partial D_i}}_{=:Y_i} \dot{D}_i \geq 0 \tag{2.23}$$

Here, the damage driving force $Y_i = -\partial\psi/\partial D_i$ is introduced. To ensure that the above equation is fulfilled, it is assumed that both summands must satisfy the inequality independently of each other, resulting in Equations (2.24):

$$Y_i \dot{D}_i \geq 0 \tag{2.24}$$

The specific damage driving forces for this material read:

$$Y_i = n_i[1 - D_1]^{n_i - 1}\psi_i - H_i\langle D_i - D_{i,0}\rangle + H_i^{\chi}\left(D_i^{\chi} - D_i\right) - K_i D_i \tag{2.25}$$

The terms $H_i^{\chi}\left(D_i^{\chi} - D_i\right)$ show here the coupling of the local and micromorphic damage variables.

For both damage variables D_i, independent damage loading functions are defined:

$$\Phi_i(Y_i) = Y_i - Y_{i,0} \tag{2.26}$$

Due to this independence, the present material model can be considered as a 'two surface approach' (see, e.g. [Brepols et al., 2020]). Variables $Y_{i,0}$ in Equation (2.26) represent positive damage thresholds, which can be considered as additional material parameters. Finally, the loading and unloading conditions are defined by:

$$\dot{D}_i \geq 0, \quad \dot{D}_i \Phi_i = 0, \quad \Phi_i \leq 0 \tag{2.27}$$

These conditions can be fulfilled in two ways. If $\Phi_i \leq 0$, no damage evolution takes place and $\dot{D}_i = 0$ holds. In this case, the Clausius-Duhem inequality is fulfilled ($Y_i\dot{D}_i = 0$). If $\dot{D}_i > 0$ holds, damage evolves and $\Phi_i = 0$ has to be fulfilled. From the latter expression $Y_i = Y_{m,0}$ can be derived. With the constraints $Y_{m,0} > 0$ and $\dot{D}_i > 0$ the Clausius-Duhem inequality ($Y_i\dot{D}_i \geq 0$) is fulfilled as well.

2.3 Finite element implementation

A short summary of the finite element implementation will be presented in the following. This paper follows the derivations of [Holthusen et al., 2020] and [Brepols et al., 2020].

2.3.1 Weak form and its linearization

The weak form is derived by multiplication of Equations (2.19), (2.21) and (2.22) with their corresponding test functions ($\delta\boldsymbol{u}$ and δD_i) and integration over the volume. After application of the divergence theorem, the result reads as follows:

$$g_u = \int_{\Omega_0} \boldsymbol{S} \cdot \delta\boldsymbol{E} \, \mathrm{d}V - \int_{\Omega_0} \boldsymbol{f}_0 \cdot \delta\boldsymbol{u} \, \mathrm{d}V - \int_{\partial_n\Omega_0} \boldsymbol{t}_0 \cdot \delta\boldsymbol{u} \, \mathrm{d}A \tag{2.28}$$

$$g_{D_i} = \int_{\Omega_0} \delta D_i^\chi \, H_i^\chi \left(D_i - D_i^\chi\right) \, \mathrm{d}V - \int_{\Omega_0} \nabla_0(\delta D_i^\chi) \cdot \left(E_i l_i^2 \boldsymbol{T}_i \left[\nabla_0 D_i^\chi\right]\right) \, \mathrm{d}V \tag{2.29}$$

Term $\delta\boldsymbol{E}$ in Equation (2.28) is defined as $\delta\boldsymbol{E} = \frac{1}{2}[\boldsymbol{F}^T\nabla_0(\delta\boldsymbol{u}) + \nabla_0(\delta\boldsymbol{u})^T\boldsymbol{F}]$. In the course of the Newton Raphson implementation, the linearization of the terms introduced above with respect to the increments $\Delta\boldsymbol{u}$ and ΔD_i^χ is necessary.

In the present linearization, it is assumed that the body force ($\boldsymbol{f}_0$) and traction vector ($\boldsymbol{t}_0$) are independent of the displacement state:

$$\Delta g_u = \int_{\Omega_0} \Delta\boldsymbol{S} \cdot \delta\boldsymbol{E} \mathrm{d}V + \int_{\Omega_0} \boldsymbol{S} \cdot \Delta\delta\boldsymbol{E} \mathrm{d}V \tag{2.30}$$

$$\Delta g_{D_i} = \int_{\Omega_0} \delta D_i^\chi H_i^\chi (\Delta D_i - \Delta D_i^\chi) \mathrm{d}V - \int_{\Omega_0} \nabla_0(\delta D_i^\chi) \cdot (E_i l_i^2 \boldsymbol{T}_i \nabla_0(\Delta D_i^\chi)) \mathrm{d}V \tag{2.31}$$

The relation between $\Delta\boldsymbol{S}$, ΔD_i, $\Delta\boldsymbol{E}$ and ΔD_i^χ needed for the presented material model can be expressed via the following equations:

$$\begin{aligned} \Delta\boldsymbol{S} &= \mathcal{C}_{\boldsymbol{E}} : \Delta\boldsymbol{E} + \sum_{i=1}^{2} \boldsymbol{C}_{D_i^\chi} \Delta D_i^\chi \\ \Delta D_i &= \boldsymbol{K}_{i,\boldsymbol{E}} \cdot \Delta\boldsymbol{E} + K_{D_i^\chi} \Delta D_i^\chi \end{aligned} \tag{2.32}$$

In Equation (2.32) $\mathcal{C}_{\boldsymbol{E}}$ (fourth-order tensor) and $\boldsymbol{C}_{D_i^\chi}$ (second-order tensors) denote the sensitivities of the stress to changes in the strain and the micromorphic damage variables, respectively. The terms $\boldsymbol{K}_{m,\boldsymbol{E}}$ (second order tensors) and $K_{D_i^\chi}$ (scalars) denote the sensitivities of damage to changes in the strain and the micromorphic damage variables.

2.3.2 Discretization of the weak form

For the discretization of the linearized weak form of Equations (2.30) and (2.31) the body Ω_0 is approximated by Ω_0^h, which in turn is split into subdomains Ω_0^e:

$$\Omega_0 \approx \Omega_0^h = \bigcup_{e=1}^{n_{el}} \Omega_0^e \tag{2.33}$$

Here, index e indicates quantities within a subdomain which will later on be called element. Variable n_{el} specifies the number of elements into which the body is divided. Within these elements, the field variables $\boldsymbol{u}(\boldsymbol{X})$ and $D_i^\chi(\boldsymbol{X})$ (with $\boldsymbol{X} \in \Omega_0^e$) are described via the respective nodal quantities $\mathbf{D}_i^{\chi,e}$ and $\mathbf{u}^e$ and corresponding shape functions $\mathbf{N}(\boldsymbol{X})$ (matrices):

$$\begin{aligned} \boldsymbol{u}^e(\boldsymbol{X}) &= \mathbf{N}_u^e(\boldsymbol{X})\mathbf{u}^e & \delta\boldsymbol{u}^e(\boldsymbol{X}) &= \mathbf{N}_u^e(\boldsymbol{X})\delta\mathbf{u}^e \\ D_i^{\chi,e}(\boldsymbol{X}) &= \mathbf{N}_D^e(\boldsymbol{X})\mathbf{D}_i^{\chi,e} & \delta D_i^{\chi,e}(\boldsymbol{X}) &= \mathbf{N}_D^e(\boldsymbol{X})\delta\mathbf{D}_i^{\chi,e} \end{aligned} \tag{2.34}$$

Within the finite element code, the given field variables as well as the nodal variables are stored in Voigt notation (column vectors). The gradients of the field variables can be expressed via:

$$\begin{aligned} \nabla_0\boldsymbol{u}^e(\boldsymbol{X}) &= \mathbf{B}_u(\boldsymbol{X})\mathbf{u}^e & \nabla_0\delta\boldsymbol{u}^e(\boldsymbol{X}) &= \mathbf{B}_u(\boldsymbol{X})\delta\mathbf{u}^e \\ \nabla_0 D_i^{\chi,e}(\boldsymbol{X}) &= \mathbf{B}_D(\boldsymbol{X})\mathbf{D}_i^{\chi,e} & \nabla_0\delta D_i^{\chi,e}(\boldsymbol{X}) &= \mathbf{B}_D(\boldsymbol{X})\delta\mathbf{D}_i^{\chi,e} \end{aligned} \tag{2.35}$$

Here, $\mathbf{B}_u(\boldsymbol{X}) := \nabla_0\mathbf{N}_u(\boldsymbol{X})$ and $\mathbf{B}_D(\boldsymbol{X}) := \nabla_0\mathbf{N}_D(\boldsymbol{X})$ are matrices containing the derivatives of the shape functions with respect to $\boldsymbol{X}$. Analogously, the Green Lagrange strain increment $\Delta\boldsymbol{E}$ and the virtual strains $\delta\boldsymbol{E}$ can be expressed as:

$$\Delta\boldsymbol{E}^e(\boldsymbol{X}) = \mathbf{G}_{0,u}(\boldsymbol{X})\Delta\mathbf{u}^e \quad \delta\boldsymbol{E}^e(\boldsymbol{X}) = \mathbf{G}_{0,u}(\boldsymbol{X})\delta\mathbf{u}^e \tag{2.36}$$

In Equation (2.36), $\mathbf{G}_{0,u}$ is a matrix containing products of the shape function derivatives with the deformation gradient $\boldsymbol{F}$. Quantities $\mathbf{N}$, $\mathbf{B}$, and $\mathbf{G}$ are introduced here in a general form. Choices like spatial dimension of the prescribed problem, element type and specific interpolation have an influence on the particular shape of the given matrices. Details can be found in various publications (see, e.g. [Holthusen et al., 2020]) or text books (see, e.g. [Wriggers, 2008] or [Belytschko et al., 2014]).

By inserting (2.33) to (2.35) into (2.28) and (2.29), the the following discretized weak form of the

problem is obtained:

$$g_u^h = \bigcup_{e=1}^{n_e} \delta\mathbf{u}^{e,T} \overbrace{\int_{\Omega_0^e} \left[{\mathbf{G}_{0,u}}^T \boldsymbol{S}^e - {\mathbf{N}_u^e}^T \boldsymbol{f}_0^e \right] \mathrm{d}V - \int_{\partial_n \Omega_0} {\mathbf{N}_u^e}^T \boldsymbol{t}_0^e \, \mathrm{d}A}^{\boldsymbol{r}_u^e} \tag{2.37}$$

$$g_{D_i}^h = \bigcup_{e=1}^{n_e} \delta\mathbf{D}_i^{\chi,e} \underbrace{\int_{\Omega_0^e} \left[{\mathbf{N}_D^e}^T H_i^\chi \left(D_i^e - D_i^{\chi,e} \right) - {\mathbf{B}_D}^T \left(E_i l_i^2 \boldsymbol{T}_i \nabla_0 D_i^{\chi,e} \right) \right] \mathrm{d}V}_{\boldsymbol{r}_{D_i}^e} \tag{2.38}$$

Here, $\boldsymbol{r}_u^e$ and $\boldsymbol{r}_{D_i}^e$ represent the element residual vectors for the displacement and the nonlocal stiffness variables, respectively. Furthermore, inserting (2.33) to (2.35) into the linerized weak form (Equations (2.30) and (2.31)) leads to:

$$\begin{aligned} \Delta g_u^h = \bigcup_{e=1}^{n_e} \delta\mathbf{u}^{e,T} \Bigg\{ & \overbrace{\left(\int_{\Omega_0^e} \left[{\mathbf{G}_{0,u}^e}^T \, \mathcal{C}_{\boldsymbol{E}}^e \, \mathbf{G}_{0,u}^e + {\mathbf{B}_u^e}^T \, \mathcal{D}_{\boldsymbol{E}}^e \, \mathbf{B}_u^e \right] \mathrm{d}V \right)}^{=:\boldsymbol{K}_{u,u}^e} \Delta\mathbf{u}^e \\ & + \sum_{m=1}^{2} \underbrace{\left(\int_{\Omega_0^e} {\mathbf{G}_{0,u}^e}^T \, \boldsymbol{C}_{D_i^\chi} \, \mathbf{N}_D^e \, \mathrm{d}V \right)}_{=:\boldsymbol{K}_{u,D_i^\chi}^e} \Delta\mathbf{D}_i^{\chi,e} \Bigg\} \end{aligned} \tag{2.39}$$

$$\begin{aligned} \Delta g_{D_i}^h = \bigcup_{e=1}^{n_e} \delta D^{\chi,eT} \Bigg\{ & \overbrace{\left(\int_{\Omega_0^e} H_i^\chi \, {\mathbf{N}_u^e}^T \, \boldsymbol{K}_{m,E} \, \mathbf{G}_{0,u} \, \mathrm{d}V \right)}^{=:\boldsymbol{K}_{D_i^\chi,u}^e} \Delta\mathbf{u}^e \\ & + \underbrace{\left(\int_{\Omega_0^e} \left[H_i^\chi {\mathbf{N}_D^e}^T \left(K_{D_i}^\chi - 1 \right) \mathbf{N}_D^e - {\mathbf{B}_D^e}^T E_i l_i^2 \boldsymbol{T}_i \mathbf{B}_D^e \right] \mathrm{d}V \right)}_{=:\boldsymbol{K}_{D_i^\chi,D_i^\chi}^e} \Delta\mathbf{D}_i^{\chi,e} \Bigg\} \end{aligned} \tag{2.40}$$

In Equation (2.39), term $\mathcal{D}_{\boldsymbol{E}}^e$ denotes a special fourth order tensor (see, e.g. [de Souza Neto et al., 2008]) which accounts for the geometric stiffness. Its definition reads as:

$$\mathcal{D}_{\boldsymbol{E}}^e = (\boldsymbol{I} \otimes \boldsymbol{S})^{\overset{23}{T}} \tag{2.41}$$

Here, $(*)^{\overset{23}{T}}$ represents a transposition of the second and third base vector. Abbreviations $\boldsymbol{K}_{\boldsymbol{u},\boldsymbol{u}}^e$, $\boldsymbol{K}_{\boldsymbol{u},D_i^\chi}^e$, $\boldsymbol{K}_{D_i^\chi,\boldsymbol{u}^e}$ and $\boldsymbol{K}_{D_i^\chi,D_i^\chi}^e$ represent certain parts of the element stiffness matrix. Terms $\Delta\mathbf{u}^e$ and $\Delta\mathbf{D}_i^{\chi,e}$ are the element nodal increments of displacement and micromorpic damage, respectively.

Taking into account that $\delta\mathbf{u}^e$ and $\delta\mathbf{D}_i^{\chi,e}$ can take arbitrary values, applying the Dirichlet boundary

conditions and assembling the residuals and stiffnesses, the global finite element equations are:

$$\begin{pmatrix} \boldsymbol{K}_{\boldsymbol{u},\boldsymbol{u}} & \boldsymbol{K}_{\boldsymbol{u},D_1^\chi} & \boldsymbol{K}_{\boldsymbol{u},D_2^\chi} \\ \boldsymbol{K}_{D_1^\chi,\boldsymbol{u}} & \boldsymbol{K}_{D_1^\chi,D_1^\chi} & \mathbf{0} \\ \boldsymbol{K}_{D_2^\chi,\boldsymbol{u}} & \mathbf{0} & \boldsymbol{K}_{D_2^\chi,D_2^\chi} \end{pmatrix} \begin{pmatrix} \Delta\mathbf{u} \\ \Delta\mathbf{D}_1^\chi \\ \Delta\mathbf{D}_2^\chi \end{pmatrix} = - \begin{pmatrix} \boldsymbol{r}_u \\ \boldsymbol{r}_{D_1} \\ \boldsymbol{r}_{D_2} \end{pmatrix} \tag{2.42}$$

From Equation (2.42) it becomes clear again that there is no direct coupling between both micromorpic damage variables.

2.3.3 Consistent tangent operators

For the implementation of the described material model into a finite element program, the consistent algorithmic tangent moduli have to be computed. Deriving the tangents in a consistent way ensures quadratic convergence (see [Simo and Taylor, 1985]). By using the chain rule, the tangent operators in Equation (2.32) can be rewritten as follows:

$$\mathcal{C}_{\boldsymbol{E}} = \frac{\partial \boldsymbol{S}}{\partial \boldsymbol{E}} + \sum_{i=1}^{2} \frac{\partial \boldsymbol{S}}{\partial D_i} \otimes \frac{\partial D_i}{\partial \boldsymbol{E}} \tag{2.43}$$

$$\boldsymbol{C}_{D_i^\chi} = \frac{\partial \boldsymbol{S}}{\partial D_i} \frac{\partial D_i}{\partial D_i^\chi} \tag{2.44}$$

$$\boldsymbol{K}_{m,\boldsymbol{E}} = \frac{\partial D_i}{\partial \boldsymbol{E}} \tag{2.45}$$

$$K_{D_i^\chi} = \frac{\partial D_i}{\partial D_i^\chi} \tag{2.46}$$

The specific expressions of the algorithmic tangents can be found in Appendix 2.6.2.

2.4 Results

In this section, results from experimental tensile tests and numeric results, including a mesh convergence study and an investigation of Tensors $\boldsymbol{T}_m$, will be shown.

2.4.1 Experimental results

For a validation of the presented material model, tensile experiments of unidirectional CFRP specimens were conducted. More precisely, a total of seven test series with ten samples each were carried out. As shown in Fig. 2.2, the angle α between the normal vector of the unidirectional fibers and the pulling direction of the tensile test was varied in every test series.

In Fig. 2.3a the experimental setup is shown. In the clamping area, load input elements consisting of glass fiber reinforced plastics were used to prevent fiber breaking. The screws on the left are mechanical

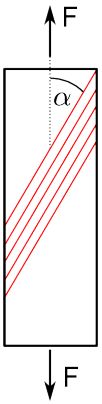

Figure 2.2: Visualization of the fiber angle $\alpha = [0°, 15°, 30°, 45°, 60°, 75°, 90°]$

stops to ensure an alignment of the samples with the pulling direction. In the red areas, the non-tactile laser measurement of the elongation of the samples can be seen. The width of the test samples was $20\,\mathrm{mm}$ while the thickness was $1.5\,\mathrm{mm}$. The free moving length was $120\,\mathrm{mm}$ and the displacement speed was set to $1\,\mathrm{mm\,min^{-1}}$, resulting in a nearly quasi static strain rate of less than $1 \times 10^{-2}\,\mathrm{min^{-1}}$. Figs. 2.3b and Fig. 2.3c show the specimens with $\alpha = 0°$ and $\alpha = 15°$ at the end of the experiments, respectively. In both cases, the crack propagates particularly along the fiber direction. While for the $15°$ specimen one macroscopic crack along the fiber direction occured, the failure of several fiber bundles and several parallel cracks along the fiber direction can be seen in the case of the $0°$ specimen.

Additionally to the laser extensiometer, a measurement with the digital image correlation system Aramis® was performed. Via image correlation it is possible to calculate the strain field of a sample. Since only recorded image data is used, this method is non-tactile as well.

In Fig. 2.4, the strain field measurement of Aramis® is shown. The strain field is characterized by two localization bands, which are parallel to the fiber direction and the later occurring macroscopic crack visible in Fig. 2.5. Fig. 2.5 shows the strain field after failure. The macroscopic crack is clearly visible on the right of the picture. The direction of the crack is parallel to the fiber direction and parallel to the orientation of the localization bands. After cracking, small residual strains remain. A statistical analysis of the strain field (with 512 data points, red box in Fig. 2.5) showed a mean residual strain of 0.023% with a standard deviation of 0.017%.

From the development (under loading) and disappearance (after unloading) of the localization bands it can be deduced that this is localization due to local softening of the material and especially not plastic behavior. However, some strains that are evenly distributed in the specimen have evolved during deformation.

In addition to the monotonic tensile tests, tensile tests with cyclic loading were performed for $\alpha = 15°$ test specimens. The specimens were loaded in three steps, where each step has a loading phase and an unloading phase. The steps with their particular color code are summarized in Fig. 2.6. The amount of loading in Fig. 2.6 is given in percentage of the average maximum load bearing capacity. A

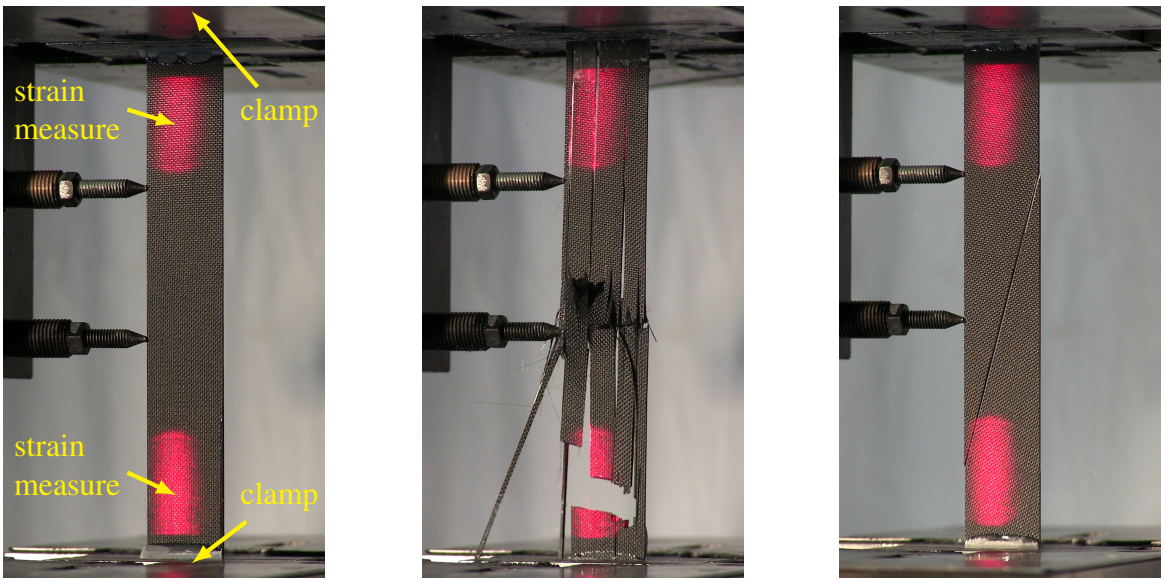

(a) Experimental setup for tensile testing

(b) Specimen for $0°$ test after failure

(c) Specimen for $15°$ test after failure

Figure 2.3: Experimental setup for tensile testing

corresponding stress strain curve of one cyclic tensile test is visualized in Fig. 2.7.

Fig. 2.7 shows the nonlinearity of the force strain curve and the hysteresis for load steps 1 and 3 is visible. During load step 2, almost no damage occurs and the loading and unloading curves are very similar to each other. Additionally, the different slopes of the unloading curves in steps 1 and 3 can be seen. This indicates the appearance of material softening due to further loading.

In addition to the material softening behavior, a remaining strain after unloading becomes apparent which is about 0.013 [%] and stays constant in all load steps. This observation is qualitatively in agreement with the results of the previous measurements with the Aramis® strain measurement for the $\alpha = 45°$ specimen. Furthermore, the stress strain curves show a (small) hysteresis even for elastic loading/unloading (see the black curve in Fig. 2.7). This might be due to viscous effects which are still present, but only have a minor influence and are therefore neglected.

The results from the Aramis® strain measurement and the results from the force strain curves both indicate that material softening is the cause of the observed nonlinearities. If significant plasticity had occurred, the localization bands would still have to be visible in the strain plot of Fig. 2.5 after unloading due to cracking. In addition, a change in the remaining strains would be visible in tests results with cyclic loading of Fig. 2.7. Since both effects do not occur, it can be assumed that plasticity does only play a minor role for this composite and can therefore be neglected.

The origin of the remaining strain is not entirely clear. One reason might be the viscosity of the material. An alternative cause could be the manufacturing process itself. Here, the composite is hardened under pressure at elevated temperatures (see, e.g. [Pantelelis and Bistekos, 2010]). This, as reported

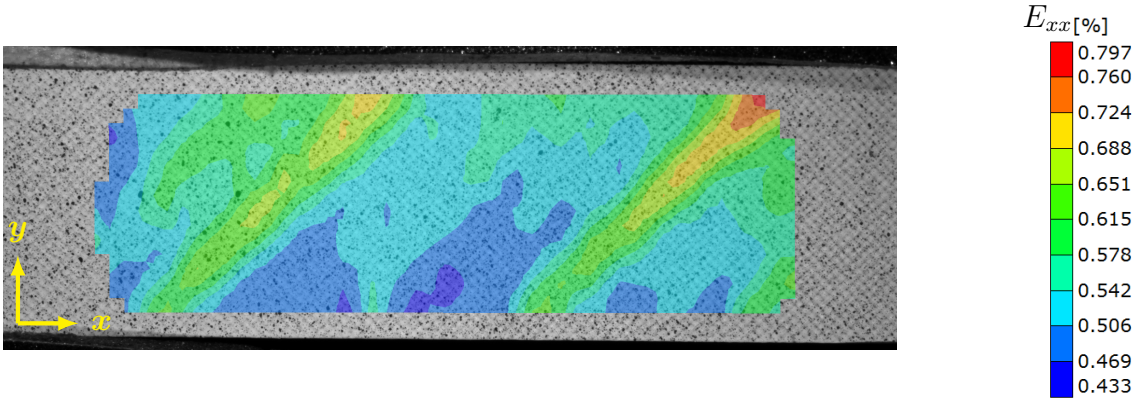

Figure 2.4: Strain field (cauchy strain E_{xx} in tensile direction x) of $\alpha = 45°$ specimen from Aramis® measurement right before cracking

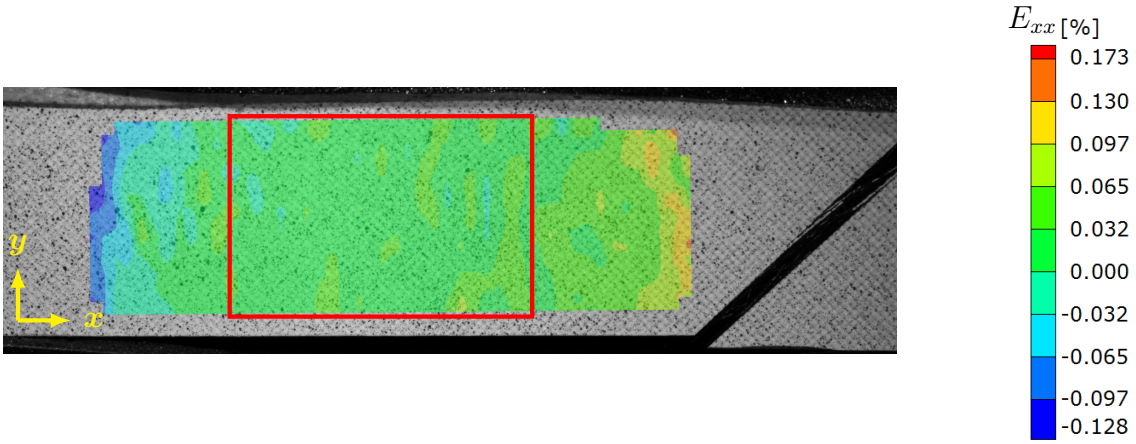

Figure 2.5: Strain field (cauchy strain E_{xx} in tensile direction x) of $45°$ specimen from Aramis® measurement after cracking

e.g. by [Hobbiebrunken et al., 2004], can lead to thermal induced residual stresses after cooling. However, the investigation of this effect is of minor importance for the present study and beyond the scope of this paper.

In Fig. 2.8, box plots of the maximum forces of all tests are shown. For each test series, orange lines represent the median and the surrounding boxes indicate the first and third quartiles. The whiskers range from the maximum to the minimum value within each test series. For better understanding, the results are plotted with and without the $\alpha = 0°$ specimen in Figs. 2.8a and 2.8b, respectively. As can be seen, the strength of the material increases, if the angle α between the fiber direction and the direction of tension decreases. In particular, Fig. 2.8a illustrates how severely the strength of the material increases, if fiber and tension direction are parallel (i.e. $\alpha = 0$.

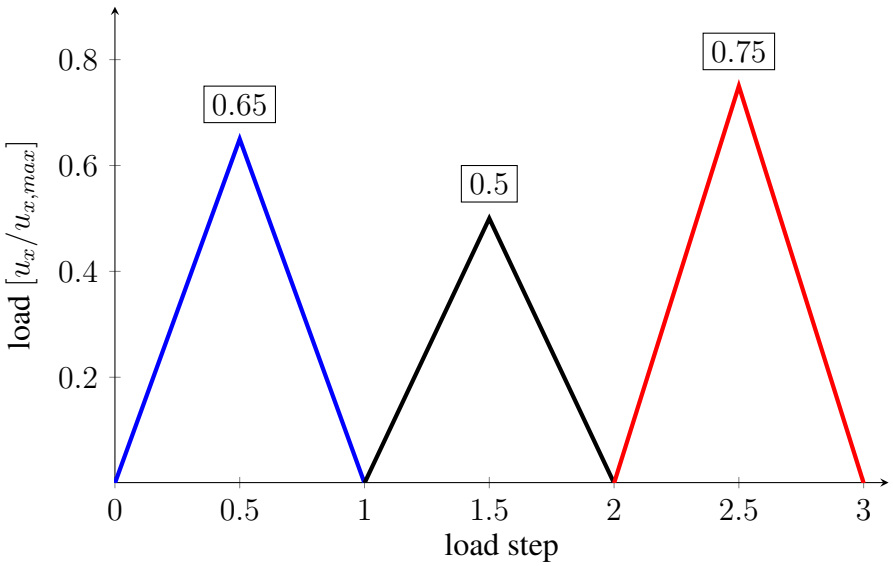

Figure 2.6: Vizualization of displacement over time

2.4.2 Numerical results

In order to compare the described material model with the given experimental results, finite element simulations of the tensile tests discussed in the previous Section 2.4.1 are carried out.

2.4.2.1 Setup of the boundary value problem

As exemplary shown in Figs. 2.9a and 2.9b, the entire tensile specimens including the load input elements are simulated. The geometric aspects of the tensile specimens are the same as in Section 2.4.1.

All displayed boundary conditions are applied on the upper and lower surface of the load input elements. On the left side, the specimen is entirely fixed. On the right side, a movement is only allowed in tensile direction (green arrows). The specimen is then loaded by applying a homogeneously distributed force in tension direction. The boundary value problem is solved by using the academic finite element software FEAP. For this, the proposed material model is implemented as a user element in the code. The elements used in this paper are 8 node hexahedral elements.

2.4.2.2 Fitting of the material parameters

The material parameters which are used in the simulations are fitted to the experimental data and are summarized in Tab. 2.1. The aim of the fitting procedure is to get the same results in stiffness (force/displacement ratio) and strength (maximum force) for the global force displacement curves of the experimental tensile tests for the cases $\alpha = 0°$ and $\alpha = 90°$, respectively.

From Aramis® measurements of the $\alpha = 0°$ specimen, a Poisson's Ratio of 0.3 is defined for the

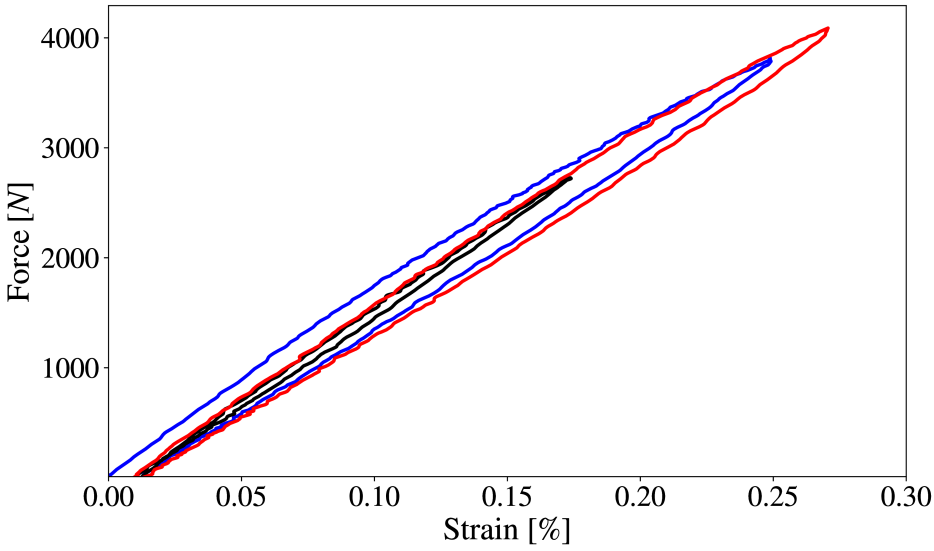

Figure 2.7: Hysteresis curve for cyclic loading of $15°$ tensile specimen

isotropic part. The anisotropic extention does not contribute to the Poisson's Ratio. Therefore, the ratio of λ_1 and μ_1 is fixed. From $\alpha = 90°$ experiments and corresponding numerical results, parameters λ_1 and μ_1 are then adjusted, until the relative error in the initial stiffness is less than $0.1\,\%$. Hereby, parameter E_2 is initially chosen in a way that in correspondence to experimental results the deformation in fiber direction (perpendicular to loading direction) is negligible small. Finally, parameter E_2 is adjusted, until the relative error in the initial stiffness of $\alpha = 0°$ tests and correspondent numerical results is less than $0.1\,\%$ as well. Afterwards, parameters Y_1 and Y_2 are adjusted separately, until the relative errors in the peak forces (between $\alpha = 90°$ and $\alpha = 0°$ test results and corresponding simulations) is again less than $0.1\,\%$. Parameter γ is increased until the desired crack path is achieved. A more detailed investigation of the influence of this parameter can be found in Section 2.4.2.5. Parameters l_1 and l_2 are adjusted in such a way that a relatively fine crack develops. It should be mentioned that l_1 and l_2 influence the fracture energy inherent to the model significantly. However, this material property is not measured and fracture energy related investigations are neglected here for simplicity.

Parameter	Value	Parameter	value	Parameter	value
λ_1	$5308\,\mathrm{MPa}$	μ_1	$3538\,\mathrm{MPa}$	E_2	$163\,200\,\mathrm{MPa}$
Y_1	$0.0672\,\mathrm{MPa}$	Y_2	$9.412\,\mathrm{MPa}$	γ	0.8
K_1	$0.205\,\mathrm{MPa}$	K_2	$1.0\,\mathrm{MPa}$	H_i	$1 \times 10^8\mathrm{MPa}$
l_1	$1.95 \times 10^{-2}\mathrm{mm}$	l_2	$0.25\,\mathrm{mm}$	H_1^χ	$2 \times 10^4\mathrm{MPa}$
H_2^χ	$3 \times 10^4\mathrm{MPa}$	$D_{i,0}$	0.9995	n_i	2

Table 2.1: Fitted material parameters; parameters with undefined index i are set to the same values in both material parts, respectively.

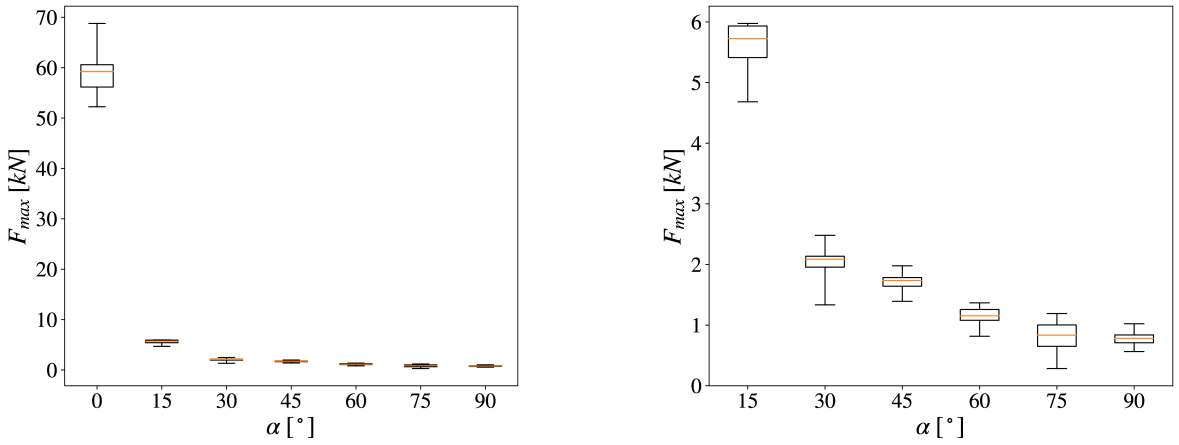

(a) Box plot of maximum force for $\alpha \in [0°, 90°]$

(b) Magnification: Box plot of maximum force for $\alpha \in [15°, 90°]$

Figure 2.8: Measured maximum forces in experimental tests

Figs. 2.9a and 2.9b show two of the meshes with meshsizes $1\,\mathrm{mm}$ and $0.33\,\mathrm{mm}$, respectively. Both meshes are used to simulate the case of $\alpha = 90°$ and show the refined mesh in the area where the crack appears. Since a plane stress state (zero stress in z-direction) is expected in the free moving part, only one layer of elements over the thickness is used. Five different meshes with an increasing number of elements over the width of the specimen in the fine meshed region are used. The number of elements over the width is varied from 10 elements with an approximate size of $2\,\mathrm{mm}$ to 80 elements with an approximate size of $0.25\,\mathrm{mm}$. A notch with a width of $1\,\mathrm{mm}$ and a height corresponding to the characteristic length of the element (marked in orange in Figs. 2.9a and 2.9b) with a reduced failure threshold ($0.6\,Y_1$) is used to trigger damage evolution in the refined region.

2.4.2.3 Mesh convergence study

The force-displacement curves plotted in Fig. 2.10 summarize the findings from the simulations of the $\alpha = 90°$ specimen with decreasing mesh size in the refined region. The curves show the severe snapback behavior of this boundary value problem. To follow the load path, the arclength method which is integrated in FEAP is used. The load paths show a converging behavior for decreasing mesh sizes. For an objective interpretation of the convergence, the total dissipated energy $\mathcal{D}_{tot} = \int F(u)\mathrm{d}u$ is calculated for all curves. For numerical integration, the Midpoint rule was applied and all simulations were terminated at a displacement of $u = 0.2\,\mathrm{mm}$ after the crack was fully developed.

The numerical values are summarized in Tab. 2.2. Here, the relative deviation (e_{rel}) of all mesh sizes in comparison to the smallest mesh size are calculated, which is assumed to represent the converged result. All relative errors are calculated with respect to this result. As can be seen, the relative error for the dissipated energy is already below 5% for a mesh size of $0.5\,\mathrm{mm}$ and decreases below 1% for the

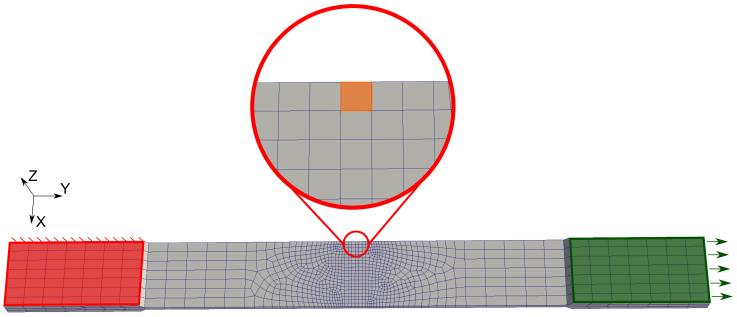

(a) Examplary mesh (mesh size 1.00 mm) with zoom into refined mesh regime

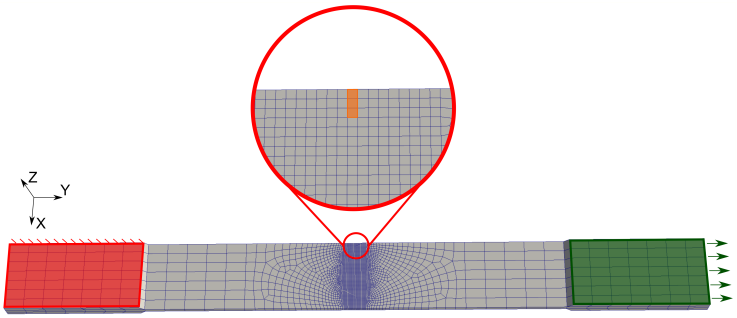

(b) Examplary mesh (mesh size 0.33 mm) with zoom into refined mesh regime

Figure 2.9: Meshes and boundary conditions of simulated tensile test ($\alpha = 90°$), region of material imperfection marked in orange.

mesh size of $0.33\,\mathrm{mm}$. Fig. 2.10 shows the force maximum is almost identical for all mesh sizes. Even for the coarsest mesh, the maximum force deviates only by about 0.3% from the smallest mesh size. In the terms of maximum forces, a mesh size of $1\,\mathrm{mm}$ or lower can be considered a converged solution.

2.4.2.4 Investigation of the influence of the material imperfection

To investigate the influence of the reduced threshold on the overall material response and dissipated energy, a parameter study is conducted. For this study, the realization with a mesh size of $1\,\mathrm{mm}$ is used. The reduced failure threshold is varied from $0.4\,Y_1$ to $0.9\,Y_1$. In Fig. 2.11 and Tab. 2.3 the results are summarized. As in the previous section, the dissipation is calculated from the force-displacement curves via the Midpoint rule. Again, all simulations were terminated at a displacement of $u = 0.2\,\mathrm{mm}$ after the crack was fully developed.

It can be seen in Fig. 2.11 that the force-displacement curves only differ by a small amount. Additionally, it becomes apparent that the curve with the highest damage threshold differs the most. The

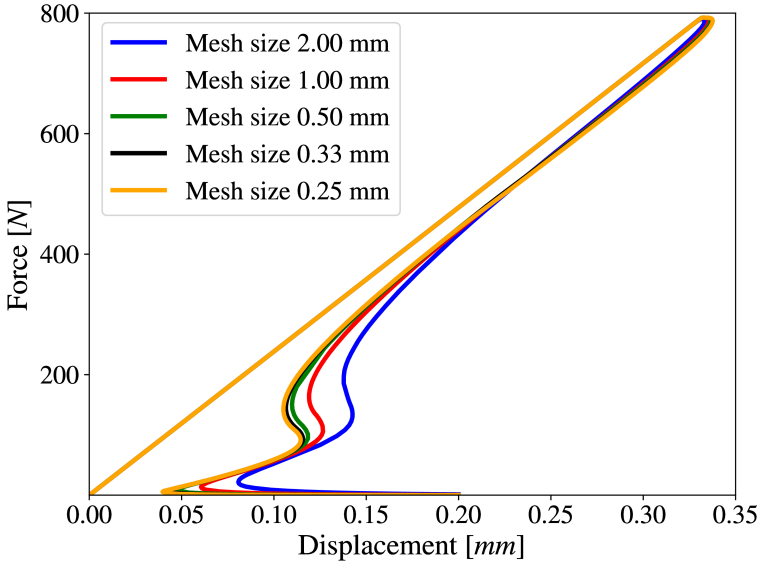

Figure 2.10: Force-displacement curves for different meshes of the $\alpha = 90°$ simulation

Mesh size [mm]	$\mathcal{D}_{tot}$ [N mm]	$e_{rel,\mathcal{D}}$ [%]	F_{max} [N]	$e_{rel,\mathrm{F}}$ [%]
2.0	28.188	34.41	790.03	-0.319
1.0	23.750	13.25	792.31	-0.032
0.5	21.673	3.34	792.51	-0.006
0.33	21.108	0.65	792.55	-0.001
0.25	20.972	-	792.56	-

Table 2.2: Dissipated energy for different mesh sizes; The relative deviation e_{rel} is calculated with respect to the smallest mesh size of $0.25\,\mathrm{mm}$

same behavior can be seen with regard to the dissipated energy. Here, the highest damage threshold also shows the highest dissipation. The reason for that can be found in Figs. 2.12a to 2.12c, where damage contour plots for three different damage thresholds (of the material imperfection) are shown. The snapshots are taken right before the damage starts to localize in the region of the imperfection.

It can be seen in Figs. 2.12a to 2.12c that for an increased damage threshold in the imperfection, the overall damage evolution increases as well. Especially for the case $0.9\,Y_1$ it is observed, that in the region of the coarse mesh (for this state) a significant amount of damage accumulates. The accumulation of damage is in accordance with the observed increased dissipated energy in Tab. 2.3. As mentioned above, damage begins to localize in the notch from this time step. Thus, the accumulated damage outside the region of the refined mesh only has a minor influence on the force-displacement curves, as can be seen in the force-displacement curves in Fig. 2.11. To reduce the effect of damage in the region of the coarse mesh, a damage threshold of $0.6\,Y_1$ is used in all simulations with $\alpha = 90°$.

Failure threshold	Dissipated energy [N mm]
$0.4\,Y_1$	23.572
$0.5\,Y_1$	23.650
$0.6\,Y_1$	23.750
$0.7\,Y_1$	23.902
$0.8\,Y_1$	24.108
$0.9\,Y_1$	24.559

Table 2.3: Dissipated energy for different reduced failure thresholds in the weakened notch of the $\alpha = 90°$ simulation

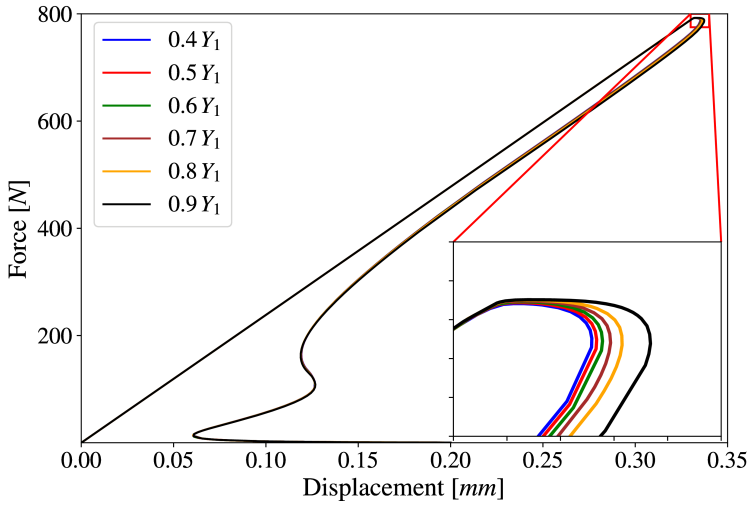

Figure 2.11: Force-displacement curves for different reduced failure thresholds in the weakened notch of the $\alpha = 90°$ simulation

2.4.2.5 Investigation of the crack path and influence of parameter γ

In Fig. 2.13, the damage contour plot for a tensile test with $\alpha = 45°$ fiber orientation is shown. The area where damage D_1 reaches a value of ≥ 0.994 will be referred to as the crack in the following. For angles other than $0°$ and $90°$, no weakened elements for material imperfection are used. The anisotropic behavior and the resulting inhomogeneous stress and strain distributions within the free moving part are sufficient to trigger damage evolution.

As can be seen in Fig. 2.13, the crack does not completely follow the fiber direction near the boundaries. The reason for this is the fact that the gradient of the damage field has to fulfill the boundary condition introduced in Equation (2.21). Due to this condition, no damage gradients are allowed on $\partial\Omega$, thus leading to a crack which is normal to the boundary. Apparently, the crack path follows the fiber orientation in the middle of the specimen, where the influence of the boundary effects are smaller.

The necessity of introducing a direction dependence of $\nabla_0 D_1^X$ shown in Equation (2.14) becomes

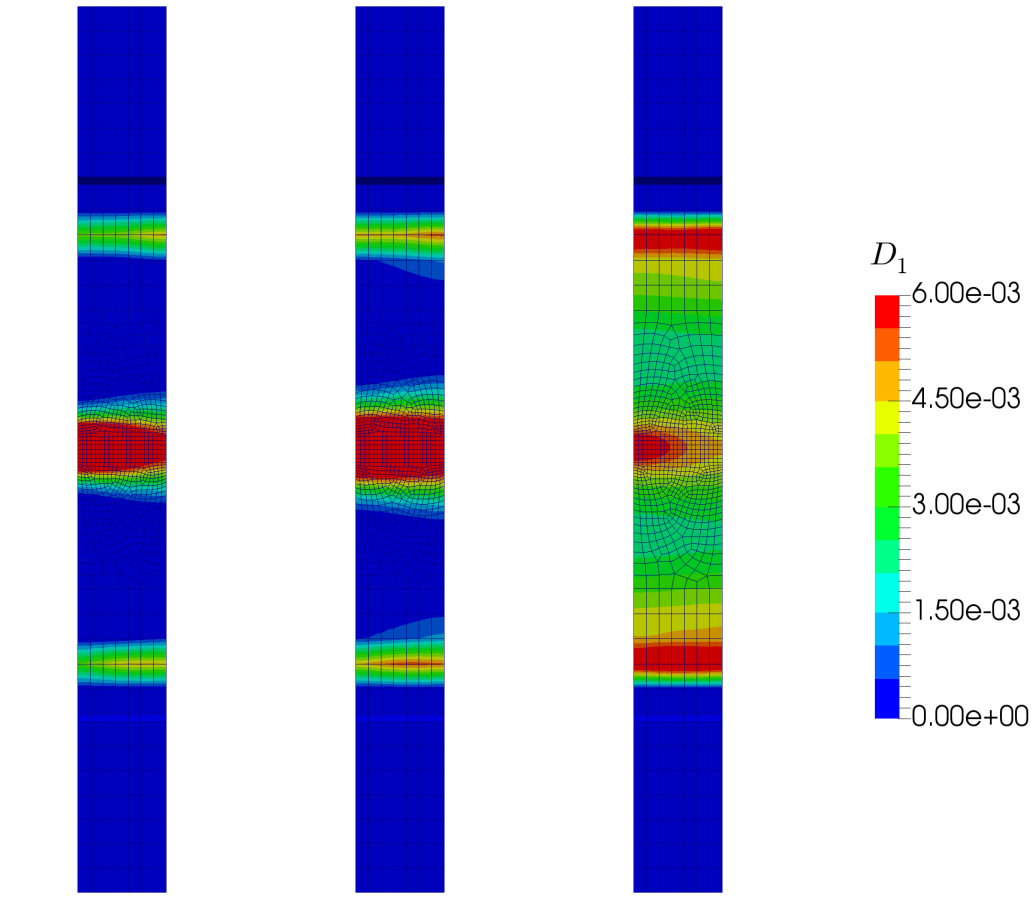

(a) $0.4\,Y_1$ (b) $0.6\,Y_1$ (c) $0.9\,Y_1$

Figure 2.12: Comparison of Damage contour plots for different damage threshold variables in the region of material imperfection; mesh size $1\,\mathrm{mm}$

clear when comparing the damage contours in Fig. 2.13 with the damage contours in Fig. 2.14.

For the simulation of Fig. 2.14, the set of parameters given in Tab. 2.1, with the exception of $\gamma = 0$, is used. As for simulation in Fig. 2.13, the fiber angle was set to $\alpha = 45°$. The only difference between the simulations in Fig. 2.13 and Fig. 2.14 is the direction dependence $\nabla_0 D_1^X$, respectively. For the isotropic case (Fig. 2.14), the crack path is almost perpendicular to the loading direction and therefore not parallel to the fiber direction. The introduction of a direction dependence of $\nabla_0 D_1^X$ is therefore considered to be necessary in order to get the same crack paths as shown by experimental results.

2.4.2.6 Comparison of numerical and experimental results

In Fig. 2.15, the results for the maximum forces from experiments and simulations are compared. The resultant forces for the $\alpha = 0°$ and $\alpha = 90°$ specimens are captured quite precisely. Since the material was constructed in a way that it can adjust material properties in - and perpendicular to - the fiber

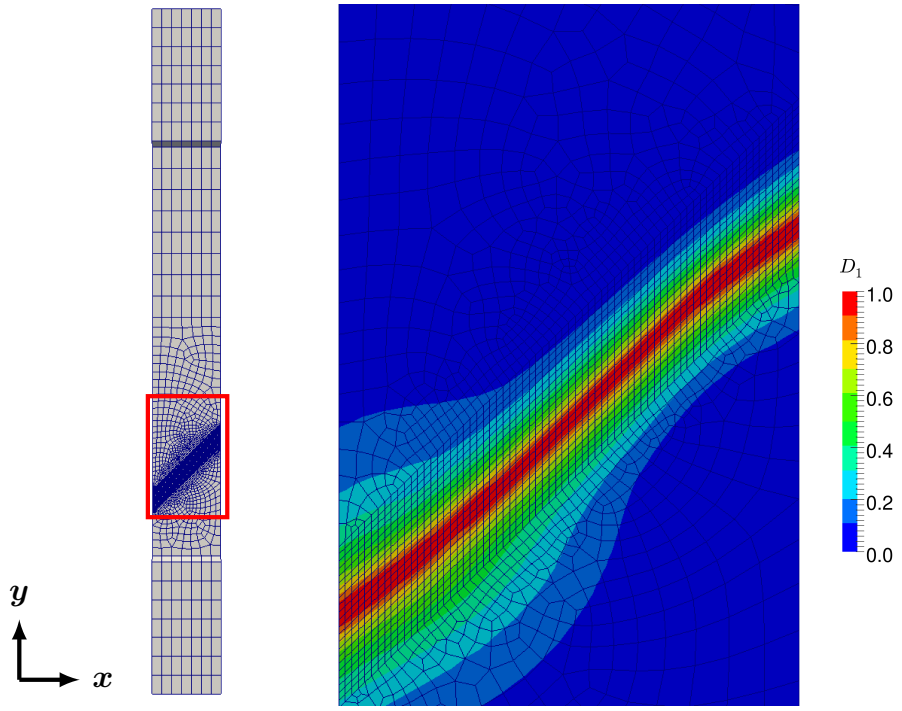

Figure 2.13: Overview and damage contour plot (D_1) of marked section for $\alpha = 45°$ simulation; $\gamma = 0.8$

direction, this result is reasonable. However, the results differ for the $\alpha = 15°$ to $\alpha = 60°$ test cases.

The influence of damage hardening parameter K_1 on the improvement of the fitting was investigated. Therefore, all parameters except K_1 were fixed. The parameter K_1 was varied to fit the maximum force in case of the $\alpha = 45°$ specimen. With this new value ($K_1 = 2.8\,\mathrm{MPa}$), the specimens for $\alpha = 15°$ and $\alpha = 90°$ were simulated. The results are shown in Fig. 2.16. With $K_1 = 2.8\,\mathrm{MPa}$, the results for $\alpha = 45°$ and $\alpha = 15°$ have been improved, but now the results for the $\alpha = 90°$ specimens do not fit any more.

Alternatively, a different rule for damage hardening (e.g. Voce type hardening) could improve the results, but a detailed investigation is out of the scope of this paper.

2.5 Conclusion and outlook

In this work, a novel geometricaly nonlinear model for simulating the damage and failure behavior of CFRPs under shear cutting was derived. Due to large rotations in the cutting plane, the use of geometric nonlinearity is necessary. Experimental tests suggested to use a St. Venant type material model for the isotropic part, since the maximum endurable elongation at tension was about 2%. A gradient extension based on the micromorphic approach was used to overcome undesired mesh dependencies. Additionally, experimental tension tests were conducted. Uniaxial tension tests for seven different fiber

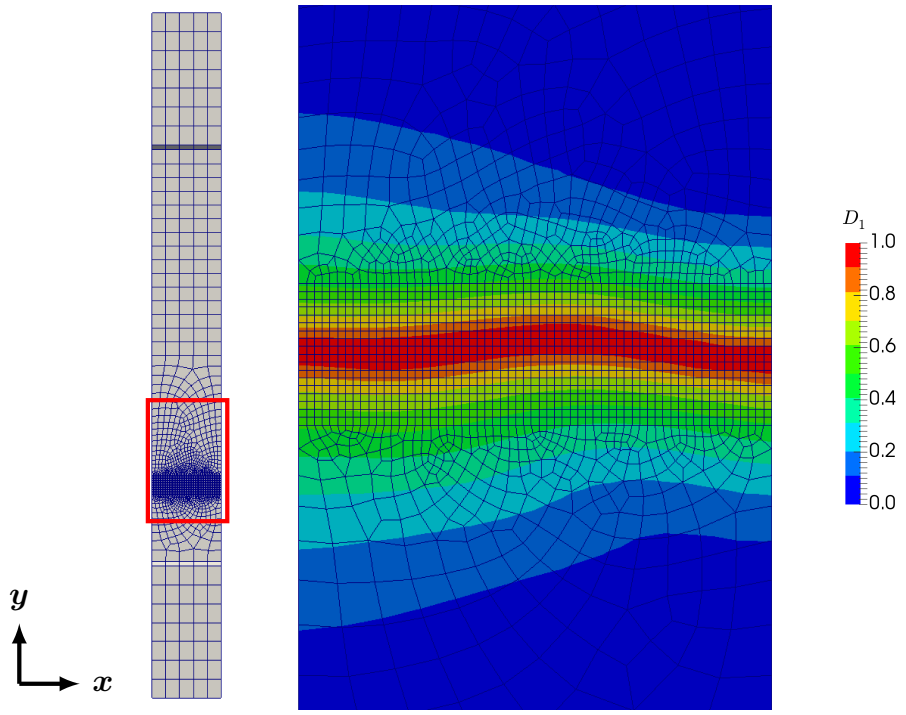

Figure 2.14: Overview and damage contour plot (D_1) of marked section for $\alpha = 45°$ simulation; $\gamma = 0.0$

orientations with then samples each were performed to generate data points for fitting and testing of the proposed material model. Furthermore, loading and unloading experiments were conducted. From these experiments and measurements using the Aramis® system it was shown that residual strains remain after unloading. Suggestions for the origin of these strains were given. A detailed investigation of this particular effect is left for further research.

A mesh convergence study showed that the micromorphic approach cures the undesired mesh dependence and convergence (with regard to the dissipated energy and maximum force) could be achieved. Furthermore, it was shown that the introduction of a direction dependence of the gradient extension is necessary, to achieve a correct evolution of the crack path. Comparison of the fitted material model and experimental results for the force maximum showed a good agreement for the $\alpha = 90°$ and $\alpha = 0°$ test specimens. For the other test specimen, the results tend to differ from each other.

It is therefore assumed that more investigation into the hardening function should be invested. Additionally, an extension to the commonly known transversally isotropic model might further improve the results. As shown by [Reese, 2003] and [Holthusen et al., 2020], a transversally isotropic model additionally accounts for the fifth and first invariant in the anisotropic extension. Due to these terms, the anisotropic extension shows a sensitivity for shear deformation, which might improve the material response for fiber angles other than $\alpha = 0°$ and $\alpha = 90°$.

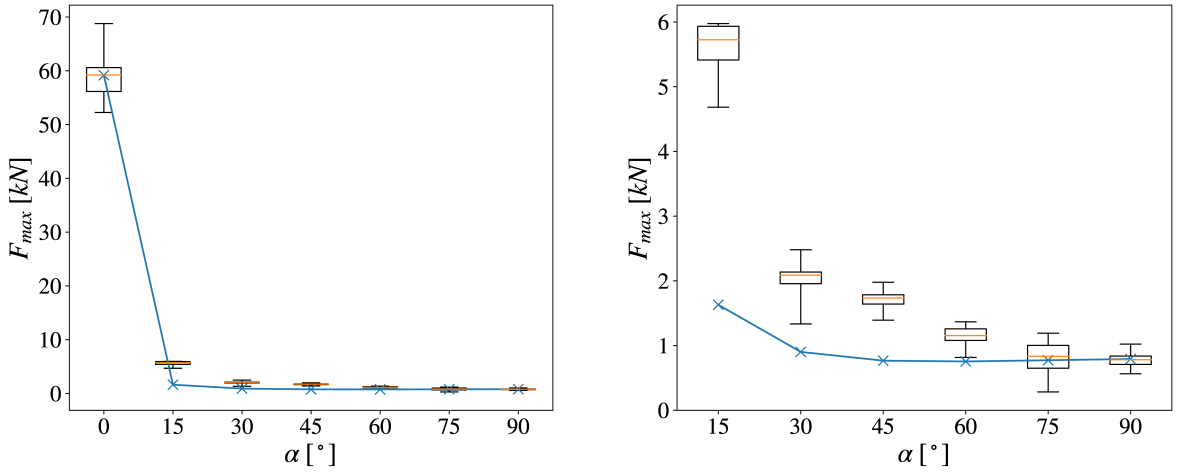

(a) Comparison of maximum forces in experiments and numerical simulations for $\alpha \in [0°, 90°]$

(b) Magnification: Comparison of maximum forces in experiments and numerical simulations for $\alpha \in [15°, 90°]$

Figure 2.15: Comparison of numerical and experimental results

Acknowledgements

The financial support of the DFG Projects 'Scherschneiden kohlenstofffaserverstärkter Kunststoffe. Fertigungstechnologie und numerische Modellierung' (RE 1057/38-1), 'Experimentelle und numerische Untersuchung von geschichteten, faserverstärkten Kunststoffen bei Crash - Beanspruchungen' (RE 1057/46-1), 'Mehrskalige Modellierung des Anisotropen, nichtlinearen Schädigungsverhaltens von carbonfaserverstärkten Kunststoffen' (SI 1959/7-1), 'Polymorphe Unschärfemodellierungen für den numerischen Entwurf von Strukturen - Modellreduktion in Raum und Parameterdimension - Schädigungsbasierte Modellierung polymorpher Unschärfe im Zusammenhang mit Robustheit und Zuverlässigkeit' (RE 1057/40-1), 'Modellierung der Struktur und der Fluid-Struktur-Interaktion biohybrider Herzklappen auf die Gewebereifung' (RE 1057/45-1) and Subproject D3 of the Transregional Collaborative Research Center (SFB/ TRR 40) is gratefully acknowledged. Additionally, S. Wulfinghoff would like to acknowledge the support by the German Federal Ministry for Economic Affairs and Energy with the project 'Innovations for the development of turbo-generators for the support of the energy revolution' (FKZ 03ET7087E).

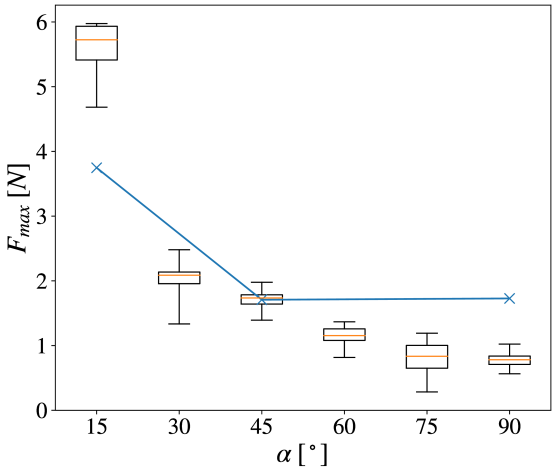

Figure 2.16: Comparison of numerical and experimental results for $k_1 = 2.8$

2.6 Appendix

2.6.1 Derivation of stress and stress like quantities

The specific choice of ψ introduced in section 2.2 lead to the following equation for the Second Piola Kirchhoff stress $\boldsymbol{S}$:

$$\boldsymbol{S} = \frac{\partial \psi}{\partial \boldsymbol{E}} = [1 - D_1]^{n_1} \left(\lambda_1 \text{tr}[\boldsymbol{E}]\boldsymbol{I} + 2\mu\boldsymbol{E}\right) + [1 - D_2]^{n_2} \left(E_2 \text{ tr}\left[\boldsymbol{E}\boldsymbol{H}\right] \boldsymbol{H}\right) \tag{2.47}$$

The work conjugated stress like quantities for the nonlocal damage variables can be derived as

$$a_i = \frac{\partial \psi}{\partial D_i^{\chi}} = H_i(D_i^{\chi} - D_i) \tag{2.48}$$

$$\boldsymbol{b}_i = \frac{\partial \psi}{\partial \nabla_0 D_i^{\chi}} = E_i l_i \, \boldsymbol{T}_i \, \nabla_0 D_i^{\chi} \tag{2.49}$$

2.6.2 Computation of the material tangents

As it can be seen in section 2.3.3, several derivatives are needed to form the consistent tangent. For the given material model, the derivatives used in equations (2.43) to (2.46) will be given in this section. The derivatives of $\boldsymbol{S}$ with respect to the variables ($\boldsymbol{E}$, D_1 and D_2) can be derived from equation (2.47)

and read

$$\frac{\partial \boldsymbol{S}}{\partial \boldsymbol{E}} = [1-D_1]^{n_1}\left(\lambda_1 \boldsymbol{I}\otimes\boldsymbol{I} + 2\mu\,\mathbb{I}\right) + [1-D_2]^{n_2}\left(E_2\,\boldsymbol{H}\otimes\boldsymbol{H}\right), \tag{2.50}$$

$$\frac{\partial \boldsymbol{S}}{\partial D_1} = n_1[1-D_1]^{n_1-1}\left(\lambda_1 \mathrm{tr}[\boldsymbol{E}]\boldsymbol{I} + 2\mu\boldsymbol{E}\right) \text{ and} \tag{2.51}$$

$$\frac{\partial \boldsymbol{S}}{\partial D_2} = n_2[1-D_2]^{n_2-1}\left(E_2\,\mathrm{tr}\left[\boldsymbol{E}\boldsymbol{H}\right]\boldsymbol{H}\right). \tag{2.52}$$

$$\tag{2.53}$$

Here, $\boldsymbol{I}$ and $\mathbb{I}$ denote the second order and symmetric fourth order identity tensor, respectively. To obtain the remaining derivatives, it is necessary to exploit the consistency conditions of the damage loading functions Φ_i introduced at the end of section 2.2.2. If D_i evolves, $\Phi_i = 0$ has to be fulfilled. Furthermore, the total differential $\mathrm{d}\Phi_i$ has to be zero as well. This leads to the following relation:

$$\mathrm{d}\Phi_i = 0 = \frac{\partial \Phi_i}{\partial D_i}\mathrm{d}D_i + \frac{\partial \Phi_i}{\partial D_i^{\chi}}\mathrm{d}D_i^{\chi} + \frac{\partial \Phi_i}{\partial \boldsymbol{E}}\mathrm{d}\boldsymbol{E} \tag{2.54}$$

Equation (2.54) can be rewritten as:

$$\mathrm{d}D_i = \left(\frac{\partial \Phi_i}{\partial D_i}\right)^{-1}\left(-\frac{\partial \Phi_i}{\partial D_i^{\chi}}\mathrm{d}D_i^{\chi} - \frac{\partial \Phi_i}{\partial \boldsymbol{E}}\mathrm{d}\boldsymbol{E}\right) \tag{2.55}$$

It can be seen that the necessary partial derivatives can be derived from these equations. It is possible to construct the following auxiliary functions:

$$g_1(D_1) = \frac{\partial \Phi_1}{\partial D_1} = n_1(n_1-1)\,(1-D_1)^{n_1-2}\,\psi_1(\boldsymbol{E}) - H_1\mathcal{H}(D_1 - D_{1,0}) - H_1^{\chi}D_1 - K_1 \tag{2.56}$$

$$g_2(D_2) = \frac{\partial \Phi_2}{\partial D_2} = n_2(n_2-1)\,(1-D_2)^{n_2-2}\,\psi_2(\boldsymbol{E},\boldsymbol{H}) - H_2\mathcal{H}(D_2 - D_{2,0}) - H_2^{\chi}D_2 - K_2 \tag{2.57}$$

Here, $\mathcal{H}(*)$ denotes the step function.

$$\mathcal{H}(*) = \begin{cases} 0 & \text{for } * \leq 0 \\ 1 & \text{for } * > 0 \end{cases} \tag{2.58}$$

With this auxiliary function, the partial derivatives take the following form:

$$\frac{\partial D_1}{\partial \boldsymbol{E}} = g_1(D_1)^{-1}\lambda_1 \mathrm{tr}[\boldsymbol{E}]\boldsymbol{I} + 2\mu \boldsymbol{E}\boldsymbol{I} \tag{2.59}$$

$$\frac{\partial D_2}{\partial \boldsymbol{E}} = g_2(D_2)^{-1}E_2 \mathrm{tr}[\boldsymbol{E}]\boldsymbol{H} \tag{2.60}$$

$$\frac{\partial D_1}{\partial D_i^{\chi}} = g_1(D_1)^{-1}H_1^{\chi} \tag{2.61}$$

$$\frac{\partial D_2}{\partial D_i^{\chi}} = g_2(D_2)^{-1}H_2^{\chi} \tag{2.62}$$

3 Article 2: Failure zone homogenization for modeling damage- and debonding-induced softening in composites including gradient-extended damage at finite strains

This article was published as:

Poggenpohl, L., Holthusen, H. and Simon, J.-W. [2022], 'Failure zone homogenization for modeling damage- and debonding-induced softening in composites including gradient-extended damage at finite strains', *International Journal of Plasticity* **154**, 103277.

Disclosure of the individual authors' contributions to the article:

L. Poggenpohl adjusted the material model presented in previous article. Furthermore, he wrote the scripts for geometry generation and set up the numerical simulations. The results were analyzed and visualized by L. Poggenpohl as well. Further, it was L. Poggenpohl who wrote the main part of the publication. H. Holthusen gave valuable feedback during result discussion and paper writing. In addition, the work and paper writing was supervised by J.-W. Simon who gave valuable feedback as well. All authors approved the publication of the final version of the manuscript.

Abstract. Within multiscale modeling strategies for composite materials, Standard Hill averaging is widely used for homogenization of repeating unit cells (RUCs). However, Hill's homogenization approach reaches its limitations at the presence of strain softening, because in the standard averaging sense the representativeness of the considered micro-scale volume is lost. Hence, in order to overcome these limitations, we propose a new failure zone averaging scheme at finite strains, which is also applicable in the softening regime. First, starting from Hill's assumption of equal virtual work densities on different scales, a novel homogenization approach is derived analytically. Then, the analytical results are verified by numerical simulations evaluating different RUC sizes and accounting for varying geometric realizations in a statistical manner. It is shown that the proposed homogenization scheme yields size-independent stress-strain relations even after localized damage has occured leading to strain softening within the RUCs. In addition, the material model for the epoxy bulk is valid for the description of damage progression at large deformations using a gradient-enhanced damage model. It turns out that the micromorphic power density — related to the gradient enhancement — of the failure zone gives significant values during the formation of localization while the overall work density is small. Thus, it can be concluded that for accurate failure zone homogenization, the contribution of gradient terms has to be considered. Further, cohesive zone elements are incorporated to consider the decohesion between fibers and matrix. As a result, the stress-strain curves show a lower peak stress and a higher scatter in the stress response compared to samples with perfect interfaces. In contrast, the work density plots show a higher dissipation for the RUC with damaging interfaces.

3.1 Introduction

Due to high stiffness and strength combined with low density, carbon fiber reinforced plastics (CFRPs) were used in a growing number of applications (see, e.g. Rösler et al. [2013]). For example, in civil engineering, new construction methods used CFRPs as reinforcement of concrete as was shown, e.g. in [Karayannis et al., 2018]. Additionally, the beneficial properties of CFRPs had been exploited in applications such as aerospace technology or wind turbines for a long time. Most commonly, CFRPs were fabricated either as laminates with tailored material properties or with a woven structure on the micro level. In the latter, even simple loading conditions such as uniaxial tension led to inhomogeneous strains and complex load states within the microstructure due to the complex microscopic geometry (see, e.g. [Stier et al., 2015] or [Höwer et al., 2019]).

Since CFRPs with a woven microstructure generally showed a complex damage behavior, it is hardly possible to describe this behavior with only one scalar damage variable and one damage function. As was shown in e.g. [van der Meer and Sluys, 2009], [Mukhopadhyay and Hallett, 2019], [Poggenpohl et al., 2021] or [Dean et al., 2021] one approach was to use a set of scalar damage variables to differentiate between damage of the fibers and damage of the matrix. Alternatively, one damage variable with two different damage functions for fiber and matrix as shown, e.g. in [Mandal et al., 2020] was used.

In other models, six scalars (see, e.g. [Chen and Aliabadi, 2019] or [He et al., 2020]) or even a fourth order Tensor (see, e.g. [Chow and Wei, 1999] or [Ryvkin and Aboudi, 2020]) was used to account for anisotropic stiffness degradation of CFRPs. Another approach was shown, e.g. in [Simon et al., 2017; Bednarcyk et al., 2015], where a general framework for damage evolution in woven composites was given. There, a damage interaction matrix was introduced to control the evolution and interaction of different damage mechanisms. However, the damage evolution and interaction of those models have to be justified numerically or experimentally. Here, RUC simulations offer the opportunity to grant insight into the damage evolution since the loading scenario can be controlled precisely.

Additionally, CFRPs generally fail in a brittle manner. Thus, high safety factors are required in order to prevent catastrophic failure. A more accurate failure prediction is desired, since it leads to decreasing factors of safety and consequently better material performance (see, e.g. [Wu et al., 2020]). More insight into the microscopic failure mechanisms of CFRPs is needed.

The analysis of representative unit cells (RUCs) in a staggered or FE^2 scheme is a helpful method to gain a better understanding of the mechanisms at the micro level. For that, Hill's approach (see [Hill, 1967, 1972]) is widely used to compute a homogenized mechanical as well as thermal responses from the results obtained from RUC simulations (see, e.g. [Mikeš et al., 2021] for a comparative study). Hill's approach is used exemplary in [Tsalis et al., 2013] for elastoplastic composites, in [Chatzigeorgiou et al., 2016] for a thermomechanicaly coupled material, in [Meade et al., 2021] to predict the ductile failure of high strength aluminum due to void growth or in [Cao et al., 2020] for a FFT based analysis of concrete cracking just to name a few. Additionally, as suggested, e.g. in [Settgast et al., 2020], Hill's approach is used to generate training data for neuronal network applications. As can be seen, e.g. in [Elnekhaily and Talreja, 2018; He et al., 2020] Hill's approach was used as well to analyze the effect of micro geometry on the homogenized behavior of carbon fiber reinforced materials. In [Elnekhaily and Talreja, 2018], RUC simulations were used to investigate the influence of fiber distribution on the failure onset. However, the simulation was restricted to the onset of failure, while the failure process itself was not analyzed. In [He et al., 2020], a multiscale simulation using several scales was presented. The analysis took into account the micro scale which consisted of carbon fibers and epoxy matrix, the meso scale which consisted of the woven yarns and the macro scale on the structural level. The material model (invoking elasticity, plasticity and failure as well as temperature dependency of the material parameters) was tested against experimental data. However, the RUC size was only determined by the means of the elastic response as was suggested in [Melro et al., 2012]. As will be shown later, the definition of a representative RUC size might be different in the hardening and softening regime, where for the latter, the convergence should be investigated individually.

It was shown in in several publications, for instance in [Gitman et al., 2004], [Gitman et al., 2007] or [Geers et al., 2010] that standard homogenization using Hill's approach was not applicable at the presence of localization phenomena and a representative size of the RUC could not be uniquely defined. In [Gitman et al., 2007], it was concluded that a mismatch of dimensions between dissipative volume

and RUC volume (i.e. the volume of the stored elastic energy) was the main cause that Hill's approach was not applicable.

In order to counteract this inconsistency, the failure zone averaging method was developed in [Nguyen et al., 2010]. There, the failure zone averaging method was shown to be insensitive to the size converging problem of Hill's approach for RUCs undergoing localizing phenomena. This method circumvented the mismatch between elastic energy and dissipated energy, since the analyzed domain was restricted to the actively damaging volume of the RUC. Using this method, a representative size of the RUC was identified. In more recent publications, computational aspects were investigated ([Nguyen et al., 2011]) and the method was applied to a FE^2 scheme with complex microstructure of concrete aggregates at the micro level ([Nguyen et al., 2012]). More recently, the failure zone averaging method has been applied to microscopical cracks using cohesive zone elements (see, e.g. [Turteltaub et al., 2018; Turteltaub and de Jong, 2019; Turteltaub and Suárez-Millán, 2020] or [Ke and Van Der Meer, 2021]). There, cohesive zone elements were used at the micro scale to model the debonding of the interface as well as cracks of the bulk material.

In this publication, the failure zone averaging method is adapted to the investigation of repeating unit cells (RUCs) of long carbon fiber reinforced plastics subjected to transversal tension. For the failure of the resin matrix, an isotropic brittle damage model at finite strains is used while the fibers behave linear elastically at finite strains. To overcome undesired mesh size sensitivity, the micromorphic approach as introduced in [Forest, 2009] is adopted, leading to a gradient-enhancement in the damage formulation. As shown e.g. in [Peerlings et al., 1996] or [Peerlings et al., 2001], the introduction of higher order gradients can cure undesired mesh size sensitivity. In recent publications, gradient enhanced damage is applied to damage-plasticity (see, e.g. [Miehe et al., 2016]), damage-viscoplasticity (see, e.g. [Mozaffari and Voyiadjis, 2016]) as well as thermo-mechanicaly coupled damage-plasticity (see, e.g. [Felder et al., 2022]).

3.2 Material modeling

In the following, the material models for the bulk (which in turn consist of epoxy matrix and carbon fibers) and interfaces are presented. The nomenclature of vectors, tensors and base operators – which are defined exclusively in the euclidean space – is summarized in the following:

a, A	Scalar	
$\boldsymbol{a}$	First order tensor	
$\mathbf{a}$	Vector $n \times 1$	
$\boldsymbol{A}$	Second order tensor	
$\mathbf{A}$	Matrix $n \times m$	
$\mathbb{A}$	Fourth order tensor	
$\cdot$	Single contraction, i.e.	$\boldsymbol{A} \cdot \boldsymbol{B} = A_{ij}B_{jk}$
:	Double contraction, i.e.	$\boldsymbol{A} : \boldsymbol{B} = A_{ij}B_{ij}$
$\boldsymbol{a} \otimes \boldsymbol{b}$	Dyadic product, i.e.	$\boldsymbol{a} \otimes \boldsymbol{b} = a_i b_j$
$\boldsymbol{A}^T$	Transpose, i.e.	$A^T_{ij} = A_{ji}$

3.2.1 Bulk material model

For the simulation of the bulk material behavior of the RUC, the isotropic part of the material model introduced in [Poggenpohl et al., 2021] was used. In the following, the material model is introduced and a brief summary of the implementation into a finite element code is presented. For more details, the reader is referred to the publication mentioned above.

The material model presented in the following is of brittle damaging type. As shown, e.g. in [Rocha et al., 2019] or [Morelle et al., 2017], epoxy can show a significant amount of plasticity until failure occurs. However, plastic strains are often dependent on triaxial stress states. From the experimental data given in [Poggenpohl et al., 2021], which showed no considerable amount of irreversible deformation, a brittle damaging behavior of the epoxy matrix was deduced.

Overall, the volume specific free energy of the material consist of four parts:

$$\psi(\boldsymbol{E}, D, D^\chi) = \psi_{mech}(\boldsymbol{E}, D) + \psi_h(D) + \psi_g(\nabla_0 D^\chi) + \psi_\chi(D, D^\chi) \tag{3.1}$$

In above equation (3.1), the scalar damage variable D describes the amount of stiffness degradation of a material point. Here, $D = 0$ refers to a virgin material with no stiffness degradation, while $D = 1$ refers to a complete loss of material stiffness. Generally, $0 \leq D \leq 1$ holds in case of numeric simulations. The variable $\boldsymbol{E}$ is the Green-Lagrange strain tensor which is defined as

$$\boldsymbol{E} = \frac{1}{2}[\boldsymbol{F}^T \cdot \boldsymbol{F} - \boldsymbol{I}], \tag{3.2}$$

where $\boldsymbol{I}$ is the unit tensor and $\boldsymbol{F}$ is the deformation gradient defined as the derivative of the current (deformed) configuration $\boldsymbol{x}$ with respect to the reference (undeformed) configuration $\boldsymbol{X}$:

$$\boldsymbol{F} = \nabla_0 \boldsymbol{x} = \frac{\partial \boldsymbol{x}}{\partial \boldsymbol{X}} \tag{3.3}$$

As can be seen in in Eq. (3.3), ∇_0 refers to the spatial gradient with respect to the reference config-

uration. Furthermore, the variable D^χ in equation (3.1) is the micromorphic counterpart of the local damage variable D and is treated as an additional degree of freedom. The four parts of the free energy density (3.1) are discussed in the following.

The material model used for the elastic response (ψ_e) is the St. Venant-Kirchhoff material model which in general reads

$$\psi_e^*(\boldsymbol{E}) = \frac{\lambda}{2}\mathrm{tr}(\boldsymbol{E})^2 + \mu\,\mathrm{tr}(\boldsymbol{E}^2). \tag{3.4}$$

Here, parameters λ and μ are the Lamé constants and $\mathrm{tr}(\boldsymbol{A})$ denotes the trace of Tensor $\boldsymbol{A}$, i.e. $\mathrm{tr}(\boldsymbol{A}) = A_{ii}$).

Inspired by [Fassin et al., 2019*b*], a tension-compression asymmetry is introduced in the stiffness degradation due to local material softening in the first term of Eq. (3.4) giving the mechanical part of the total free energy:

$$\psi_{mech}(\boldsymbol{E}, D) = [1-D]^n\,\frac{\lambda}{2}\left[\mathrm{tr}^+(\boldsymbol{E})\right]^2 + (1-h_{tc}D)^n\,\frac{\lambda}{2}\left[\mathrm{tr}^-(\boldsymbol{E})\right]^2 + [1-D]^n\mu\,\mathrm{tr}(\boldsymbol{E}^2) \tag{3.5}$$

In the above, for $n=1$ the present model reduces to the equivalent strain model, where for $n=2$ the energy equivalent model is obtained. In addition, the degree of crack closure is controlled through the parameter h_{tc}. For $h_{tc} = 1$ damage influences the compression part in the same way as the tension part, no crack closure effects are present. Complementary, for $h_{tc} = 0$ damage is not considered in the compressive regime at all, which corresponds to the highest degree of crack closure. Generally, intermediate states (i.e. $0 \leq h_{tc} \leq 1$) are used. The tension ($\mathrm{tr}^+(\boldsymbol{E})$) and compression ($\mathrm{tr}^-(\boldsymbol{E})$) parts are defined as

$$\mathrm{tr}^+(\boldsymbol{E}) = \langle \mathrm{tr}(\boldsymbol{E})\rangle \quad \text{and} \quad \mathrm{tr}^-(\boldsymbol{E}) = -\langle -\mathrm{tr}(\boldsymbol{E})\rangle\,. \tag{3.6}$$

Here, $\langle a\rangle$ denotes the Macauley brackets:

$$\langle a\rangle = \begin{cases} 0 & \text{for } a \leq 0 \\ a & \text{for } a > 0 \end{cases} \tag{3.7}$$

Additional to the mechanical part, damage hardening is introduced, giving the second part of the free energy

$$\psi_h = \frac{K}{2}D^2 \tag{3.8}$$

In the equation above, parameter K controls the degree of damage hardening. It shall be noted that the terminology originates from the analogy to plastic hardening. In Fig. 3.1, a Gauss point study of parameter K is shown. The material parameters used are those for the matrix material shown in Tab. 3.1 in Sec.3.6. As can be seen, $K = 0\,\mathrm{MPa}$ leads to a very brittle material response while for increasing K, damage is delayed. Higher values of K lead to a slower evolution of damage and thus, a slower decrease of strength and stiffness as well as an increase of maximum load.

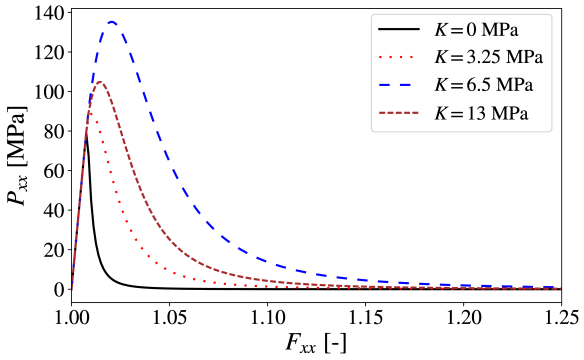

Figure 3.1: Stress-stretch curves for different hardening parameters K.

When using material models which exhibit softening, strain localizations may occur, which causes undesired mesh dependency of the solution. Therefore, the micromorphic extension as introduced, e.g. in [Forest, 2009] is applied. Micromorphic energetic terms ψ_g and ψ_χ (the last two parts of the free energy) are defined as

$$\psi_\chi = \frac{H^\chi}{2}\left[D^\chi - D\right]^2 \tag{3.9}$$

$$\psi_g = \frac{El^2}{2}\left[\nabla_0 D^\chi \cdot \nabla_0 D^\chi\right]. \tag{3.10}$$

In Eqs. (3.9) and (3.10), the micromorphic extension consists of a coupling term ψ_χ and a gradient term ψ_g. The coupling term of Eq. (3.9) with penalty factor H^χ couples the local and the micromorphic damage variable and is chosen sufficiently high, such that the difference between D^χ and D is at least two magnitudes smaller than the numeric value of D itself. As suggested in [Fassin et al., 2019*a*], the Young's modulus E and an internal length scale factor l are used within ψ_g.

Due to the micromorphic extension of the local energy, an extended Clausius-Duhem inequality (see, e.g.[Forest, 2019]) is obtained

$$-\dot{\psi} + \boldsymbol{S} : \dot{\boldsymbol{E}} + \underbrace{a\dot{D}^\chi + \boldsymbol{b} \cdot \nabla_0 \dot{D}^\chi}_{\text{micromorphic extension}} \geq 0, \tag{3.11}$$

where $\boldsymbol{S}$ is the second Piola-Kirchhoff stress tensor, while a and $\boldsymbol{b}$ denote the work conjugate stress-like quantities of the additional degree of freedom D^χ and its gradient $\nabla_0 D^\chi$, respectively. Applying the chain rule on $\dot{\psi}$ and rearranging the terms results in the following expanded inequality:

$$\left[\boldsymbol{S} - \frac{\partial \psi}{\partial \boldsymbol{E}}\right] : \dot{\boldsymbol{E}} + \left[a - \frac{\partial \psi}{\partial D^\chi}\right] \dot{D}^\chi + \left[\boldsymbol{b} - \frac{\partial \psi}{\partial \nabla_0 D^\chi}\right] \cdot \nabla_0 \dot{D}^\chi - \frac{\partial \psi}{\partial D}\dot{D} \geq 0 \tag{3.12}$$

To ensure that Inequality (3.12) holds for arbitrary processes, it is chosen, following the argumentations of [Coleman and Noll, 1961] and [Forest, 2016], to set the brackets to zero. This results in the following

relations:

$$\boldsymbol{S} = \frac{\partial \psi}{\partial \boldsymbol{E}}, \quad a = \frac{\partial \psi}{\partial D^{\chi}}, \quad \boldsymbol{b} = \frac{\partial \psi}{\partial \nabla_0 D^{\chi}} \tag{3.13}$$

The introduction of the stress-like quantities a and $\boldsymbol{b}$ leads to the micromorphic balance equation, which has to be solved additionally to the balance of linear momentum with $\boldsymbol{f}_0$ denoting the conventional body forces (see,e.g. [Peerlings et al., 1996, 2004] or [Forest, 2016]). Hence, the balance equations, which have to be solved read:

$$\text{Div}\,(\boldsymbol{F} \cdot \boldsymbol{S}) + \boldsymbol{f}_0 = \boldsymbol{0}\,; \quad \text{Div}\,(\boldsymbol{b}) - a = 0 \quad \text{in} \quad \Omega_0 \tag{3.14}$$

Equations (3.14) form the strong form of the boundary value problem which have to be fulfilled in every material point of the bulk of body Ω_0. Here, $\boldsymbol{f}_0$ denotes the conventional body forces.

To complete the boundary value problem, Dirichlet and Neumann conditions are defined on the boundary:

$$\begin{array}{rr} \underline{\text{BC for balance of linear momentum:}} & \underline{\text{BC for micromorphic balance:}} \\ [\boldsymbol{F} \cdot \boldsymbol{S}] \cdot \boldsymbol{n}_0 = \boldsymbol{t}_0 \quad \text{on} \quad \partial\Omega_{0,n} & \nabla_0 D^{\chi} \cdot \boldsymbol{n}_0 = 0 \quad \text{on} \quad \partial\Omega_0 \\ \boldsymbol{u} = \hat{\boldsymbol{u}} \quad \text{on} \quad \partial\Omega_{0,d} & \end{array} \tag{3.15}$$

As can be seen in Eq. (3.15), the boundary of the body Ω_0 is decomposed into a Neumann ($\partial\Omega_{0,n}$) and a Dirichlet part ($\partial\Omega_{0,d}$) for the balance of linear momentum. However, in case of the micromorphic balance equation, only Neumann-type boundary conditions are prescribed on $\partial\Omega_0$. Furthermore, the gradient of D^{χ} has to vanish in normal direction on $\partial\Omega_0$, which is equivalent to requiring the crack (or localization zone) to be perpendicular on the boundary. This might seem as an arbitrary restriction, but also widely used in other publications (see, e.g. Clasen et al. [2013], [Holthusen et al., 2020], [Forest, 2009, 2016], [Fassin et al., 2019*a*], [Brepols et al., 2020]) and will be of importance in the following section 3.4.

After application of Eq. (3.13) on the Clausius-Duhem inequality (3.12), the reduced dissipation inequality has to hold:

$$\underbrace{-\frac{\partial \psi}{\partial D}}_{=:Y} \dot{D} \geq 0 \tag{3.16}$$

Here, the damage driving force Y is introduced. Accordingly, the damage driving force for the material model given reads:

$$Y = -\frac{\partial \psi}{\partial D} = n[1-D]^{n-1}\psi_e + H^{\chi}\left[D^{\chi} - D\right] - KD. \tag{3.17}$$

Here, the coupling between the local damage variable D and the micromorphic damage variable D^{χ} becomes apparent. Using the damage driving force Y, a loading function analogous to the yield function

in plasticity can be constructed, where $Y_0 \geq 0$ indicates the damage threshold variable.

$$\Phi(Y) := Y - Y_0 \leq 0 \tag{3.18}$$

Loading and unloading conditions (Karush-Khun-Tucker conditions) ensure that the Clausius-Duhem inequality is fulfilled at any time. For the given damage model, they read:

$$\dot{D} \geq 0, \quad \dot{D}\Phi = 0, \quad \Phi \leq 0 \tag{3.19}$$

Noticeably, damage healing is not considered here.

3.2.2 Interface material model

For the simulation of the interface response between epoxy matrix and carbon fibers, the cohesive zone (CZ) formulation of [Rezaei et al., 2017] is used. Generally speaking, an interface connects two phases $\Omega_{0,1}$ and $\Omega_{0,2}$, while $\boldsymbol{g} = [g_n, g_{s1}, g_{s2}]^T$ and $\boldsymbol{t} = [t_n, t_{s1}, t_{s2}]^T$ describe the gap and traction vectors between the two phases. Here, subscripts n, $s1$ and $s2$ denote the components in normal and both shear directions. The free energy per unit area is given by

$$\psi_{CZ} = \frac{1}{2}(1 - D_{CZ})k_0\lambda_{CZ}^2 + \frac{1}{2}k_p\langle -g_n\rangle^2, \tag{3.20}$$

with $\lambda_{CZ} = \sqrt{\langle g_n\rangle^2 + \beta^2(g_{s1}^2 + g_{s2}^2)}$ denoting the effective separation, where β defines the influence of shear components (see, e.g. [Simon et al., 2015]). The initial stiffness of the interface is denoted by k_0. In the present study, β is set to 1.0 so that the normal and shear gap contribution to the effective separation is the same. Self-penetration of the interface is prevented by the last term with penalty parameter k_p and the negative normal gap $\langle -g_n\rangle$.

From Eq. (3.20), the components of the stress vector can be derived

$$t_n := \frac{\partial\psi_{CZ}}{\partial g_n} = (1 - D_{CZ})k_0\langle g_n\rangle - k_p\langle -g_n\rangle \tag{3.21}$$

$$t_{s1} := \frac{\partial\psi_{CZ}}{\partial g_{s1}} = (1 - D_{CZ})k_0\, g_{s1}\beta^2 \tag{3.22}$$

$$t_{s2} := \frac{\partial\psi_{CZ}}{\partial g_{s2}} = (1 - D_{CZ})k_0\, g_{s2}\beta^2. \tag{3.23}$$

In addition, the effective traction t_{CZ} can be derived as well, giving

$$t_{CZ} = \frac{\partial\psi_{CZ}}{\partial\lambda_{CZ}} = \sqrt{t_n^2 + \beta^{-2}(t_{s1}^2 + t_{s2}^2)} = (1 - D_{CZ})k_0\lambda_{CZ}\,. \tag{3.24}$$

A bilinear traction-separation law is adopted (see Fig. 3.2). It is defined by the maximum traction t_0, the separation at maximum traction λ_0 and the separation at final failure λ_f. Based on the traction-

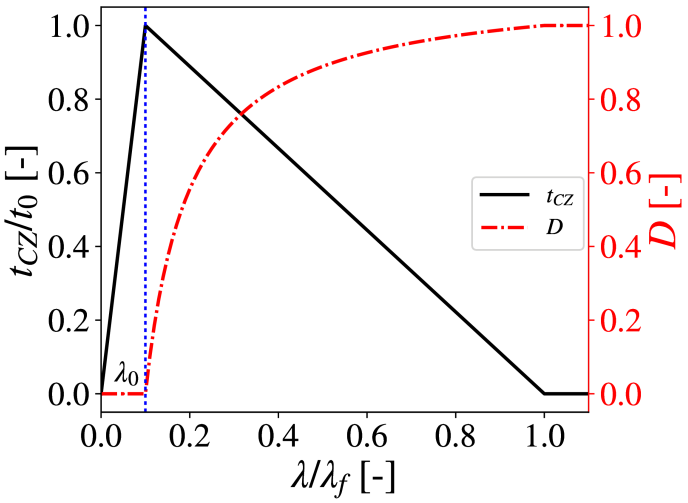

Figure 3.2: Visualization of traction and damage evolution of a bilinear traction-separation law; traction and separation are normalized to maximum traction t_0 and failure separation λ_f.

separation law, the following damage evolution equation has to hold:

$$D_{CZ} = \begin{cases} 0 & \text{if } \lambda < \lambda_0 \\ \frac{\lambda_f}{\lambda_f - \lambda_0} \frac{\lambda - \lambda_0}{\lambda} & \text{if } \lambda_0 < \lambda < \lambda_f \\ 1 & \text{if } \lambda_f < \lambda \end{cases} \tag{3.25}$$

Following the derivation in [Rezaei et al., 2017] and in analogy to the reduced dissipation inequality (cf. Section 3.2.1), the dissipation related to the cohesive zone is obtained as

$$\mathcal{D}_{CZ} = Y_{CZ} \dot{D}_{CZ} = \frac{1}{2} k_0 \lambda^2 \dot{D}_{CZ} \geq 0. \tag{3.26}$$

Here, $Y_{CZ} = -\partial \psi_{CZ} / \partial D_{CZ}$ is the damage driving force of the interface. Since $\frac{1}{2} k_0 \lambda^2 \geq 0$ is fulfilled at any time, the inequality can be reduced to

$$\dot{D}_{CZ} \geq 0, \tag{3.27}$$

showing that no damage healing takes place on the interface.

3.3 Finite element implementation

In the following, we focus on the implementations of the material models introduced in Sec. 3.2 as user-defined elements into the finite element software FEAP.

3.3.1 Implementation of bulk

First, the implementation of the balance of linear momentum and the additional micromorphic balance – as introduced in Sec. 3.2.1 – are presented. While only the key aspects are described here, more detailed investigations can be found, e.g. in [Holthusen et al., 2020], [Fassin et al., 2019*b*] or [Barfusz et al., 2021*a*].

The domain Ω_0^h is introduced as an approximation of the referential body Ω_0. The domain Ω_0^h in turn is split into sub domains Ω_0^e, which will later on be referred to as elements. Index e refers to a unique element identifier (e.g. element number):

$$\Omega_0 \approx \Omega_0^h = \bigcup_{e=1}^{n_{el}} \Omega_0^e \tag{3.28}$$

with n_{el} being the total number of elements. Furthermore, shape functions $\mathrm{N}(\boldsymbol{X})$ (with $\mathrm{N}(\boldsymbol{X})$ being a matrix with dimensions adjusted to the field interpolated) are introduced to approximate the field variables $\boldsymbol{u}(\boldsymbol{X})$ and $D^\chi(\boldsymbol{X})$ from point-wise defined nodal values u^e and $\mathrm{D}^{\chi,e}$.

$$\boldsymbol{u}(\boldsymbol{X}) = \mathrm{N}(\boldsymbol{X}) \cdot \mathrm{u}^e \; ; \quad D^\chi(\boldsymbol{X}) = \mathrm{N}(\boldsymbol{X}) \cdot \mathrm{D}^{\chi,e} \tag{3.29}$$

The same type of trilinear shape functions are used for the displacement and micromorphic damage field, respectively.

As shown in [Poggenpohl et al., 2021], the corresponding weak forms (g_u and g_D) of the balance equations are found by multiplying both parts of Eq. (3.14) with their corresponding test functions ($\delta\boldsymbol{u}$ and δD^χ) and integration over the volume. The weak forms are then linearized with respect to the corresponding increments ($\Delta\delta\boldsymbol{u}$ and $\Delta\delta D^\chi$):

$$g_u := \int_{\Omega_0} \boldsymbol{S} : \delta\boldsymbol{E} \, \mathrm{d}V - \int_{\Omega_0} \boldsymbol{f}_0 \cdot \delta\boldsymbol{u} \, \mathrm{d}V - \int_{\partial_n\Omega_0} \boldsymbol{t}_0 \cdot \delta\boldsymbol{u} \, \mathrm{d}A = 0 \tag{3.30}$$

$$g_D := \int_{\Omega_0} \delta D^\chi \; H^\chi \left[D - D^\chi\right] \, \mathrm{d}V - \int_{\Omega_0} \nabla_0[\delta D^\chi] \cdot \left[El^2 \nabla_0 D^\chi\right] \, \mathrm{d}V = 0 \tag{3.31}$$

$$\Delta g_u = \int_{\Omega_0} \Delta\boldsymbol{S} : \delta\boldsymbol{E} \mathrm{d}V + \int_{\Omega_0} \boldsymbol{S} \cdot \Delta\delta\boldsymbol{E} \, \mathrm{d}V \tag{3.32}$$

$$\Delta g_D = \int_{\Omega_0} \delta D^\chi H^\chi [\Delta D - \Delta D^\chi] \, \mathrm{d}V - \int_{\Omega_0} \nabla_0[\delta D^\chi] \cdot \left[El^2 \nabla_0[\Delta D^\chi]\right] \, \mathrm{d}V \tag{3.33}$$

Here, $\delta\boldsymbol{E}$ is defined as $\delta\boldsymbol{E} = \frac{1}{2}[\boldsymbol{F}^T \cdot \nabla_0(\delta\boldsymbol{u}) + \nabla_0(\delta\boldsymbol{u})^T \cdot \boldsymbol{F}]$, while $\Delta\boldsymbol{S}$ and ΔD describe the sensitivity of stress and damage with respect to changes in $\boldsymbol{u}$ and D^χ, respectively. A more detailed description can be found in [Poggenpohl et al., 2021].

The integrals of Eqs. (3.30) to (3.33) can be divided into the aforementioned element domains Ω_0^e.

Hence, the weak forms and their corresponding linearizations read:

$$g_u^h = \bigcup_{e=1}^{n_e} \delta\mathbf{u}^{e,T} \cdot \mathbf{r}_u^e, \quad \Delta g_u^h = \bigcup_{e=1}^{n_e} \delta\mathbf{u}^{e,T} \cdot \left[\mathbf{K}_{u,u}^e \cdot \Delta\mathbf{u}^e + \mathbf{K}_{u,D^\chi}^e \cdot \Delta\mathbf{D}^{\chi,e}\right] \tag{3.34}$$

$$g_D^h = \bigcup_{e=1}^{n_e} \delta\mathbf{D}^{\chi,e} \cdot \mathbf{r}_D^e, \quad \Delta g_D^h = \bigcup_{e=1}^{n_e} \delta\mathbf{D}^{\chi,eT} \cdot \left[\mathbf{K}_{D^\chi,u}^e \cdot \Delta\mathbf{u}^e + \mathbf{K}_{D^\chi,D^\chi}^e \cdot \Delta\mathbf{D}^{\chi,e}\right] \tag{3.35}$$

In above Eqs. (3.34) and (3.35) $\mathbf{r}_u^e$ and $\mathbf{r}_{D_i}^e$ represent the element residual vectors, while $\mathbf{K}_{u,u}^e$, $\mathbf{K}_{u,D_i^\chi}^e$, $\mathbf{K}_{D_i^\chi,u}^e$ and $\mathbf{K}_{D_i^\chi,D_i^\chi}^e$ refer to the element stiffness matrices. A detailed discussion of the residual vectors and stiffness matrices can be found in [Poggenpohl et al., 2021].

Within a Newton-Raphson iteration, the sum of the weak form and its linearization have to be zero. Furthermore, it has to be taken into account that $\delta\boldsymbol{u}$ and δD^χ can take arbitrary (but nonzero) values. Thus, the element stiffness matrix and element residual vector can be found:

$$\begin{pmatrix} \mathbf{K}_{\boldsymbol{u},\boldsymbol{u}}^e & \mathbf{K}_{\boldsymbol{u},D^\chi}^e \\ \mathbf{K}_{D^\chi,\boldsymbol{u}}^e & \mathbf{K}_{D^\chi,D^\chi}^e \end{pmatrix} \begin{pmatrix} \Delta\mathbf{u}^e \\ \Delta\mathbf{D}^{\chi,e} \end{pmatrix} = - \begin{pmatrix} \mathbf{r}_u^e \\ \mathbf{r}_D^e \end{pmatrix} \tag{3.36}$$

Within a finite element code, these element-wise equation systems are then assembled to form the global system of equations, which in turn is solved using the boundary conditions defined.

Finally, to ensure numerical stability and to prevent snapback behavior, an artificial viscosity as introduced in [Fassin et al., 2019*a*] or [Holthusen et al., 2020] is utilized. Here, the viscosity term is added to the stress and stiffness of the mechanical part on the Gauss point level, which are computed from:

$$\boldsymbol{S}_{vis} = \eta \frac{\Delta\boldsymbol{E}}{\Delta t} \tag{3.37}$$

$$\mathbb{C}_{vis} = \frac{\eta}{\Delta t}\mathbb{I} \tag{3.38}$$

In the above, Δ denotes the increment of the current step with respect to the previous calculated step and $\mathbb{I}$ is the fourth order identity tensor. It shall be noted that the strain increment $\Delta\boldsymbol{E}$ is calculated from

$$\Delta\boldsymbol{E} = \boldsymbol{F}_{n+1}^T \cdot \boldsymbol{F}_{n+1} - \frac{1}{2}\boldsymbol{F}_n^T \cdot \boldsymbol{F}_{n+1} - \frac{1}{2}\boldsymbol{F}_{n+1}^T \cdot \boldsymbol{F}_n \tag{3.39}$$

to give consistent results. Here, $\boldsymbol{F}_{n+1}^T$ denotes the deformation gradient of the current time step while $\boldsymbol{F}_n^T$ denotes the deformation gradient of the previous time step.

3.3.2 Implementation of the interface

The implementation of the interface response into cohesive zone elements (CZE) is based on the formulation introduced in [Rezaei et al., 2017]. The CZE is introduced as an eight node element between two phases of a body (denoted here as $\Omega_{0,1}$ and $\Omega_{0,2}$) as indicated in Fig.3.3. Here, the surface of one

phase is indicated by Γ_+, while the surface of the other phase is indicated by Γ_-.

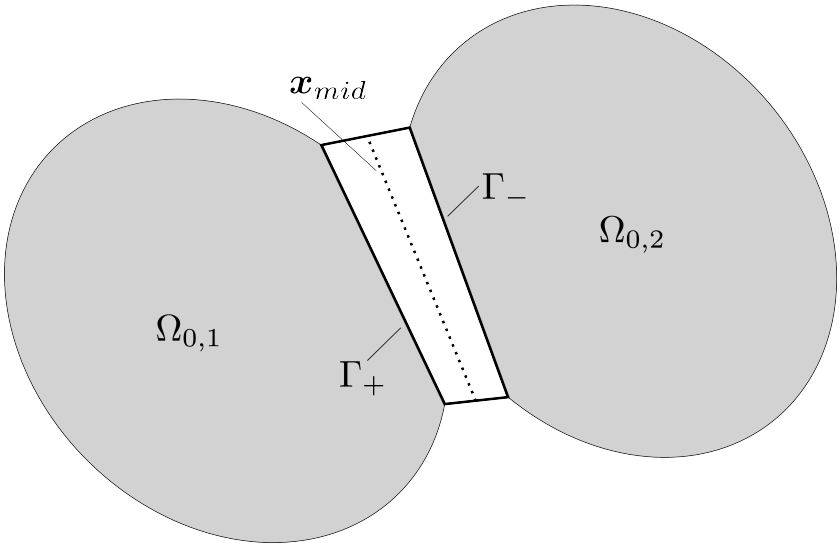

Figure 3.3: Visualization of a cohesive zone element.

For a better approximation of quantities, a middle plane is introduced:

$$\boldsymbol{x}_{mid} = \frac{1}{2}(\boldsymbol{x}_+ + \boldsymbol{x}_-) \tag{3.40}$$

Here, $\boldsymbol{x}_+$ and $\boldsymbol{x}_-$ are the position vectors (in reference configuration) on each side of the cohesive zone. For a zero thickness CZE the position vectors of the undeformed configuration for each side of the CZ are identical (i.e. $\boldsymbol{X}_+ \equiv \boldsymbol{X}_-$). However, due to numerical reasons, the CZs used in this publication initially have a – small – thickness. Gap and traction vectors are calculated with respect to this middle plane. Details on how to calculate the effective traction and gap vectors of the middle plane can be found in [Rezaei et al., 2017].

The CZE is restricted to a certain normal direction of the local coordinate system. However, within the meshes used here, the orientation of the local coordinate system cannot be known a priori. Therefore, a renumbering of the nodes at the element level is introduced as suggested in [Reese, 2007] for solid shell elements.

Additionally, the CZ element residual vector and stiffness matrix have to be extended to fit the shape of the residual vector and stiffness matrix of the bulk, respectively. It is assumed that the interface does not influence or is influenced by the micromorphic damage field. Therefore, it is sufficient to use the local form of the damage formulation here. The residuum and stiffness associated with the micromorphic damage field are zero:

$$\begin{pmatrix} \mathbf{K}^e_{\boldsymbol{u},\boldsymbol{u}} & \mathbf{0} \\ \mathbf{0} & \mathbf{0} \end{pmatrix} \begin{pmatrix} \Delta\mathbf{u}^e \\ \Delta\mathbf{D}^{\chi,e} \end{pmatrix} = - \begin{pmatrix} \mathbf{r}^e_u \\ \mathbf{0} \end{pmatrix} \tag{3.41}$$

From Eq. (3.41) it can be seen that the CZE elements decouple the phases in case of the micromorphic variable. As will be shown later, the carbon fibers are assumed to have a much higher damage resistance than the surrounding matrix material and do not damage at the given loading. Hence, the effect of hypothesizing such a decoupled micromorphic damage field is assumed to be negligible.

3.4 Homogenization theory

In the following, the classical Hill homogenization approach will be enhanced for gradient-extended material models based on the micromorphic concept.

For that, Hill's approach is applied first on an RUC with perfect interfaces between fibers and matrix and without localization. Next, the influence of damaging interfaces — i.e. debonding between fibers and matrix — will be taken into account. Finally, the novel failure zone homogenization scheme tackling both, damage- and debonding-induced, softening is derived, leading to an advanced homogenization formulation.

In the following, a subscript M denotes quantities of the macro level, while m denotes quantities of the micro level.

3.4.1 Homogenization scheme accounting for gradient-extended (micromorphic) damage

Based on the hypothesized equivalence of virtual work density on the microscopic and macroscopic level, the Hill-Mandel condition [Hill, 1967, 1972] states that for a representative volume element the product of the averages is equal to the average of the products:

$$\delta\mathcal{W}_M = \{\delta\mathcal{W}_m\}_{\Omega_0} \qquad \Longleftrightarrow \qquad \{\boldsymbol{P}_m\}_{\Omega_0} : \{\delta\boldsymbol{F}_m\}_{\Omega_0} = \{\boldsymbol{P}_m : \delta\boldsymbol{F}_m\}_{\Omega_0} \tag{3.42}$$

Here, $\boldsymbol{P}_m$ is the first Piola-Kirchhoff stress tensor of the micro scale, which is the work conjugate stress quantity to the deformation gradient of the micro scale $\boldsymbol{F}_m$. Further, $\{*\}_{\Omega_0}$ denotes the volume average, i.e.:

$$\{*\}_{\Omega_0} = \frac{1}{|\Omega_0|}\int_{\Omega_0} (*)\ \mathrm{dV}, \tag{3.43}$$

where, $|\Omega_0|$ refers to the volume of Ω_0. As described, e.g. in [Geers, Kouznetsova, Matouš and Yvonnet, 2017], one can show that for certain sets of boundary conditions such as periodic boundary conditions, Eq. (3.42) implies that the stress of a macroscale material point, $\boldsymbol{P}_M$, is the same as the volume averaged stresses within the corresponding volume element on the micro-scale:

$$\boldsymbol{P}_M = \{\boldsymbol{P}_m\}_{\Omega_0} \tag{3.44}$$

Nevertheless, further investigations are necessary when considering gradient materials, as shown e.g. in [Hirschberger et al., 2008], because for an accurate homogenization, the work conjugates of the gradient terms have to be taken into account as well. Hence, the contribution of micromorphic work conjugates a and $\boldsymbol{b}$ has to be considered, giving

$$\{\boldsymbol{P}_m\}_{\Omega_0} : \{\delta\boldsymbol{F}_m\}_{\Omega_0} = \{\boldsymbol{P}_m : \delta\boldsymbol{F}_m + a\,\delta D^\chi + \boldsymbol{b}\cdot\nabla_0\delta D^\chi\}_{\Omega_0}. \tag{3.45}$$

However, according to [Clasen et al., 2013], for micromorphic extended material models the virtual work done by the work conjugates for the entire body (Ω_0) vanishes. For completeness, the important steps are shown in the following.

Starting from the sum of all virtual work contributions in Eq. (3.45), the latter term of this equation can be rewritten by exploiting the product rule:

$$\begin{aligned} &\mathrm{Div}(\boldsymbol{b}\delta D^\chi) = \mathrm{Div}(\boldsymbol{b})\delta D^\chi + \boldsymbol{b}\cdot\nabla_0 D^\chi \\ \Leftrightarrow\quad &\boldsymbol{b}\cdot\nabla_0\delta D^\chi = \mathrm{Div}(\boldsymbol{b}\delta D^\chi) - \mathrm{Div}(\boldsymbol{b})\delta D^\chi \end{aligned} \tag{3.46}$$

Rearranging the micromorphic balance equation (Eq. (3.14)) yields:

$$\mathrm{Div}(\boldsymbol{b}) = a \tag{3.47}$$

Hence, application of Eqs. (3.13) and (3.10) to Eq. (3.15), the following condition for $\boldsymbol{b}$ at the boundary is achieved:

$$\boldsymbol{b}\cdot\boldsymbol{n}_0 = El^2\,\nabla_0 D^\chi\cdot\boldsymbol{n}_0 = 0 \quad \text{on } \partial\Omega_0 \tag{3.48}$$

Then, the virtual work of of the micromorphic extension can be rewritten using above Eqs. (3.46) to (3.48) and applying the divergence theorem:

$$\begin{aligned} \int_{\Omega_0}\left[a\,\delta D^\chi + \boldsymbol{b}\cdot\nabla_0\delta D^\chi\right]\,\mathrm{d}V &\overset{(3.46)}{=} \int_{\Omega_0}\left[a\,\delta D^\chi + \mathrm{Div}(\boldsymbol{b}\delta D^\chi) - \mathrm{Div}(\boldsymbol{b})\,\delta D^\chi\right]\,\mathrm{d}V \\ &\overset{(3.47)}{=} \int_{\Omega_0}\left[a\,\delta D^\chi + \mathrm{Div}(\boldsymbol{b}\delta D^\chi) - a\,\delta D^\chi\right]\,\mathrm{d}V = \int_{\Omega_0}\mathrm{Div}(\boldsymbol{b}\delta D^\chi)\,\mathrm{d}V \\ &= \int_{\partial\Omega_0}\boldsymbol{b}\cdot\boldsymbol{n}_0\,\delta D^\chi\,\mathrm{d}A \overset{(3.48)}{=} 0 \end{aligned} \tag{3.49}$$

From Eq. (3.49) it becomes apparent that the classical Hill's theorem (3.42) applies even at the presence of micromorphic entities. Noticeably, this only holds true for homogenization over the whole computational domain and perfect interfaces.

3.4.2 Homogenization scheme accounting for debonding of non-perfect interfaces

In what follows, we derive the homogenization scheme including non-perfect interfaces based on the derivations provided in [Geers, Kouznetsova, Matouš and Yvonnet, 2017]. For RUCs of carbon fiber reinforced plastics, this refers to the interface of carbon fibers and epoxy matrix. Hence, the homogenization approach presented in the previous Sec. 3.4.1 has to be extended. For simplicity, one inclusion and its interface are considered here, but the methodology also holds for more inclusions. As can be

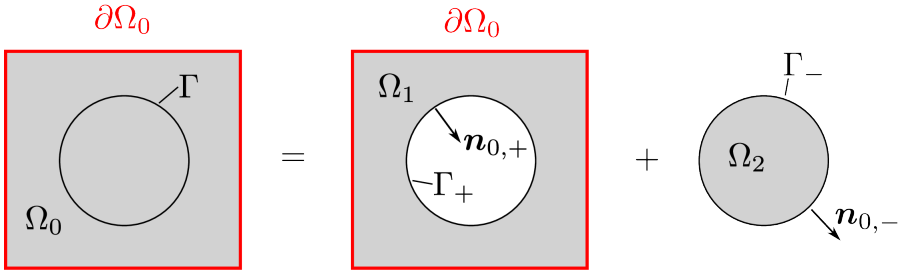

Figure 3.4: Matrix (Ω_1) and embedded inclusion (Ω_2) separated in subdomains by a cohesive zone (Γ_+ and Γ_-).

seen in Fig. 3.4, the body Ω_0 is separated by the cohesive zone into the sub domains Ω_1 and Ω_2 with boundaries $\partial\Omega_0$, Γ_+ and Γ_-, respectively. Normal vectors $\boldsymbol{n}_{0,+}$ and $\boldsymbol{n}_{0,-}$ are introduced for each of the boundaries. Hence, the subscripts $+$ and $-$ denote quantities on the boundaries of Ω_1 and Ω_2 (i.e. on the different sides of the interface), respectively.

Based on the separation in Fig. 3.4, the volume integral of the stress can be divided into volume integrals of the two subdomains which, in turn, can be transformed into three surface integrals:

$$\begin{aligned}\frac{1}{|\Omega_0|}\int_{\Omega_0}\boldsymbol{P}_m\,\mathrm{d}V =& \frac{1}{|\Omega_0|}\left(\int_{\Omega_1}\boldsymbol{P}_m\,\mathrm{d}V+\int_{\Omega_2}\boldsymbol{P}_m\,\mathrm{d}V\right)\\ =& \frac{1}{|\Omega_0|}\left(\int_{\partial\Omega_0}\underbrace{\boldsymbol{n}_{0,0}\cdot\boldsymbol{P}_{m,0}^T}_{\boldsymbol{t}_0}\otimes\boldsymbol{X}_{m,0}\,\mathrm{d}A+\int_{\Gamma_+}\underbrace{\boldsymbol{n}_{0,+}\cdot\boldsymbol{P}_{m,+}^T}_{\boldsymbol{t}_{0,+}}\otimes\boldsymbol{X}_{m,+}\,\mathrm{d}A\right.\\ &\left.+\int_{\Gamma_-}\underbrace{\boldsymbol{n}_{0,-}\cdot\boldsymbol{P}_{m,-}^T}_{\boldsymbol{t}_{0,-}}\otimes\boldsymbol{X}_{m,-}\,\mathrm{d}A\right)\end{aligned}\tag{3.50}$$

Within the surface integrals, the surface tractions $\boldsymbol{t}-0$, $\boldsymbol{t}_{0,+}$ and $\boldsymbol{t}_{0,-}$ on the boundaries are introduced. Furthermore, since all quantities are defined in the reference configuration, it can be assumed that the boundaries Γ_+ and Γ_- coincide (i.e. $\Gamma_+=\Gamma_-=\Gamma$). In addition, the stress continuity condition can be applied

$$\boldsymbol{P}_{m,+}=\boldsymbol{P}_{m,-}\tag{3.51}$$

and the normal vectors shall be consistent through all sub geometries

$$\boldsymbol{n}_0 = \boldsymbol{n}_{0,+} = -\boldsymbol{n}_{0,-} \ . \tag{3.52}$$

Thus, the surface tractions on each side of the interface are equal in amount but opposite in direction. Consequently, Eq. (3.50) can be simplified to form

$$\begin{aligned}\frac{1}{|\Omega_0|}\int_{\Omega_0} \boldsymbol{P}_m \,\mathrm{d}V =& \frac{1}{|\Omega_0|}\left(\int_{\partial\Omega_0} \boldsymbol{n}_0 \cdot \boldsymbol{P}_m^T \otimes \boldsymbol{X}_m \,\mathrm{d}A + \int_{\Gamma} \boldsymbol{t} \otimes \boldsymbol{X}_m \,\mathrm{d}A + \int_{\Gamma} -\boldsymbol{t} \otimes \boldsymbol{X}_m \,\mathrm{d}A\right) \\ =& \frac{1}{|\Omega_0|}\left(\int_{\partial\Omega_0} \boldsymbol{n}_0 \cdot \boldsymbol{P}_m^T \otimes \boldsymbol{X}_m \,\mathrm{d}A \ .\right)\end{aligned} \tag{3.53}$$

As a result, the introduction of an interface does not affect the volume average of the stresses.

In analogy to $\boldsymbol{P}$, the following is found for $\boldsymbol{F}$:

$$\begin{aligned}\frac{1}{|\Omega_0|}\int_{\Omega_0} \boldsymbol{F}_m \,\mathrm{d}V =& \frac{1}{|\Omega_0|}\left(\int_{\Omega_1} \boldsymbol{F}_m \,\mathrm{d}V + \int_{\Omega_2} \boldsymbol{F}_m \,\mathrm{d}V\right) \\ =& \frac{1}{|\Omega_0|}\left(\int_{\partial\Omega_0} \boldsymbol{x} \otimes \boldsymbol{n}_0 \,\mathrm{d}A + \int_{\Gamma_+} \boldsymbol{x} \otimes -\boldsymbol{n}_0 \,\mathrm{d}A + \int_{\Gamma_-} \boldsymbol{x} \otimes \boldsymbol{n}_0 \,\mathrm{d}A\right)\end{aligned} \tag{3.54}$$

In contrast to the traction, a continuity condition does not exist for the deformation field. Therefore, the displacement jump over the interface

$$\boldsymbol{g} = \boldsymbol{x}_- - \boldsymbol{x}_+ \tag{3.55}$$

is defined. Consequently, the displacement jump over the interface is equal to the gap vector of the CZE as described in Sec. 3.2.2. Hence, Eq. (3.54) can be rewritten, yielding:

$$\underbrace{\frac{1}{|\Omega_0|}\int_{\Omega_0} \boldsymbol{F}_m \,\mathrm{d}V}_{\boldsymbol{F}_{bulk}} = \underbrace{\frac{1}{|\Omega_0|}\int_{\partial\Omega_0} \boldsymbol{x} \otimes \boldsymbol{n}_0 \,\mathrm{d}A}_{\boldsymbol{F}_{ext}} - \underbrace{\frac{1}{|\Omega_0|}\int_{\Gamma} \boldsymbol{g} \otimes \boldsymbol{n}_0 \,\mathrm{d}A}_{\boldsymbol{F}_{CZ}} \tag{3.56}$$

It shall be noted that coinciding Γ_+ and Γ_- is used here. Then, the displacement gradient averaged over the bulk ($\boldsymbol{F}_{bulk}$) is the same as the displacement gradient measured over the external boundary ($\boldsymbol{F}_{ext}$) subtracted by the displacement gradient of the interface ($\boldsymbol{F}_{CZ}$). Rearanging Eq. (3.56) yields

$$\boldsymbol{F}_{ext} = \boldsymbol{F}_{bulk} + \boldsymbol{F}_{CZ} \ , \tag{3.57}$$

which states that the (externally measured) displacement is composed of the displacement of the bulk as well as the displacement jump of the interface.

From these derivations for stress and deformation gradient, a homogenization approach at the pres-

ence of interfaces can be derived accordingly for the virtual work of the bulk:

$$\begin{aligned}\frac{1}{|\Omega_0|}\int_{\Omega_0}\boldsymbol{P}_m:\delta\boldsymbol{F}_m\,\mathrm{d}V &= \frac{1}{|\Omega_0|}\left(\int_{\Omega_1}\boldsymbol{P}_m:\delta\boldsymbol{F}\,\mathrm{d}V+\int_{\Omega_2}\boldsymbol{P}_m:\delta\boldsymbol{F}\,\mathrm{d}V\right)\\ &= \frac{1}{|\Omega_0|}\left(\int_{\partial\Omega_0}\boldsymbol{n}_0\cdot\boldsymbol{P}_m^T\delta\boldsymbol{x}\,\mathrm{d}A+\int_{\Gamma_+}-\boldsymbol{n}_0\cdot\boldsymbol{P}_m^T\delta\boldsymbol{x}\,\mathrm{d}A+\int_{\Gamma_-}\boldsymbol{n}_0\cdot\boldsymbol{P}_m^T\delta\boldsymbol{x}\,\mathrm{d}A\right)\\ &= \frac{1}{|\Omega_0|}\int_{\partial\Omega_0}\boldsymbol{n}_0\cdot\boldsymbol{P}_m^T\delta\boldsymbol{x}\,\mathrm{d}A-\frac{1}{|\Omega_0|}\int_{\Gamma}\overbrace{\boldsymbol{n}_0\cdot\boldsymbol{P}_m^T}^{\boldsymbol{t}}\delta\boldsymbol{g}\,\mathrm{d}A\end{aligned}\tag{3.58}$$

In case of the virtual work, the analogy to the deformation gradient becomes apparent. Above equation can be rearranged, giving:

$$\underbrace{\frac{1}{|\Omega_0|}\int_{\partial\Omega_0}\boldsymbol{n}_0\cdot\boldsymbol{P}_m^T\cdot\delta\boldsymbol{x}\,\mathrm{d}A}_{\delta\mathcal{W}_{ext}}=\underbrace{\frac{1}{|\Omega_0|}\int_{\Omega_0}\boldsymbol{P}_m:\delta\boldsymbol{F}_m\,\mathrm{d}V}_{\delta\mathcal{W}_{bulk}}+\underbrace{\frac{1}{|\Omega_0|}\int_{\Gamma}\boldsymbol{t}\cdot\delta\boldsymbol{g}\,\mathrm{d}A}_{\delta\mathcal{W}_{CZ}}\tag{3.59}$$

Here, the external virtual work, which is equal to the macroscopic virtual work, is composed of the virtual work of the bulk and the virtual work of the interface. Therefore, a homogenization scheme also has to account for the contributions of the interface.

3.4.3 Failure zone homogenization scheme with gradient-extended (micromorphic) damage and debonding

In what follows, the results from previous sections 3.4.1 and 3.4.2 are combined. Moreover, the failure zone averaging method introduced by [Nguyen et al., 2010], which ensures size-independent results even in the softening regime, is extended accordingly.

It was shown e.g. in [Gitman et al., 2007] that classical Hill-Mandel homogenization is not applicable at the presence of localization phenomena. This is related to a mismatch in the dimensions between the elastic volume (scaling with W×H per unit depth) and the dissipating volume (scaling only with W×ℓ or H×ℓ per unit depth) as visualized in Fig. 3.5. This mismatch causes the RUC to show a more brittle behavior with increasing size as will be shown in Sec. 3.6.3.

The failure zone averaging as introduced in [Nguyen et al., 2010] has proven to overcome the afore mentioned dimension mismatch by applying the volume averaging only on the actively damaging domain Ω_d which is defined as

$$\Omega_d := \{\boldsymbol{x}\ \in\ \Omega_0 \mid \dot{D}(\boldsymbol{x})>0\}.\tag{3.60}$$

A representation of the failure zone is shown in Fig. 3.5, where Ω_e describes the elastically unloading zone. Analogously, a domain of actively damaging interfaces can be identified as well:

$$\Gamma_d := \{\boldsymbol{x}\ \in\ \Gamma_0 \mid \dot{D}(\boldsymbol{x})>0\}\tag{3.61}$$

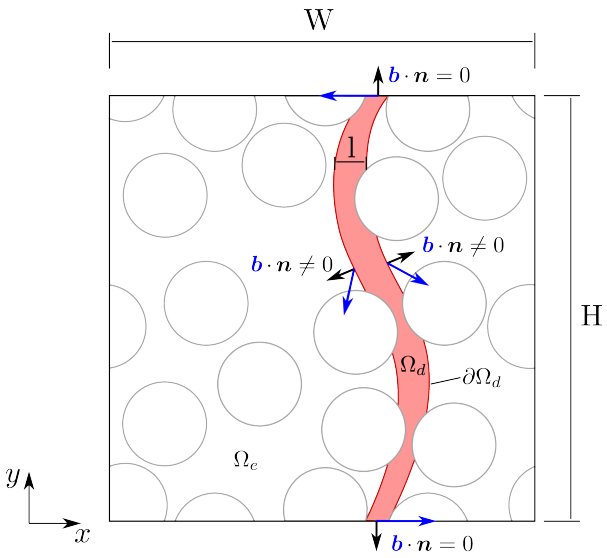

Figure 3.5: Exemplary geometry with failure zone Ω_d (red) and elastically unloading zone Ω_e; normal vector ($\boldsymbol{n}$) and micromorphic stress vector ($\boldsymbol{b}$) are shown at the boundary of Ω_d.

It was shown in [Nguyen et al., 2010] and following publications (e.g. [Nguyen et al., 2011] or [Turteltaub and de Jong, 2019]) that this averaging technique resolves the issue of dimension mismatch. Thus, a representative size for the RUCs can be found.

As derived in Eq. (3.49), the virtual work of the micromorphic constituents vanishes when averaging over the whole domain. But as can be seen in Eq. (3.48), this depends on the boundary condition applied on $\nabla_0 D^\chi$. In general, as indicated in Fig. 3.5, the boundaries $\partial\Omega_d$ and $\partial\Omega_0$ do not coincide, and therefore, the micromorphic quantities do not vanish. Consequently, the Hill condition in this case must be adjusted:

$$\begin{aligned}\{\boldsymbol{P}_m\}_{\Omega_d} : \{\delta\boldsymbol{F}_m\}_{\Omega_d} &= \frac{1}{|\Omega_d|}\int_{\Omega_d}\left[\boldsymbol{P}_m : \delta\boldsymbol{F}_m + a\delta D^\chi + \boldsymbol{b}\cdot\nabla_0\delta D^\chi\right]\,\mathrm{d}V \\ &= \frac{1}{|\Omega_d|}\int_{\Omega_d}\left[\boldsymbol{P}_m : \delta\boldsymbol{F}_m + \mathrm{Div}\left(\boldsymbol{b}\,\delta D^\chi\right)\right]\,\mathrm{d}V \\ &= \frac{1}{|\Omega_d|}\int_{\partial\Omega_d}\left[\boldsymbol{n}_0\cdot\boldsymbol{P}_m^T\cdot\delta\boldsymbol{x}_m + \boldsymbol{n}_0\cdot\boldsymbol{b}\,\delta D^\chi\right]\,\mathrm{d}A\end{aligned} \tag{3.62}$$

In consequence, the mechanical virtual work generally is accompanied by the micromorphic virtual work. In line with [Geers, Kouznetsova, Matouš and Yvonnet, 2017], the following relation for $\delta\boldsymbol{x}_m$ is introduced

$$\delta\boldsymbol{x}_m = \{\delta\boldsymbol{F}_m\}_{\Omega_d}\cdot\boldsymbol{X}_m + \delta\boldsymbol{w}_m \tag{3.63}$$

assuming that the virtual deformation of a material point, $\delta\boldsymbol{x}_m$, can be described via a virtual average deformation, $\{\delta\boldsymbol{F}_M\}_{\Omega_d}\cdot\boldsymbol{X}_m$, and a virtual fluctuation term, $\delta\boldsymbol{w}_m$. Application of Eq. (3.63) on

Eq. (3.62) yields:

$$\begin{aligned}\{\boldsymbol{P}_m\}_{\Omega_d} : \{\delta\boldsymbol{F}_m\}_{\Omega_d} &= \frac{1}{|\Omega_d|}\int_{\partial\Omega_d}\left[\boldsymbol{n}_0\cdot\boldsymbol{P}_m^T\cdot(\{\delta\boldsymbol{F}_m\}_{\Omega_d}\cdot\boldsymbol{X}_m+\delta\boldsymbol{w}_m)+\boldsymbol{n}_0\cdot\boldsymbol{b}\,\delta D^\chi\right]\,\mathrm{d}A\\ &= \frac{1}{|\Omega_d|}\Bigg(\overbrace{\int_{\partial\Omega_d}\boldsymbol{n}_0\cdot\boldsymbol{P}_m^T\otimes\boldsymbol{X}_m\,\mathrm{d}A}^{\int_{\Omega_d}\boldsymbol{P}_m\mathrm{d}V}:\{\delta\boldsymbol{F}_m\}_{\Omega_d}+\overbrace{\int_{\partial\Omega_d}\boldsymbol{n}_0\cdot\boldsymbol{P}_m^T\cdot\delta\boldsymbol{w}_m\,\mathrm{d}A}^{=0?}\\ &+\underbrace{\int_{\partial\Omega_d}\boldsymbol{n}_0\cdot\boldsymbol{b}\,\delta D^\chi\,\mathrm{d}A}_{\neq 0}\Bigg)\end{aligned}\tag{3.64}$$

From Eq. (3.64) it becomes apparent that the virtual work of the bulk in the actively damaging zone, Ω_d, can be decomposed into three parts which are defined on the boundary of Ω_d. As given in [Geers, Kouznetsova, Matouš and Yvonnet, 2017], the first term leads to the homogenization relation of the stress, Eq. (3.44), but only if the second term vanishes. It is shown in the latter publication that the second term vanishes for certain boundary conditions (e.g. periodic or fixed boundary conditions). However, as indicated in Eq. (3.64), it is questionable whether these boundary conditions also apply on the boundary of Ω_d. Likewise, the third term does not vanish in the case of failure zone averaging. Therefore, a homogenization condition for the Stress would have to account for this energetic contribution additionally to the contribution of the mechanical parts.

As shown in Eq. (3.64), it has to be determined whether the second term vanishes. Therefore, the surface integral is transformed into a volume integral giving

$$\int_{\Omega_d}\left(\mathrm{Div}\,(\boldsymbol{P}_m)\cdot\delta\boldsymbol{w}_m+\boldsymbol{P}_m:\nabla_0(\delta\boldsymbol{w}_m)\right)\,\mathrm{d}V=0.\tag{3.65}$$

Here, the first term vanishes since $\mathrm{Div}\,(\boldsymbol{P}_m)=0$ holds for static problems without body forces. Then, the virtual fluctuations $\delta\boldsymbol{w}_m$ can be rewritten using reformulated Eq. (3.63):

$$\int_{\Omega_d}\boldsymbol{P}_m:\nabla_0(\delta\boldsymbol{x}_m-\{\delta\boldsymbol{F}_m\}_{\Omega_d}\cdot\boldsymbol{X}_m)\,\mathrm{d}V=0\tag{3.66}$$

Rearranging above equation yields

$$\begin{aligned}\int_{\Omega_d}\boldsymbol{P}_m:\nabla_0(\delta\boldsymbol{x}_m)\,\mathrm{d}V&=\int_{\Omega_d}\boldsymbol{P}_m:\nabla_0(\{\delta\boldsymbol{F}_m\}_{\Omega_d}\cdot\boldsymbol{X}_m)\,\mathrm{d}V\\ \Leftrightarrow\int_{\Omega_d}\boldsymbol{P}_m:\delta\boldsymbol{F}_m\,\mathrm{d}V&=\int_{\Omega_d}\boldsymbol{P}_m\,\mathrm{d}V:\{\delta\boldsymbol{F}_m\}_{\Omega_d},\end{aligned}\tag{3.67}$$

where it was exploited that $\{\delta\boldsymbol{F}_m\}_{\Omega_d}$ is constant in Ω_d. Eq. (3.67) divided by Ω_d gives

$$\{\boldsymbol{P}_m\}_{\Omega_d}:\{\delta\boldsymbol{F}_m\}_{\Omega_d}=\{\boldsymbol{P}_m:\delta\boldsymbol{F}_m\}_{\Omega_d},\tag{3.68}$$

which is equal to the equation investigated in [Nguyen et al., 2011]. There, Eq. (3.68) was substantiated with numerical results. As shown here, this equation is equal to the assumption that the second term in Eq. (3.64) vanishes. In Sec. 3.6.3 it is numerically investigated whether Eq. (3.68) holds true.

In Sec. 3.4.2 it was shown that the virtual work of the bulk must be extended by the virtual work of the interface. Similarly, this also holds true for the failure zone averaging:

$$\{\boldsymbol{P}_m\}_{\Omega_d} : \{\delta\boldsymbol{F}_m\}_{\Omega_d} = \frac{1}{|\Omega_d|}\left(\int_{\partial\Omega_d} \boldsymbol{n}_0 \cdot \boldsymbol{P}_m^T \otimes \boldsymbol{X}_m \,\mathrm{d}A : \delta\boldsymbol{F}_M + \int_{\partial\Omega_d} \boldsymbol{n}_0 \cdot \boldsymbol{P}_m^T \cdot \delta\boldsymbol{w}_m \,\mathrm{d}A \right.$$
$$\left. + \int_{\partial\Omega_d} \boldsymbol{n}_0 \cdot \boldsymbol{b}\delta D^\chi \,\mathrm{d}A + \int_{\Gamma_d} \boldsymbol{t} \cdot \delta\boldsymbol{g} \,\mathrm{d}A \right) \tag{3.69}$$

Likewise to the extension in Eq. 3.59, the virtual work in Eq. 3.64 has been extended by the energetic contribution of the actively damaging interfaces.

3.5 Generating repeating unit cells (RUCs)

The material of interest was long fiber reinforced plastic. It was assumed that the fibers were perfect cylinders and no inhomogeneities appeared along the fiber direction. The diameter of the fibers was assumed constant at $7\,\mu\mathrm{m}$ which is in accordance with e.g. [Makeev et al., 2019]. The geometries of the repeating unit cells were generated using three different approaches:

1. A regular pattern with manually defined fiber distribution,
2. the so-called *randomized* method, and
3. the *random sequential absorbtion* (*RSA*) method (see, e.g. [Illian et al., 2008] or [Schneider et al., 2016]).

The latter two methods were used to automatically generate random fiber distributions. The volume fraction of the fibers was kept the same for all RUCs and was approximately 53.5%. A mesh with one layer (with a constant thickness of $1\,\mu\mathrm{m}$) of three dimensional, eight node, hexahedral elements was used for both, bulk and interface. Furthermore, height and width of the RUCs were chosen to be equal.

The RUCs resulting from the *regular* grid resemble the hexagonal close packing as visualized in Fig 3.6. Noticeably, the fibers at the lower left corner (marked in red) were shifted with respect to their position in a regular grid. This imperfection was applied to trigger damage evolution and avoid numerical instabilities due to bifurcation.

The *randomized* method for geometry generation was based on the regular grid, where a random shift was applied to each of the fibers as visualized in Fig. 3.7. In addition, the shift applied to each of the fibers was restricted to prevent overlapping fibers.

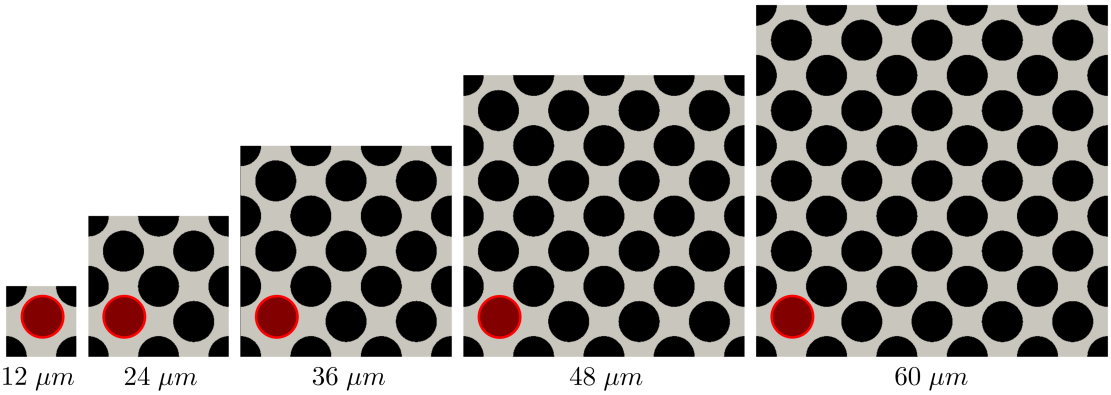

Figure 3.6: Different sizes of RUCs used for a regular grid with imperfection (marked in red); RUC sizes range from $12\,\mu\text{m} \times 12\,\mu\text{m} \times 1\,\mu\text{m}$ (left) to $60\,\mu\text{m} \times 60\,\mu\text{m} \times 1\,\mu\text{m}$ (right)

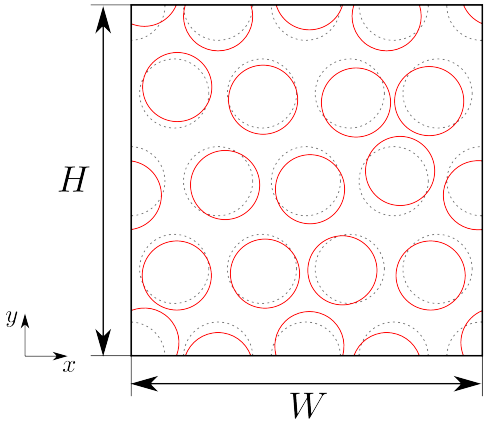

Figure 3.7: Visualization of the generation of a *randomized* RUC geometry; solid black: RUC boundary, dashed: original regular distribution of fibers, red: final distribution of fibers

Another set of RUCs was generated using the *random sequential absorbtion* (*RSA*) method. As described in [Illian et al., 2008; Schneider et al., 2016], fibers were sequentially placed into the RUC with random coordinates for each fiber, where only those fibers were accepted that did not overlap any of the already existing ones (see 3.8). To prevent narrow gaps, new fibers that were too close to already existing fibers were rejected in this approach as well. New fibers were generated until the desired amount of fiber volume fraction was reached. RUCs generated by this approach were referred as *RSA* RUCs.

Comparison of Figs. 3.7 and 3.8 showed that for the *RSA* generation method a higher degree of clustering occured. *Randomized* RUCs in general showed a more even fiber distribution compared to *RSA* RUCs. Furthermore, fibers which overlapped the edges of the RUC were mirrored to the other side to create a repetitive geometry.

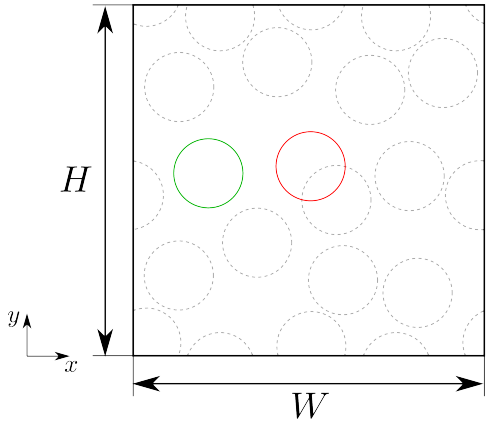

Figure 3.8: Visualization of the generation of an *RSA* RUC geometry; solid black: RUC boundary, dashed: existing fibers, red: rejected fiber due to overlapping, green: accepted fiber

In Fig. 3.9, the deformed mesh of a *RSA* RUC with periodic boundary conditions at tensile loading is shown. The local fluctuations of the current configuration, which are mirrored at the edges (as marked here for the left and right edge) become visible. The periodic boundary conditions can be described via

$$\boldsymbol{x}_r^i - \boldsymbol{x}_l^i = \boldsymbol{F}_M \cdot (\boldsymbol{X}_r^i - \boldsymbol{X}_l^i), \tag{3.70}$$

where superscript i indicates a pair of nodes with the same reference coordinates in all but one direction. Exemplary, a pair of nodes for the left and right edges would have the same y- and z-coordinates but a constant difference in the x-coordinate. The macroscopic or far field deformation is indicated here by $\boldsymbol{F}_M$. It shall be noted that due to these boundary conditions, the displacement difference of each node pair is defined leaving enough freedom for the nodal deformation for local (repeating) fluctuations as indicated in Fig. 3.9. The periodic boundary conditions described here for the x-direction are applied in y- and z-direction as well. It shall be noted that no geometrical inhomogeneities are present in z-direction and all RUCs can be considered flat (i.e. the dimensions in x- and y-direction are much larger than in z-direction). Thus, the periodicity conditions in z-direction generally lead to material behavior comparable to plane strain. Within the software FEAP, the repeating boundary conditions were applied via the solution command *ELINk*, while the far field deformation gradient is applied via the solution command *PERIodic,CAUChy*. For the latter, the macroscopic displacement gradient ($\boldsymbol{H}_M = \boldsymbol{F}_M - \boldsymbol{I}$) is defined directly, while within FEAP displacement boundary conditions were derived from this input.

3.6 Numerical Results

All RUCs were loaded with far field stretches in tensile direction (i.e. Mode I), while periodic boundary conditions were applied. It shall be emphasized that the homogenization procedure is applicable in the

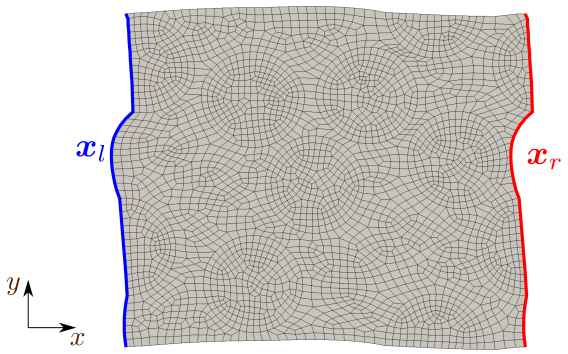

Figure 3.9: Exemplary mesh and deformation of an $24\,\mu\mathrm{m} \times 24\,\mu\mathrm{m} \times 1\,\mu\mathrm{m}$ RUC. Deformations magnified by a factor of 50.

case of three dimensional RUCs as well. Due to the high numerical costs and challenges in mesh generation, the present study is restricted to the two dimensional case using one eight node element over the thickness of the RUC. Unless specifically stated, Tab. 3.1 lists the material parameters used. Parameters were taken from [Poggenpohl et al., 2021], where they had been fitted to experimental data.

Parameter l_1 was changed to fit the new length scales of the RUCs simulated. Here, parameter l_1 is treated as a numerical parameter and part of the micromorphic extension. In principle, this parameter could become physically relevant, if information about the localization zone width at the microscale is provided (e.g. via micro CT- or SEM scans). Generally, to high values for l_1 would lead to an even distribution of damage and thus, no localization band would form. In contrast, if parameter l_1 is chosen to small, the failure zone shrinks and a higher mesh density is needed in order to achieve mesh convergence. Here, parameter l_1 is chosen in a way, that a reasonable localization zone develops.

Here, parameter l is used as a numerical parameter to create a satisfactory failure zone width. If the parameter is chosen to large, all material points will have the same damage variable and no failure zone will develop. If parameter l is chosen to small, the failure zone shrinks and a higher mesh density is needed in order to achieve mesh convergence. In principle, in situ measurements of the localization zone of real specimen at the micro scale, e.g. micro CT or SEM scans, could give physical meaning to the length scale parameter l.

The fibers were modeled using an elastic, isotropic, material model. This simplification was made since the fibers were stiff compared to the matrix material and did not damage which is in accordance to, e.g. [Fantoni et al., 2020], [Guillén-Hernández et al., 2020] or [Liu et al., 2021]. Also, since the investigated effects were driven by and restricted to the behavior of the compliant matrix material the transverse isotropy of the fibers was neglected. To achieve the elastic response, the damage threshold of the fibers was chosen very high. Additionally, the micromorphic parameters of the fibers were chosen in a way that they do not influence the micromorphic field of the matrix.

In the following sections, the theoretical considerations will be underpinned by numerical examples.

Table 3.1: Material parameters for the resin matrix (index 1) and carbon fibers (index 2). If no index is used, the same parameter was applied to both constituents.

	Parameter	Value	Parameter	Value	Parameter	Value
Matrix	λ_1	$5308\,\mathrm{MPa}$	K_1	$6.5\,\mathrm{MPa}$		
	μ_1	$3538\,\mathrm{MPa}$	H_1^χ	$2 \times 10^4 \mathrm{MPa}$		
	$Y_{0,1}$	$0.0672\,\mathrm{MPa}$	l_1	$6.4 \times 10^{-4} \mathrm{mm}$		
Fiber	λ_2	$423\,077\,\mathrm{MPa}$	K_2	$0\,\mathrm{MPa}$		
	μ_2	$84\,615\,\mathrm{MPa}$	H_2^χ	$1\,\mathrm{MPa}$		
	$Y_{0,2}$	$1 \times 10^8\,\mathrm{MPa}$	l_2	$0.0\,\mathrm{mm}$		
Matrix & Fiber	h_{tc}	1	η	$1 \times 10^{-3}\,\mathrm{MPa\,s}$	n	2

This includes:

- In the next section, a mesh convergence study is performed showing the effective treatment of mesh size sensitivity.
- Afterwards, the influence of the artificial viscosity on numerical results is presented.
- Thereafter, results obtained using the standard Hill's approach and the failure zone averaging method are compared.
- Next, a statistical investigation of the effect of generation algorithms on RUC response is given. Here, RUCs generated by the *randomized* and *RSA* approach are compared.
- Further, five different RUC sizes are compared in a statistical analysis of the deviations between different realizations of each RUC size.
- Then, micromorphic power and micromorphic work of the same sets of RUCs are investigated separately as numerical evidence for the derivation in Sec. 3.4.3.
- Finally, a statistical investigation of ten *RSA* RUCs with damaging interfaces is shown. Here, the statistical evolution of the work of bulk and interface is investigated.

3.6.1 Mesh convergence study

For a mesh convergence study, an RUC of size $48\,\mu\mathrm{m} \times 48\,\mu\mathrm{m} \times 1\,\mu\mathrm{m}$ using a regular grid for the fiber distribution was generated. Here, different mesh sizes ranging from $0.25\,\mu\mathrm{m}$ to $2\,\mu\mathrm{m}$ were used. It shall be noted that only the characteristic element length in plane of the RUC was varied, while one element over the thickness was used in all RUC simulations. Stresses and stretches were computed as volume averages of the whole computational domain Ω_0.

Fig. 3.10 shows stress-stretch curves for the RUC at different mesh densities. Mesh sizes of $0.5\,\mu\mathrm{m}$ and $0.25\,\mu\mathrm{m}$ show almost the same stress-stretch curves. As shown, all simulations were terminated at a far field deformation of $F_{xx} = 1.025$.

Additionally, for an objective interpretation of the results, the total work density ($\mathcal{W}_{tot}$) was calculated

$$\mathcal{W}_{tot} := \int \{\boldsymbol{P} : \dot{\boldsymbol{F}}\}_{\Omega_0} \, \mathrm{d}t, \tag{3.71}$$

where for numerical time integration the Midpoint Rule was applied.

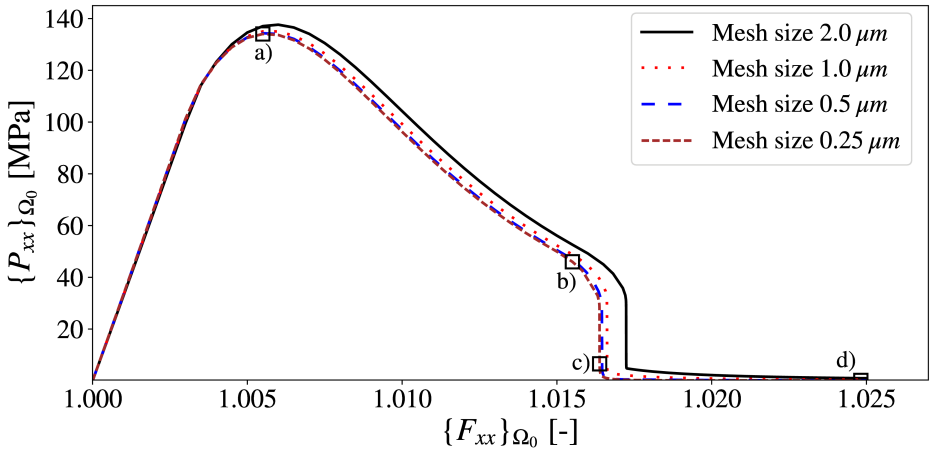

Figure 3.10: Stress-stretch curves for different meshes of the regular RUC of size $48\,\mu\mathrm{m} \times 48\,\mu\mathrm{m} \times 1\,\mu\mathrm{m}$; damage contour plots of the fines mesh at the different stages a) to d) are shown in Figs. 3.11a to 3.11d.

As a result, numerical values for the work density and stress maximum can be found in Tab. 3.2. Here, the finest mesh was assumed to show the converged solution, and the relative errors were computed with respect to these results, such that

$$e_{rel,\mathcal{W}} = \frac{\mathcal{W}_{tot} - \mathcal{W}_{tot}^{0.25\,\mu\mathrm{m}}}{\mathcal{W}_{tot}^{0.25\,\mu\mathrm{m}}} \qquad e_{rel,\sigma} = \frac{\sigma_{max} - \sigma_{max}^{0.25\,\mu\mathrm{m}}}{\sigma_{max}^{0.25\,\mu\mathrm{m}}} \tag{3.72}$$

Table 3.2: Work densities, maximum stresses, and relative errors according to (3.72) for different mesh sizes.

Mesh size [μm]	$\mathcal{W}_{tot}$ [J mm^{-3}]	$e_{rel,\mathcal{W}}$ [%]	σ_{max} [MPa]	$e_{rel,\sigma}$ [%]
2.00	1.516	9.73	137.49	1.82
1.00	1.425	3.16	135.76	0.54
0.50	1.383	0.10	135.14	0.08
0.25	1.381	-	135.02	-

From Fig. 3.10 and Tab. 3.2 a clear convergence trend can be observed, highlighting that mesh dependence was successfully cured by the micromorphic extension of the damage formulation. Further, the numerical values in Tab. 3.2 suggest that a mesh size of $0.5\,\mu\mathrm{m}$ gave almost the same numerical value as the finest mesh in terms of work density and maximum stress. Therefore, a mesh size of $0.5\,\mu\mathrm{m}$ was used in the subsequent simulations.

In Figs. 3.11a to 3.11d damage contour plots also showing the deformed mesh are given. The different stages of deformation are indicated in Fig. 3.10. From Figs. 3.11a and 3.11b it becomes apparent that until load drop, damage was distributed homogeneously within the matrix. Fig. 3.11c shows the damage contour after load drop, where the localization zone has formed while Fig. 3.11d shows the deformed mesh at the end of simulation. From comparison of Figs. 3.11c and 3.11d it can be deduced that the damage contour does not change, but almost all deformation is accumulated in the heavily deformed localization zone. This result is underpinned by Figs. 3.11e and 3.11f where the actively damaging zone is plotted. While for $\{F_{xx}\}_{\Omega_0} = 1.0164$ a broad band is damaging, Ω_d is reduced to almost one layer of elements for $\{F_{xx}\}_{\Omega_0} = 1.025$.

In Fig. 3.12, the failure zone (i.e. the volume where $D \geq 0.8$ holds) including mesh deformation is shown. While from Fig. 3.11d a diffusive damage distribution might be deduced, the narrow failure (or localization) zone is seen in Fig. 3.12. As mentioned above, the width of the failure zone is controlled via parameter l_1. Lower values of l_1 would result in less diffusion damage and a smaller failure zone.

The reduction of the actively damaging region to one layer of elements (Fig. 3.11f) might contradict the findings in Fig. 3.10 and Tab. 3.2. The reason for this inconsistency is found in the damage function of quadratic type as well as the fact, that almost no damage evolution takes place between $\{F_{xx}\}_{\Omega_0} = 1.0164$ and $\{F_{xx}\}_{\Omega_0} = 1.025$. Due to the quadratic failure function, a material point at $D = 0.995$ ($(1 - 0.995)^2 = 2.5 \times 10^{-5}$) has a much lower stiffness than a material point at $D = 0.98$ ($(1 - 0.98)^2 = 4 \times 10^{-4}$). A further increase in damage decreases the overall stress significantly. At the same time, the gradient between $D = 0.995$ and $D = 0.98$ is quite low leading to a decreased effect of the micromorphic extension. Thus, a damage zone as shown in Fig. 3.11f might develop way after full failure occurred. However, the mesh convergence shown in Fig. 3.10 and the actively damaging region right at the end of final failure (Fig. 3.11e) show that the solution is no longer mesh size dependent.

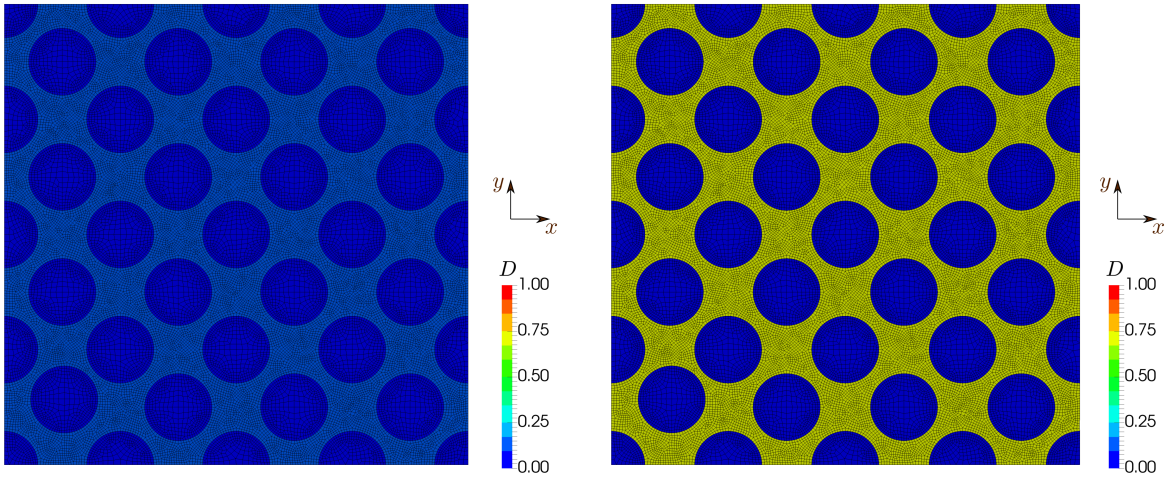

(a) $\{F_{xx}\}_{\Omega_0} = 1.0055$ (b) $\{F_{xx}\}_{\Omega_0} = 1.0155$

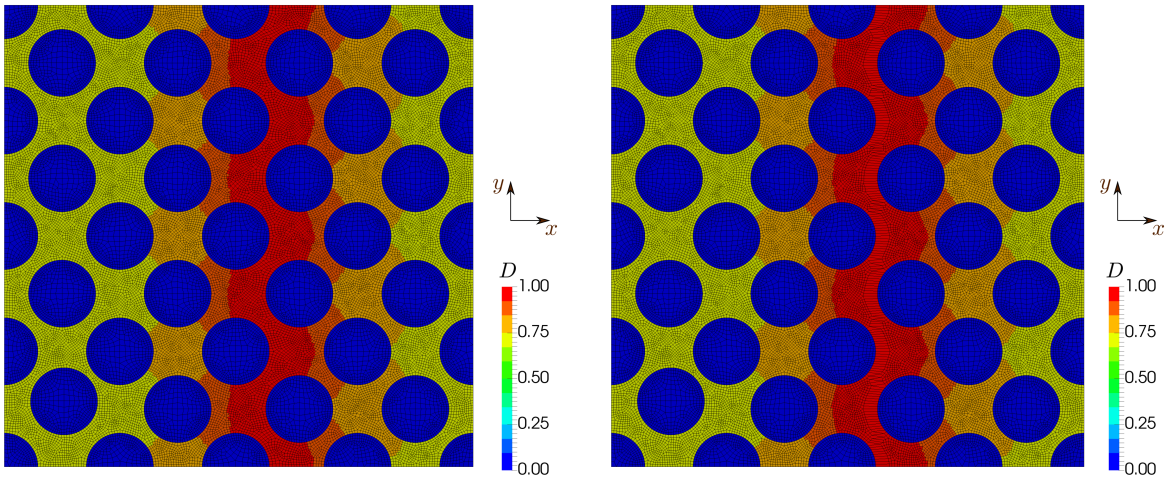

(c) $\{F_{xx}\}_{\Omega_0} = 1.0164$ (d) $\{F_{xx}\}_{\Omega_0} = 1.025$

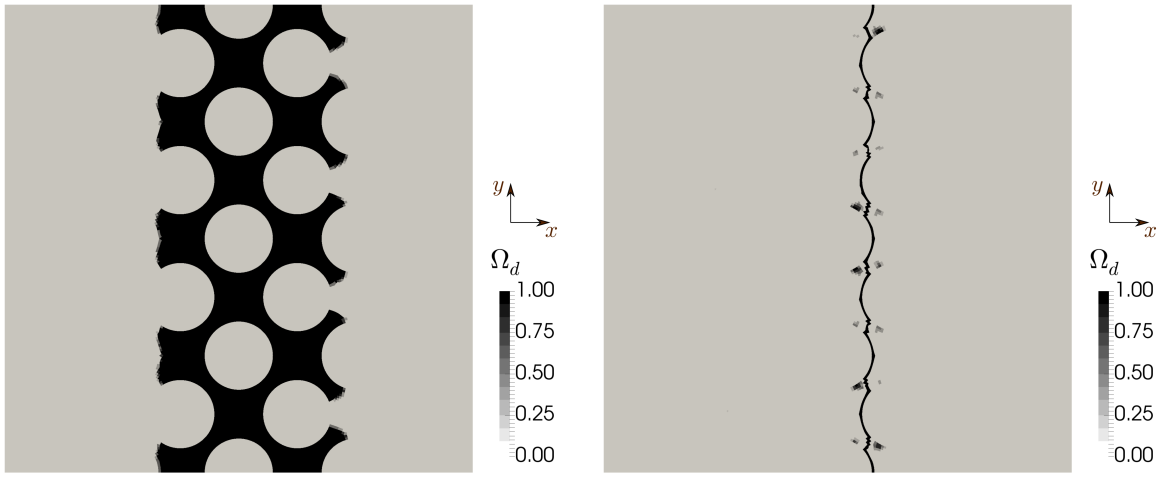

(e) $\{F_{xx}\}_{\Omega_0} = 1.0164$ (f) $\{F_{xx}\}_{\Omega_0} = 1.025$

Figure 3.11: Damage contour plots with mesh deformation factor 1 (Figs. a to d) and actively damaging zone Ω_d (Figs. e and f) for mesh size $0.25\,\mu\mathrm{m}$ at different stages of deformation as indicated in Fig. 3.10.

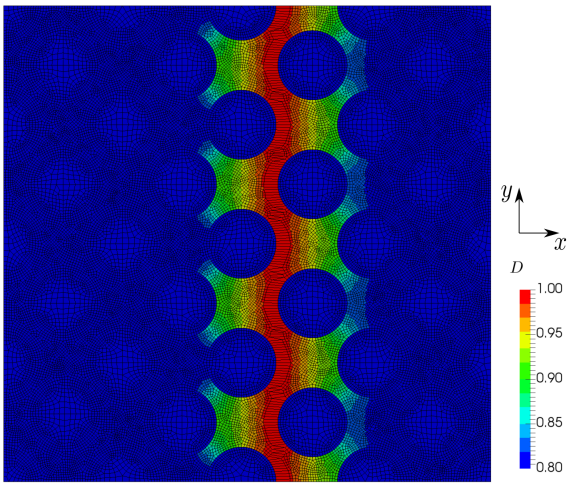

Figure 3.12: Damage contour plot of the failure zone (i.e. volume of high damage) with mesh deformation factor 1 for mesh size $0.25\,\mu\mathrm{m}$ at the end of deformation ($\{F_{xx}\}_{\Omega_0} = 1.025$) as indicated in Fig. 3.10.

3.6.2 Influence of the artificial viscosity

In order to investigate the influence of artificial viscosity, the same RUC as for the mesh convergence study (Sec. 3.6.1) was used. Here, seven different simulations with viscosities ranging from $1 \times 10^{-3}\,\mathrm{MPa\,s}$ to $1 \times 10^{-1}\,\mathrm{MPa\,s}$ were calculated. Simulations with lower viscosities were carried out as well, but failed due to numerical instabilities. Again, stresses and stretches were computed as volume averages of the whole computational domain Ω_0 and simulations were terminated at a far field deformation of $F_{xx} = 1.025$. In Figs. 3.13a and 3.13b, the stress-stretch curves and the evolution of the volume $|\Omega_d|$ of the actively damaging domain Ω_d normalized w.r.t. the overall volume $|\Omega_0|$ are shown, respectively.

As desired, the stresses-stretch curves only show a minor dependence on the artificial viscosity, such that the curves for $\eta = 1 \times 10^{-2}\,\mathrm{MPa\,s}$ and $\eta = 1 \times 10^{-3}\,\mathrm{MPa\,s}$ are almost identical. However, the curves of the actively damaging volume as presented in Fig. 3.13b show a quite significant dependence on the pseudo viscosity. From these results it was concluded that a viscosity of $\eta = 1 \times 10^{-3}\,\mathrm{MPa\,s}$ leads to the best compromise between numerical stability and accuracy of the solution.

3.6.3 RUC size comparison

A size convergence study was performed using five RUCs with regular pattern and varying sizes as shown in Fig. 3.6. Stresses and stretches were calculated using the volume average of *(i)* the complete computational domain Ω_0 following the standard homogenization approach and *(ii)* the actively damaging domain Ω_d according to failure zone homogenization scheme proposed here.

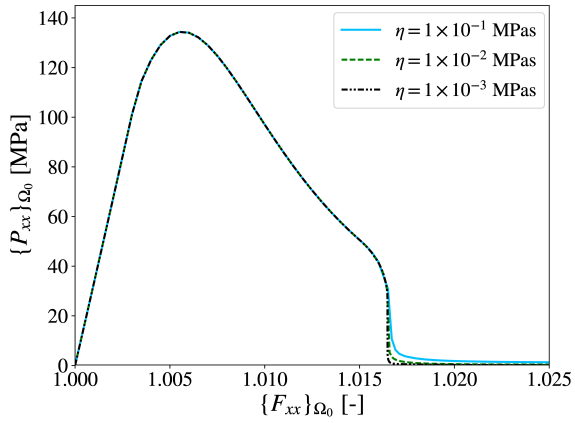

(a) Stress-stretch curves for different viscosities.

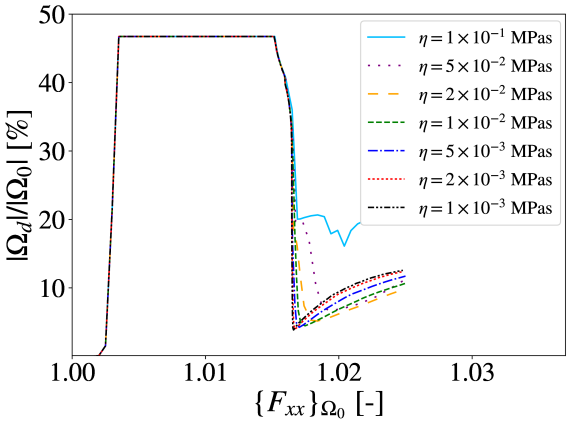

(b) Normalized volume of the actively damaging domain Ω_d for different viscosities.

Figure 3.13: Numerical results for different values of the pseudo viscosity for a regular RUC of size $48\,\mu\text{m} \times 48\,\mu\text{m} \times 1\,\mu\text{m}$.

Stress-stretch curves based on standard homogenization are visualized in Fig. 3.14. The curves are almost identical in the elastic region. At the onset of strain softening (peak of the curve), the stress-stretch curve of the smallest RUC differs from the others. This effect results from the bigger influence of the imperfection on the smallest RUC. Thereafter, the curves differ in the onset of final failure, which is related to the formation of a localization band. Moreover, increasing the RUC size results in lower deformations at which the final load drop occurs.

In Fig. 3.15, the corresponding stress-stretch curves of the failure zone homogenization scheme are show. As can be seen, the curves are independent of the RUC size. The small differences in the final (residual) stresses can be related to artificial viscosity. Due to the loading rate of the RUC being the same for all RUC sizes, the strain rate of the localization zone (and therefore the viscous residual stresses) slightly increase for increasing RUC size.

Numerical evidence for Eq. (3.67) is shown in Fig. 3.16. Here, the left and right hand side are given as individual curves. The curves are plotted from the onset of localization until end of simulation. Overall, the curves show a good correlation thus indicating that Eq. (3.67) holds. The small peak at $\{\boldsymbol{F}_{xx}\}_{\Omega_0} = 1.028$ can be associated to viscous effects when the deformation localizes in on layer of elements as shown by Figs. 3.11c and 3.11d.

3.6.4 Comparison of *randomized* and *RSA* RUCs

Two sets of 10 realizations each were created for the $48\,\mu\text{m} \times 48\,\mu\text{m} \times 1\,\mu\text{m}$ RUCs with the randomization approach and the *RSA* method, respectively. The corresponding stress-stretch curves homogenized over the whole domain Ω_0 are plotted in Figs. 3.17 and 3.18, respectively, together with the result of the regular RUC of the same size (green marks in Fig. 3.14). In what follows, the results are summarized

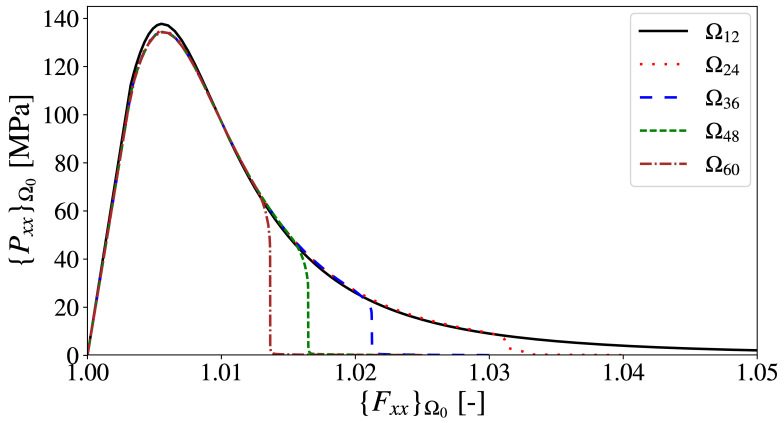

Figure 3.14: Stress-stretch curves for different RUC sizes for standard homogenization. The RUC sizes range from $12\,\mu m \times 12\,\mu m \times 1\,\mu m$ (Ω_{12}) to $60\,\mu m \times 60\,\mu m \times 1\,\mu m$ (Ω_{60}).

by a mean curve and an encasing scatter showing the maximum and minimum of the ten realizations.

All ten realizations generated using the randomization approach (see Fig. 3.17) show the same global stress-stretch curves until failure. Here, the onset of failure differs due to differences in the microstructure. Generally, the curves for the regular RUC and the 10 *randomized* RUCs are close.

On the contrary, the stress-stretch curves of the *RSA* RUCs (see Fig. 3.17) differ in both, the peak load as well as the point of final failure. In addition, compared to *randomized* RUCs, all *RSA* RUCs show a higher peak load, higher elastic stiffness, lower stretches at failure, and the stress-stretch curves show a greater scatter. Interestingly, even though the maximum stress is different, the deformation at which the maximum stress is reached is quite the same for all realizations of both generation algorithms.

Moreover, the failure zone homogenization scheme was applied to the same sets of realizations, such that the averaging was restricted to the actively damaging domain Ω_d. The corresponding stress-stretch relations are visualized in Figs. 3.19 and 3.20.

As illustrated in Fig. 3.19, the stress-stretch curves of the *randomized* RUC realizations do not show any differences until a deformation of 1.04 is reached. Thereafter, the curves diverge by a small amount until asymptotically converging towards zero stress. The stress-stretch curve of the regular pattern lies within the scatter (maximum and minimum) of the different curves of the ten realizations.

In contrast, the stress-stretch curves of the *RSA* RUCs show a noticeable scatter in the whole deformation range with a maximum scatter at about a stretch of 1.04. Overall, the peak stress is lower in comparison to the peak stress of the regular pattern. Additionally, the stress-stretch curves of the *RSA* RUCs approach zero stress at lower deformations than the curves of the regular or *randomized* RUCs.

All in all, the curves of the *RSA* RUCs show a higher deviation than the *randomized* RUCs. Failure appears earlier in terms of global stress-stretch curves and showed a much faster asymptotic approach towards zero stress when failure zone averaging is applied. While the peak of *RSA* curves is higher for

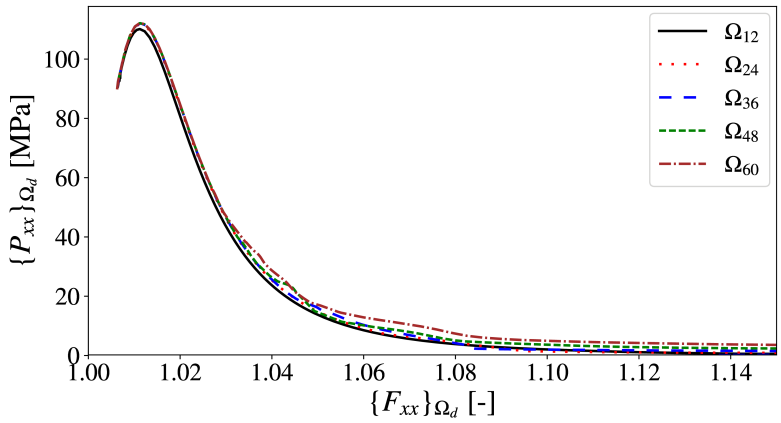

Figure 3.15: Stress-stretch curves for different RUC sizes for failure zone homogenization. The RUC sizes range from $12\,\mu\text{m} \times 12\,\mu\text{m} \times 1\,\mu\text{m}$ (Ω_{12}) to $60\,\mu\text{m} \times 60\,\mu\text{m} \times 1\,\mu\text{m}$ (Ω_{60}).

standard averaging, it is lower when failure zone averaging is applied.

The effect of fiber clustering, present in the *RSA* approach, might explain the differences in the maximum peak load and elastic response of the *RSA* RUCs. In [Kulosa et al., 2017], it was shown that in RUCs of sintered ceramics so-called load transfer paths develop. These load transfer paths are regions of high stresses which transfer most of the load through the RUC.

In Figs. 3.21a and 3.21b, the first Piola-Kirchhoff stress contour plots of a *randomized* and a *RSA* RUC at the same far field deformation are shown. It shall be noted that the maximum stress of the *RSA* RUC was at approximately $50\,\text{MPa}$. For convenience and comparability, the color scale was lowered and chosen the same for both plots. Apparantly, the stress distribution of the *RSA* RUC was much more heterogeneous and in line with the load transfer paths shown in [Kulosa et al., 2017]. These load paths mainly pass through fibers and close gaps between adjacent fibers. Overall, the fibers are loaded with higher stresses compared to the *Randomized* RUC in Fig. 3.21a. These higher stresses in regions of higher stiffness are assumed to cause the difference in the elastic response.

The same effect is assumed to have caused the lower peak stress when failure zone averaging was applied. At the peak load, the actively damaging region was the matrix region. From Fig. 3.21b it can be seen that the matrix region shows small areas of high stresses and some larger areas of low or even zero stress. In an averaged sense, the regions of low stress outweighed the regions of high stresses, thus – in average – causing the lower peak stresses.

The results show that the fiber distribution has an impact on the elastic and inelastic response of the RUC. Therefore, the fiber distribution of the RUC should correspond to the fiber distribution found in CFRPs. Since the *RSA* method provides fiber distributions which are closer to the fiber distribution in real CFRPs (see e.g. Fig. 13 in [París et al., 2018]), this method will be used for RUC generation in the following.

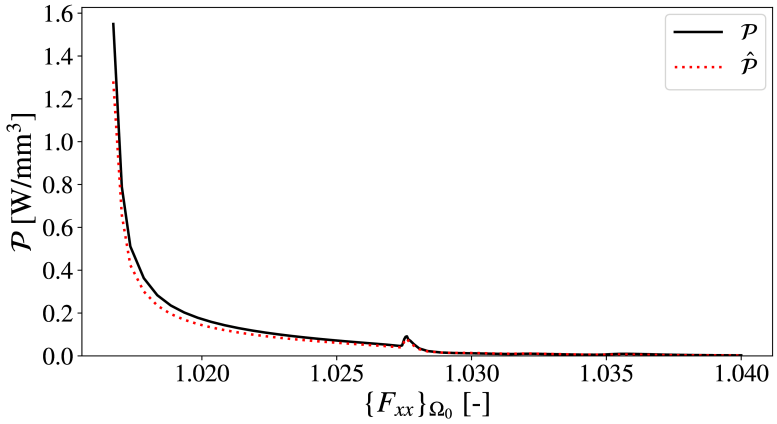

Figure 3.16: Comparison of left and right hand side of Eq. (3.67) for the $48\,\mu\text{m} \times 48\,\mu\text{m} \times 1\,\mu\text{m}$ RUC after onset of localization; average of the products ($\mathcal{P} = \frac{1}{\Omega_0}\int_{\Omega_d} \boldsymbol{P}_m^T : \delta\boldsymbol{F}_m \; \mathrm{d}V$, black) and product of the averages ($\hat{\mathcal{P}} = \frac{1}{\Omega_0}\int_{\Omega_d} \boldsymbol{P}_m^T \, \mathrm{d}V : \{\delta\boldsymbol{F}_m\}_{\Omega_d}$, red).

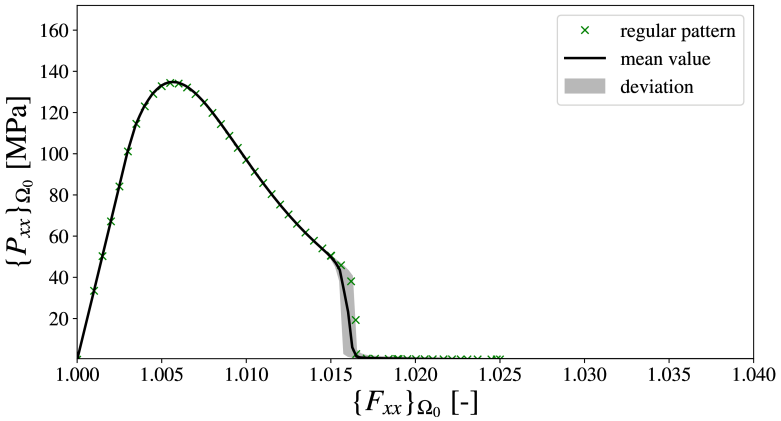

Figure 3.17: Stress-stretch curves resulting from standard homogenization for *randomized* and regular RUCs of size $48\,\mu\text{m} \times 48\,\mu\text{m} \times 1\,\mu\text{m}$; black: Mean value of 10 realizations, grey: Scatter (maximum and minimum) of 10 realizations, green: Response of the regular RUC.

3.6.5 Statistical investigation of representative RUC size

A statistical investigation of the RUC size ranging from an edge length of $12\,\mu\text{m}$ to $60\,\mu\text{m}$ was performed (cf. Fig. 3.6). For each RUC size, ten realizations were generated using the *RSA* method. First, stresses and stretches were calculated using the standard averaging over the entire domain Ω_0. The resulting homogenized stress-stretch curves are summarized in Figs. 3.22 to 3.25. Further, the results for RUCs with an edge length of $48\,\mu\text{m}$ have been displayed already in Fig. 3.18.

In Figs. 3.22 to 3.25 one can observe that the stress-stretch curves show less differences in the elastic

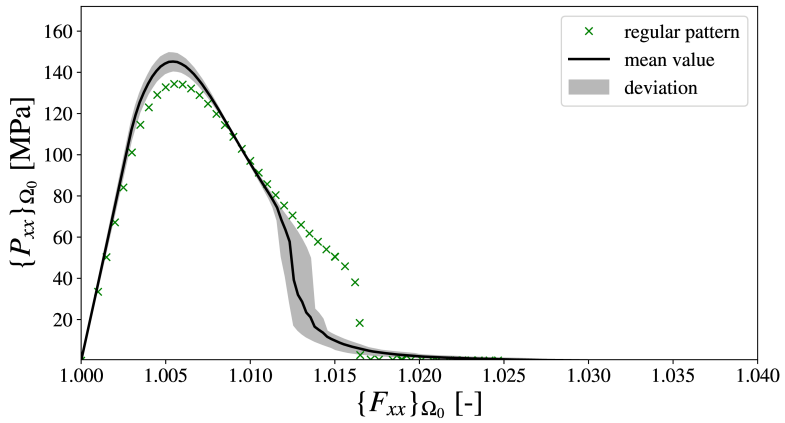

Figure 3.18: Stress-stretch curves for *RSA* and regular RUCs of size $48\,\mu\mathrm{m} \times 48\,\mu\mathrm{m} \times 1\,\mu\mathrm{m}$; black: Mean value of 10 realizations, grey: Scatter of 10 realizations, green: stress-stretch response of the regular RUC.

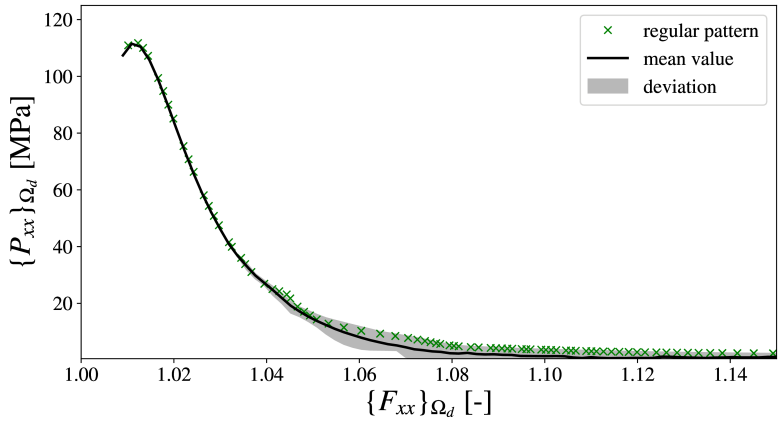

Figure 3.19: Stress-stretch curves for failure zone averaging of *randomized* RUCs; black: Mean value of 10 realizations, grey: Scatter of 10 realizations, green: stress-stretch response of the regular RUC.

regime and the peak stresses, the bigger the RUC size gets. Also, larger RUCs show an earlier load drop, which agrees with the findings from Sec. 3.6.3. Moreover,when comparing the results of *RSA* RUCs to those with regular patterns, the peak stresses of the *RSA* RUCs are larger and the load drops take place at lower stretches.

Additionally, in order to get more insight into the question of representativeness, the mechanical work density of the entire domain Ω_0 was computed according to eq. 3.71. The result is plotted in Fig. 3.26 together with the corresponding deviation. In addition to the results generated from the *RSA* RUCs, the results from the *regular* RUCs (including new RUC sizes of $72\,\mu\mathrm{m}$ and $84\,\mu\mathrm{m}$) are shown here as well. It can be concluded, that the variation decreases with larger RUC size, but the mean values

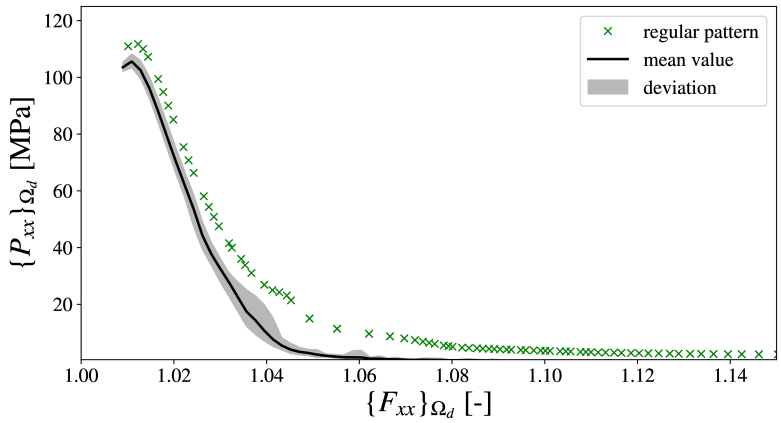

Figure 3.20: stress-stretch curves for failure zone averaging of *RSA* RUCs; black: mean value of 10 realizations, grey: upper and lower bound, green: stress-stretch response of the regular RUC.

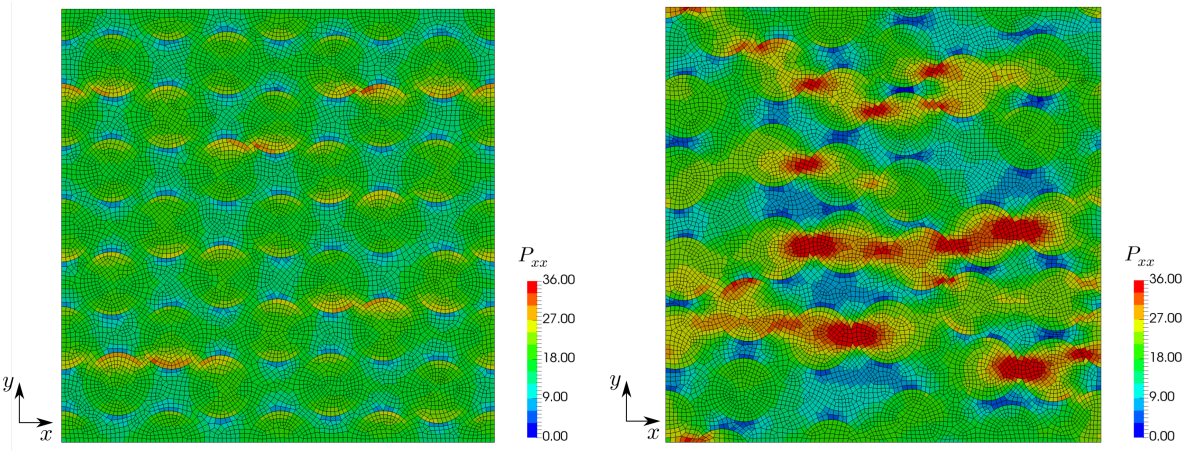

(a) *Randomized* RUC.

(b) *RSA* RUC.

Figure 3.21: First Piola-stress contour plots (in MPa) of a *randomized* and *RSA* RUC of size $48\,\mu\mathrm{m} \times 48\,\mu\mathrm{m} \times 1\,\mu\mathrm{m}$ at an elastic far field deformation of $\boldsymbol{F}_{xx} = 1.0005$.

do not show any convergence with respect to the RUC size. Hence, no representative RUC size can be identified using the standard homogenization approach.

Furthermore, the same RUCs also were investigated using the failure zone homogenization scheme with averaging over the actively damaging domain Ω_d, leading to the stress-stretch curves shown in Figs. 3.27 to 3.30.

Figures 3.27 to 3.30 confirm the same trends already explained in the previous Sec. 3.6.4. When failure zone homogenization is used, the maximum stresses of the *RSA* RUCs generally are lower compared to the maximum stresses of the regular RUCs. However, in Fig. 3.27 the upper bound of the $12\,\mu\mathrm{m}$ *RSA* RUCs does exceed the peak stress of the regular RUC of the same size. Nevertheless, even

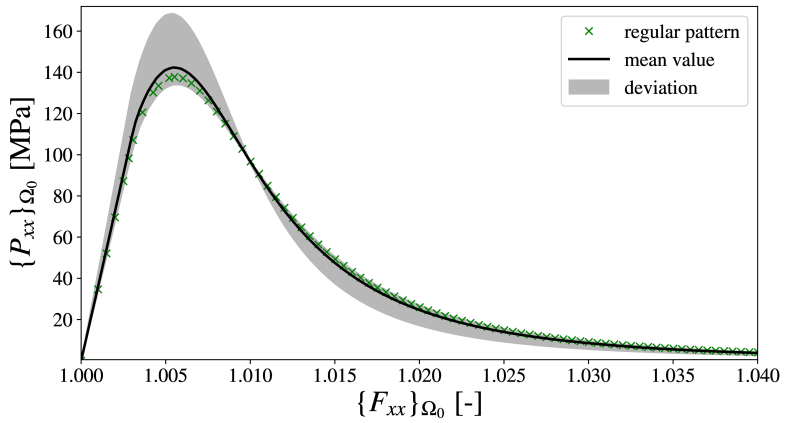

Figure 3.22: Stress-stretch curves resulting from standard homogenization for *RSA* and regular RUCs of size $12\,\mu\mathrm{m} \times 12\,\mu\mathrm{m} \times 1\,\mu\mathrm{m}$; black: Mean value of 10 realizations, grey: Scatter of 10 realizations, green: Response of the regular RUC.

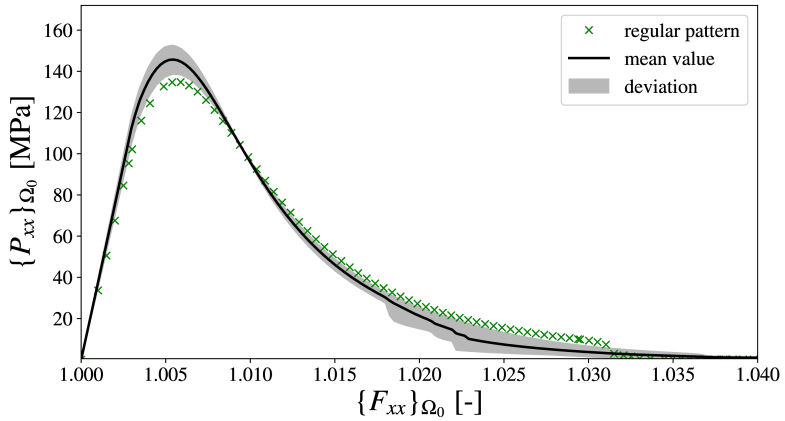

Figure 3.23: Stress-stretch curves resulting from standard homogenization for *RSA* and regular RUCs of size $24\,\mu\mathrm{m} \times 24\,\mu\mathrm{m} \times 1\,\mu\mathrm{m}$; black: Mean value of 10 realizations, grey: Scatter of 10 realizations, green: Response of the regular RUC.

for this RUC size, the mean of the maximum stresses is lower. Noteworthy, the difference between the *regular* and *RSA* RUCs increases with increasing RUC size. Therefore, it is concluded that geometric features do play an important role in strain hardening as well as strain softening.

Concluding, also the mechanical work density of the failure zone Ω_d was investigated. The result is plotted in Fig. 3.31 together with the corresponding deviation. In addition to the results generated from the *RSA* RUCs, the results from the *regular* RUCs (including new RUC sizes of $72\,\mu\mathrm{m}$ and $84\,\mu\mathrm{m}$) are shown here as well. Similarly to the standard homogenization case (see Fig. 3.26), the overall higher variation decreases with increasing RUC size. But in contrast to the averaged global mechanical work density for the entire domain, the mean value decreases way less when the failure zone homogenization

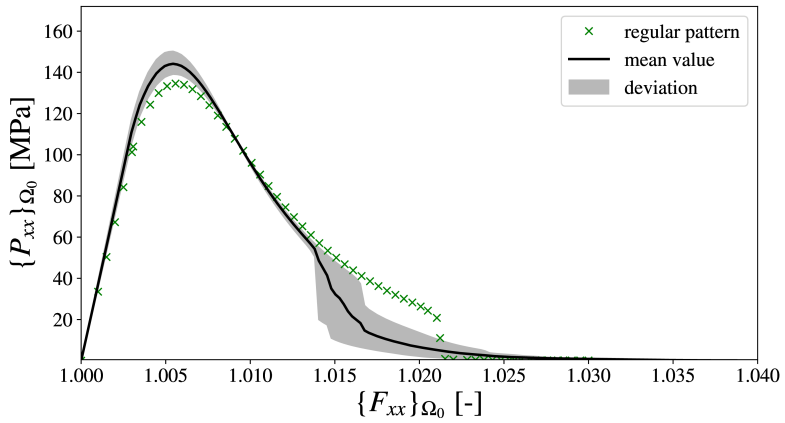

Figure 3.24: Stress-stretch curves resulting from standard homogenization for *RSA* and regular RUCs of size $36\,\mu\mathrm{m} \times 36\,\mu\mathrm{m} \times 1\,\mu\mathrm{m}$; black: Mean value of 10 realizations, grey: Scatter of 10 realizations, green: Response of the regular RUC.

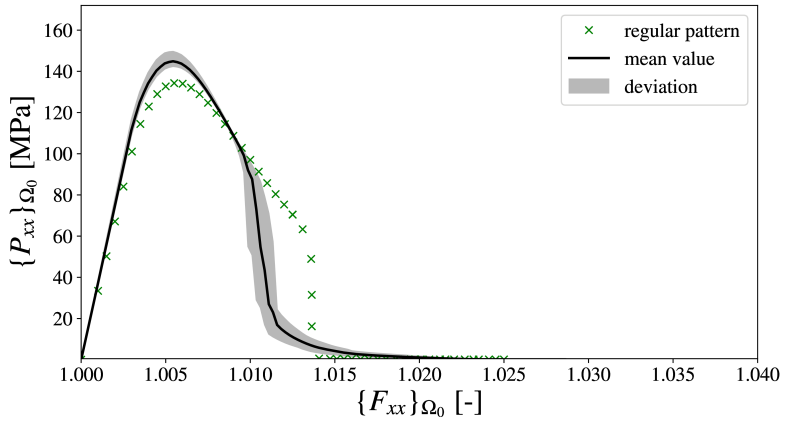

Figure 3.25: Stress-stretch curves resulting from standard homogenization for *RSA* and regular RUCs of size $60\,\mu\mathrm{m} \times 60\,\mu\mathrm{m} \times 1\,\mu\mathrm{m}$; black: Mean value of 10 realizations, grey: Scatter of 10 realizations, green: Response of the regular RUC.

scheme is applied. Interestingly, the results of the regular RUCs and the *RSA* RUCs coincide better. However, when regarding the *regular* RUC size of $84\,\mu\mathrm{m}$, an increase in dissipation is observed. This is due to higher strain rates within the failure zone when the RUC size is increased. This leads to considerable viscous stresses from the pseudo viscosity and in turn higher dissipated energy. However, applying the proposed failure zone homogenization approach results in a much lower slope of the dissipated work density. As such, an RUC size of $72\,\mu\mathrm{m}$ is considered converged.

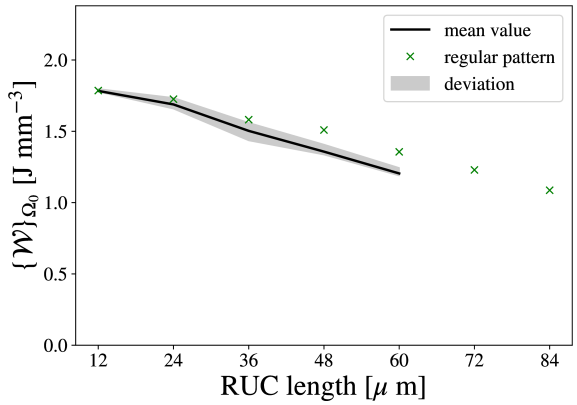

Figure 3.26: Summary of the total mechanical work density of the simulated *RSA* RUCs

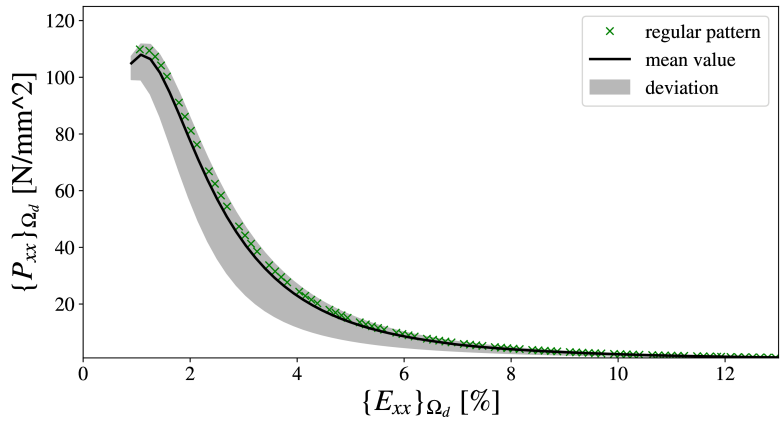

Figure 3.27: Stress-stretch curves resulting from failure zone homogenization for *RSA* and regular RUCs of size $12\,\mu\mathrm{m} \times 12\,\mu\mathrm{m} \times 1\,\mu\mathrm{m}$; black: Mean value of 10 realizations, grey: Scatter of 10 realizations, green: Response of the regular RUC.

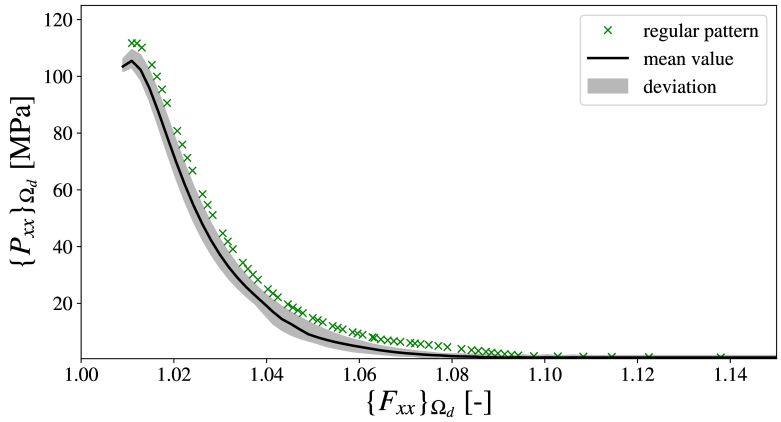

Figure 3.28: Stress-stretch curves resulting from failure zone homogenization for *RSA* and regular RUCs of size $24\,\mu\mathrm{m} \times 24\,\mu\mathrm{m} \times 1\,\mu\mathrm{m}$; black: Mean value of 10 realizations, grey: Scatter of 10 realizations, green: Response of the regular RUC.

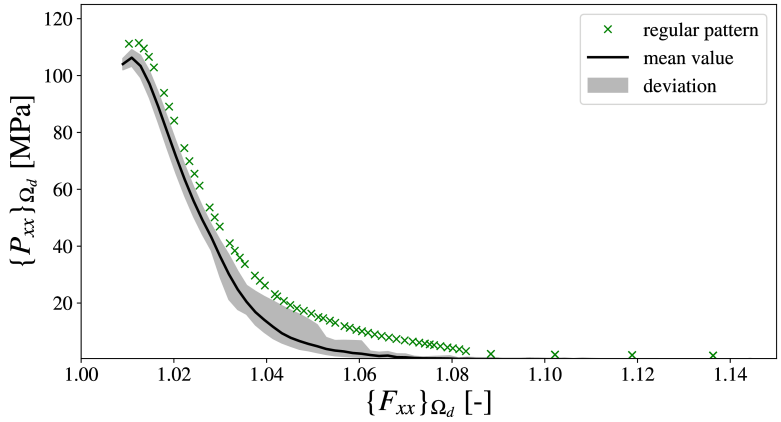

Figure 3.29: Stress-stretch curves resulting from failure zone homogenization for *RSA* and regular RUCs of size $36\,\mu\mathrm{m} \times 36\,\mu\mathrm{m} \times 1\,\mu\mathrm{m}$; black: Mean value of 10 realizations, grey: Scatter of 10 realizations, green: Response of the regular RUC.

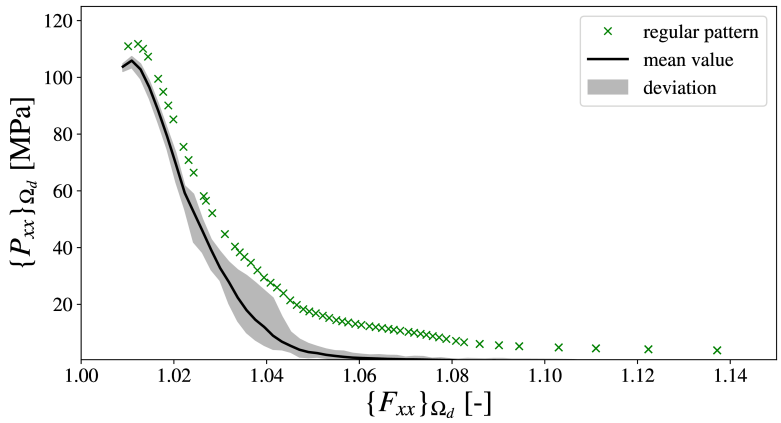

Figure 3.30: Stress-stretch curves resulting from failure zone homogenization for *RSA* and regular RUCs of size $60\,\mu\mathrm{m} \times 60\,\mu\mathrm{m} \times 1\,\mu\mathrm{m}$; black: Mean value of 10 realizations, grey: Scatter of 10 realizations, green: Response of the regular RUC.

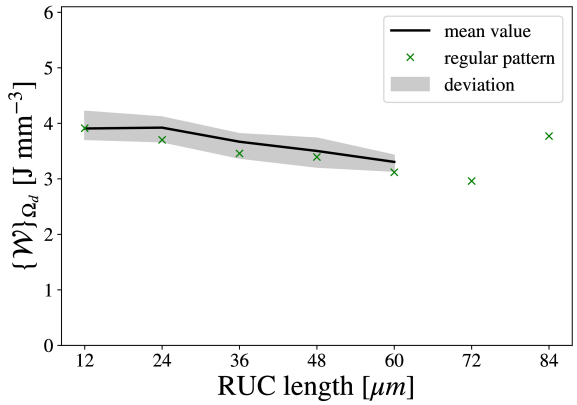

Figure 3.31: Summary of the mechanical work density of the failure zone of simulated *RSA* RUCs

3.6.6 Numerical investigation of micromorphic power

In Secs. 3.4.1 and 3.4.3, it was shown analytically that the micromorphic virtual work has to vanish when integrated over the entire volume, but not necessarily when failure zone averaging is applied. In order to investigate the effect of this micromorphic virtual work in the failure zone, a parameter study of the micromorphic parameters l_1 and H^χ was performed in [Poggenpohl and Simon, 2021]. There, an RUC of size $60\,\mu\text{m} \times 60\,\mu\text{m} \times 1\,\mu\text{m}$ with regular pattern was evaluated w.r.t. the influence of these parameters on the micromorphic power integrated over the whole computational domain and the actively damaging zone, respectively. Exemplarily, one result from this investigation with a specific set of micromorphic parameters ($l_1 = 3.2 \times 10^{-4}\,\mu\text{m}$ and $H^\chi = 4.0 \times 10^2\,\text{MPa}$) is shown in Fig. 3.32. Here, the term power density refers to the time derivative of the mechanical or micromorphic work density, i.e.

$$\mathcal{P}_{mech} = \boldsymbol{P} : \dot{\boldsymbol{F}} \tag{3.73}$$

$$\mathcal{P}_{mic} = \boldsymbol{b} \cdot \nabla \dot{D} + a\dot{D}. \tag{3.74}$$

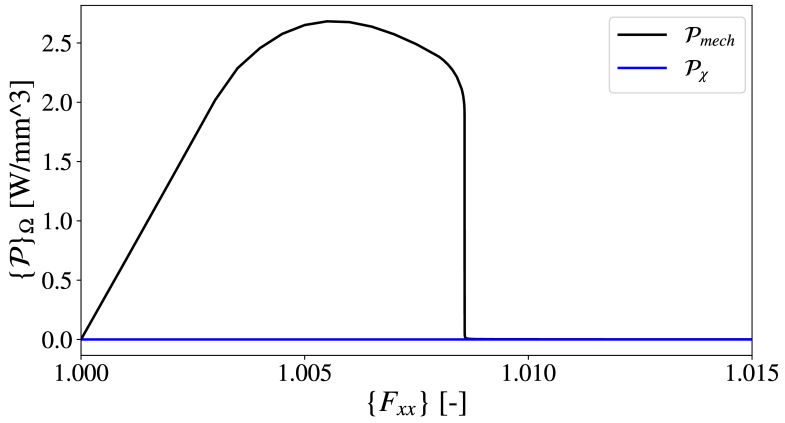

Figure 3.32: Mechanical and micromorphic power averaged over the whole computational domain; data from [Poggenpohl and Simon, 2021].

As can be observed in Fig. 3.32, the micromorphic power density integrated over the whole computational domain Ω_0 is negligible compared to the mechanical power density, which numerically substantiates the analytical result of Eq. 3.49.

In contrast, the micromorphic power density does have significant values during the formation of the localized failure zone, i.e. during the load drops, when only the actively damaging domain Ω_d is considered (see Fig. 3.33). Thus, this result confirms the findings in Sec. 3.4.3 noting that the micromorphic power (and therefore power density) of the failure zone does not necessarily vanish, even though it is zero before and shortly after the load drop (cf. zoom in of Fig. 3.33. It shall be

noted that for better comparison, the micromorphic power density of the actively damaging domain was scaled to the whole computational domain, i.e.

$$\mathcal{P}_{\chi,d} = \frac{\Omega_d}{\Omega_0} \{\mathcal{P}_\chi\}_{\Omega_d} . \tag{3.75}$$

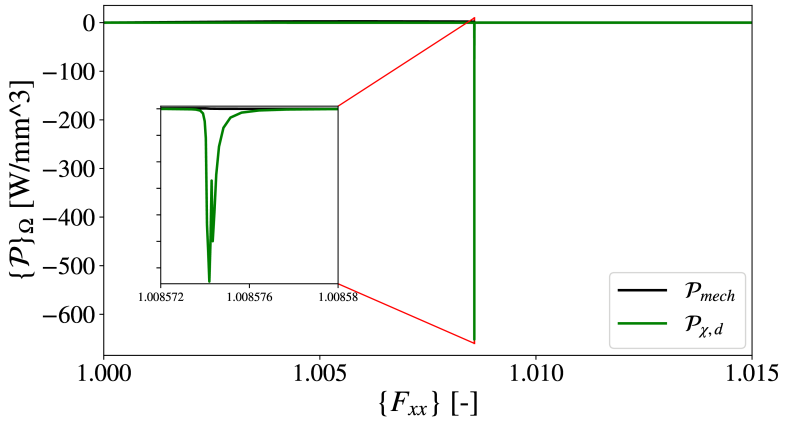

Figure 3.33: Mechanical $\mathcal{P}_{mech}$ and micromorphic power $\mathcal{P}_{\chi,d}$ of the actively damaging region Ω_d, both averaged over the whole computational domain Ω_0; data taken from [Poggenpohl and Simon, 2021].

Finally, the mean mechanical work density $\mathcal{W}_{mech}$ and the mean micromorphic work density $\mathcal{W}_{\chi,d}$ of the actively damaging domain were compared for the *RSA* RUCs from Sect. 3.6.5 with different sizes and 10 realizations each. Both quantities were calculated as time integrals of the coresponding power densities $\mathcal{P}_{mech}$ and $\mathcal{P}_{\chi,d}$, respectively. The results are presented in Tab. 3.3.

Table 3.3: Comparison of the work densities of *RSA* RUCs with different RUC sizes; mean values from 10 realizations each.

	12 µm	24 µm	36 µm	48 µm	60 µm
$\mathcal{W}_{mech}$ [J mm^{-3}]	1.7774	1.6816	1.4977	1.3471	1.1859
$\mathcal{W}_{\chi,d}$ [J mm^{-3}]	-0.0175	-0.0163	-0.0141	-0.0118	-0.0099
$\mathcal{W}_{\chi,d}/\mathcal{W}_{mech}$ [%]	-0.9865	-0.9709	-0.9416	-0.8769	-0.8323

As can be seen from Tab. 3.3, the overall work generated by the micromorphic terms of the actively damaging domain is negative. It is much lower (in terms of absolute values) than the overall work generated by the mechanical terms as well. Findings in [Poggenpohl and Simon, 2021] showed that the micromorphic power only took significant values for a short period of time and were close to zero otherwise (cf. Fig. 3.33). Thus, low values for the overall generated work in combination with much higher peaks are plausible. Overall, the quotient of $\mathcal{W}_{\chi,d}$ and $\mathcal{W}_{mech}$ is lower than 1% in the means of absolute values. For the parameter set chosen, the overall micromorphic power appears to be of

minor importance. However, it is shown that the micromorphic power can take significant values and therefore should not be neglected without being proven negligible.

3.6.7 Results of *RSA* RUCs with damaging interfaces

Ten realizations of size $24\,\mu\mathrm{m} \times 24\,\mu\mathrm{m} \times 1\,\mu\mathrm{m}$ were simulated accounting for both, damaged and debonding induced softening. This reduced RUC size was chosen despite the question of representative size (c.f. Sec. 3.6.5). Reason for this are the numerically expensive simulations when bulk damage and debonding are simulated.[1] To model the debonding of interfaces between fiber and matrix, the cohesive zone elements introduced in Sec. 3.3.2 were used. The material properties of the matrix and fibers of Tab. 3.1 were retained, and the thickness of the interface was chosen to be of 1/1000 of the fiber diameter (i.e. $7 \times 10^{-3}\,\mu\mathrm{m}$).

Parameter	Value	Parameter	Value	Parameter	Value
t_0	$50\,\mathrm{MPa}$	λ_0	$2 \times 10^{-2}\,\mu\mathrm{m}$	λ_f	$2 \times 10^{-1}\,\mu\mathrm{m}$
η_{CZ}	$0.5\,\mathrm{MPa\,s\,m^{-1}}$	β	1	H_{pen}	$5000\,\mathrm{MPa\,mm^{-1}}$

Table 3.4: Material parameters of the interface.

The material properties of the interfaces are summarized in Tab. 3.4, where t_0 denotes the maximum traction of the interface. This value was taken from experimental investigations of carbon fibers–epoxy matrix interfaces presented in [Zhang et al., 2018]. The cohesive zone gap opening at maximum traction (λ_0) and at full failure (λ_f) were chosen to give reasonable results. Further, β was chosen to be one such that the shear and the normal gap opening contributed to the effective gap opening by the same factor. As for the bulk material model, a pseudo viscosity (η_{CZ}) was used. This parameter was chosen as small as possible while achieving numerical stability. Self penetration was avoided with help of the penalty parameter H_{pen}, for which half the stiffness of the weakest bulk constituent was used as suggested e.g. in [Rezaei et al., 2017]).

In Fig. 3.34, the stresses for ten realizations using standard homogenization are summarized. As shown in Sec. 3.4.1, the homogenization of the deformation gradient at the presence of damaging interfaces is not straight forward. Therefore, the externally applied (macroscopic) deformation gradient is used here. It can be observed, that the peak stress of RUCs with damaging interfaces is much lower compared to the results shown in Fig. 3.23 without debonding. Additionally, the deviation of the different realizations is higher at the beginning of softening. Starting at $F_{xx,ext} = 1.03$, the deviation is reduced and comparable to the deviation of RUCs with perfect interfaces. At about $F_{xx,ext} = 1.08$, the stresses are zero, indicating complete failure. The far field deformation at the peak load varies as well.

[1] The simulations took about 15 to 20 days on Intel Xeon E5-2670 and E5-2667 v2 pocessors using 2 cpus per simulation.

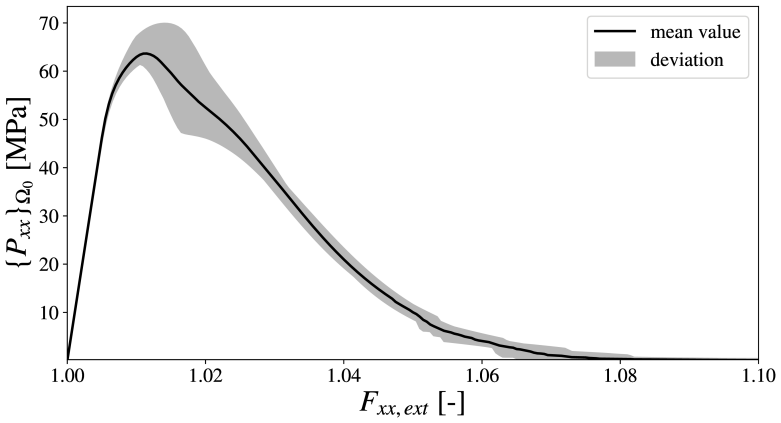

Figure 3.34: Stress-stretch curves resulting from standard homogenization for *RSA* RUCs of size $24\,\mu\mathrm{m} \times 24\,\mu\mathrm{m} \times 1\,\mu\mathrm{m}$ with damaging interfaces; black: Mean value of 10 realizations, grey: Scatter of 10 realizations.

This is in contrast to the RUCs with perfect interfaces, where the stretch at peak load was the same for the same RUC size.

The work densities of the different constituents are summarized in Fig. 3.35. Here, $\mathcal{W}_{ext}$ denotes the external work density of the RUC, while $\mathcal{W}_{\Omega_d}$ and $\mathcal{W}_{\Omega_e}$ denote the work densities of the active damaging domain and the elastic domain of the bulk, respectively. The active damaging and elastic work densities of the interface are denoted by $\mathcal{W}_{\Gamma_d}$ and $\mathcal{W}_{\Gamma_e}$, respectively. Noteworthy, since the quantities shown here are work related quantities, negative values are possible. This is especially the case for material points outside of the localization zone. During damage loading (positive contribution) these material points contribute to the damaging work densities, while at elastic unloading (negative contribution) they contribute to the elastic work densities. In Figs. 3.36a to 3.36c, three damage contour plots showing the deformed mesh are visualized. Their corresponding solution times are indicated in Fig. 3.35.

The evolution of the virtual work densities shown in Fig. 3.35 is as follows. The external work first is governed by elastic parts of the bulk and the interface. Then, the interface start to damage and the work of both elastic parts stays constant. Subsequently, the bulk material begins to fail and the work of the elastic part of the interfaces decreases. At about $F_{xx,ext} = 1.02$, the work of the actively damaging bulk exceeds the work of the actively damaging interface, which stays constant from about $F_{xx,ext} = 1.03$ on. At about $F_{xx,ext} = 1.08$, all work quantities are constant indicating that the failure process is finished. This particular order of failure mechanisms was reported by [Guillén-Hernández et al., 2020] as well, where the so called in-situ strength effect was investigated numerically. The failure mechanisms are shown in Figs. 3.36a to 3.36c as well. From Fig. 3.36a, the opening of the interfaces is observed, where no significant damage is accumulated within the matrix. Fig. 3.36b shows the subsequent accumulation of damage within the matrix without the formation of a localization band. In

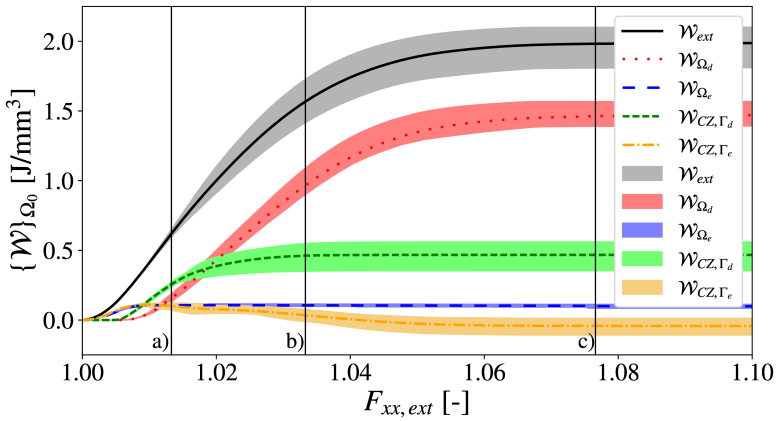

Figure 3.35: Work contributions of the different constituents for the $24\,\mu\mathrm{m}$ *RSA* RUCs with damaging interfaces; black: external work, red: actively damaging matrix material, blue: elastic matrix material, green: actively damaging interface and orange: elastic interface; damage contour plots of one realization showing mesh deformation of different stages a) to c) are shown in Figs. 3.36a to 3.36c.

Figs. 3.36c and 3.36d, final failure with a localization zone is visualized. As can be seen, the crack mainly extends over the interphase between fiber and matrix while only the matrix shows an actively damaging zone. This is due to the interfaces being fully damaged with a complete loss of interface stiffness.

Further, the work densities of the overall actively damaging and elastic domain are compared to the external work in Fig. 3.37. Here, $\mathcal{W}_{\Omega_d+\Gamma_d}$ and $\mathcal{W}_{\Omega_e+\Gamma_e}$ describe the combined overall work densities of the actively damaging and elastic domains of bulk and interface, respectively.

Here, the external work is completely governed by the bulk until $F_{xx,ext} = 1.006$. At the onset of damage evolution at $F_{xx,ext} = 1.006$, the work in the bulk then slowly decreases, while the work of the actively damaging domain increases faster than the external work. At the end, the external work and the work of the actively damaging domain are almost equal while the work of the bulk is close to zero.

For comparison, the same work densities as in Fig. 3.37 are shown in Fig. 3.38 with perfect interfaces. Both curves show a similar behavior. Until the onset of failure, the external work is completely governed by the elastic part. Thereafter, the work of the actively damaging domain and the external work evolve identically while the work of the elastic part stays constant. Finally, the external work is nearly completely governed by the work of the actively damaging domain.

While qualitatively showing the same effects, differences between the simulations with and without damaging interfaces arose from the computational time and the deviations. When debonding of interfaces was included, the RUCs failed at far field deformations that were twice as large as in the case with perfect bonding. Moreover, the external work density was higher for the RUCs with damaging interfaces, even though the peak stresses were significantly lower. It is concluded that the higher work

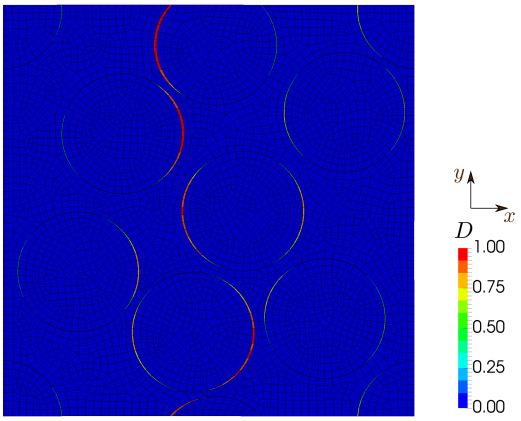

(a) $F_{xx,ext} = 1.0133$

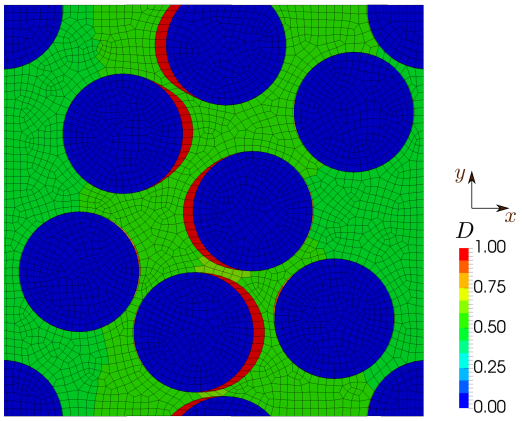

(b) $F_{xx,ext} = 1.0333$

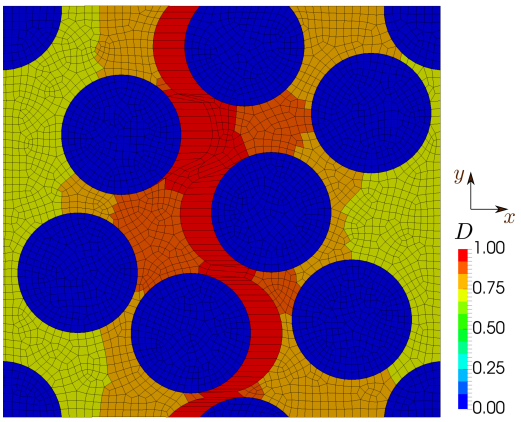

(c) $F_{xx,ext} = 1.0766$

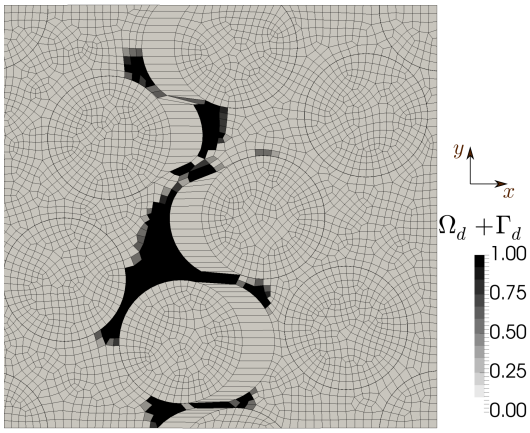

(d) $F_{xx,ext} = 1.0766$

Figure 3.36: Damage contour plots (a to c) and actively damaging zone for bulk and cohesive zone elements at different stages of deformation as indicated in Fig. 3.35 with mesh deformation factor 1.

density is a result of the much higher deformation. Finally, the RUCs with damaging interfaces showed a higher scattering compared to the RUCs with perfect interfaces.

3.7 Conclusion and outlook

In this work, a failure zone homogenization scheme was proposed based on the approach of Nguyen et al. [2010]. The aim was to develop a homogenization strategy which takes into account all energetic contributions and finite strains. For this, the newly developed failure zone homogenization approach was tested using a statistical analysis of RUCs of carbon fiber reinforced plastics. For the simulation of material failure at the micro-scale, a St. Venant type material model for finite strains with isotropic

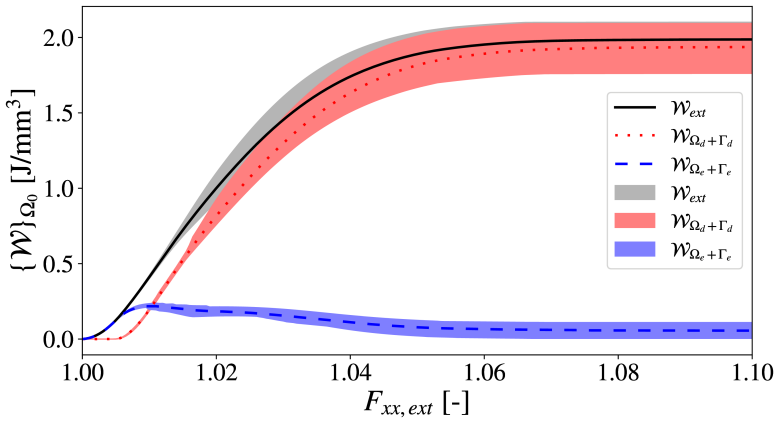

Figure 3.37: Work contributions for the 24 µm *RSA* RUCs with damaging interfaces; red: actively damaging constituents, blue: elastic constituents and black: external work.

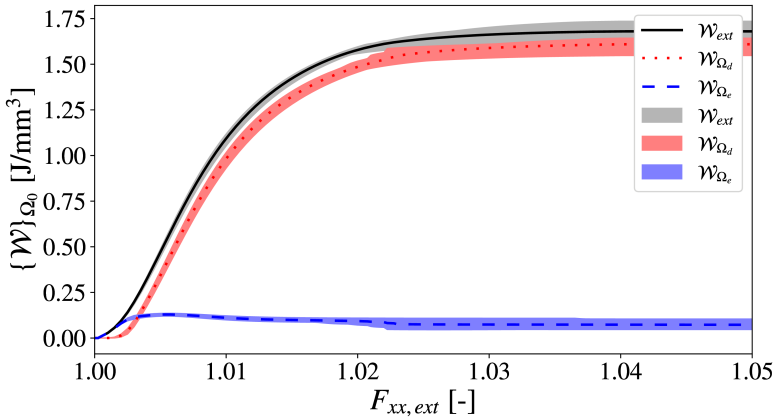

Figure 3.38: Work contributions for the 24 µm *RSA* RUCs without damaging interfaces from previous Sec. 3.6.5; red: actively damaging constituents, blue: elastic constituents and black: external work.

damage was introduced. Further, to overcome undesired mesh dependence, a gradient extension based on the micromorphic approach is used. Additionally, the debonding of interface between carbon fibers and epoxy matrix was simulated using cohesive zone elements.

A possible extension of the material model used would be the introduction of plasticity and damage via a so-called two-surface material model as shown, e.g. in [Brepols et al., 2017] or [Holthusen et al., 2020]. However, the experimental data provided by [Poggenpohl et al., 2021] did not show considerable plastic deformations. Therefore, the material model used was restricted to brittle damage.

To ensure that no numerical artifacts affect the statistical analysis and that the homogenization procedures work, the following tests were performed: (I) A mesh convergence study, (II) a sensitivity analysis for the artificial viscosity, (III) a size convergence study as well as (IV) an analysis of different

RUC generation algorithms. From the mesh convergence study it was shown that the mesh dependency was successfully cured. Further, a sensitivity analysis showed that introducing an artificial viscosity for stabilization had no effect on the overall stress-stretch response, while a significant effect on the evolving actively damaging domain was observed.

Further, the RUC size convergence study showed that standard averaging based on Hill's approach showed satisfactory results in the elastic region but RUC size dependent results in the softening region. In contrast, the failure zone homogenization scheme showed converged results w.r.t. the RUC size even in the softening region. Finally, two different RUC generation algorithms *randomized* and *RSA* were compared. It was shown that the different generation algorithms led to significant differences in the overall as well as the failure zone stress-stretch curves. Since the *RSA* RUCs provided fiber distributions which were closer to the distributions of real CFRPs, this generation method was used for the statistical analysis.

For the statistical analysis, five different RUC sizes with ten realizations each were evaluated. It was shown that Hill's approach led to converging results until maximum stress. However, the stress-stretch curves showed failure at lower stretch with increasing RUC size. Analysis of the dissipated work density supported these results.

Statistical analysis using the failure zone averaging showed convergence with respect to the RUC size which was supported by an analysis of the dissipated work density as well. Additionally, an analysis of the micromophic power and work densities of the failure zone averaging of the *RSA* RUCs was conducted. It was shown that the micromorphic power density of the failure zone gives significant values during the formation of localization while the overall work density is small. Thus, it was concluded that for accurate failure zone homogenization, the contributions of micromorphic terms have to be considered. It is assumed that other gradient enhanced methods show a similar contribution of the power and work density. Thus, these contributions should be addressed when using failure zone averaging.

Finally, a statistical analysis of RUCs with damaging interfaces was conducted. In total, ten realizations of one particular RUC size were used. Stress strain curves show a lower peak stress and a higher scatter in the stress response. The use of bulk and cohesive zone elements allowed for an analysis of the energetic contributions of both softening effects. It was shown that the energetic contribution of the interface is lower than that of the bulk but still significant. Additionally, the RUCs with non perfect interfaces showed a higher dissipation potential and doubled far field strains until final failure.

In brief, the argument given in Nguyen et al. [2010] still holds: if the homogenization is performed within the failure zone, an RVE can be uniquely identified. In the current work, this concept was underpinned through deriving and evaluating the corresponding energetic contributions analytically and numerically. It was shown that the RVE still exists even for large deformations, with micromophic/gradient-extended damage formulations, and when both, damage- and debonding-induced softening was considered. However, when homogenizing stresses and strains within a multiscale framework (out of the scope of this paper) the energy contributions from the boundary terms of the damaging

domain must be considered.

In future works, the new homogenization approach shall be applied to shear and mixed mode loading. Further, the approach could – in principle – be applied to FE^2 simulations as shown in [Nguyen et al., 2012], where a traction separation law is defined by micro simulations. However, the stress and stretch within the failure zone are not defined a priori, but calculated a posteriori. Thus, new or updated boundary conditions would need to be applied in order to achieve the desired stretch within the failure zone in order to allow for a use of the results within a multi scale framework.

Finally, the new homogenization method could be applied to investigate the in-situ strength effect of cross ply laminates as shown experimentally by [Parvizi et al., 1978] and investigated numerically by [Guillén-Hernández et al., 2020]. However, new boundary conditions in accordance to those applied by [Guillén-Hernández et al., 2020] would be needed.

Acknowledgements

The financial support of Deutsche Forschungsgemeinschaft (DFG, German Research Foundation) within the project SI1959/7-1 (project number: 404502442) is gratefully acknowledged. Furthermore, H. Holthusen would like to acknowledge the project RE1057/46-1 (project number: 404502442).

4 Article 3: Failure zone homogenization at mode II and mixed mode loading including gradient-extended damage and interface debonding at finite strains

This article was published as:

Poggenpohl, L., Holthusen, H. and Simon, J.-W. [2022], 'Failure zone homogenization at mode II and mixed mode loading including gradient-extended damage and interface debonding at finite strains', *Composite Structures* **298**, 115997.

Disclosure of the individual authors' contributions to the article:

The material model used in this article is the same as in the previous article. Thus, no further development was needed. The set up (including geometry generation) and analysis of the simulations were carried out by L.Poggenpohl. Further, it was L. Poggenpohl who wrote the main part of the publication. H. Holthusen gave valuable feedback during result discussion and paper writing. In addition, the work and paper writing was supervised by J.-W. Simon who gave valuable feedback as well. All authors approved the publication of the final version of the manuscript.

Abstract. Homogenization based on Hills approach is widely used in many scale breaching applications such as the analysis of repeating unit cells (RUCs). However, it was shown that Hills approach is not applicable at the presence of localization phenomena, since in the standard averaging sense the representativeness of the considered micro-scale volume is lost. The failure zone averaging method was shown to overcome these drawbacks and yield converging results even in the softening region. In this paper the failure zone homogenization approach is applied to shear and mixed mode loading of long fiber reinforced plastics. For an accurate description of material failure within the epoxy matrix, a scalar damage model at large strains with gradient enhancement – for mesh size independent results – is used. After a mesh and size convergence study, a statistical analysis of different RUC sizes with random micro structures is performed. Further, the influence of crack closure effects as well as different loading conditions such as simple shear and mixed mode loading are analyzed. It is shown that the implementation of crack closure and application of simple shear lead to different stress-stretch responses. Additionally, crack closure can lead to a different orientation of the failure zone. Finally, an analysis of RUCs with cohesive zone elements for fiber-matrix debonding are shown. Here, lower stresses but higher strains until final failure are observed as well as generally higher dissipation compared to RUCs with perfect interfaces.

4.1 Introduction

Carbon fiber reinforced plastics (CFRPs) show higher ratios of strength and stiffness with respect to their density when compared to, e.g. metals (see, e.g. [Rösler et al., 2013]). Thus, CFRPs are the optimal material for light weight construction. Nowadays, CFRPs are used in CFRP reinforced concrete (c.f. [Karayannis et al., 2018]) or wind turbine blades (c.f. [Bae and Kim, 2019]). Generally, CFRPs are fabricated using either laminates (as for wind turbine blades) or a woven micro structure where for the former, tailored material properties can be achieved. As shown, e.g. by [Stier et al., 2015] or [Höwer et al., 2019], complex load states occur within woven CFRPs even for simple loading conditions due to the complex micro structure.

Different approaches have been made to account for these complex load states on the higher scale (i.e. the macro level). Amongst many others, a general framework is introduced, e.g. in [Simon et al., 2015; Bednarcyk et al., 2015]. There, a damage interaction matrix is applied to the damage evolution of woven composites to control the evolution and interaction of different damage mechanisms caused by the complex load states. Nevertheless, all models need damage evolution or interaction rules which have to be justified. This can either be achieved through experiments or through numerical simulations. The latter yield the benefit of offering tailored loading scenarios which grant better insight into the material behavior.

For the analysis of repeating unit cells (RUCs) in a staggered or FE^2 scheme, generally Hill's approach (see [Hill, 1967, 1972]) is used. So-called Hill homogenization is not restricted to the me-

chanical response but can also be used for diffusive and thermal processes as shown, e.g. in [Mikeš et al., 2021] or [Pak et al., 2021]. Further, as shown in [Chen and Wang, 2020], Hill's approach is also applicable for piezoelectricity. However, the analysis was restricted to single cell RVEs and no size convergence study was shown. In [Choi et al., 2019] or [Ge et al., 2021], Hill's approach is applied in a two scale simulation of woven composites. However, the micro simulations were restricted to single cell RVEs for both publications and no RUC size convergence study is shown.

As shown in the publications of [Gitman et al., 2004, 2007; Geers et al., 2010] standard volume averaging following hills approach is not applicable at the presence of localization phenomena. Thus, a representative size of the RUC could not be defined uniquely. In [Gitman et al., 2007] it is found that the quotient of localization volume (i.e. dissipative volume) and RUC volume (i.e. the volume of the stored elastic energy) is not constant but dependent on the edge length of the RUC. This inconsistency is thought to be the cause for Hill's approach to fail.

In [Nguyen et al., 2010], the failure zone averaging method was developed to counteract the aforementioned inconsistency. It was shown that this method was insensitive to the size converging problem of Hill's approach for RUCs undergoing localizing phenomena. For the failure zone averaging method, the computational domain was split into elastic and actively damaging domain, where the averaging was only applied on the latter sub domain. Thus, the problem reported in [Gitman et al., 2007] was circumvented. The failure zone averaging method was further investigated by means of numerical aspects in [Nguyen et al., 2011] and was applied to an FE^2 scheme for the simulation of fracture of concrete in [Nguyen et al., 2012]. In another recent approach, the failure zone averaging method has been applied to RUC simulations with cracks and nonperfect interfaces between fibers and matrix (see, e.g. [Turteltaub et al., 2018; Turteltaub and de Jong, 2019; Turteltaub and Suárez-Millán, 2020] or [Ke and Van Der Meer, 2021]). In [Pineda et al., 2013], RUCs of CFRPs with a damaging material model for the matrix are investigated using the generalized method of cells (GMC) at the micro level. There, the RUC size dependency is cured using the crack band theory linking the RUC size to the element size of the macro level. Here, the size of the RUC is defined by the size of the finite element of the macro level and can not be chosen arbitrary.

In the recent publication [Poggenpohl et al., 2022*a*], a failure zone homogenization approach was derived based on the failure zone averaging method. There, the energetic contributions of the mechanical part, the micromorphic gradient extension as well as the interfaces between carbon fibers and epoxy matrix were analyzed. However, the analysis was restricted to pure tensile loading. For the use of this homogenization approach in multi scale analysis, it has to be investigated whether or not this approach is applicable in more complex loading scenarios. Thus, the failure zone homogenization will be applied to RUCs of long carbon fiber reinforced plastics at pure shear, simple shear and mixed mode loading. The loading is applied in the plain perpendicular to the fiber direction. While the fibers are simulated linear elastic, a material model for brittle damage is used for the matrix material. Since the introduction of material models with softening can lead to undesired mesh dependent results, the micromorphic

gradient damage approach (c.f. [Forest, 2009]) is used. The introduction of higher order gradients was shown to cure undesired mesh dependencies. In addition, RUCs with imperfect interfaces between fibers and matrix will be shown. Here, cohesive zone elements were used to simulate the decohesion of matrix and fiber as well as matrix cracking (i.e. cracks in the bulk).

4.2 Material modeling

In the following, the material models for the bulk which, in turn, consist of epoxy matrix and carbon fibers and interfaces are presented in brief. A detailed description of the material models as well as finite element implementation can be found in [Poggenpohl et al., 2021, 2022*a*].

The nomenclature of vectors, tensors and operators – which are defined exclusively in the euclidean space – is summarized in the following:

a, A	Scalar	
$\boldsymbol{a}$	First order tensor	
$\mathbf{a}$	Tuple $n \times 1$	
$\boldsymbol{A}$	Second order tensor	
$\mathbf{A}$	Matrix $n \times m$	
$\mathbb{A}$	Fourth order tensor	
$\cdot$	Single contraction, i.e.	$\boldsymbol{A} \cdot \boldsymbol{B} = A_{ij} B_{jk}$
:	Double contraction, i.e.	$\boldsymbol{A} : \boldsymbol{B} = A_{ij} B_{ij}$
$\boldsymbol{a} \otimes \boldsymbol{b}$	Dyadic product, i.e.	$\boldsymbol{a} \otimes \boldsymbol{b} = a_i b_j$
$\boldsymbol{A}^T$	Transpose, i.e.	$A^T_{ij} = A_{ji}$

4.2.1 Bulk material model

The bulk material behavior of the RUC is simulated using the isotropic part of the material model introduced in [Poggenpohl et al., 2021]. The material model is briefly introduced in the following.

Overall, the volume specific free energy of the material is assumed as:

$$\psi(\boldsymbol{E}, D, D^\chi) = \psi_{mech}(\boldsymbol{E}, D) + \psi_h(D) + \psi_g(\nabla_0 D^\chi) + \psi_\chi(D, D^\chi) \tag{4.1}$$

In Eq. (4.1), the amount of stiffness degradation is described using the scalar damage variable D. Here, $D = 0$ refers to a virgin material with no stiffness degradation, while $D = 1$ refers to a complete loss of material stiffness. In the above, the Green-Lagrange strain tensor $\boldsymbol{E}$ is used, which is defined as

$$\boldsymbol{E} = \frac{1}{2}[\boldsymbol{F}^T \cdot \boldsymbol{F} - \boldsymbol{I}] \tag{4.2}$$

where $\boldsymbol{I}$ and $\boldsymbol{F}$ represent the unit tensor and the deformation gradient, respectively. The latter is defined as the derivative of the current (deformed) configuration $\boldsymbol{x}$ with respect to the reference (undeformed)

configuration $\boldsymbol{X}$:

$$\boldsymbol{F} = \nabla_0 \boldsymbol{x} = \frac{\partial \boldsymbol{x}}{\partial \boldsymbol{X}} \tag{4.3}$$

As can be seen in in Eq. (4.3), ∇_0 refers to the spatial gradient with respect to the reference configuration. Finally, the micromorphic damage variable D^χ, which is an additional degree of freedom, is introduced as counter part of the local damage variable D. In what follows, the four parts of the free energy density (4.1) are briefly discussed.

Analogously to [Fassin et al., 2019*b*], a tension-compression asymmetry (TCA) is introduced. It is applied to the first two terms of Eq. (4.4) giving the mechanical part of the total free energy, which is of St. Venant-Kirchhoff type.

$$\psi_{mech}(\boldsymbol{E}, D) = [1-D]^n \, \frac{\lambda}{2} \left[\mathrm{tr}^+(\boldsymbol{E})\right]^2 + (1 - h_{tc} D)^n \, \frac{\lambda}{2} \left[\mathrm{tr}^-(\boldsymbol{E})\right]^2 + [1-D]^n \mu \, \mathrm{tr}(\boldsymbol{E}^2) \tag{4.4}$$

The material parameters describing the elastic response are the Lamé constants λ and μ. In addition, parameter h_{tc} controls the degree of crack closure. For $h_{tc} = 1$ no crack closure effects are present such that damage influences the compression part in the same way as the tension part. In contrast, the highest degree of crack closure is achieved for $h_{tc} = 0$, where damage has no influence in the compressive regime at all. Intermediate states (i.e. $0 \leq h_{tc} \leq 1$) are used in general. Noteworthy, TCA is only applied on the first term, while the shear terms are not effected which is a simplification of the model presented in [Fassin et al., 2019*b*]. Crack closure was introduced, since epoxy resin shows a significant asymmetry between tensile and compressive loading. While at tensile loading, a rather brittle material response is observed (see, e.g. [Poggenpohl et al., 2021]), plastic shear bands can be seen at compressive loading (see, e.g. [González and LLorca, 2007]). To account for this effect in a simplified way, crack closure is implemented in the material model used here. The tension ($\mathrm{tr}^+(\boldsymbol{E})$) and compression ($\mathrm{tr}^-(\boldsymbol{E})$) parts are defined as

$$\mathrm{tr}^+(\boldsymbol{E}) = \langle \mathrm{tr}(\boldsymbol{E}) \rangle \quad \text{and} \quad \mathrm{tr}^-(\boldsymbol{E}) = -\langle -\mathrm{tr}(\boldsymbol{E}) \rangle \, . \tag{4.5}$$

Here, $\langle a \rangle$ denotes the Macauley brackets:

$$\langle a \rangle = \begin{cases} 0 & \text{for } a \leq 0 \\ a & \text{for } a > 0 \end{cases} \tag{4.6}$$

The second part of the free energy (4.1) denotes the damage hardening energy which is assumed to be of quadratic type

$$\psi_h = \frac{K}{2} D^2. \tag{4.7}$$

In Eq. (4.7), the degree of damage hardening is controlled by material parameter K. Roughly speaking, damage hardening delays the damage evolution, the terminology ‘hardening’ originates from the

analogy to plastic hardening.

The last two terms of Eq. (4.1) denote the micromorphic extension and are – strictly speaking – not part of the material model but rather an extension. Material formulations that exhibit softening tend to show undesired mesh size dependent results of the solution due to strain localization. In this work, mesh size dependency is cured using the micromorphic extension as introduced, e.g. in [Forest, 2009]. The energetic terms related to the micromorphic extension read

$$\psi_\chi = \frac{H^\chi}{2}\left[D^\chi - D\right]^2 \tag{4.8}$$

$$\psi_g = \frac{El^2}{2}\left[\nabla_0 D^\chi \cdot \nabla_0 D^\chi\right]. \tag{4.9}$$

The micromorphic extension consists of a coupling term ψ_χ and a gradient term ψ_g. In the micromorphic coupling term ψ_χ, the penalty factor H^χ couples the local and the micromorphic damage variable. This parameter has to be chosen sufficiently high, such that the difference between D^χ and D should be at least two magnitudes smaller than the numeric value of D itself. In the gradient term ψ_g, the Young's modulus E and an internal length scale factor l are used (cf. [Fassin et al., 2019*a*]).

Considering the micromorphic extension leads to an extension of the Clausius-Duhem inequality (see, e.g.[Forest, 2019])

$$-\dot{\psi} + \boldsymbol{S} : \dot{\boldsymbol{E}} + \underbrace{a\dot{D}^\chi + \boldsymbol{b}\cdot\nabla_0\dot{D}^\chi}_{\text{micromorphic extension}} \geq 0. \tag{4.10}$$

Here, $\boldsymbol{S}$ is the second Piola-Kirchhoff stress tensor. Additionally, a and $\boldsymbol{b}$ denote the work conjugate stress-like quantities of the additional degree of freedom D^χ and its gradient $\nabla_0 D^\chi$, respectively. The expanded inequality is obtained by applying the chain rule on $\dot{\psi}$ and rearranging the terms resulting in:

$$\left[\boldsymbol{S} - \frac{\partial\psi}{\partial\boldsymbol{E}}\right] : \dot{\boldsymbol{E}} + \left[a - \frac{\partial\psi}{\partial D^\chi}\right]\dot{D}^\chi + \left[\boldsymbol{b} - \frac{\partial\psi}{\partial\nabla_0 D^\chi}\right]\cdot\nabla_0\dot{D}^\chi - \frac{\partial\psi}{\partial D}\dot{D} \geq 0 \tag{4.11}$$

Following the argumentations of [Coleman and Noll, 1961] and [Forest, 2016], the bracket terms are set to zero in order to ensure that inequality (4.11) holds for arbitrary processes. This results in the following relations:

$$\boldsymbol{S} = \frac{\partial\psi}{\partial\boldsymbol{E}}, \quad a = \frac{\partial\psi}{\partial D^\chi}, \quad \boldsymbol{b} = \frac{\partial\psi}{\partial\nabla_0 D^\chi} \tag{4.12}$$

From the principle of virtual work, the stress-like quantities a and $\boldsymbol{b}$ lead to the micromorphic balance equation. This balance equation has to be solved additionally to the balance of linear momentum, where $\boldsymbol{f}_0$ denotes the conventional body forces (cf., e.g. [Peerlings et al., 1996, 2004] or [Forest, 2016]). The complete set of balance equations reads:

$$\mathrm{Div}\left(\boldsymbol{F}\cdot\boldsymbol{S}\right) + \boldsymbol{f}_0 = \boldsymbol{0}\,; \quad \mathrm{Div}\left(\boldsymbol{b}\right) - a = 0 \quad \text{in} \quad \Omega_0 \tag{4.13}$$

Equations (4.13) have to be fulfilled in every material point of the bulk of body Ω_0, thus giving the

strong form of the boundary value problem.

Dirichlet and Neumann conditions are defined on the boundary to complete the boundary value problem:

$$\begin{aligned} &\underline{\text{BC for balance of linear momentum:}} && \underline{\text{BC for micromorphic balance:}} \\ &[\boldsymbol{F}\cdot\boldsymbol{S}]\cdot\boldsymbol{n}_0=\boldsymbol{t}_0 \quad \text{on} \quad \partial\Omega_{0,n} && \nabla_0 D^\chi\cdot\boldsymbol{n}_0=0 \quad \text{on} \quad \partial\Omega_0 \\ &\boldsymbol{u}=\hat{\boldsymbol{u}} \quad \text{on} \quad \partial\Omega_{0,d} \end{aligned} \tag{4.14}$$

In case of mechanical boundary conditions (BCs), Neumann ($\partial\Omega_{0,n}$) and a Dirichlet ($\partial\Omega_{0,d}$) boundary conditions are applied. However, only Neumann-type boundary conditions are prescribed on $\partial\Omega_0$ for the micromorphic extension.

Inserting the relations of Eq. (4.12) into the Clausius-Duhem inequality (4.11), the reduced dissipation inequality is obtained:

$$\underbrace{-\frac{\partial\psi}{\partial D}}_{=:Y}\dot{D}\geq 0 \tag{4.15}$$

Here, the damage driving force Y is introduced. Analogous to the yield function in plasticity, a damage loading function

$$\Phi(Y):=Y-Y_0\leq 0 \tag{4.16}$$

is constructed, where Y_0 is the damage threshold parameter. The Karush-Kuhn-Tucker conditions for the given damage model read:

$$\dot{D}\geq 0, \quad \dot{D}\Phi=0, \quad \Phi\leq 0 \tag{4.17}$$

Noticably, damage healing is not considered within this model.

4.2.2 Interface material model

As in [Poggenpohl et al., 2022*a*], interface debonding between epoxy matrix and carbon fibers is simulated using the cohesive zone (CZ) formulation of [Rezaei et al., 2017]. Here, $\boldsymbol{g}=[g_n,g_{s1},g_{s2}]^T$ and $\boldsymbol{t}=[t_n,t_{s1},t_{s2}]^T$ describe the gap and traction vectors between matrix and fiber. The subscripts n, $s1$ and $s2$ denote the components in normal and both shear directions. Here, the free energy per unit area reads

$$\psi_{CZ}=\frac{1}{2}(1-D_{CZ})k_0\lambda_{CZ}^2+\frac{1}{2}k_p\langle -g_n\rangle^2, \tag{4.18}$$

with $\lambda_{CZ}=\sqrt{\langle g_n\rangle^2+\beta^2(g_{s1}^2+g_{s2}^2)}$ denoting the effective separation and parameter β defining the influence of the shear components (see, e.g. [Simon et al., 2015]). In this study, the shear contribution is assumed equal to the normal contribution and therefore $\beta=1.0$ is used. Further, the initial interface stiffness is defined by parameter k_0, while the internal variable D_{CZ} denotes the stiffness degradation due to interface damage. Finally, to prevent self penetration, the penalty parameter k_p and the negative

normal gap $\langle -g_n \rangle$ are introduced.

From the derivatives of the free energy (4.18) with respect to the gap vector, the components of the traction vector are obtained:

$$t_n := \frac{\partial \psi_{CZ}}{\partial g_n} = (1 - D_{CZ}) k_0 \langle g_n \rangle - k_p \langle -g_n \rangle \tag{4.19}$$

$$t_{s1} := \frac{\partial \psi_{CZ}}{\partial g_{s1}} = (1 - D_{CZ}) k_0 \, g_{s1} \beta^2 \tag{4.20}$$

$$t_{s2} := \frac{\partial \psi_{CZ}}{\partial g_{s2}} = (1 - D_{CZ}) k_0 \, g_{s2} \beta^2. \tag{4.21}$$

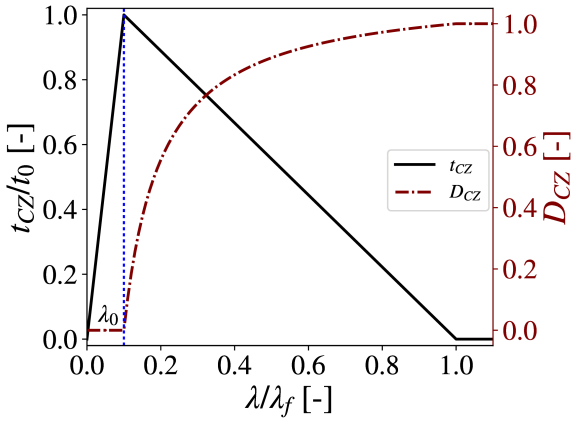

Figure 4.1: Visualization of traction and damage evolution of a bilinear traction-separation law; traction and separation are normalized to maximum traction t_0 and failure separation λ_f.

As shown in Fig. 4.1, a bilinear traction-separation law is adopted. It is defined by the material parameters maximum traction (t_0), separation at maximum traction (λ_0) and final failure (λ_f). The corresponding damage evolution law reads:

$$D_{CZ} = \begin{cases} 0 & \text{if } \lambda < \lambda_0 \\ \frac{\lambda_f}{\lambda_f - \lambda_0} \frac{\lambda - \lambda_0}{\lambda} & \text{if } \lambda_0 < \lambda < \lambda_f \\ 1 & \text{if } \lambda_f < \lambda \end{cases} \tag{4.22}$$

Analogous to the reduced dissipation inequality (cf. Section 4.2.1), the dissipation related to the cohesive zone reads

$$Y_{CZ} \dot{D}_{CZ} = \frac{1}{2} k_0 \lambda^2 \dot{D}_{CZ} \geq 0. \tag{4.23}$$

Here, $Y_{CZ} = -\partial \psi_{CZ} / \partial D_{CZ}$ is the damage driving force of the interface. For the first term the

inequality is fulfilled at any time ($\frac{1}{2}k_0\lambda^2 \geq 0$), such that

$$\dot{D}_{CZ} \geq 0 \tag{4.24}$$

has to hold. Consequently, it is necessary that no damage healing takes place on the interface in order to fulfill the dissipation inequality.

4.3 Homogenization approach

Two different homogenization approaches will be used in the following:

- Classical Hill homogenization and
- Failure zone homogenization which is based on the failure zone averaging approach of [Nguyen et al., 2010].

Classical Hill homogenization originates from the assumption that the work density of a material point of the so-called macro level is equal to the averaged work density of the micro level (i.e. the RVE)

$$\delta\mathcal{W}_M = \{\delta\mathcal{W}_m\}_{\Omega_0} \ . \tag{4.25}$$

Here, $\delta\mathcal{W}$ denotes the virtual work density, while subscripts M and m denote quantities of the macro and micro level, respectively. Additionally, $\{*\}_{\Omega_0}$ denotes the volume average with respect to Ω_0, i.e.:

$$\{*\}_{\Omega_0} = \frac{1}{|\Omega_0|}\int_{\Omega_0} (*)\ \mathrm{d}V \tag{4.26}$$

In the above, $|\Omega_0|$ refers to the volume of Ω_0. For the material model used here, the virtual work density of the micro level consists of a mechanical part and a micromorphic part

$$\mathcal{W}_M = \{\delta\mathcal{W}_m\}_{\Omega_0} = \{\boldsymbol{P} : \boldsymbol{F} + \boldsymbol{b}\cdot\nabla_0 D^\chi + aD^\chi\}_{\Omega_0} \ . \tag{4.27}$$

However, as was shown in [Clasen et al., 2013], the micromorphic virtual power vanishes when integrated over Ω_0. Following the derivations of e.g. [Geers et al., 2010], Eq. (4.25) together with appropriate mechanical boundary conditions the classical homogenization approach for the stress is obtained

$$\boldsymbol{P}_M = \{\boldsymbol{P}_m\}_{\Omega_0}. \tag{4.28}$$

As shown, e.g. in [Geers, Kouznetsova, Matouš and Yvonnet, 2017], the introduction of damaging or non-perfect interfaces leads to displacement jumps. Thus, the displacement field is no longer continuous and the externally applied deformation ($\boldsymbol{F}_{ext}$) is split into bulk ($\boldsymbol{F}_{bulk}$) and cohezive ($\boldsymbol{F}_{CZ}$)

parts:

$$\underbrace{\frac{1}{|\Omega_0|}\int_{\partial\Omega_0} \boldsymbol{x}\otimes\boldsymbol{n}_0\,\mathrm{d}A}_{\boldsymbol{F}_{ext}} = \underbrace{\frac{1}{|\Omega_0|}\int_{\Omega_0} \boldsymbol{F}_m\,\mathrm{d}V}_{\boldsymbol{F}_{bulk}} + \underbrace{\frac{1}{|\Omega_0|}\int_{\Gamma} \boldsymbol{g}\otimes\boldsymbol{n}_0\,\mathrm{d}A}_{\boldsymbol{F}_{CZ}} \tag{4.29}$$

The same holds for the virtual work, where externally measured virtual work density ($\mathcal{W}_{ext}$) is split into bulk ($\mathcal{W}_{bulk}$) and cohesive ($\mathcal{W}_{CZ}$) parts:

$$\underbrace{\frac{1}{|\Omega_0|}\int_{\partial\Omega_0} \boldsymbol{n}_0\cdot\boldsymbol{P}_m^T\cdot\delta\boldsymbol{x}\,\mathrm{d}A}_{\delta\mathcal{W}_{ext}} = \underbrace{\frac{1}{|\Omega_0|}\int_{\Omega_0} \boldsymbol{P}_m:\delta\boldsymbol{F}_m\,\mathrm{d}V}_{\delta\mathcal{W}_{bulk}} + \underbrace{\frac{1}{|\Omega_0|}\int_{\Gamma} \boldsymbol{t}\cdot\delta\boldsymbol{g}\,\mathrm{d}A}_{\delta\mathcal{W}_{CZ}} \tag{4.30}$$

A detailed derivation of Eqs. (4.29) and (4.30) can be found in [Poggenpohl et al., 2022*a*]. From Eq. (4.30), the introduction of damaging interfaces leads to an extension of the formulation of the virtual work density as introduced in Eq. (4.27).

As shown in [Gitman et al., 2007], classical Hill homogenization is not applicable at the presence of localization phenomena. As will be seen in Sec. 4.6.2 and Sec. 4.6.3, classical Hill homogenization leads to more brittle results when the RUC size is increased. The reason for this is found in a mismatch of the dimensions between the elastic volume (scaling with W×H per unit depth) and the dissipating volume (scaling only with W×ℓ or H×ℓ per unit depth) as visualized in Fig. 4.2.

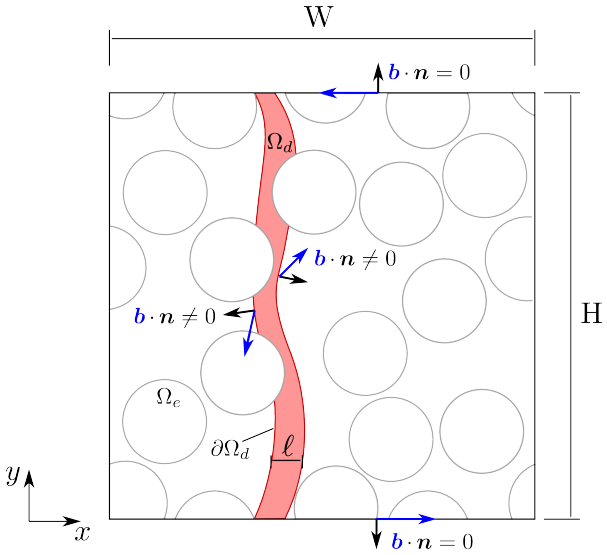

Figure 4.2: Exemplary geometry with failure zone Ω_d (red) and elastically unloading zone Ω_e ; normal vector ($\boldsymbol{n}$) and micromorphic stress vector ($\boldsymbol{b}$) are shown at the boundary of Ω_d.

To overcome the dimension mismatch, failure zone averaging was introduced in [Nguyen et al., 2010]. Here, the volume average is only applied on the actively damaging domain Ω_d which is defined

as

$$\Omega_d := \{\boldsymbol{x} \in \Omega_0 \mid \dot{D}(\boldsymbol{x}) > 0\}. \tag{4.31}$$

It shall be noted that, depending on the local evolution of loading, material points can join, as well as leave the actively damaging domain. Thus, the size and shape of the failure zone can change noticeably. In [Poggenpohl et al., 2022*a*] a detailed discussion of the evolution of the actively damaging domain is given. In Fig. 4.2 a representation of the failure zone is shown. A domain of actively damaging interfaces can be identified analogously:

$$\Gamma_d := \{\boldsymbol{x} \in \Gamma_0 \mid \dot{D}(\boldsymbol{x}) > 0\} \tag{4.32}$$

From [Nguyen et al., 2010] and following publications (e.g. [Nguyen et al., 2011] or [Turteltaub and de Jong, 2019]) it is shown that failure zone averaging resolves the issue of dimension mismatch. Hence, a representative size for the RUC can be identified.

Moreover, it was shown that a homogenization approach for the failure zone averaging leads to several surface integrals, which have to be investigated separately. In the following the derivations of [Poggenpohl et al., 2022*a*] are given in brief.

The Hill condition of the failure zone reads

$$\{\boldsymbol{P}_m\}_{\Omega_d} : \{\delta\boldsymbol{F}_m\}_{\Omega_d} = \frac{1}{|\Omega_d|}\int_{\Omega_d} \left[\boldsymbol{P}_m : \delta\boldsymbol{F}_m + a\delta D^\chi + \boldsymbol{b}\cdot\nabla_0\delta D^\chi\right] \mathrm{d}V \ . \tag{4.33}$$

Second term of Eq. (4.33) can be transformed into a surface integral, giving

$$\{\boldsymbol{P}_m\}_{\Omega_d} : \{\delta\boldsymbol{F}_m\}_{\Omega_d} = \frac{1}{|\Omega_d|}\int_{\partial\Omega_d} \left[\boldsymbol{n}_0\cdot\boldsymbol{P}_m^T\cdot\delta\boldsymbol{x}_m + \boldsymbol{n}_0\cdot\boldsymbol{b}\,\delta D^\chi\right] \mathrm{d}A \ . \tag{4.34}$$

As can be seen, the contributions of the micromorphic and mechanical parts have to be considered in general. Next, the following relation for $\delta\boldsymbol{x}_m$ is introduced

$$\delta\boldsymbol{x}_m = \{\delta\boldsymbol{F}_m\}_{\Omega_d}\cdot\boldsymbol{X}_m + \delta\boldsymbol{w}_m \tag{4.35}$$

assuming that the virtual deformation of a material point $\delta\boldsymbol{x}_m$ can be described via a virtual average deformation $\{\delta\boldsymbol{F}_M\}_{\Omega_d}\cdot\boldsymbol{X}_m$ and a virtual fluctuation term $\delta\boldsymbol{w}_m$. This is in line with the derivations in

[Geers, Kouznetsova, Matouš and Yvonnet, 2017]. Inserting Eq. (4.35) into Eq. (4.33) yields:

$$\begin{aligned}\{\boldsymbol{P}_m\}_{\Omega_d} : \{\delta\boldsymbol{F}_m\}_{\Omega_d} &= \frac{1}{|\Omega_d|}\int_{\partial\Omega_d}\left[\boldsymbol{n}_0\cdot\boldsymbol{P}_m^T\cdot(\{\delta\boldsymbol{F}_m\}_{\Omega_d}\cdot\boldsymbol{X}_m+\delta\boldsymbol{w}_m)+\boldsymbol{n}_0\cdot\boldsymbol{b}\,\delta D^\chi\right]\,\mathrm{d}A\\ &= \frac{1}{|\Omega_d|}\Bigg(\overbrace{\int_{\partial\Omega_d}\boldsymbol{n}_0\cdot\boldsymbol{P}_m^T\otimes\boldsymbol{X}_m\,\mathrm{d}A}^{\int_{\Omega_d}\boldsymbol{P}_m\mathrm{d}V}:\{\delta\boldsymbol{F}_m\}_{\Omega_d}+\underbrace{\int_{\partial\Omega_d}\boldsymbol{n}_0\cdot\boldsymbol{b}\,\delta D^\chi\,\mathrm{d}A}_{\neq 0}\\ &\quad+\overbrace{\int_{\partial\Omega_d}\boldsymbol{n}_0\cdot\boldsymbol{P}_m^T\cdot\delta\boldsymbol{w}_m\,\mathrm{d}A}^{=0?}\Bigg)\end{aligned}\tag{4.36}$$

Eq. (4.36) shows that the virtual work within the bulk of the actively damaging zone Ω_d can be composed into three parts. All three parts are defined on the boundary $\partial\Omega_d$, where the first term leads to the homogenization relation of the stress as shown, e.g. in [Geers, Kouznetsova, Matouš and Yvonnet, 2017]. As indicated in Eq. (4.36), the second term does not vanish since the normality rule cannot be applied on $\partial\Omega_d$ as illustrated in Fig. 4.2. Hence, this term has to be considered within a homogenization relation.

Additionally, it has to be determined whether the third term vanishes. The requirement of this term to vanish leads to the relation

$$\{\boldsymbol{P}_m\}_{\Omega_d} : \{\delta\boldsymbol{F}_m\}_{\Omega_d} = \{\boldsymbol{P}_m : \delta\boldsymbol{F}_m\}_{\Omega_d},\tag{4.37}$$

which, as shown e.g. in [Nguyen et al., 2011; Poggenpohl et al., 2022*a*], can be substantiated with numerical results.

As derived for Eq. 4.30, the virtual work density of the bulk has to be extended by the virtual work of the interfaces if non perfect interfaces are considered. Applied to the failure zone averaging, this yields

$$\begin{aligned}\{\boldsymbol{P}_m\}_{\Omega_d} : \{\delta\boldsymbol{F}_m\}_{\Omega_d} = \frac{1}{|\Omega_d|}\Bigg(&\int_{\partial\Omega_d}\boldsymbol{n}_0\cdot\boldsymbol{P}_m^T\otimes\boldsymbol{X}_m\,\mathrm{d}A:\delta\boldsymbol{F}_M+\int_{\partial\Omega_d}\boldsymbol{n}_0\cdot\boldsymbol{P}_m^T\cdot\delta\boldsymbol{w}_m\,\mathrm{d}A\\ &+\int_{\partial\Omega_d}\boldsymbol{n}_0\cdot\boldsymbol{b}\delta D^\chi\,\mathrm{d}A+\int_{\Gamma_d}\boldsymbol{t}\cdot\delta\boldsymbol{g}\,\mathrm{d}A\Bigg),\end{aligned}\tag{4.38}$$

giving all energetic contributions which have to be considered in a failure zone homogenization approach involving non perfect interfaces and micromorphic damage.

As will be shown later, Hill's approach shows reasonable results for elasticity as well as strain hardening. Failure zone homogenization, on the other hand, is applicable in the strain softening region. As shown, e.g. in [Nguyen et al., 2012] or [Turteltaub and de Jong, 2019], the homogenization procedure has to be changed during simulation. There, Hill's approach was used until a crack has formed and

failure zone homogenization was used to model crack opening and propagation.

4.4 Geometry generation

The materials modeled were long fiber reinforced plastics. For the generation of RUCs, the geometry was assumed to have no inhomogeneities in fiber direction. Thus, the fibers were modeled as perfect cylinders and with a diameter of $7\,\mu\mathrm{m}$ which is in accordance with e.g. [Makeev et al., 2019]. Geometries were generated from a regular distribution or from the *random sequential absorption* (*RSA*) method (see, e.g. [Illian et al., 2008; Schneider et al., 2016]).

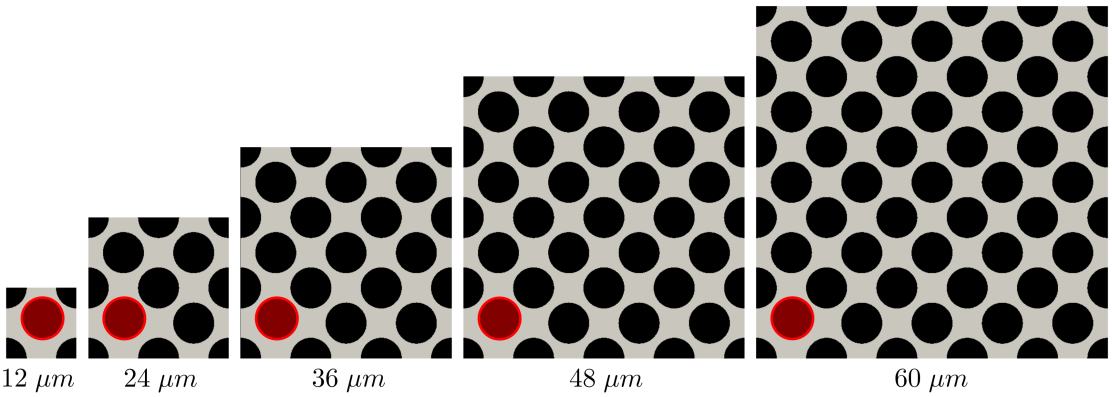

Figure 4.3: Different sizes of RUCs used for a regular grid with imperfection (marked in red) taken from [Poggenpohl et al., 2022*a*]; RUC sizes range from $12\,\mu\mathrm{m} \times 12\,\mu\mathrm{m} \times 1\,\mu\mathrm{m}$ (left) to $60\,\mu\mathrm{m} \times 60\,\mu\mathrm{m} \times 1\,\mu\mathrm{m}$ (right) with a constant fiber volume fraction of 53.5%

In Fig. 4.3, the geometries generated from the *regular* pattern are visualized. As visualized, the distribution resembles hexagonal closed packing but one fiber (marked in red) is shifted with respect to its regular position. This imperfection was implemented to trigger damage evolution and to avoid numerical instabilities due to bifurcation.

The *RSA* method was used to automatically generate RUCs with a random fiber distribution as can be seen in Fig. 4.4. For geometry generation, fibers with random coordinates were placed into the RUC and it was checked whether the new fiber overlaps with already existing fibers. Only if no overlaps were found, the new fiber was accepted. To prevent narrow gaps, fibers which were too close to existing fibers were rejected as well. New fibers were generated until the desired number of accepted fibers (i.e. fiber volume fraction) was reached. For the current work, the fiber volume fraction was chosen to be 53.5% for all RUCs. As shown in Fig. 4.4, fibers who overlap the boundary were mirrored to the other side to form a periodic geometry.

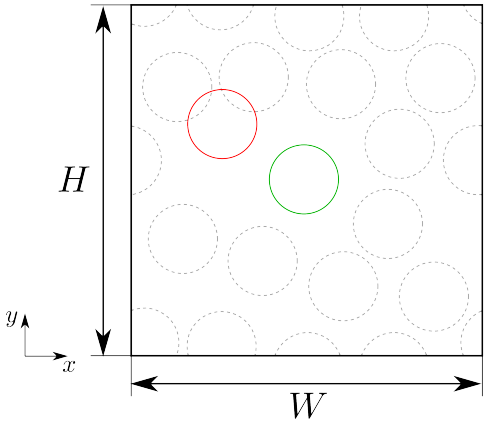

Figure 4.4: Visualization of the generation of an *RSA* RUC geometry; solid black: RUC boundary, dashed: existing fibers, red: rejected fiber due to overlapping, green: accepted fiber

4.5 Solution of the boundary value problem

The material model presented in Sec. 4.2 was implemented into the academic finite element program FEAP. Details about the finite element implementation can be found in [Poggenpohl et al., 2021, 2022*a*].

For the solution of the microscopic boundary value problem, periodic boundary conditions are widely used (see, e.g. [Nguyen et al., 2010, 2011, 2012; Turteltaub et al., 2018; Turteltaub and de Jong, 2019]) and applied here as well. Based on the periodic geometry, a periodic mesh was generated as well. Periodic boundary conditions were prescribed via

$$\boldsymbol{x}_r^i - \boldsymbol{x}_l^i = \boldsymbol{F}_M \cdot (\boldsymbol{X}_r^i - \boldsymbol{X}_l^i), \tag{4.39}$$

where superscript i indicates a node pair. A node pair is characterized by two nodes on the boundary sharing two out of three coordinates. For instance, two nodes on the left (l) and right (r) boundary which have the same y- and z-coordinates are considered a node pair. Introduction of a deformation offset between the nodes of a node pair leaves enough freedom for micro fluctuations on the boundary. Within the software FEAP, two sets of solution commands were necessary. First, node pairs are identified and coupled via the solution command *ELINk*. Then, the far field deformation gradient is applied via the solution command *PERIodic,CAUChy* and the displacement gradient ($\boldsymbol{H}_M = \boldsymbol{F}_M - \boldsymbol{I}$). Periodic displacement BCs were derived within the software FEAP based on this input.

For the numerical investigations, different far field deformations were applied:

- Pure shear deformation with a displacement gradient of

$$\boldsymbol{H} = \begin{bmatrix} 0.00 & 0.02 \\ 0.02 & 0.00 \end{bmatrix} \boldsymbol{e}_i \otimes \boldsymbol{e}_j \ , \tag{4.40}$$

- Simple shear deformation with a displacement gradient of

$$\boldsymbol{H} = \begin{bmatrix} 0.00 & 0.00 \\ 0.02 & 0.00 \end{bmatrix} \boldsymbol{e}_i \otimes \boldsymbol{e}_j \tag{4.41}$$

  and

- Mixed mode deformation with a displacement gradient of

$$\boldsymbol{H} = \begin{bmatrix} 0.02b & 0.02 \\ 0.02 & 0.00 \end{bmatrix} \boldsymbol{e}_i \otimes \boldsymbol{e}_j \quad \vee \quad \begin{bmatrix} 0.00 & 0.02 \\ 0.02 & 0.02c \end{bmatrix} \boldsymbol{e}_i \otimes \boldsymbol{e}_j \ , \tag{4.42}$$

  where parameters b and c indicate different amounts of additional tensile deformation.

For the results presented in following Sec. 4.6, pure shear deformations were used for a mesh and size convergence study as well as a statistical analysis of different RUC sizes with and without damaging interfaces. Further, pure shear deformations were applied on a size convergence study. Finally, mixed mode deformations were applied to ten realizations of size $48\,\mu\mathrm{m} \times 48\,\mu\mathrm{m} \times 1\,\mu\mathrm{m}$ generated using the RSA method.

4.6 Numerical Results

Numerical results of the simulations are investigated in the following. The material parameters, mainly taken from [Poggenpohl et al., 2021], are summarized in table 4.1. There, elastic as well as damage material parameters of the epoxy resin (i.e. isotropic part of the material model) and the carbon fibers (i.e. the anisotropic extension) were fitted to experimental data by hand. In contrast to experimental data of laminates consisting of different lamina with fiber orientations (see, e.g. [Clay and Knoth, 2017]), unidirectional CFRPs investigated in [Poggenpohl et al., 2021] showed a brittle material response with low to none strain hardening. Adjustment had to be made on the internal length of the matrix material (l_1) in order to obtain a reasonable width of the localization zone. A reasonable width was restricted by numerical aspects such as stability and small viscous stresses (providing a lower bound) and the requirement of showing an inhomogeneous damage distribution for the smallest RUC size (providing an upper bound). Furthermore, the value of the pseudo viscosity term was adapted from [Poggenpohl et al., 2022*a*] where it was tested for tensile loading. A gauss point study of the material model used for the matrix material is given in [Poggenpohl et al., 2022*a*] as well.

In accordance to e.g. [Fantoni et al., 2020], [Guillén-Hernández et al., 2020] and [Liu et al., 2021], the fibers were modeled using an elastic, isotropic material model which was achieved by setting the damage threshold to very high values. This assumption was made, since the fibers are considered stiff in comparison to the matrix material and generally do not damage during loading perpendicular to the fiber direction. In all simulations shown below, the fibers do not damage. However, the elastic response of

Table 4.1: Material parameters (as introduced in Sec. 4.2) for the resin matrix (index 1) and carbon fibers (index 2) taken from [Poggenpohl et al., 2021]; parameters without index were applied to both constituents.

	Parameter	Value	Parameter	Value
Matrix	λ_1	$5308\,\mathrm{MPa}$	K_1	$0.205\,\mathrm{MPa}$
	μ_1	$3538\,\mathrm{MPa}$	H_1^X	$2 \times 10^4\mathrm{MPa}$
	$Y_{0,1}$	$0.0672\,\mathrm{MPa}$	l_1	$6.4 \times 10^{-4}\mathrm{mm}$
Fiber	λ_2	$423\,077\,\mathrm{MPa}$	K_2	$0\,\mathrm{MPa}$
	μ_2	$84\,615\,\mathrm{MPa}$	H_2^X	$1\,\mathrm{MPa}$
	$Y_{0,2}$	$1 \times 10^8\,\mathrm{MPa}$	l_2	$0.0\,\mathrm{mm}$
Matrix & Fiber	h_{tc}	0	η	$1 \times 10^{-3}\,\mathrm{MPa\,s}$
	n	2		

the fibers is still important for both, the elastic and inelastic response of the RUC. Thus, it is important to include the elastic response of the fibers within the simulations. Additionally, the micromorphic parameters of the fibers were chosen in a way that they do not influence the micromorphic field of the matrix.

The numerical results of this section are structured as follows:

- In the following section, a mesh convergence study is shown, indicating that mesh size sensitivity is treated effectively.
- Next, the results from standard Hill's approach and failure zone averaging are compared by means of *regular* RUCs (Sec. 4.6.2).
- Thereafter, in Sec. 4.6.3 a statistical analysis of *RSA* RUCs is performed to investigate the effects of variance within the geometry.
- Afterwards, the influence of the tension-compression asymmetry on the numerical results is shown in Sec. 4.6.4 and in following Sec. 4.6.5 the influence of loading condition simple shear is investigated.
- Further, in Sec. 4.6.6 the influence of mixed mode loading conditions on the evolution of the localization zone is investigated.
- Finally, a statistical investigation of ten RSA RUCs with damaging interfaces is shown in Sec. 4.6.7. Here, the statistical evolution of the work of bulk (which is based on $\boldsymbol{P} : \dot{\boldsymbol{F}}$) and interface is investigated.

4.6.1 Mesh convergence study

For a mesh convergence study, pure shear loading was applied on a *regular* RUC of size $48\,\mu\text{m} \times 48\,\mu\text{m} \times 1\,\mu\text{m}$ (as visualized in Fig. 4.3). Here, the RUC was meshed using different characteristic element lengths in plane of the RUC while one element over the thickness was used in all simulations. The mesh size in plane was ranging from $0.25\,\mu\text{m}$ to $2\,\mu\text{m}$. To account for different material responses with and without tension compression asymmetry (TCA), simulations were carried out using $h_{tc} = 1$ (inactive TCA) and $h_{tc} = 0$ (active TCA).

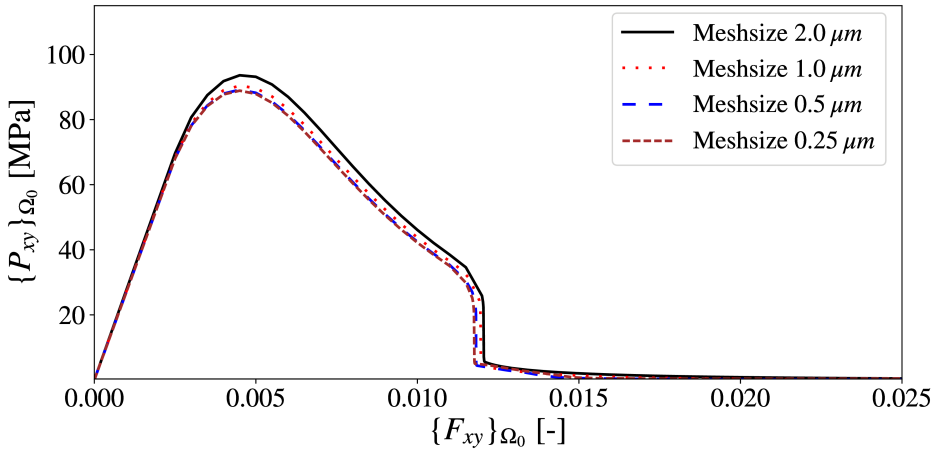

Figure 4.5: Stress-stretch curves for different meshes of the *regular* RUC of size $48\,\mu\text{m} \times 48\,\mu\text{m} \times 1\,\mu\text{m}$ *without* TCA at pure shear loading.

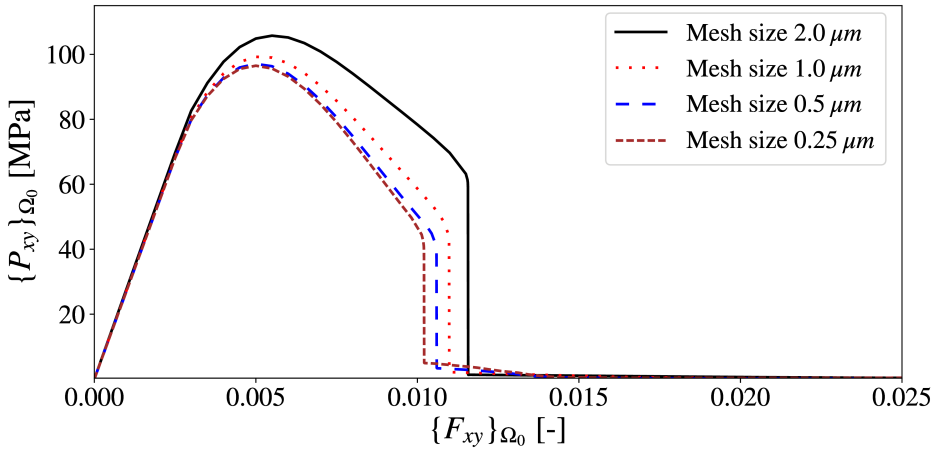

Figure 4.6: Stress-stretch curves for different meshes of the *regular* RUC of size $48\,\mu\text{m} \times 48\,\mu\text{m} \times 1\,\mu\text{m}$ *with* TCA at pure shear loading.

In Figs. 4.5 and 4.6, the results of mesh convergence studies with and without TCA are summarized. While the stress-stretch curves for $h_{tc} = 1$ are quite similar, the curves related to $h_{tc} = 0$ show a higher

sensitivity with respect to the mesh size. As can be seen for both sets, the simulations were terminated at a stretch of $F_{xy} = 0.025$, which is far beyond the failure stretch.

The higher mesh size sensitivity of the simulations *with* TCA can be linked to the finite element formulation used. It is well known in the literature (see, e.g. [Barfusz et al., 2021*b*]) that standard linear elements with eight Gauss points do suffer from so called locking phenomena. For material models with damage, highly distorted elements generally feature low material stiffness. Thus, the artificial stiffening from locking is reduced w.r.t. the global stress-stretch curve. With activated TCA, heavily distorted elements might recover their initial stiffness due to local compressive loads. In this case, the artificial stiffening from locking is more pronounce w.r.t. the global stress-stretch curve.

In addition, the total work density

$$\mathcal{W}_{tot} := \int \{\boldsymbol{P} : \dot{\boldsymbol{F}}\}_{\Omega_0} \, \mathrm{d}t, \tag{4.43}$$

was calculated for an objective interpretation of the results. Here, the mid-point rule was applied for time integration of the mechanical power density.

The results as well as the total number of elements used are summarized in table 4.2. The relative errors were calculated with respect to the results of the finest mesh, i.e.:

$$e_{rel,\mathcal{W}} = \frac{\mathcal{W}_{tot} - \mathcal{W}_{tot}^{0.25\,\mu\mathrm{m}}}{\mathcal{W}_{tot}^{0.25\,\mu\mathrm{m}}} \tag{4.44}$$

Table 4.2: Work densities, maximum stresses, and relative errors according to (4.44) for different mesh sizes.

		$h_{tc} = 1$		$h_{tc} = 0$	
Mesh size [µm]	# of elements	$\mathcal{W}_{tot}$ [J mm^{-3}]	$e_{rel,\mathcal{W}}$ [%]	$\mathcal{W}_{tot}$ [J mm^{-3}]	$e_{rel,\mathcal{W}}$ [%]
2.00	1066	1.4993	8.68	1.8064	28.89
1.00	3123	1.4212	3.02	1.5492	10.54
0.50	11702	1.3824	0.21	1.4441	3.04
0.25	31861	1.3795	-	1.4015	-

From Figs. 4.5 and 4.6 as well as table 4.2, a clear convergence trend is observed, indicating that the mesh size dependency was successfully cured using the micromorphic extension. It was concluded from the numerical results in table 4.2 that a mesh size of $0.5\,\mu\mathrm{m}$ is sufficiently accurate for simulations with *active* TCA and *inactive* TCA. Hence, if not mentioned otherwise, this mesh size as well as *active* TCA was used in the subsequent simulations.

4.6.2 RUC size comparison

Based on the *regular* RUCs shown in Fig 4.3, a size comparison study was performed using pure shear loading. Therefore, the homogenization approaches of (*i*) standard homogenization (volume average of Ω_0) and (*ii*) failure zone homogenization (volume average of Ω_d) were used. In Fig. 4.7, stress-stretch

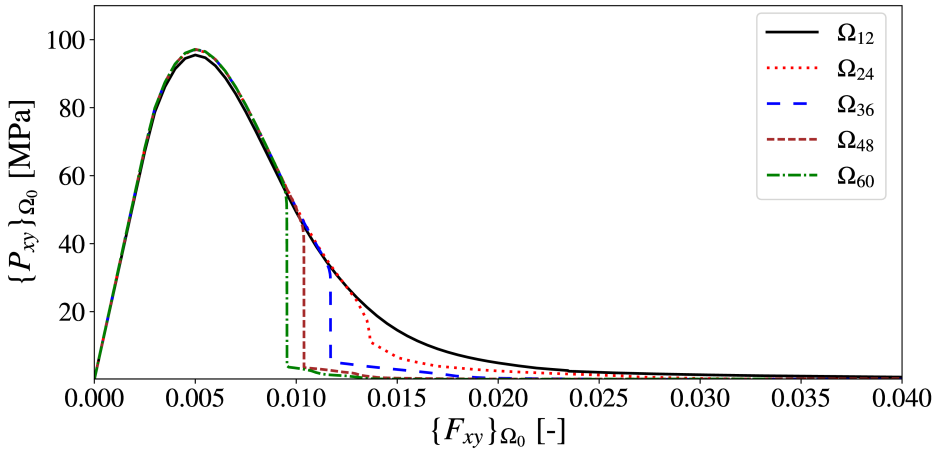

Figure 4.7: Stress-stretch curves for different *regular* RUC sizes from $12\,\mu\text{m} \times 12\,\mu\text{m} \times 1\,\mu\text{m}$ to $60\,\mu\text{m} \times 60\,\mu\text{m} \times 1\,\mu\text{m}$ at pure shear loading.

curves based on standard homogenization are shown. The curves are almost identical within the elastic and in the beginning of the softening region. Only the smallest RUC differs from the others. This effect can be related to the inhomogeneity, which naturally has the strongest influence on the smallest RUC. Afterwards, the curves differ in the onset of final failure, which is related to the formation of a localization band. Noteworthy, the load drop ends at a residual stress which is comparable for all RUC sizes. Afterwards, the stress tends asymptotically towards zero. The residual stress can be related to crack closure effects. Overall, the following holds: An increase in RUC size results in lower stretches at which final failure occurs.

Stress-stretch curves based on failure zone homogenization are visualized in Fig. 4.8. The curves show almost no dependence of the RUC size. Again, the smallest RUC shows a small deviation in the softening region, which again is related to the stronger effect of the inhomogeneity. Noteworthy, the stretches within the localization zone are higher compared to standard homogenization (see Fig. 4.7) while stresses are generally lower. Furthermore, the peak stress is half of the stress calculated for standard homogenization. Reason for this is found in the carbon fibers which are modeled stiff and elastic. The carbon fibers bear a significant amount of the load applied but are excluded within the failure zone homogenization. Thus, the stress for the failure zone homogenization is reduced.

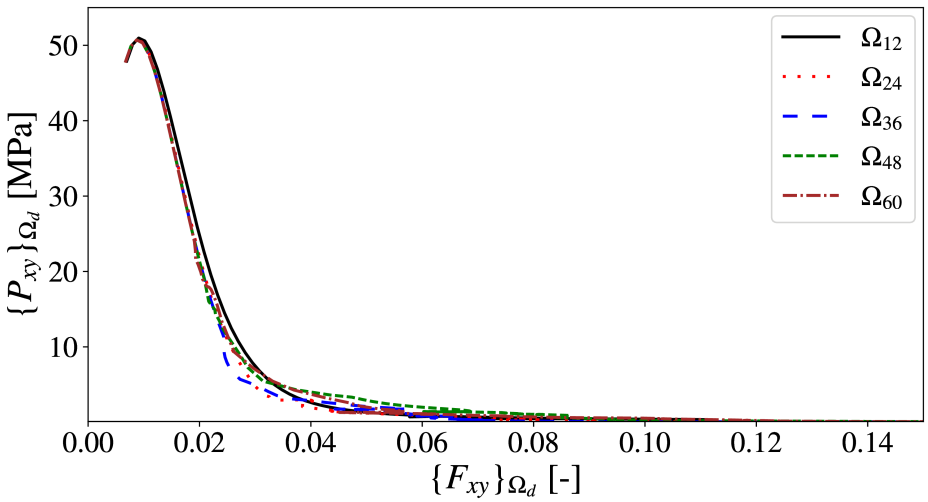

Figure 4.8: Stress-stretch curves of failure zone for different *regular* RUC sizes from $12\,\mu\text{m} \times 12\,\mu\text{m} \times 1\,\mu\text{m}$ to $60\,\mu\text{m} \times 60\,\mu\text{m} \times 1\,\mu\text{m}$ at pure shear loading.

4.6.3 Statistical investigation of representative RUC size

For five different RUC sizes ranging from $12\,\mu\text{m} \times 12\,\mu\text{m} \times 1\,\mu\text{m}$ to $60\,\mu\text{m} \times 60\,\mu\text{m} \times 1\,\mu\text{m}$, a statistical analysis of RUCs with random geometry was performed. For each RUC size, ten realizations were generated using the RSA method and a pure shear loading was applied. In following Figs. 4.9a to 4.9f, the stress-stretch curves generated from standard homogenization (i.e. the volume average of Ω_0) are summarized. For convenience, the different stress-stretch curves of ten realizations of size $36\,\mu\text{m} \times 36\,\mu\text{m} \times 1\,\mu\text{m}$ are given in Fig. 4.9d. Here, the different strains of the load drop varying from approximately $F_{xy} = 0.0115$ to $F_{xy} = 0.0135$ can be seen.

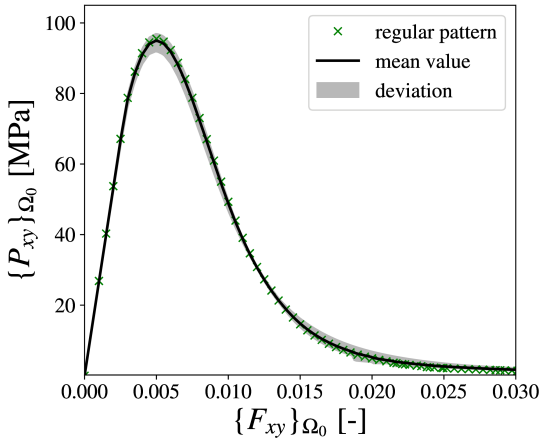

(a) RUC sizes 12 µm × 12 µm × 1 µm

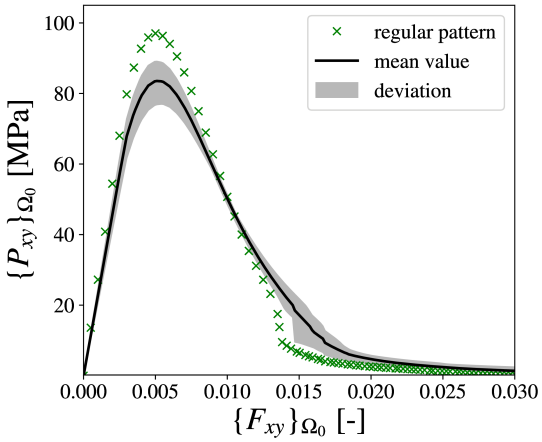

(b) RUC sizes 24 µm × 24 µm × 1 µm

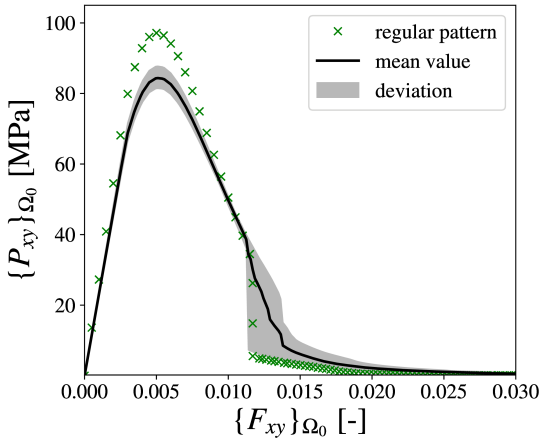

(c) RUC sizes 36 µm × 36 µm × 1 µm

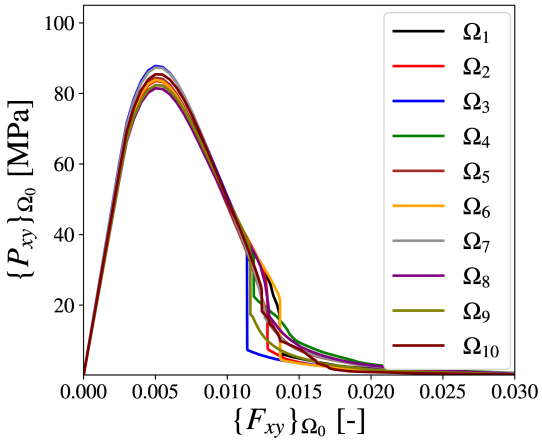

(d) Individual plot of ten realizaions of RUC size 36 µm × 36 µm × 1 µm

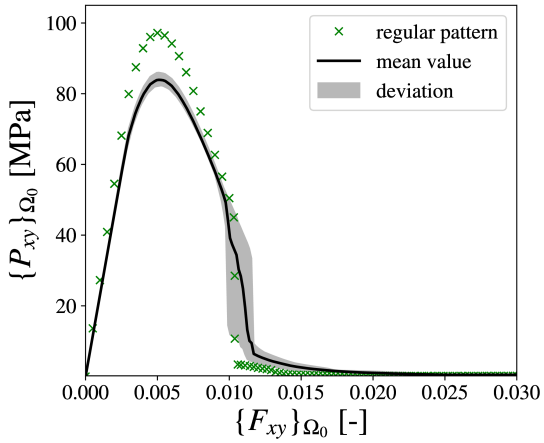

(e) RUC sizes 48 µm × 48 µm × 1 µm

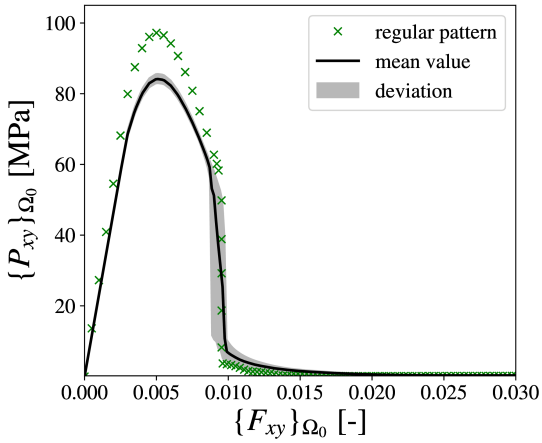

(f) RUC sizes 60 µm × 6 µm × 1 µm

Figure 4.9: Stress-stretch curves resulting from standard homogenization for *RSA* and *regular* RUCs of sizes 12 µm × 12 µm × 1 µm to 60 µm × 60 µm × 1 µm; black: Mean value of 10 realizations, grey: Scatter of 10 realizations, green: Response of the corresponding *regular* RUC of Fig. 4.7.

In Fig. 4.9a, the stress stretch responses of the $12\,\mu\mathrm{m}$ RUCs are given. The curves show a quite low deviation and a good agreement with the results of the *regular* RUC. Reason for this is found in the micromorphic regularization. In Fig. 4.10, the damage contour plot of one $12\,\mu\mathrm{m}$ RUC at the end of simulation is shown. As can be seen, the damage distribution is almost homogeneous throughout the matrix and thus, a homogeneous response is expected.

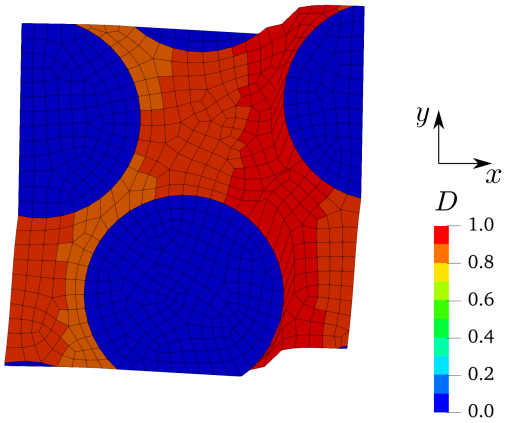

Figure 4.10: Damage contour plot for one $12\,\mu\mathrm{m} \times 12\,\mu\mathrm{m} \times 1\,\mu\mathrm{m}$ realization with mesh deformation factor 0.5.

From Figs. 4.9b to 4.9f an overall decrease in variance is observed when the RUC size is increased. This decrease is observed in the elastic region, for the maximum stress as well as for the stretch at which final failure occurs. Noteworthy, the peak stress and elastic stiffness of all of these *RSA* RUCs is lower in comparison to the *regular* RUCs. Additionally, it is observed that the load drops of *RSA* RUCs generally appear at higher stretches compared to *regular* RUCs but show a better agreement when the RUC size is increased.

For an objective analysis of representativeness, the maximum stress with respect to standard homogenization as well as the mechanical work density within Ω_0 were computed according to Eq. (4.43). The results of *regular* and *RSA* RUCs (mean value and standard deviation) are summarized in Figs. 4.11a and 4.11b, respectively. With respect to the maximum stress, regular as well as *RSA* RUCs show a size convergence. However, they converge to different values due to their different geometries. For the mechanical work density, a different result is obtained. As can be observed, the standard deviation decreases with increasing RUC size, but the mean value does not show a convergence with respect to an increasing RUC size. In comparison to the results of *regular* RUCs, the decrease is noticeably higher. Thus, a representative RUC size can not be identified for the strain softening region when the standard homogenization approach is used.

The same RUCs were investigated as well using the failure zone homogenization (i.e. the volume average of Ω_d). However, the investigation is not straight-forward since a unique stress-stretch pair (F_{xy},P_{xy}) or (F_{yx},P_{yx}) cannot be identified. Reason for this is discussed in the following where

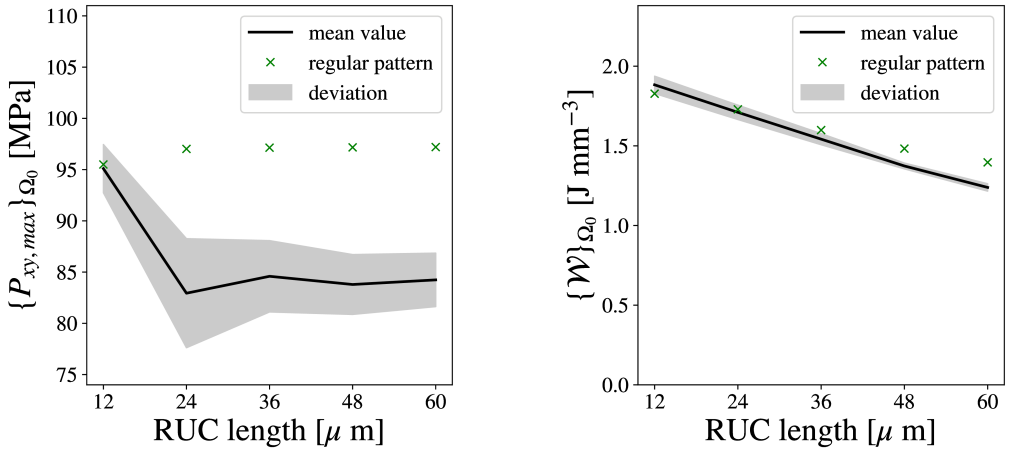

(a) Maximum stress (b) Total mechanical work density

Figure 4.11: Summary of the maximum stress as well as the total mechanical work density of the simulated *RSA* RUCs compared to the regular RUCs for standard homogenization.

Figs. 4.12a and 4.12b show stress-stretch curves of both shear components of ten RUC realizations of size $48\,\mu\text{m} \times 48\,\mu\text{m} \times 1\,\mu\text{m}$ and Figs. 4.13a and 4.13b show damage contour plots of two different realizations.

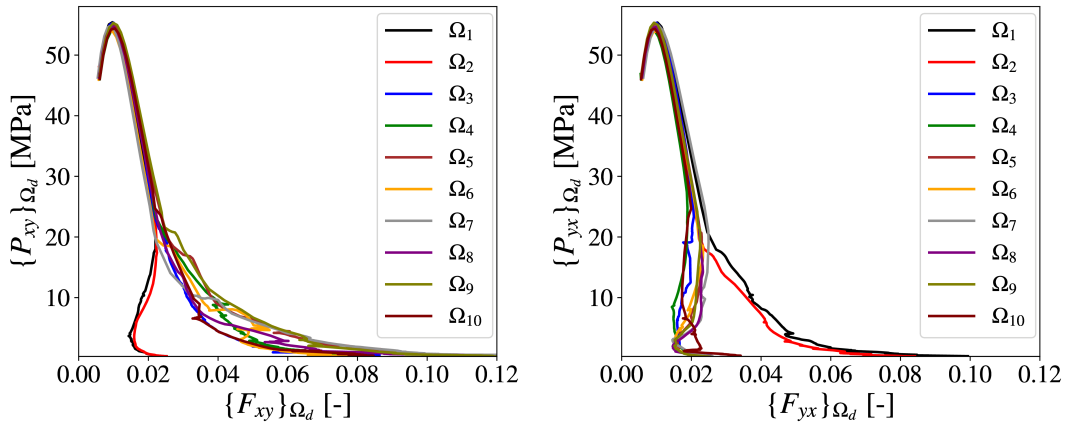

(a) Shear part $\{F_{xy}\}_{\Omega_d}$ (b) Shear part $\{F_{yx}\}_{\Omega_d}$

Figure 4.12: Stress-stretch curves resulting from failure zone homogenization for *RSA* RUCs of size $48\,\mu\text{m} \times 48\,\mu\text{m} \times 1\,\mu\text{m}$

In Figs. 4.12a and 4.12b, the homogenized shear stretches (F_{xy} and F_{yx}) within the failure zone are not equal, but there is always a dominant shear direction after the onset of failure. This is related to the orientation of the localization zone as indicated by the damage contour plots in Figs. 4.13a and 4.13b. From comparison of Figs. 4.12a and 4.12b to Figs. 4.13a and 4.13b, it becomes apparent that a

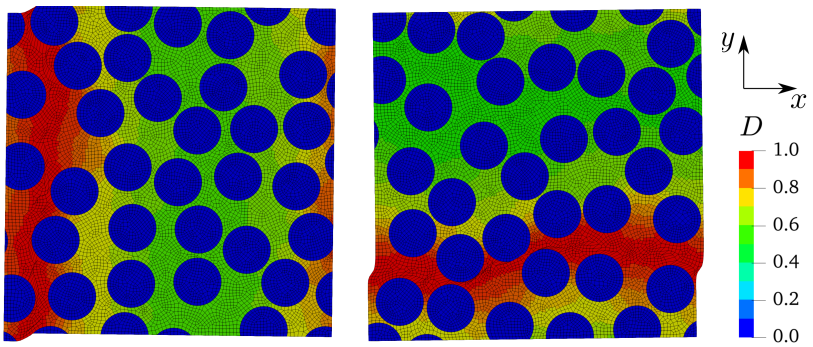

(a) Vertical failure zone for realization 1

(b) Horizontal failure zone for realization 4

Figure 4.13: Damage contour plots with mesh deformation factor 1 for two different $48\,\mu\mathrm{m} \times 48\,\mu\mathrm{m} \times 1\,\mu\mathrm{m}$ RUCs showing a vertical and horizontal failure zone.

vertical failure zone is associated with F_{yx} being the dominant stretch while a horizontal failure zone is associated with F_{xy} being the dominant stretch. Noteworthy, there were only two realizations showing a vertical failure zone (and thus F_{yx} as the dominant stretch), while an equal distribution was expected. Reason for this is found in the low number of samples.

In order to get reasonable results, the aforementioned effect is accounted for in the following. The stretches and stresses are either (F_{xy},P_{xy}) or (F_{yx},P_{yx}) depending on the dominant stretch. Further, as discussed in the appendix, the introduction of TCA leads to anomalies in the stress-stretch curves. This effect was accounted for by manually adjusting these curves. The resulting stress-stretch curves are shown in Figs. 4.14a to 4.14e.

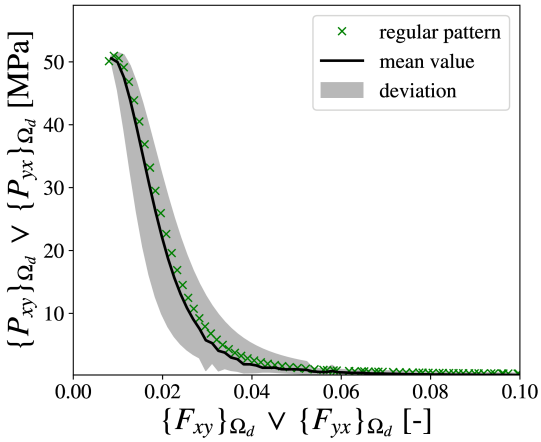

(a) RUC sizes 12 µm × 12 µm × 1 µm

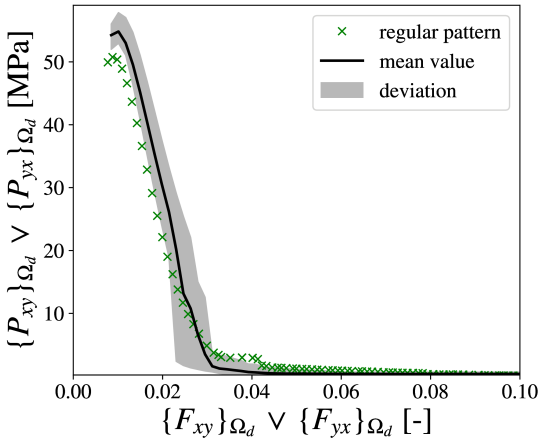

(b) RUC sizes 24 µm × 24 µm × 1 µm

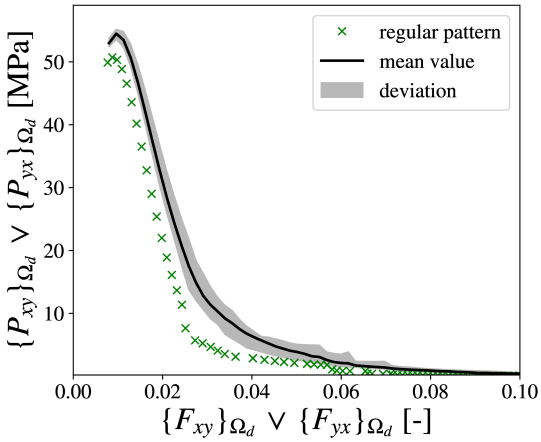

(c) RUC sizes 36 µm × 36 µm × 1 µm

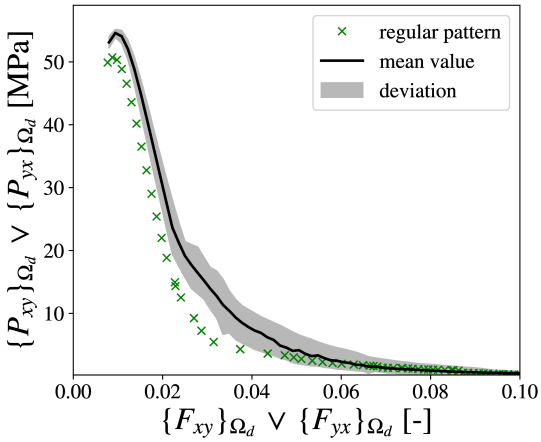

(d) RUC sizes 48 µm × 48 µm × 1 µm

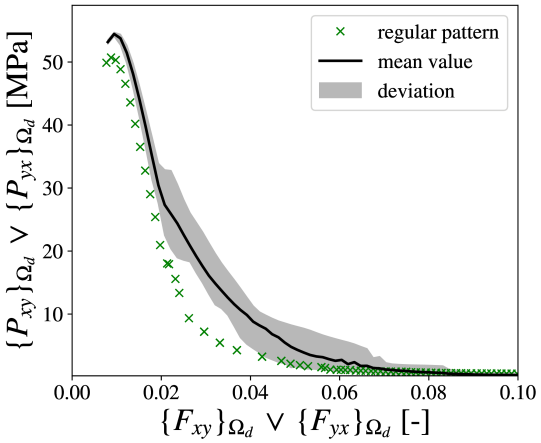

(e) RUC sizes 60 µm × 6 µm × 1 µm

Figure 4.14: Stress-stretch curves resulting from failure zone homogenization for *RSA* and *regular* RUCs of sizes 12 µm × 12 µm × 1 µm to 60 µm × 60 µm × 1 µm; black: Mean value of 10 realizations, grey: Scatter of 10 realizations, green: Response of the *regular* RUC of Fig. 4.8.

Figs. 4.14a to 4.14e indicate a different material behavior when failure zone averaging is applied. Here, the *RSA* RUCs generally show higher stresses compared to the *regular* RUCs of the same size. Only the $12\,\mu\mathrm{m}$ RUC shows a lower stress response. Noteworthy, the deviation at the onset of softening reduces with increased RUC size, however there appears to be no trend for the deviation later in the failure process.

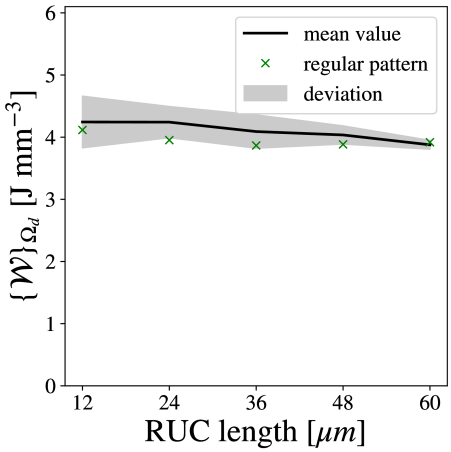

Figure 4.15: Summary of the mechanical work density of the failure zone of the simulated *RSA* RUCs for failure zone homogenization.

Finally, the mechanical work density was calculated for the failure zone homogenization as well. The results are summarized in Fig. 4.15. In comparison to Fig. 4.11b, the overall higher deviation becomes apparent. However, the deviation decreases to a similar amount at an RUC size of $60\,\mu\mathrm{m}$ with a size of $48\,\mu\mathrm{m}$ already showing satisfactory results. Moreover, the mean mechanical work density decreases way less and shows a better agreement with the work density of the *regular* RUCs. The overall lower decrease and better agreement with *regular* RUCs allows for the definition of a representative RUC size of at least $48\,\mu\mathrm{m}$ for the pure shear case.

4.6.4 Influence of the tension compression asymmetry

Comparing Figs. 4.5 and 4.6 in Sec. 4.6.1, the introduction of TCA leads to significant changes in the mesh convergence as well as overall stress-stretch response. As mentioned in Sec. 4.6.1, TCA was active in the previous size convergence study. In what follows, the influence of TCA on numerical results is discussed.

In Figs. 4.16a and 4.16b, the results of a size convergence study using standard and failure zone averaging at pure shear loading are shown. The results *without* TCA are given as line curves while exemplary results *with* TCA are indicated via crosses. For convenience, the results of the $12\,\mu\mathrm{m}$ RUC were omitted in Fig. 4.16b since they are quite close to the results of the $60\,\mu\mathrm{m}$ RUC as can be seen in

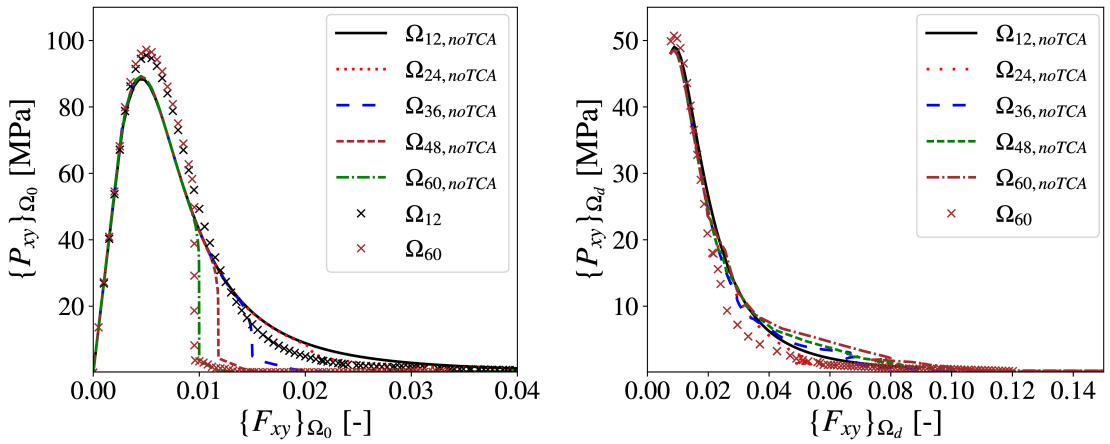

(a) Standard homogenization. (b) Failure zone homogenization

Figure 4.16: Stress-stretch curves for standard and failure zone homogenization of different *regular* RUC sizes from $12\,\mu m \times 12\,\mu m \times 1\,\mu m$ to $60\,\mu m \times 60\,\mu m \times 1\,\mu m$ at pure shear loading *without* TCA; results of the $12\,\mu m \times 12\,\mu m \times 1\,\mu m$ and $60\,\mu m \times 60\,\mu m \times 1\,\mu m$ RUCs *with* TCA are marked with crosses.

Fig. 4.8. From Fig. 4.16a, the higher peak stress as well as the failure at lower stretches are presented. Furthermore, when comparing Fig. 4.16a to Fig. 4.7, a lower asymptotic convergence towards zero stress is observed. Finally, the stretches at which final failure occurs are further apart when TCA is not applied.

In comparison, a higher peak stress is seen in Fig. 4.16b as well, but the stresses in the case of the simulations without TCA are larger from a stretch of about 0.02. The inhomogeneities at e.g. 0.08 stretch for the $60\,\mu m$ RUC or at 0.07 stretch for the $36\,\mu m$ RUC are related to local numerical artifacts. Locally, the finite elements are deformed quite heavily (cf. Fig 4.17a) and thus, the standard finite element implementation reaches its limitations. However, convergence was achieved for all time steps.

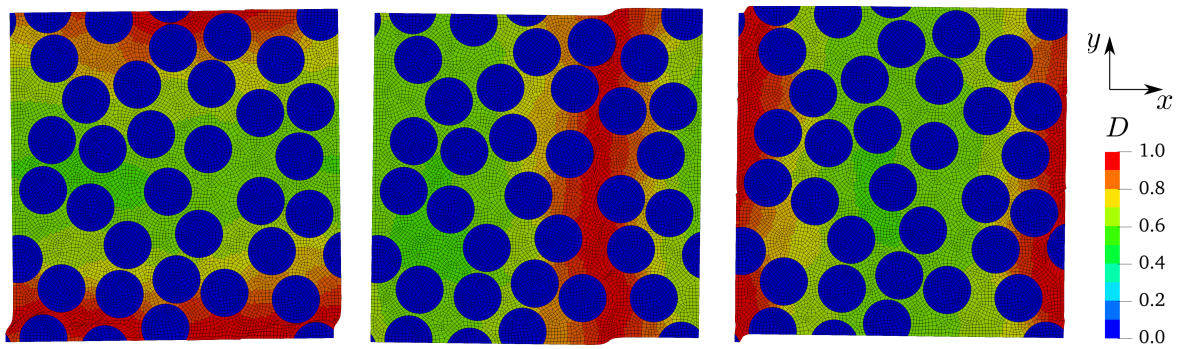

(a) Full TCA, i.e. $h_{tc} = 0.0$. (b) Reduced TCA, i.e. $h_{tc} = 0.5$. (c) Deactivated TCA, i.e. $h_{tc} = 1.0$.

Figure 4.17: Damage contour plots with mesh deformation factor 1 for different values of h_{tc}.

Additionally, ten realizations used for $48\,\mu\text{m} \times 48\,\mu\text{m} \times 1\,\mu\text{m}$ were simulated using different values for the tension compression parameter h_{tc}. As described in Sec. 4.2, parameter h_{tc} describes the amount of damage considered in the compressive region. For $h_{tc} = 0.0$, no damage is considered in the compressive region, while for $h_{tc} = 1.0$, the material response in tension and compression are equal. In Figs. 4.17a to 4.17c, the damage contour plots with mesh deformation are shown. The failure zone orientation changes from horizontally to vertically, when the effect of TCA is reduced (i.e. h_{tc} is increased from 0.0 to 0.5). Furthermore, the location of the localization zone changes, when TCA is fully activated (i.e. $h_{tc} = 1.0$).

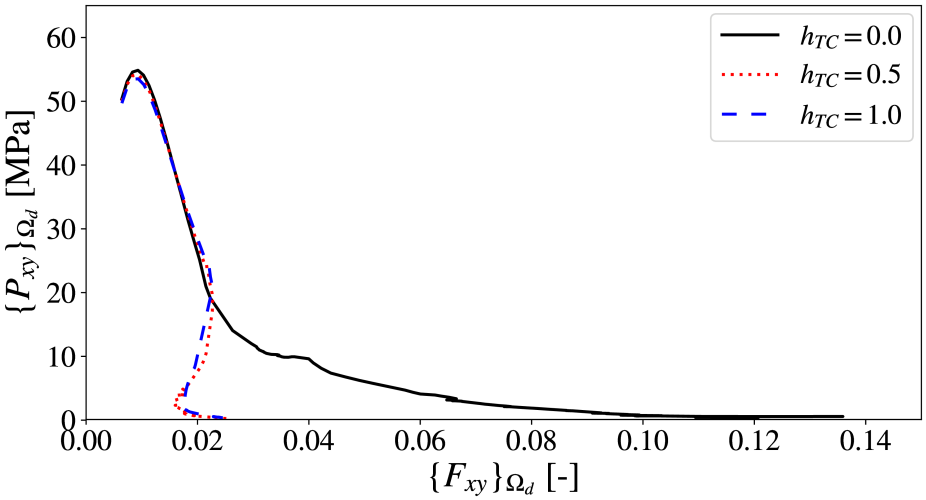

Figure 4.18: Stress-stretch curves for failure zone homogenization of the *RSA* RUC shown in Figs. 4.17a to 4.17c with different values for h_{tc}.

As can be seen in Fig. 4.18, the stress-strain response of the failure zone homogenization changes as well, when the orientation of the failure zone changes. For the peak load, only minor differences are observed and all three curves show the same stress strain response until the onset of failure. However, only the simulation with $h_{tc} = 0.0$ showed F_{xy} as the dominant stretch and thus a quite different material response.

4.6.5 Influence of different loading conditions

In addition to the activation or deactivation of TCA, the choice of the far field deformation applied might have an influence on the stress-stretch response. As shown, e.g. in [Nguyen et al., 2012], the boundary conditions applied to an RUC during an FE^2 scheme are more comparable to simple shear loading than pure shear. In Fig. 4.19, the stress-stretch response of pure shear (*PS*) and simple shear (*SS*) with respect to standard homogenization are compared. In the following, only the result of *PS* loading of the *regular* $60\,\mu\text{m}$ RUC is given.

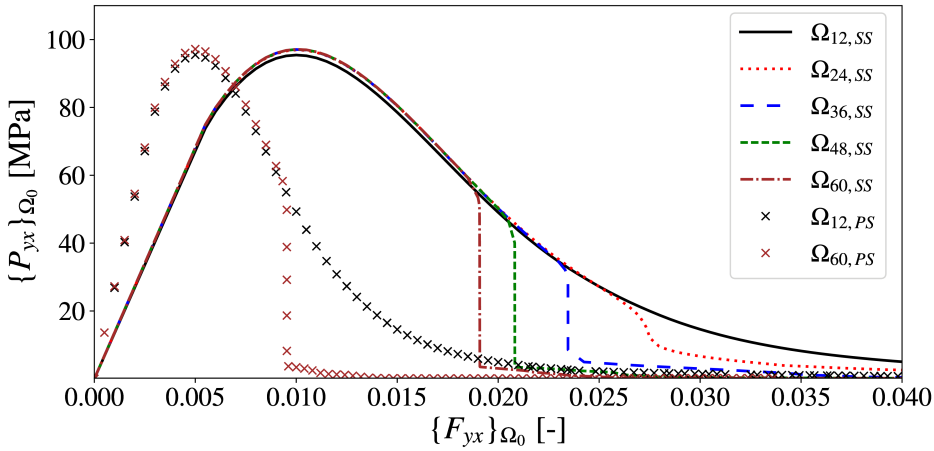

Figure 4.19: Stress-stretch curves for different *regular* RUC sizes from $12\,\mu\text{m} \times 12\,\mu\text{m} \times 1\,\mu\text{m}$ to $60\,\mu\text{m} \times 60\,\mu\text{m} \times 1\,\mu\text{m}$ at *simple shear* loading; results of the $12\,\mu\text{m} \times 12\,\mu\text{m} \times 1\,\mu\text{m}$ and $60\,\mu\text{m} \times 60\,\mu\text{m} \times 1\,\mu\text{m}$ RUCs at *pure shear* loading are marked with crosses.

Here, the maximum stresses are identical, but the elastic slopes of the *SS* RUCs are much lower. However, the stretches at peak load as well as the stretches at final failure are higher compared to the *PS* case. From a comparison of the stress-stretch curves, the overall dissipated energy of the SS case should be higher. However, a calculation of the total work density according to Eq. (4.43) showed that the overall work densities are quite comparable ($1.396\,\text{J}\,\text{mm}^{-3}$ for *PS* and $1.348\,\text{J}\,\text{mm}^{-3}$ for *SS*). In fact, the simple shear case is even showing a slightly lower dissipated work density. Reason for this is found in the complex stress and strain states within the RUC which lead to significant contributions of tensile and other shear components than the dominant one.

In contrast, the stress-stretch curves show an opposing trend when failure zone homogenization is applied (see Fig. 4.20). Here, the maximum stress again is comparable, but the stretches are lower in the *SS* case. Generally, the curves approach zero at lower stretches compared to the *PS* case.

Additionally, a comparison of the total dissipated mechanical work density (within the actively damaging domain Ω_d) was performed. The numerical values ($3.918\,\text{J}\,\text{mm}^{-3}$ for *PS* and $3.674\,\text{J}\,\text{mm}^{-3}$ for *SS*) again show only minor differences contrary to the stress-stretch curves, highlighting the importance of the non dominant stress and stretch components within the failure zone as well.

4.6.6 Mixed mode loading

To investigate the influence of mixed mode loading, a far field stretch as described at the end of Sec. 4.5 was applied on ten realizations of the $48\,\mu\text{m} \times 48\,\mu\text{m} \times 1\,\mu\text{m}$ *RSA* RUCs used for the statistical investigation in Sec. 4.6.3. As described in Sec. 4.5, parameter b and c indicate a superposition of pure shear and tensile loading in x- or y-direction, respectively. Here, the numerical values show the amount of

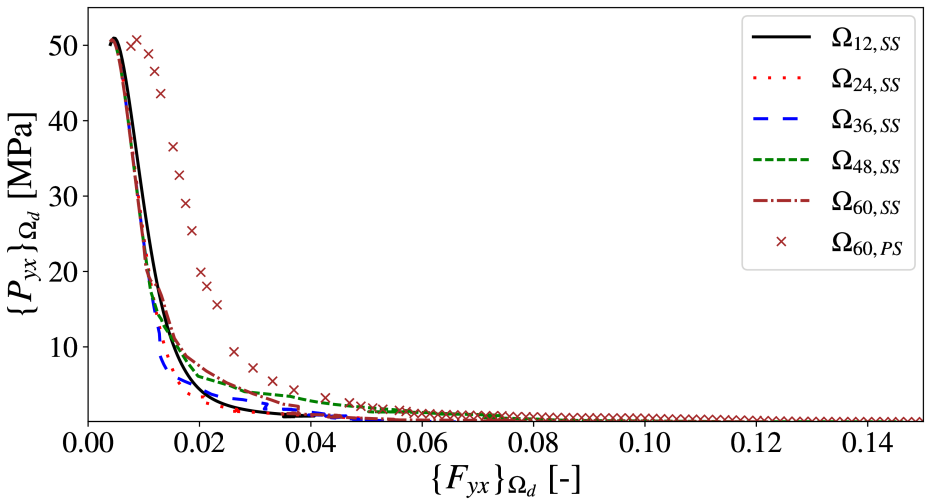

Figure 4.20: Stress-stretch curves of failure zone for different *regular* RUC sizes from $12\,\mu m \times 12\,\mu m \times 1\,\mu m$ to $60\,\mu m \times 60\,\mu m \times 1\,\mu m$ at *simple shear* loading.

additional loading which was applied.

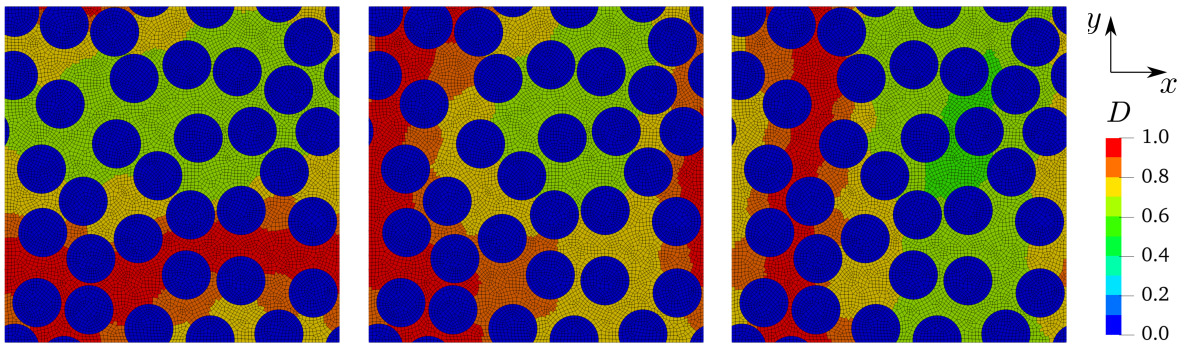

(a) $b = 0.604$ (b) $b = 0.606$ (c) $b = 0.608$

Figure 4.21: Damage contour plots of one realization of one RUC of size $48\,\mu m \times 48\,\mu m \times 1\,\mu m$ for different values of mixed mode parameter b (tensile loading in x-direction).

As shown in Figs. 4.13a and 4.13b, pure shear loading leads to failure zones which are oriented in horizontal or vertical direction. In order to change the orientation of the localization zone, a tensile loading in the direction of the failure zone (b for horizontal c for vertical direction) was superimposed. The additional loading was increased until the failure zone orientation changed. In Figs. 4.21a to 4.21c, three damage contour plots for different parameters b (i.e. superimposed tensile load in horizontal direction) are shown. As can be seen, the orientation of the localization zone switched from horizontal (for $b = 0.604$) to vertical (for $b = 0.606$) direction. No intermediate state with failure zone bifurcation was observed. Thus, it was concluded that for the given material model and set of parameters only

switches in the orientation of the localization zone occur. Hence, mixed mode loadings with different values for b and c were applied and the value at which the switch occurred was noted. The results are summarized in table 4.3.

Table 4.3: Summary of the loading parameters at which a switch in the orientation of the failure zone took place; parameter b represents additional loading in x-direction, while parameter c represents additional loading in y-direction.

Realization number	Loading parameter at the switch
1	$c = 0.46$
2	$c = 0.40$
3	$b = 0.38$
4	$b = 0.606$
5	$b = 0.22$
6	$b = 0.47$
7	$b = 0.01$
8	$b = 0.51$
9	$b = 0.25$
10	$b = 0.62$

From table 4.3 it is observed that for most (in total 8) realizations parameter b is used. Comparing to the far field deformations shown in Sec. 4.5 this represents an additional tensile loading in x-direction. In theory, an even distribution was expected, but this can be related to the low sample size. Furthermore, the additional loading required for the localization zone orientation to the switch was between 0.22 and 0.62 with one outlier at 0.01 (realization 7). This realization is the same which showed high sensitivity towards the crack closure parameter h_{tc} in Figs. 4.17a to 4.17c. In general, the results show a statistical scatter which was expected for realizations with random fiber distributions.

Additionally, the same RUCs were simulated using a different internal length $l = 8.0 \times 10^{-5}\mathrm{mm}$, which is $\frac{1}{8}$ of the internal length generally used. For these parameter sets, the same study as above was conducted for an RUC size of $48\,\mu\mathrm{m} \times 48\,\mu\mathrm{m} \times 1\,\mu\mathrm{m}$. In contrast to the study shown above, there were several results showing failure zone bifurcation comparable to crack bifurcation as shown, e.g. in [Turteltaub et al., 2018], when the superimposed tensile loading was increased. In Fig. 4.22, the damage contour plot of one exemplary RUC is shown. As indicated, a tensile loading in horizontal direction was superimposed. For small values of b, only a horizontal failure zone was observed. However, two perpendicular failure zone bands formed when a value of $b = 0.4$ was reached. It would need to be clarified whether failure zone averaging is applicable in this case. However, this is out of the scope of this paper.

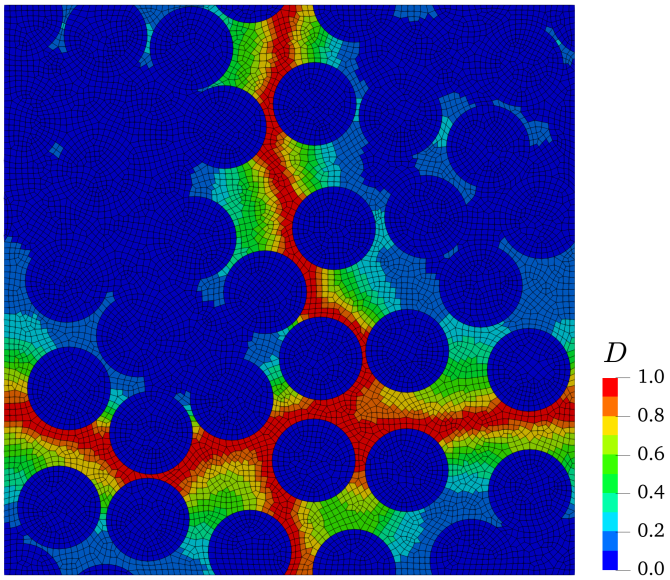

Figure 4.22: Damage contour plot of one realization of one RUC of size $48\,\mu\mathrm{m} \times 48\,\mu\mathrm{m} \times 1\,\mu\mathrm{m}$ showing failure zone bifurcation; loading parameter $b = 0.4$.

4.6.7 RUCs with damaging interfaces

In the following, the results of ten realizations of size $24\,\mu\mathrm{m} \times 24\,\mu\mathrm{m} \times 1\,\mu\mathrm{m}$ with softening induced via damage and debonding of the matrix-fiber interface are presented. This RUC size was chosen despite a bigger RUC size was found to show converged results. The lower RUC size was chosen because of the numerically expensive simulations when bulk damage and debonding are simulated. One simulation took about nine days on Intel Xeon E5-2670 and E5-2667 v2 processors using two CPUs per simulation compared to eight hours of the same RUCs without damaging interfaces. As discussed below, numerical instabilities occurred during simulation which caused a low convergence rate as well as small time stepping. To model the debonding, cohesive zone elements using the cohezive model introduced in Sec. 4.2.2 were applied. Material parameters of the bulk were retained from previous simulations (i.e. are summarized in table 4.1), while cohezive zones with a finite thickness of 1/1000 of the fiber diameter (i.e. $7 \times 10^{-3}\,\mu\mathrm{m}$) were used.

Table 4.4: Material parameters of the interface.

Parameter	Value	Parameter	Value	Parameter	Value
t_0	$50\,\mathrm{MPa}$	λ_0	$2 \times 10^{-2}\,\mu\mathrm{m}$	λ_f	$2 \times 10^{-1}\,\mu\mathrm{m}$
η_{CZ}	$0.5\,\mathrm{MPa\,s\,m^{-1}}$	β	1	H_{pen}	$5000\,\mathrm{MPa\,mm^{-1}}$

In table 4.4, the material parameters of the interface are summarized. The values were taken from literature (i.e. the maximum stress t_0 from [Zhang et al., 2018]) and chosen to yield reasonably results.

A detailed discussion of the material parameters is found in [Poggenpohl et al., 2022*a*].

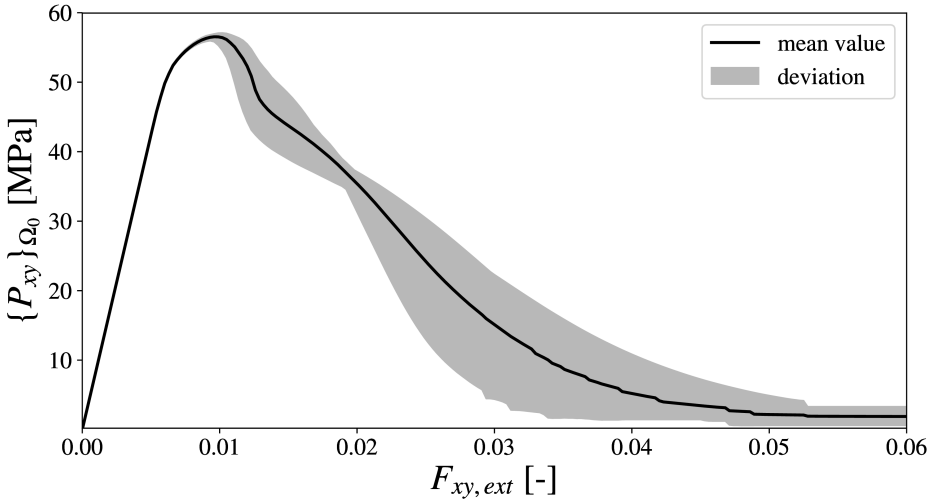

Figure 4.23: Stress-stretch curves resulting from standard homogenization for *RSA* RUCs of size $24\,\mu\mathrm{m} \times 24\,\mu\mathrm{m} \times 1\,\mu\mathrm{m}$ with damaging interfaces; black: Mean value of 10 realizations, grey: Scatter of 10 realizations.

In Fig. 4.23 the stress-stretch plots of ten realizations using standard homogenization for the stress and externally applied deformation gradient for the stretch are summarized. As described in Sec. 4.3, the externally applied (macroscopic) deformation gradient is split into parts of the bulk and interfaces. Thus, using standard homogenization approach of only the bulk (i.e. $\boldsymbol{F}_{\Omega_0/\Gamma_0}$) would lead to false results. Accordingly, the globally determined deformation gradient $\boldsymbol{F}_{ext}$ was chosen here. All simulations were carried out until final failure but became unstable right after. Thus, only a few simulations reached $F_{xy,ext} = 0.06$. The reason for this are the highly distorted finite elements within the failure zone which lead to numerical instabilities. In Figs. 4.24a and 4.24d, the four components of the deformation gradient in the x-y-plane are visualized. As can be seen, some elements reach extreme values in shear or compression and thus might cause numerical instabilities within the material routines. Consequently, not all simulations reached the desired far field stretch. For the analysis, it was assumed that stresses were constant from the last converged step.

Comparing Fig. 4.23 (simulations with damaging interfaces) to 4.9b (simulations with perfect interfaces) the much lower peak stresses become apparent. Furthermore, a higher stretch at peak stress is observed as well as different stretches at which the peak stress occurs. Generally, there is no visible deviation in the elastic as well as in the stretch hardening regime. After peak load, the curves start to deviate and show a neck at a stretch of about 0.02. Afterwards the deviation reaches its maximum at approx. 0.03 stretch and decreases while the curves asymptotically approach zero stress. The necking of the deviation can be related to the different failure mechanisms when damage and debonding are simulated. As shown in Figs. 4.25a to 4.25c, the interface of fibers and matrix is damaged first. Then,

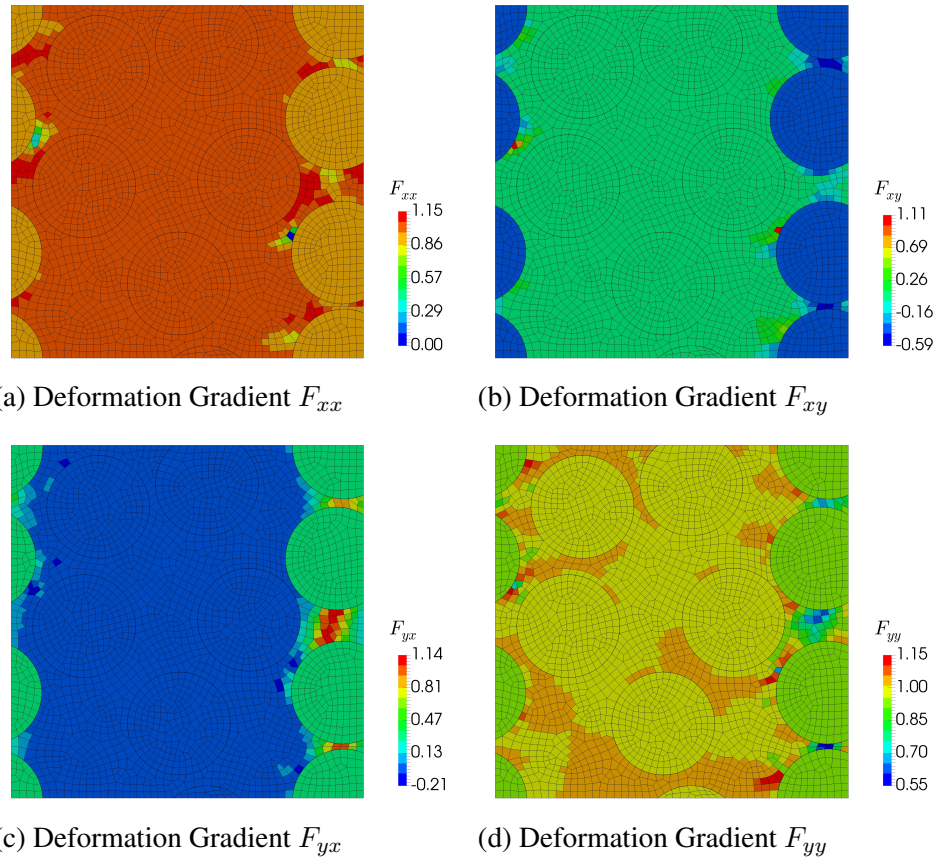

(a) Deformation Gradient F_{xx} (b) Deformation Gradient F_{xy}

(c) Deformation Gradient F_{yx} (d) Deformation Gradient F_{yy}

Figure 4.24: Plots of the components of the deformation gradient of one RUC realization with damaging interfaces of size $24\,\mu\mathrm{m} \times 24\,\mu\mathrm{m} \times 1\,\mu\mathrm{m}$ at the last converged time step.

damage is accumulated within the matrix until localization takes place and a failure zone in matrix and interface develops. These different failure mechanisms are presented in Fig. 4.23 by a slight load drop after maximum stress is reached followed by a homogeneous softening and a final load drop at failure. In general, realizations with a pronounce load drop showed a higher damage resistance later on, thus, giving the neck observed.

Fig. 4.26 summarizes the different work densities evaluated during the simulation of the *RSA* RUCs with damaging interfaces. For a better comparison, the different work densities were calculated with respect to the overall RUC size. Here, the globally determined work density ($\mathcal{W}_{ext}$) as well as the work densities of the actively damaging bulk ($\mathcal{W}_{\Omega_d}$), the elastic domain ($\mathcal{W}_{\Omega_e}$), the actively damaging interfaces ($\mathcal{W}_{\Gamma_d}$) and the elastic interfaces ($\mathcal{W}_{\Gamma_e}$) are shown. For each work density, the mean curve (visualized as a solid line) as well as the the deviation of all ten realizations are shown. Since the quantities shown here are work quantities, negative values (especially for the terms related to elastic loading/unloading) might occur. Exemplary, material points of the bulk which undergo damage loading

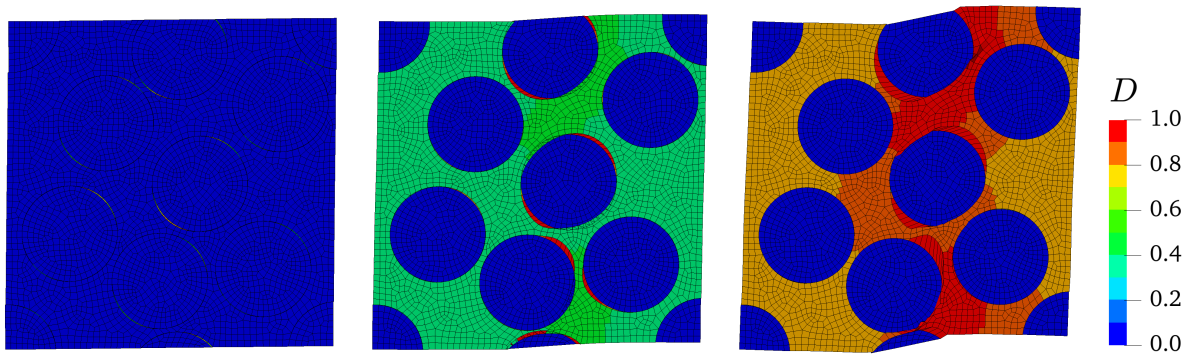

(a) $F_{xy} = 0.0088$ (b) $F_{xy} = 0.0127$ (c) $F_{xy} = 0.0406$

Figure 4.25: Damage contour plots and mesh deformation (deformation factor 1) of one RUC realization with damaging interfaces of size $24\,\mu\text{m} \times 24\,\mu\text{m} \times 1\,\mu\text{m}$ at different stages of far field deformation.

and then elastic unloading will contribute positively to the damage loading and negatively to the elastic unloading.

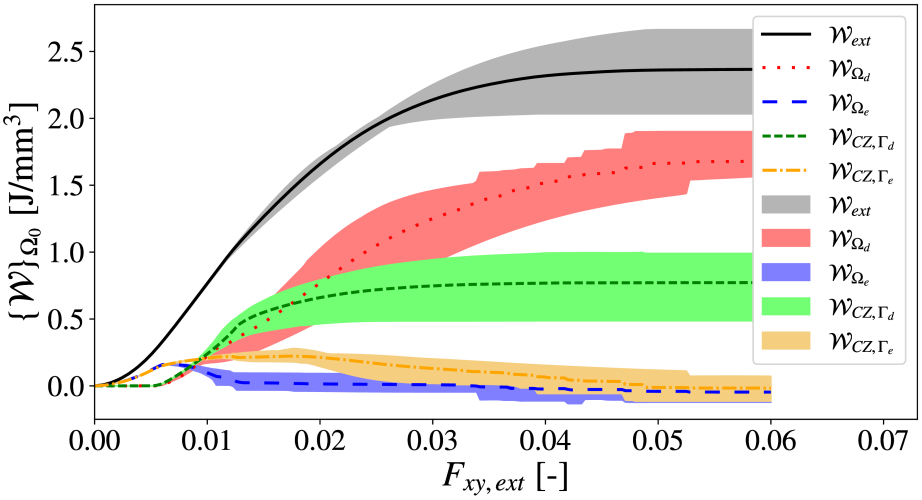

Figure 4.26: Work contributions (based on $\boldsymbol{P} : \boldsymbol{F}$) of the different constituents for the $24\,\mu\text{m}$ RSA RUCs with damaging interfaces; black: global work, red: actively damaging matrix material, blue: elastic matrix material, green: actively damaging interface and orange: elastic interface.

In Fig. 4.26 the different failure mechanisms which were already shown in Figs. 4.25a to 4.25c are seen as well. First, the total energy is governed by the elastic responses of bulk and interfaces. Then, the interfaces as well as the bulk start to damage with the work of the damaging interfaces being slightly higher than the work of the damaging bulk. The elastic work density of the bulk immediately decreases while the elastic work of the interfaces remains constant. At about 0.02 to 0.03 stretch, the work of

the damaging interfaces reach saturation and remain constant while the work of the damaging bulk increases. Between a stretch of approx. 0.033 and 0.052, the work density of the actively damaging bulk shows several distinctive jumps which are related to final failure and thus a sudden increase of work due to high strain rates.

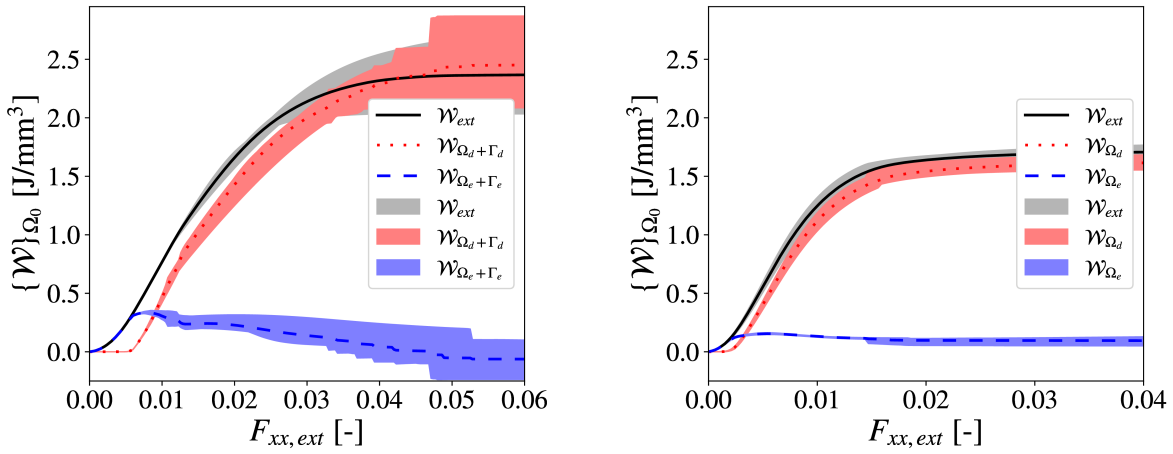

(a) Damaging interfaces (b) Perfect interfaces

Figure 4.27: Work contributions of the elastic and actively damaging regions of the $24\,\mu\text{m}$ RSA RUCs *with* and *without* damaging interfaces; black: global work, red: actively damaging matrix and interfaces, blue: elastic matrix and interfaces.

For a comparison of the work densities of RUCs with and without damaging interfaces, Figs. 4.27a and 4.27b are presented. In Fig. 4.27a, the work densities of Fig. 4.26 are summarized into actively damaging parts of bulk and interfaces as well as elastic parts of bulk and interfaces. As can be seen, the global work is governed by the elastic contributions until onset of damage at an externally applied stretch of approx. 0.006. Thereafter, the work of the elastic parts continuously declines and reaches negative values at the end of simulation. Consequently, the work density of the actively damaging region shows a higher slope than the globally determined work density and shows higher values in the end. Again, final failure can be indicated by a fast drop or rise of the work of elastic or actively damaging region, respectively.

In Fig. 4.27b, the energetic contributions of ten realizations of size $24\,\mu\text{m} \times 24\,\mu\text{m} \times 1\,\mu\text{m}$ with perfect interfaces are shown. Here, the same trends as in Fig. 4.27a can be seen. In the beginning, the global energy density is governed completely by elastic contributions. After onset of failure (at approx. 0.002 stretch), the elastic work density continuously declines but in contrast to Fig. 4.27a it does not show negative values at the end of simulation. Consequently, the globally determined work density is higher than the work density of the failure zone. In comparison to the results with damaging interfaces, the overall lower stretches as well as lower work densities become apparent. This is in contrast to the overall higher stresses observed. It is concluded that the overall higher stretches of RUCs accounting

for bulk damage and softening compensate for the lower stresses and thus show a higher dissipation potential.

4.7 Conclusion and outlook

In this work the failure zone homogenization scheme which was proposed in [Poggenpohl et al., 2022*a*] and is based on the failure zone averaging introduced in [Nguyen et al., 2010] was applied to shear and mixed mode loading. The method was applied on RUCs of carbon fiber reinforced plastics of the micro level, where single fibers were resolved. For matrix failure of the micro scale, a St. Venant type material model for finite strains with isotropic damage was introduced. To account for crack closure effects, a tension compression asymmetry was introduced. Further, a gradient damage formulation based on micromorphic damage was introduced to overcome undesired mesh dependence. Additionally, a cohesive zone formulation was introduced to account for fiber-matrix debonding.

Using a statistical analysis of ten different realizations for varying RUC sizes, the RUC size of $48\,\mu\mathrm{m} \times 48\,\mu\mathrm{m} \times 1\,\mu\mathrm{m}$ showed a converged result w.r.t. mechanical work density of the failure zone. A deeper analysis of the results of this RUC size showed different failure zone orientations which lead to different dominant shear components of the deformation tensor. Further, RUCs with damaging interfaces showed lower peak stresses but higher strains until failure and a higher scatter in the stress plots compared to results with perfect interfaces. A comparison of the work densities showed higher values despite the lower stresses observed. Reason for this was found in the higher strains until final failure.

In summary, the failure zone homogenization of [Poggenpohl et al., 2022*a*] was found applicable for large deformations with gradient enhanced damage and tension compression asymmetry in the case of pure shear and simple shear loading. The method was tested using *regular* RUCs as well as a statistical analysis of *RSA* RUCs of different sizes. A comparison of pure and simple shear loading showed that a consistent evaluation of the work needs to take into account all constituents of stress and stretch tensors.

In future works, the established method should be tested against experimental data for validation and parameter identification. The data needed could be obtained via micro DIC and micro CT analysis of CFRPs, as well as micro testing of the individual constituents. Especially the identification of the internal length l_1 would be beneficial in order to obtain a fully defined set of material parameters. With a fully defined set of material parameters at hand, numerical tests could be performed in order to better understand the failure mechanisms of CFRPs at the micro level or to perform a FE^2 analysis of failure mechanisms at the ply level, such as further investigation of the in-situ strength effect of cross ply laminates as shown experimentally by [Parvizi et al., 1978] and investigated numerically, e.g. by [Guillén-Hernández et al., 2020]. Additionally, the numerical efficiency could be improved by implementing the finite element formulation introduced by [Barfusz et al., 2021*b*] in order to investigate bigger RUCs with damaging interfaces or make them available for FE^2 simulations.

Acknowledgements

The financial support of Deutsche Forschungsgemeinschaft (DFG, German Research Foundation) within the project SI1959/7-1 (project number: 423783552) is gratefully acknowledged. Furthermore, H. Holthusen would like to acknowledge the project RE1057/46-1 (project number: 404502442).

4.8 Appendix

As shown in Fig. 4.28, the results generated by the failure zone averaging could show sudden jumps within the stretch calculated. Reason for this inconsistency is found in the TCA introduced as will be discussed in the following.

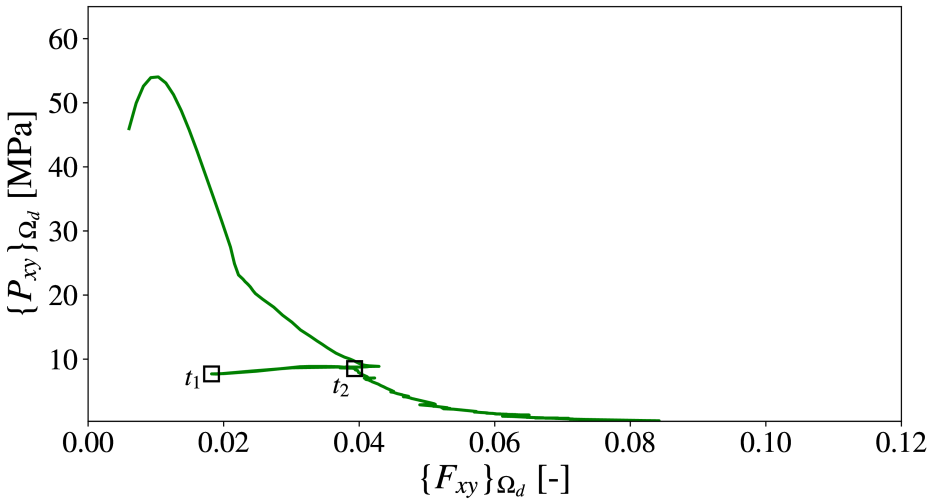

Figure 4.28: Stress-stretch curves of failure zone for one realization of size $48\,\mu\mathrm{m} \times 48\,\mu\mathrm{m} \times 1\,\mu\mathrm{m}$ at pure shear loading; contour plots of the actively damaging zone and shear terms of the deformation gradient for solution times t_1 and t_2 are shown in Figs. 4.29a to 4.29f.

In Figs. 4.29a to 4.29f, contour plots of the actively damaging domain as well as the two shear components of the deformation gradient for two different solution times t_1 and t_2 are shown. The solution times of the contour plots are indicated in Fig. 4.28 as well. As can be seen, the local stretch minimum is related directly to the formation of a band within the localization zone, where damage evolution is deactivated. This band can be related to crack closure effects due to locally compressive stretches and are in line with the area of highest shear strains.

These effects were present only for a few time steps. Thus, the time steps showing this inconsistent behavior were excluded from analysis.

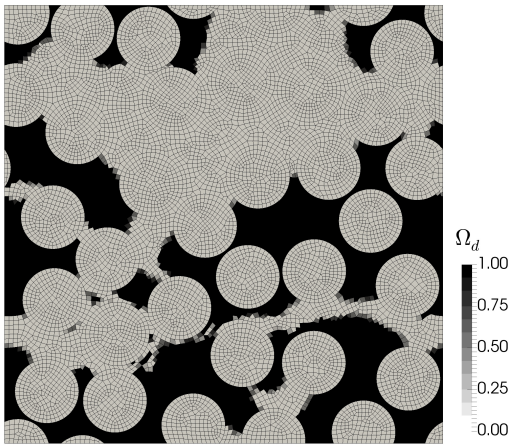

(a) Actively damaging zone at t_1

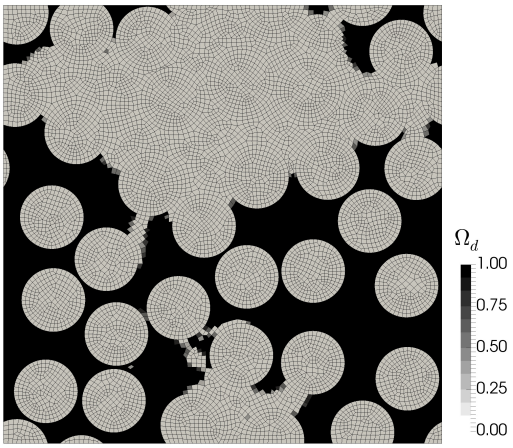

(b) Actively damaging zone at t_2

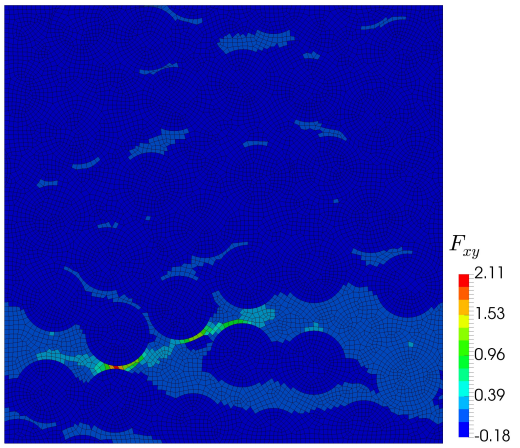

(c) Deformation gradient F_{xy} at t_1

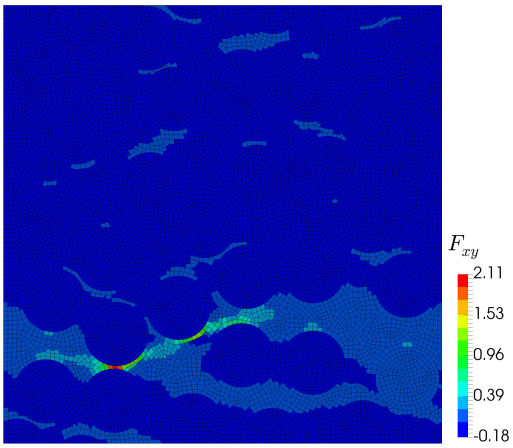

(d) Deformation gradient F_{xy} at t_2

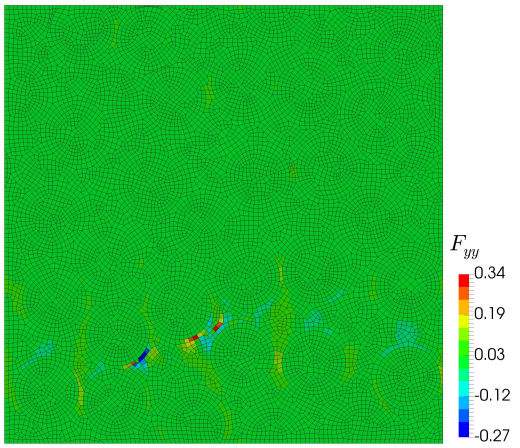

(e) Deformation gradient F_{yx} at t_1

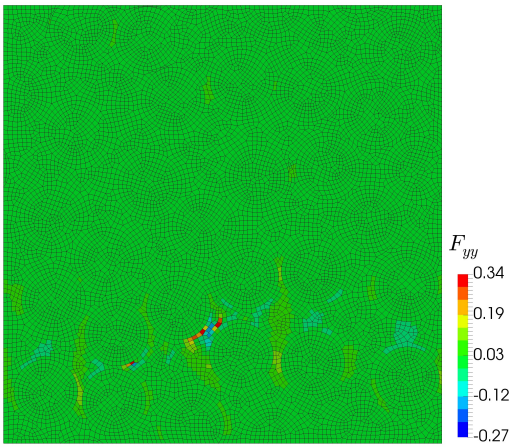

(f) Deformation gradient F_{yx} at t_2

Figure 4.29: Plots of the actively damaging zone and shear components of the deformation gradient for one realization of $48\,\mu\text{m} \times 48\,\mu\text{m} \times 1\,\mu\text{m}$ at different solution times as indicated in Fig 4.28.

5 Conclusions and Outlook

In this dissertation, the brittle damage behavior of UD-CFRPs was simulated at both macro and micro scales. In Article 1 (Chapter 2), the behavior of tensile specimens made of UD-CFRPs was investigated numerically and experimentally. A total of seven different test series with fiber orientations ranging from 0° to 90° were loaded until failure. Ten specimens were used in each test series to account for statistical variance. The maximum strain was observed in the 0° specimen and was approximately 2%. DIC measurements of the strain field showed both residual strain after fracture and localization zones before cracking. These localization zones were observed in the fiber direction and at a different location than the final macroscopic crack. In addition, cyclic loading to a maximum of 75% of the fracture strain was applied to an additional specimen. Using a force-strain curve, residual stresses comparable to those of the DIC measurement were observed, as well as a damaging material response without noticeable plastic deformation. The experimental data provided crucial information on the requirements which the material model had to meet. Thus, a material model was developed to simulate a brittle damage response of an initially anisotropic material for small strains in the context of finite deformations. This material model was implemented as a user element and as a user material in the academic finite element software FEAP. Within the material model, a St. Venant type material model was used for the isotropic part. For the anisotropic expansion, only the strains in the fiber direction were considered using structural tensors. Thus, the additional shear stiffness of the material due to the carbon fibers was neglected. Two independent damage variables were introduced to distinguish between damage in the isotropic part and in the anisotropic part. Micromorphic expansion was introduced to obtain mesh size-independent results. In addition, the structural tensor used for the anisotropic material part was introduced into the micromorphic extension of the isotropic material part. As shown in section 2.4.2.5, this was necessary to achieve a localization zone consistent with experimental results. Simulations were calculated taking into account the entire test specimen geometry and the material parameters of the model were fitted to the experimental data. Overall, good agreement was found between the experimental and numerical results for the 0° and the 90° specimens, while the results for the other fiber orientations tended to differ. Therefore, in order to provide a more accurate prediction of the material response, the material model needs to be extended.

In Article 2 (Chapter 3), a new homogenization method, called failure zone homogenization, was proposed and RUCs of long fiber CFRPs were simulated. Since the epoxy matrix and carbon fibers were spatially resolved, the material model used in Article 1 could be simplified to a St. Venant-

type isotropic material model. In this new homogenization approach, all energetic contributions of the material model, including the contributions of micromorph expansion, were taken into account. It was shown analytically that the energetic contribution of the micromorphic extension is zero in the case of standard Hill homogenization, but is generally nonzero when failure zone homogenization is applied. To rule out numerical artifacts, a series of tests were performed. First, a study of mesh convergence showed that the results were independent of the mesh size.Then, a sensitivity analysis of the artificial viscosity showed converged results for the numerical value used. Afterwards, a comparison of different geometry generation algorithms was performed with ten realizations for each generation algorithm. The results showed a significant difference in the stress-strain curves between the *randomized* and *RSA* generation algorithms. From these results, it was concluded that the *RSA* generation algorithm should be used because it provides more realistic fiber distributions than the *randomized* algorithm. A size convergence study was then performed for RUCs with a regular fiber distribution. Here, it was found that no convergent results were obtained when using the standard Hill homogenization. However, when failure zone homogenization was used, the size effect was no longer present, and the results for the different RUC sizes were in agreement. Next, a statistical analysis of five different RUC sizes was shown.For the standard Hill homogenization, the results again showed no convergence behavior. Additional analysis of the total dissipated energy density confirmed these results. However, when the fracture zone homogenization approach was applied, the stress-strain curves of the different RUC sizes agreed better. Analysis of the dissipated work density also confirmed these results. Thus, fracture zone averaging was used to determine a representative RUC size. Finally, an investigation of the energetic contribution of the micromorphic expansion was performed. The micromorph energy showed a very high peak when the final failure occurred. However, the results indicate that the overall micromorph energetic contribution is small compared to the mechanical work. The article concludes with an energetic study of RUCs with damaging interfaces. Here, the maximum strain was lower compared to the results with perfect interfaces, while a larger variation was observed between different realizations. However, the total strains to final failure were much larger. Thus, an overall higher energy density was observed when non-perfect interfaces were modeled.

In Article 3 (Chapter 3), the failure zone homogenization approach introduced in Article 2 (Chapter 3) is applied to mode II – or shear mode – and mixed mode loading. As in Article 2, the RUCs of long carbon fiber reinforced plastics were analyzed. In addition, the St. Venant-type brittle damaging material model derived from the isotropic part of the material model used in Article 1 (Chapter 2). In addition, tension-compression asymmetry was introduced to account for crack closure effects, and micromorphic extension was applied to obtain results independent of the mesh size. The geometry of the RUCs was generated using either a *regular* fiber distribution or the *RSA* generation algorithm. First, a mesh size study was performed for the pure shear and simple shear load cases. This showed that the loading due to simple shear had a higher sensitivity to mesh size, while mesh size convergence was achieved for both loading scenarios. Subsequently, a size convergence study for RUCs under pure

shear loading was analyzed with the same regular fiber distribution for each RUC size. Here, failure zone homogenization provided results that were almost independent of RUC size, while standard Hill homogenization was found to be dependent on RUC size. Afterwards, a statistical analysis of five RUC sizes, each with 10 realizations, was shown. Here, the results were obtained with the standard Hill homogenization and the fault zone homogenization. For the former, a clear dependence of the obtained stress-strain curve as well as the dissipated working density on the RUC size was exhibited. For the second method, the stress-strain curves agreed much better, and a RUC size of $48\,\mu\mathrm{m}$ showed satisfactory results regarding size convergence. However, it was shown that the shear terms of the homogenized deformation tensor ($\boldsymbol{F}_{xy}$ and $\boldsymbol{F}_{yx}$) are not the same when homogenization of the failure zone is used.It was found that there is always a dominant shear component depending on the orientation of the failure zone. Therefore, the orientation of the failure zone must be considered in the statistical analysis of the RUCs. Conversely, the orientation of the failure zone can be determined if the dominant shear strain is known. Furthermore, the influence of tension-compression asymmetry (TCA) and a change of loading scenario on simple shear strain were investigated. For the former, a slightly higher deviation of the failure strain as well as a lower maximum stress is observed. Further investigation of *RSA* RUCs showed that the introduction of TCA can lead to a different orientation of the failure zone and thus a change in the dominant shear component. A lower slope in the elastic region and generally much higher strains were observed for simple shear loading. However, the overall work density was the same, indicating the importance of considering all stresses and strains. Next, the results of the mixed mode loading were shown. Here, the additional strain required to change the orientation of the fracture zone was analyzed. In this study, the realization that showed sensitivity to TCA also showed a high sensitivity to additional tensile strain. Finally, a set of RUCs with damaging interfaces was analyzed. Here, higher overall strain to failure and lower peak stresses were observed. Furthermore, the influence of tension-compression asymmetry (TCA) and a change of loading scenario on simple shear strain were investigated. For the former, a slightly higher deviation of the failure strain as well as a lower maximum stress is observed. Further investigation of *RSA* RUCs showed that the introduction of TCA can lead to a different orientation of the failure zone and thus a change in the dominant shear component. A lower slope in the elastic region and generally much higher strains were observed for simple shear loading. However, the overall work density was the same, indicating the importance of considering all stresses and strains. Next, the results of the mixed loading were shown. Here, the additional strain required to change the orientation of the fracture zone was analyzed. Here, the transposition that showed sensitivity to TCA also showed high sensitivity to additional tensile strain. Finally, a set of RUCs with damaging interfaces was analyzed. Here, higher overall strain to failure and lower peak stress were observed. In addition, the global stress-strain curves exhibited higher deviation. In particular, a significantly higher difference was observed for strain to failure compared to the simulations with perfect interfaces.Overall, a comparison of the external working density with and without damaging interfaces showed a higher dissipation potential when of non-perfect interfaces are considered.

The new homogenization procedure investigated in Articles 2 and 3 has been shown to show results independent of RUC size for mode I and mode II loading. Based on these promising results, further investigations are possible. For example, as shown by [Morelle et al., 2017] and [Rocha et al., 2019], the epoxy matrix can exhibit significant plastic deformation to failure depending on the triaxiality of the stress state. At mode I failure, the triaxiality is generally low. However, for mode II, arbitrary stress triaxialities can occur. Therefore, a possible next step would be to extend the material model towards a two surface damage plasticity model, such as presented by [Brepols et al., 2020], [Reese et al., 2020], or [Holthusen et al., 2020].Furthermore, the new homogenization method could be used to study the effects of geometric features such as pores and interfacial defects on material behavior, as shown for example in [Nguyen et al., 2011] or [Nguyen et al., 2012]. In addition, the homogenization method could be applied to RUCs of woven CFRPs. Here, the CFRP failure model described in Article 1 could be used to model the failure within the carbon fiber tows. In addition, incorporating the new homogenization method into an FE^2 or staggered scheme would be an interesting application. For example, a tensile separation law of the macroscale was defined using RUC resutls of the microscale in [Nguyen et al., 2012]. However, the stresses and strains of the current approach are evaluated a posteriori and therefore are not known a priori. Therefore, to achieve the desired strain within the failure zone, a new set of boundary conditions would be required. Finally, the introduction of a cohesive zone formulation with better numerical performance would allow analysis of larger RUCs with non-perfect interfaces. This would allow a study of size convergence and a more in-depth comparison of RUCs with damaging interfaces. In addition, the effect of interface toughness on the total damage threshold and energy dissipation potential would be an interesting topic for further research.

List of Figures

List of Tables

Bibliography

Abdullah, A., Chan, H., Zain, M., Ishak, N. and Samad, Z. [2019], 9 - precision punching: A new method in hole-making on composite panels, *in* A. Abdullah and S. Sapuan, eds, 'Hole-Making and Drilling Technology for Composites', Woodhead Publishing Series in Composites Science and Engineering, Woodhead Publishing, pp. 115 – 133.

Azmi, A., Lin, R. and Bhattacharyya, D. [2013], 'Tool wear prediction models during end milling of glass fibre-reinforced polymer composites', *The International Journal of Advanced Manufacturing Technology* **67**(1-4), 701–718.

Bae, S.-Y. and Kim, Y.-H. [2019], 'Structural design and analysis of large wind turbine blade', *Modern Physics Letters B* **33**(14n15), 1940032.

Barfusz, O., Brepols, T., van der Velden, T., Frischkorn, J. and Reese, S. [2021*a*], 'A single gauss point continuum finite element formulation for gradient-extended damage at large deformations', *Computer Methods in Applied Mechanics and Engineering* **373**, 113440.

Barfusz, O., Brepols, T., van der Velden, T., Frischkorn, J. and Reese, S. [2021*b*], 'A single gauss point continuum finite element formulation for gradient-extended damage at large deformations', *Computer Methods in Applied Mechanics and Engineering* **373**, 113440.

Bažant, Z. P. and Gambarova, P. G. [1984], 'Crack shear in concrete: Crack band microflane model', *Journal of Structural Engineering* **110**(9), 2015–2035.

Bayerschen, E., Stricker, M., Wulfinghoff, S., Weygand, D. and Böhlke, T. [2015], Equivalent plastic strain gradient plasticity with grain boundary hardening and comparison to discrete dislocation dynamics, *in* 'Proc. R. Soc. A', Vol. 471, The Royal Society.

Bazant, Z. P., Belytschko, T. B., Chang, T.-P. et al. [1984], 'Continuum theory for strain-softening', *Journal of Engineering Mechanics* **110**(12), 1666–1692.

Bednarcyk, B. A., Stier, B., Simon, J.-W., Reese, S. and Pineda, E. J. [2015], 'Meso- and micro-scale modeling of damage in plain weave composites', *Composite Structures* **121**, 258–270.

Belytschko, T., Liu, W. K., Moran, B. and Elkhodary, K. [2014], *Nonlinear Finite Elements for Continua and Structures*, 2nd edn, Wiley.

Brepols, T., Wulfinghoff, S. and Reese, S. [2017], 'Gradient-extended two-surface damage-plasticity: micromorphic formulation and numerical aspects', *International Journal of Plasticity* **97**, 64–106.

Brepols, T., Wulfinghoff, S. and Reese, S. [2020], 'A gradient-extended two-surface damage-plasticity model for large deformations', *International Journal of Plasticity* **129**, 102635.

Cao, Y., Shen, W., Shao, J. and Wang, W. [2020], 'A novel fft-based phase field model for damage and cracking behavior of heterogeneous materials', *International Journal of Plasticity* **133**, 102786.

Catalanotti, G., Camanho, P. and Marques, A. [2013], 'Three-dimensional failure criteria for fiber-reinforced laminates', *Composite Structures* **95**, 63 – 79.

Chaboche, J. [1978], 'Description phénoménologique de la viscoplasticité cyclique avec endommagement', *Université Pierre et Marie Curie, Paris* **6**.

Chaboche, J. [1984], 'Anisotropic creep damage in the framework of continuum damage mechanics', *Nuclear Engineering and Design* **79**(3), 309–319.

Chatzigeorgiou, G., Charalambakis, N., Chemisky, Y. and Meraghni, F. [2016], 'Periodic homogenization for fully coupled thermomechanical modeling of dissipative generalized standard materials', *International Journal of Plasticity* **81**, 18–39.

Chen, Q. and Wang, G. [2020], 'Computationally-efficient homogenization and localization of unidirectional piezoelectric composites with partially cracked interface', *Composite Structures* **232**, 111452.

Chen, Y. and Aliabadi, M. [2019], 'Micromechanical modelling of the overall response of plain woven polymer matrix composites', *International Journal of Engineering Science* **145**, 103163.

Choi, H., Heinrich, C. and Ji, W. [2019], 'An efficient homogenization technique for fiber tows in textile composites with emphasis on directionally dependent nonlinear stress-strain behavior', *Composite Structures* **208**, 816–825.

Chow, C. L. and Wei, Y. [1999], 'Constitutive modeling of material damage for fatigue failure prediction', *International Journal of Damage Mechanics* **8**(4), 355–375.

Clasen, H., Hirschberger, C. B., Korelc, J. and Wriggers, P. [2013], *Fe2-homogenization of micromorphic elasto-plastic materials*, CIMNE, pp. 280 – 291.

Clay, S. B. and Knoth, P. M. [2017], 'Experimental results of quasi-static testing for calibration and validation of composite progressive damage analysis methods', *Journal of Composite Materials* **51**(10), 1333–1353.

Coleman, B. D. and Noll, W. [1961], 'Foundations of linear viscoelasticity', *Rev. Mod. Phys.* **33**, 239–249.

Cordebois, J. P. and Sidoroff, F. [1982], Damage induced elastic anisotropy, *in* J.-P. Boehler, ed., 'Mechanical Behavior of Anisotropic Solids / Comportment Méchanique des Solides Anisotropes', pp. 761–774.

Cuntze, R. [2006], Failure conditions for isotropic materials, unidirectional composites, woven fabrics-their visualization and links, *in* 'Conference on Damage in Composite Materials 2006, Online-Proceedings'.

de Borst, R., Sluys, L., Muhlhaus, H.-B. and Pamin, J. [1993], 'Fundamental issues in finite element analyses of localization of deformation', *Engineering Computations* **10**(2), 99–121.

de Souza Neto, E. A., Perić, D. and Owen, D. R. J. [2008], *Computational Methods for Plasticity: Theory and Applications*, John Wiley & Sons, Ltd.

Dean, A., Kumar, P., Babiker, A., Brod, M., Elhadi Mohamed Ahmed, S., Reinoso, J. and Mahdi, E. [2021], 'Phase-field modeling of damage and fracture in laminated unidirectional fiber reinforced polymers', *FES Journal of Engineering Sciences* **9**(2), 110–116.

Diamantopoulou, E., Labergere, C., Saanouni, K., Guelorget, B. and François, M. [2018], 'An experimental-numerical study on the plastic flow localization based on a generalized micromorphic formulation', *Technische Mechanik. Wissenschaftliche Zeitschrift für Grundlagen und Anwendungen der Technischen Mechanik* **38**(1), 3–21.

Elnekhaily, S. A. and Talreja, R. [2018], 'Damage initiation in unidirectional fiber composites with different degrees of nonuniform fiber distribution', *Composites Science and Technology* **155**, 22–32.

Fantoni, F., Bacigalupo, A., Paggi, M. and Reinoso, J. [2020], 'A phase field approach for damage propagation in periodic microstructured materials', *International Journal of Fracture* **223**(1), 53–76.

Fassin, M., Eggersmann, R., Wulfinghoff, S. and Reese, S. [2019*a*], 'Efficient algorithmic incorporation of tension compression asymmetry into an anisotropic damage model', *Computer Methods in Applied Mechanics and Engineering* **354**, 932 – 962.

Fassin, M., Eggersmann, R., Wulfinghoff, S. and Reese, S. [2019*b*], 'Gradient-extended anisotropic brittle damage modeling using a second order damage tensor - theory, implementation and numerical examples', *International Journal of Solids and Structures* **167**, 93 – 126.

Felder, S., Kopic-Osmanovic, N., Holthusen, H., Brepols, T. and Reese, S. [2022], 'Thermo-mechanically coupled gradient-extended damage-plasticity modeling of metallic materials at finite strains', *International Journal of Plasticity* **148**, 103142.

Forest, S. [2009], 'Micromorphic approach for gradient elasticity, viscoplasticity, and damage', *Journal of Engineering Mechanics* **135**(3), 117–131.

Forest, S. [2016], 'Nonlinear regularization operators as derived from the micromorphic approach to gradient elasticity, viscoplasticity and damage', **472**(2188), 20150755.

Forest, S. [2019], *Micromorphic Approach to Gradient Plasticity and Damage*, Springer International Publishing, pp. 499–546.

Ge, L., Li, H., Zheng, H., Zhang, C. and Fang, D. [2021], 'Two-scale damage failure analysis of 3d braided composites considering pore defects', *Composite Structures* **260**, 113556.

Geers, M. G. D., Kouznetsova, V. G., Matouš, K. and Yvonnet, J. [2017], *Homogenization Methods and Multiscale Modeling: Nonlinear Problems*, American Cancer Society, pp. 1–34.

Geers, M. G. D., Kouznetsova, V. G., Matouš, K. and Yvonnet, J. [2017], *Homogenization Methods and Multiscale Modeling: Nonlinear Problems*, John Wiley & Sons, Ltd, pp. 1–34.

Geers, M., Kouznetsova, V. and Brekelmans, W. [2010], 'Multi-scale computational homogenization: Trends and challenges', *Journal of Computational and Applied Mathematics* **234**(7), 2175 – 2182. Fourth International Conference on Advanced COmputational Methods in ENgineering (ACOMEN 2008).

Gitman, I., Askes, H. and Sluys, L. [2007], 'Representative volume: Existence and size determination', *Engineering Fracture Mechanics* **74**(16), 2518 – 2534.

Gitman, I. M., Askes, H., Sluys, L. J. and Valls, O. L. [2004], The concept of representative volume for elastic, hardening and softening materials, *in* 'Proceedings of XXXII International Summer School-Conference 'Advance problems in Mechanics'', pp. 180–184.

González, C. and LLorca, J. [2007], 'Mechanical behavior of unidirectional fiber-reinforced polymers under transverse compression: Microscopic mechanisms and modeling', *Composites Science and Technology* **67**(13), 2795–2806.

Guillén-Hernández, T., Quintana-Corominas, A., García, I., Reinoso, J., Paggi, M. and Turón, A. [2020], 'In-situ strength effects in long fibre reinforced composites: A micro-mechanical analysis using the phase field approach of fracture', *Theoretical and Applied Fracture Mechanics* **108**, 102621.

He, C., Ge, J., Zhang, B., Gao, J., Zhong, S., Liu, W. K. and Fang, D. [2020], 'A hierarchical multi-scale model for the elastic-plastic damage behavior of 3d braided composites at high temperature', *Composites Science and Technology* **196**, 108230.

Hill, R. [1967], 'The essential structure of constitutive laws for metal composites and polycrystals', *Journal of the Mechanics and Physics of Solids* **15**(2), 79–95.

Hill, R. [1972], 'On constitutive macro-variables for heterogeneous solids at finite strain', *Proceedings of the Royal Society of London. A. Mathematical and Physical Sciences* **326**(1565), 131–147.

Hirschberger, C. B., Sukumar, N. and Steinmann, P. [2008], 'Computational homogenization of material layers with micromorphic mesostructure', *Philosophical Magazine* **88**(30-32), 3603–3631.

Hobbiebrunken, T., Hojo, M., Fiedler, B., Tanaka, M., Ochiai, S. and Schulte, K. [2004], 'Thermomechanical analysis of micromechanical formation of residual stresses and initial matrix failure in cfrp', *JSME International Journal Series A Solid Mechanics and Material Engineering* **47**(3), 349–356.

Holthusen, H., Brepols, T., Reese, S. and Simon, J.-W. [2020], 'An anisotropic constitutive model for fiber-reinforced materials including gradient-extended damage and plasticity at finite strains', *Theoretical and Applied Fracture Mechanics* **108**, 102642.

Höwer, D., Lerch, B. A., Bednarcyk, B. A., Pineda, E. J., Reese, S. and Simon, J.-W. [2017], 'Cohesive zone modeling for mode I facesheet to core delamination of sandwich panels accounting for fiber bridging', *Composite Structures* .

Höwer, D., Yu, S., Ricks, T. M., Bednarcyk, B. A., Pineda, E. J., Stier, B., Reese, S. and Simon, J.-W. [2019], 'Weave geometry generation avoiding interferences for mesoscale rves', *Journal of Materials Science & Technology* **35**(12), 2869–2882.

Illian, J., Penttinen, A., Stoyan, H. and Stoyan, D. [2008], *Statistical analysis and modelling of spatial point patterns*, Vol. 70, John Wiley & Sons.

Itskov, M. [2009], *Tensor Algebra and Tensor Analysis for Engineers: With Applications to Continuum Mechanics*, 2nd edn, Springer-Verlag Berlin Heidelberg.

Jirásek, M. [2018], Regularized continuum damage formulations acting as localization limiters, *in* 'Computational Modelling of Concrete Structures', CRC Press, pp. 25–41.

Kachanov, L. M. [1958], 'Time of the rupture process under creep conditions, izy akad', *Nank SSR Otd Tech Nauk* **8**, 26–31.

Kammoun, S., Doghri, I., Brassart, L. and Delannay, L. [2015], 'Micromechanical modeling of the progressive failure in short glass–fiber reinforced thermoplastics – first pseudo-grain damage model', *Composites Part A: Applied Science and Manufacturing* **73**, 166–175.

Karayannis, C. G., Kosmidou, P.-M. K. and Chalioris, C. E. [2018], 'Reinforced concrete beams with carbon-fiber-reinforced polymer bars – experimental study', *Fibers* **6**(4).

Ke, L. and Van Der Meer, F. P. [2021], Computational homogenization for modeling of failure in heterogeneous materials. working paper or preprint.
URL: *https://hal.archives-ouvertes.fr/hal-03298979*

Kulosa, M., Neumann, M., Boeff, M., Gaiselmann, G., Schmidt, V. and Hartmaier, A. [2017], 'A study on microstructural parameters for the characterization of granular porous ceramics using a combination of stochastic and mechanical modeling', *International Journal of Applied Mechanics* **09**(05), 1750069.

Ladevèze, P. [1992], 'A damage computational method for composite structures', *Computers & Structures* **44**(1), 79–87. Special Issue: WCCM II.

Läufer, J., Becker, V. and Wagner, W. [2017], 'Gradient enhancement of a transversely isotropic continuum damage model', *Composite Structures* **181**, 138 – 144.

Lemaitre, J. [1971], Evaluation of dissipation and damage in metals, *in* 'Proc. ICM Kyoto', Vol. 1.

Liu, Y., van der Meer, F., Sluys, L. and Ke, L. [2021], 'Modeling of dynamic mode i crack growth in glass fiber-reinforced polymer composites: fracture energy and failure mechanism', *Engineering Fracture Mechanics* **243**, 107522.

Maimí, P., Camanho, P., Mayugo, J. and Dávila, C. [2007], 'A continuum damage model for composite laminates: Part i – constitutive model', *Mechanics of Materials* **39**(10), 897–908.

Makeev, A., Ghaffari, S. and Seon, G. [2019], 'Improving compressive strength of high modulus carbon-fiber reinforced polymeric composites through fiber hybridization', *International Journal of Engineering Science* **142**, 145–157.

Mandal, T. K., Nguyen, V. P. and Wu, J.-Y. [2020], 'A length scale insensitive anisotropic phase field fracture model for hyperelastic composites', *International Journal of Mechanical Sciences* **188**, 105941.

Meade, E. D., Sun, F., Tiernan, P. and O'Dowd, N. P. [2021], 'A multiscale experimentally-based finite element model to predict microstructure and damage evolution in martensitic steels', *International Journal of Plasticity* **139**, 102966.

Melro, A., Camanho, P. and Pinho, S. [2012], 'Influence of geometrical parameters on the elastic response of unidirectional composite materials', *Composite Structures* **94**(11), 3223–3231.

Miehe, C., Aldakheel, F. and Raina, A. [2016], 'Phase field modeling of ductile fracture at finite strains: A variational gradient-extended plasticity-damage theory', *International Journal of Plasticity* **84**, 1–32.

Mikeš, K., Bormann, F., Rokoš, O. and Peerlings, R. [2021], 'Comparative study of multiscale computational strategies for materials with discrete microstructures', *Computer Methods in Applied Mechanics and Engineering* **382**, 113883.

Morelle, X. P., Chevalier, J., Bailly, C., Pardoen, T. and Lani, F. [2017], 'Mechanical characterization and modeling of the deformation and failure of the highly crosslinked rtm6 epoxy resin', *Mechanics of Time-Dependent Materials* **21**, 419–454.

Mozaffari, N. and Voyiadjis, G. Z. [2016], 'Coupled gradient damage - viscoplasticty model for ductile materials: Phase field approach', *International Journal of Plasticity* **83**, 55–73.

Mukhopadhyay, S. and Hallett, S. R. [2019], 'A directed continuum damage mechanics method for modelling composite matrix cracks', *Composites Science and Technology* **176**, 1–8.

Murakami, S. and Ohno, N. [1981], A continuum theory of creep and creep damage, *in* A. R. S. Ponter and D. R. Hayhurst, eds, 'Creep in Structures', pp. 422–444.

Nguyen, V. P., Lloberas-Valls, O., Stroeven, M. and Sluys, L. J. [2010], 'On the existence of representative volumes for softening quasi-brittle materials - a failure zone averaging scheme', *Computer Methods in Applied Mechanics and Engineering* **199**(45), 3028 – 3038.

Nguyen, V. P., Lloberas-Valls, O., Stroeven, M. and Sluys, L. J. [2011], 'Computational homogenization for multiscale crack modeling. implementational and computational aspects', *International Journal for Numerical Methods in Engineering* **89**(2), 192–226.

Nguyen, V. P., Stroeven, M. and Sluys, L. J. [2012], 'Multiscale failure modeling of concrete: Micromechanical modeling, discontinuous homogenization and parallel computations', *Computer Methods in Applied Mechanics and Engineering* **201-204**, 139 – 156.

Pak, S. Y., Kim, S. Y., Lee, D. and Song, Y. S. [2021], 'Micro-macroscopic coupled modeling for the prediction of synergistic improvement on the thermal conductivity of boron nitride and multi-walled carbon nanotube reinforced composites', *Composites Part A: Applied Science and Manufacturing* **148**, 106474.

Pantelelis, N. and Bistekos, E. [2010], Process monitoring and control for the production of cfrp components, *in* 'at SAMPE Conference, Seattle'.

París, F., Velasco, M. L. and Correa, E. [2018], 'Micromechanical study on the influence of scale effect in the first stage of damage in composites', *Composites Science and Technology* **160**, 1–8.

Parvizi, A., Garrett, K. W. and Bailey, J. E. [1978], 'Constrained cracking in glass fibre-reinforced epoxy cross-ply laminates', *Journal of Materials Science* **13**, 195–201.

Peerlings, R., Geers, M., de Borst, R. and Brekelmans, W. [2001], 'A critical comparison of non-local and gradient-enhanced softening continua', *International Journal of Solids and Structures* **38**(44), 7723–7746.

Peerlings, R. H. J., de Borst, R., Brekelmans, W. A. M. and de Vree, J. H. P. [1996], 'Gradient enhanced damage for quasi-brittle materials', *International Journal for Numerical Methods in Engineering* **39**(19), 3391–3403.

Peerlings, R., Massart, T. and Geers, M. [2004], 'A thermodynamically motivated implicit gradient damage framework and its application to brick masonry cracking', *Computer Methods in Applied Mechanics and Engineering* **193**(30), 3403–3417. Computational Failure Mechanics.

Pietruszczak, S. and Mróz, Z. [1981], 'Finite element analysis of deformation of strain-softening materials', *International Journal for Numerical Methods in Engineering* **17**(3), 327–334.

Pineda, E. J., Bednarcyk, B. A., Waas, A. M. and Arnold, S. M. [2013], 'On multiscale modeling using the generalized method of cells: Preserving energy dissipation across disparate length scales', *Computers, Materials & Continua* **35**(2), 119–154.

Poggenpohl, L., Brepols, T., Holthusen, H., Wulfinghoff, S. and Reese, S. [2021], 'Towards brittle damage in carbon fiber reinforced plastics: A gradient extended approach', *Composite Structures* p. 112911.

Poggenpohl, L., Holthusen, H. H. and Simon, J.-W. [2022*a*], 'Failure zone homogenization for modeling damage- and debonding-induced softening in composites including gradient-extended damage at finite strains', *International Journal of Plasticity* **TBA**(TBA), TBA–TBA.

Poggenpohl, L., Holthusen, H. and Simon, J.-W. [2022*b*], 'Failure zone homogenization at mode ii and mixed mode loading including gradient-extended damage and interface debonding at finite strains', *Composite Structures* **298**, 115997.

Poggenpohl, L. and Simon, J.-W. [2021], Investigation of power contributions of repeating unit cells of carbon fiber reinforced plastics at failure, *in* 'Proceedings of 8th ECCOMAS Thematic Conference on the Mechanical Response of Composites'.

Poggenpohl, L., Wulfinghoff, S. and Reese, S. [2018], 'A new approach in material modeling towards shear cutting of carbon fiber reinforced plastics', *Technische Mechanik* **38**(1), 91–96.

Puck, A. [1992], 'A failure criterion shows the direction', *Kunststoffe German Plastics(Germany)* **82**(7), 607–610.

Puck, A. and Schürmann, H. [2002], 'Failure analysis of frp laminates by means of physically based phenomenological models', *Composites Science and Technology* **62**(12-13), 1633–1662.

Qiu, G. and Pence, T. [1997], 'Remarks on the behavior of simple directionally reinforced incompressible nonlinearly elastic solids', *Journal of Elasticity* **49**(1), 1–30.

Rabotnov, Y. N. [1963], 'Paper 68: On the equation of state of creep', *Proceedings of the Institution of Mechanical Engineers, Conference Proceedings* **178**(1), 2–117–2–122.

Rabotnov, Y. N. [1969], Creep rupture, *in* 'Applied Mechanics', Springer Berlin Heidelberg, pp. 342–349.

Reese, S. [2003], 'Meso-macro modelling of fibre-reinforced rubber-like composites exhibiting large elastoplastic deformation', *International Journal of Solids and Structures* **40**(4), 951 – 980.

Reese, S. [2007], 'A large deformation solid-shell concept based on reduced integration with hourglass stabilization', *International Journal for Numerical Methods in Engineering* **69**(8), 1671–1716.

Reese, S., Brepols, T., Fassin, M., Poggenpohl, L. and Wulfinghoff, S. [2020], 'Using structural tensors for inelastic material modeling in the finite strain regime – a novel approach to anisotropic damage', *Journal of Mechanics and Physics of Solids* . (submitted: February 2020).

Rezaei, S., Wulfinghoff, S. and Reese, S. [2017], 'Prediction of fracture and damage in micro/nano coating systems using cohesive zone elements', *International Journal of Solids and Structures* **121**, 62 – 74.

Rocha, I., van der Meer, F., Raijmaekers, S., Lahuerta, F., Nijssen, R. and Sluys, L. [2019], 'Numerical/experimental study of the monotonic and cyclic viscoelastic/viscoplastic/fracture behavior of an epoxy resin', *International Journal of Solids and Structures* **168**, 153–165.

Rösler, J., Hardes, H. and Bäcker, M. [2013], *Mechanisches Verhalten der Werkstoffe*, Springer-Verlag Berlin Heidelberg.

Ryvkin, M. and Aboudi, J. [2020], 'Three dimensional analysis of periodic fiber-reinforced composites with randomly broken and debonded fibers', *International Journal of Engineering Science* **155**, 103363.

Schneider, K., Klusemann, B. and Bargmann, S. [2016], 'Automatic three-dimensional geometry and mesh generation of periodic representative volume elements for matrix-inclusion composites', *Advances in Engineering Software* **99**, 177 – 188.

Settgast, C., Hütter, G., Kuna, M. and Abendroth, M. [2020], 'A hybrid approach to simulate the homogenized irreversible elastic-plastic deformations and damage of foams by neural networks', *International Journal of Plasticity* **126**, 102624.

Shirobokov, A., Kerchnawe, S., Terhorst, M., Mattfeld, P. and Klocke, F. [2015], 'Blanking of unidirectional carbon fibre reinforced plastics', *Applied Mechanics & Materials* **794**, 223–230.

Sidoroff, F. [1981], Description of anisotropic damage application to elasticity, *in* J. Hult and J. Lemaitre, eds, 'Physical Non-Linearities in Structural Analysis', pp. 237–244.

Simo, J. C. and Taylor, R. L. [1985], 'Consistent tangent operators for rate-independent elastoplasticity', *Computer Methods in Applied Mechanics and Engineering* **48**(1), 101 – 118.

Simon, J.-W., Höwer, D., Stier, B. and Reese, S. [2015], 'Meso-mechanically motivated modeling of layered fiber reinforced composites accounting for delamination', *Composite Structures* **122**, 477–487.

Simon, J.-W., Höwer, D., Stier, B., Reese, S. and Fish, J. [2017], 'A regularized orthotropic continuum damage model for layered composites: intralaminar damage progression and delamination', *Computational Mechanics* **60**(3), 445–463.

Skrzypek, J. J. and Ganczarski, A. [1999], *Modeling of Material Damage and Failure of Structures*, Springer, Berlin, Heidelberg.

Stier, B., Simon, J.-W. and Reese, S. [2015], 'Comparing experimental results to a numerical meso-scale approach for woven fiber reinforced plastics', *Composite Structures* **122**, 553–560.

Trofimov, A., Le-Pavic, J., Ravey, C., Albouy, W., Therriault, D. and Lévesque, M. [2021], 'Multi-scale modeling of distortion in the non-flat 3d woven composite part manufactured using resin transfer molding', *Composites Part A: Applied Science and Manufacturing* **140**, 106145.

Tsai, S. W. and Wu, E. M. [1971], 'A general theory of strength for anisotropic materials', *Journal of Composite Materials* **5**(1), 58–80.

Tsalis, D., Baxevanis, T., Chatzigeorgiou, G. and Charalambakis, N. [2013], 'Homogenization of elastoplastic composites with generalized periodicity in the microstructure', *International Journal of Plasticity* **51**, 161–187.

Turteltaub, S. and de Jong, G. [2019], 'Multiscale modeling of the effect of sub-ply voids on the failure of composite materials', *International Journal of Solids and Structures* **165**, 63 – 74.

Turteltaub, S. and Suárez-Millán, R. [2020], 'Energetically-consistent multiscale analysis of fracture in composites materials', *European Journal of Mechanics - A/Solids* **84**, 104079.

Turteltaub, S., van Hoorn, N., Westbroek, W. and Hirsch, C. [2018], 'Multiscale analysis of mixed-mode fracture and effective traction-separation relations for composite materials', *Journal of the Mechanics and Physics of Solids* **117**, 88 – 109.

Vakulenko, A. and Kachanov, M. [1971], 'Continuum theory of medium with cracks', *Mekhanika tverdogo tela* **6**(4), 159–166.

van der Meer, F. and Sluys, L. [2009], 'Continuum models for the analysis of progressive failure in composite laminates', *Journal of Composite Materials* **43**(20), 2131–2156.

Verhoosel, C. V., Remmers, J. J. C., Gutiérrez, M. A. and de Borst, R. [2010], 'Computational homogenization for adhesive and cohesive failure in quasi-brittle solids', *International Journal for Numerical Methods in Engineering* **83**(8-9), 1155–1179.

Voyiadjis, G. Z. and Deliktas, B. [2000], 'A coupled anisotropic damage model for the inelastic response of composite materials', *Computer Methods in Applied Mechanics and Engineering* **183**(3), 159–199.

Witik, R. A., Payet, J., Michaud, V., Ludwig, C. and Månson, J.-A. E. [2011], 'Assessing the life cycle costs and environmental performance of lightweight materials in automobile applications', *Composites Part A: Applied Science and Manufacturing* **42**(11), 1694–1709.

Wriggers, P. [2008], *Nonlinear Finite Element Methods*, Springer-Verlag Berlin Heidelberg.

Wu, J.-Y., Nguyen, V. P., Nguyen, C. T., Sutula, D., Sinaie, S. and Bordas, S. P. [2020], Chapter one - phase-field modeling of fracture, *in* S. P. Bordas and D. S. Balint, eds, 'Advances in Applied Mechanics', Vol. 53 of *Advances in Applied Mechanics*, Elsevier, pp. 1–183.

Wulfinghoff, S., Bayerschen, E. and Böhlke, T. [2013], 'A gradient plasticity grain boundary yield theory', *International Journal of Plasticity* **51**, 33–46.

Wulfinghoff, S., Fassin, M. and Reese, S. [2017], 'A damage growth criterion for anisotropic damage models motivated from micromechanics', *International Journal of Solids and Structures* **121**, 21–32.

Yamane, K. and Furuhama, S. [1998], 'A study on the effect of the total weight of fuel and fuel tank on the driving performances of cars', *International Journal of Hydrogen Energy* **23**(9), 825–831.

Yu, W. [2016], An introduction to micromechanics, *in* 'Composite Materials and Structures in Aerospace Engineering', Vol. 828 of *Applied Mechanics and Materials*, Trans Tech Publications Ltd, pp. 3–24.

Zhang, C., Liu, L., Xu, Z., Lv, H., Wu, N., Zhou, B., Mai, W., Zhao, L., Tian, X. and Guo, X. [2018], 'Improvement for interface adhesion of epoxy/carbon fibers endowed with carbon nanotubes via microwave plasma-enhanced chemical vapor deposition', *Polymer Composites* **39**(S2), E1262–E1268.